

**Faculty of Science and Engineering
Department of Petroleum Engineering**

Enhanced Gas Recovery by CO₂ injection

Hiwa H Amin Sidiq

**This thesis is presented for the degree of
Doctor of Philosophy
of
Curtin University of Technology**

October 2010

Declaration

To the best of my knowledge and belief this thesis contains no material previously published by any other person except where due acknowledgment has been made.

This thesis contains no material which has been accepted for the award of any other degree or diploma in any university.

Signature.....

Date.....

Acknowledgements

Sincere gratitude is expressed to my supervisor, Professor Robert Amin, for his professional guidance and continuous encouragement throughout my thesis work. His dedication and enthusiasm for scientific research is unsurpassed, and his vast knowledge and incisive insight have been inspiring.

I wish to express my thanks to Associate Professor David Pack, for his assistance during the experiments and helpful discussions. In addition, I would like to thank all staff at CGTA, Ms. Sabine Isbarn, A/Prof. Ahmed Barifcani and Mr. Al- Abri for their enormous support and help.

I gratefully acknowledge the financial support to this work from Shell Australia, especial thanks to Erik Van der Steen. I would also like to thank Mr. Tony Kennaird from Core Laboratories Australia for the valuable technical assistance. I am also grateful to the many individuals who helped me throughout this study.

I would also like to extend my sincere appreciation to my beloved wife Shoxan and my son Laso for the tremendous support and understanding received during my study.

Last but not least, I would like to acknowledge my parents and family back home in Kurdistan for their encouragement and support.

About the Project

This research work was conducted for the newly discovered natural gas reservoirs in Northwest shelf of Western Australia operated by Shell Australia Limited. Gas production can be improved by sequestering the fraction of CO₂ that is coupled with the production of natural gas. On this topic the following papers have been published in journals and presented at conferences.

Peer reviewed papers:

Al-Abri, A., H. Sidiq, and R. Amin. 2009. Experimental investigation of the velocity-dependent relative permeability and sweep efficiency of supercritical CO₂ injection into gas condensate reservoirs. *Journal of Natural Gas Science and Engineering* 1: 158-164.

Al-Abri, A., H. Sidiq, and R. Amin. 2010. Enhanced Natural Gas and Condensate Recovery by Carbon Dioxide and Methane Flooding. *Petroleum Science and Technology* in press.

Amin, R., H. Sidiq, T. Kennaird, and E. Van der Steen. 2010. Gas-Gas Experimental Interfacial Tension Measurement. *Fluid Phase Equilibria* 295 (2): 230-236.

Sidiq, H., and R. Amin. 2009. Mathematical model for calculating the dispersion coefficient of supercritical CO₂ from the results of laboratory experiments on enhanced gas recovery. *Journal of Natural Gas Science and Engineering* 1: 177-182.

Sidiq, H., and R. Amin. 2010. Impact of Pore-Pressure on CO₂-Methane Displacement. *Petroleum Science and Technology* in press.

Conference papers:

Al-Abri, A., H. Sidiq, and R. Amin. 2009. *SPE Annual Technical Conference and Exhibition, October, 4–7 2009: Enhanced Natural Gas and Condensate Recovery by Injection of Pure SCCO₂, Pure CH₄ and their Mixtures: Experimental Investigation*. New Orleans, Louisiana, USA: SPE 124145-PP.

Sidiq, H., and R. Amin. 2010. SuperCritical CO₂-Methane Relative Permeability Investigation. In *International Conference on CO₂ Capture, Storage, and Utilization*. New Orleans, Louisiana, USA. SPE 137884.

Abstract

The central issue in the physical processes of enhanced gas recovery by carbon dioxide (CO₂) injection is the extent to which the natural gas will mix with the injected CO₂ and reduce the calorific value of the natural gas. Mixing in such a system is a diffusion-like process, which definitely depends on the physical properties of the displacing and displaced phases and the heterogeneity of the medium. However CO₂ undergoes a large change in density in the gas phase as it passes through the critical pressure at temperatures near the critical temperature. At the extreme reservoir conditions with pressure of 6000 psi and temperature of 160 °C, CO₂ exhibits a greater viscosity and density when compared to methane. This variation is approximately a factor of three, which is in favour of the CO₂-natural gas displacement. In contrast, at near supercritical conditions of pressure of 1071 psi and temperature of 31 °C, the CO₂ physical properties (viscosity and density) are slightly superior methane's. Results indicated improved recovery efficiency was obtained with tests that were conducted at higher pore pressure, higher displacement speed and higher methane concentration in the in situ gas. In addition, low quality rock at a lower temperature of 95 °C also showed better ultimate recovery.

In this work, the first ever attempt for measuring interfacial tension (IFT) in a Gas-Gas system, namely supercritical carbon dioxide (SCO₂) and methane was made. Experiments were conducted at temperatures of 95 °C and 160 °C and pressures from 1000 to 6000 psia, using a modified reverse pendant drop method. It is common knowledge that a thermodynamically stable interface can only exist between two immiscible fluids, nonetheless an "immiscible interface" between two gases (CO₂-methane) has been observed and is documented within this research work.

It was noted that the IFT decreased linearly with both temperature and pressure in the low-pressure range, but was less sensitive at higher pressures. There was a zone in the vicinity of 1500 psia and above that was noted to be independent of temperature where IFT increased sharply. The IFT was almost three times higher at 3000 psia, for the same temperature, compared with 1000 psia. This is attributed to the density of SCO₂ at 1000 psia being less than 1/3 the density at 3000 psia, at the same temperature.

Nomenclature

Symbol

A	Cross sectional area, cm^2
C	Concentration
D_o	Molecular diffusion, cm^2/sec
g	Gravitational constant
G	Quantity of material diffused across a plane
$J(S)$	Dimensionless capillary pressure
K_a	Air permeability
K_i	Average SCO_2 dispersion coefficient, cm^2/min
K_{Ir}	Dispersion coefficient caused by injection rate, cm^2/min
K_{ra}	Phase relative permeability
K_w	Absolute water permeability
L	Sample length, cm
M	Mobility ratio
Δp	Pressure difference across the core sample
Q	Flow rate, cm^3 per second
Re	Reynolds number
r_e	Drainage radius
t	Time, sec
t_b	Time to breakthrough, min
u	Interstitial velocity, cm/sec
V_p	Pore volume
V_{ri}	Reference volume of cell i
X	Distance, cm
X_D	Displaced distance from the inlet of the core in case no diffusion assumed
β	Shape factor
μ	Viscosity of the injected fluid
ϕ	Porosity, volume fraction
Ω	Omega parameter

$\sigma^{\alpha,\beta}$	Surface tension, Dyne/cm
θ	Contact angle
ρ	Density
$\sigma^{l,s}$	Liquid-solid surface tension
$\sigma^{l,a}$	Liquid-air surface tension
$\sigma^{s,a}$	Solid-air surface tension
γ_{ls}	Liquid-solid surface tension
γ_{la}	Liquid-air surface tension
γ_{sa}	Solid-air surface tension

Abbreviation

C^*	Trapping characteristic constant
f_c	Fractional composition of in situ gas
f_g	Gas fractional flow
f_w	Water fractional flow
Ir	Relative injectivity = $u/\Delta p$ / (initial $u/\Delta p$), and $u=q/\Delta p$
K_{nwr}^I	Imbibition non-wetting phase relative permeability
K_{nwr}^D	Drainage non-wetting phase relative permeability
Kr_{CO_2}	SCO ₂ relative permeability
Kr_{C_1}	Methane relative permeability
Np	Cumulative production,
Q_{ci}	Injection or production rate of component c in cell i due to wells
S_{CO_2}	Fractional saturation of SCO ₂
S_{av}	Average saturation
S_{ir}	Irreducible saturation
S_{nwi}	Initial wetting saturation
S_{nwr}	Residual non-wetting saturation
S_{wi}	Irreducible water saturation
Vp	Pore volume
vX	Fluid composition (X) and molar volume (v)
Wi	Cumulative injection per Vp

Contents

Chapter 1	1
Introduction	1
<i>1.1 Statement of the Problem:</i>	3
<i>1.2 Relative permeability model of a gas-gas system:</i>	4
<i>1.3 Objective and Significance:</i>	7
<i>1.4 Thesis outline:</i>	9
Chapter 2	11
Background History	11
<i>2.1 Introduction:</i>	11
<i>2.2 Methane-CO₂ phase behaviour:</i>	11
<i>2.3 Physical properties of methane-CO₂:</i>	13
<i>2.4 CO₂ for enhanced gas recovery:</i>	14
2.4.1 <i>Mixing gas-gas by dispersion:</i>	16
<i>2.5 CO₂ for enhanced oil recovery:</i>	18
<i>2.6 CO₂ for enhanced coal bed methane recovery:</i>	21
<i>2.7 SCO₂ disposal into aquifer:</i>	22
2.7.1 <i>Chemical process during CO₂ injection:</i>	23
<i>2.8 Relative Permeability:</i>	24
2.8.1 <i>Fluid distribution on the pore scale:</i>	29
2.8.2 <i>Effect of miscibility:</i>	30
2.8.3 <i>Effect of interfacial tension:</i>	31
2.8.4 <i>Effect of wettability:</i>	32
2.8.5 <i>Effect of capillarity:</i>	34
2.8.6 <i>Effect of high capillary number:</i>	37
2.8.7 <i>Effect of Bond number:</i>	37
2.8.8 <i>Effect of viscosity contrast:</i>	38
2.8.9 <i>Effect of pores morphology:</i>	39
Chapter 3	41
Experiments and Equipment Set-up	41
<i>3.1 Introduction:</i>	41
<i>3.2 Equipment set-up for IFT measurements:</i>	41
3.2.1 <i>Test producers:</i>	42
<i>3.3 Core-flooding setup and apparatus:</i>	43
<i>3.4 Calibrations producers:</i>	47
Chapter 4	50
Interfacial Tension Measurements	50
<i>4.1 Introduction:</i>	50
<i>4.2 Theory back ground:</i>	50
4.2.1 <i>Properties of supercritical CO₂-methane:</i>	51

4.3 Methodology:	53
4.4 Experimental results:	57
4.4.1 Results of tests conducted at 95 °C.....	57
4.4.1 Results of tests conducted at 160 °C.....	58
4.5 Evolution of Gas-Gas Gradient Zone:	59
4.6 Discussion:.....	61
Chapter 5	63
Unsteady state experiments.....	63
5.1 Introduction:.....	63
5.2 Preliminary tests:.....	64
5.3 Test sequences:	65
5.4 Fluid flow in porous media:	68
5.4.1 Permeability calculation:	68
5.4.2 Basic permeability measurements:.....	70
5.4.3 Screening test:.....	74
5.5 Relative permeability:.....	77
5.5.1 Gas-water relative permeability:.....	77
5.5.2 Effect of permeability heterogeneity:.....	87
Chapter 6	89
Gas-Gas displacement.....	89
6.1 Introduction:.....	89
6.2 Impact of composition:.....	90
6.3 Impact of displacement rate:	96
6.3.1 Repeatability tests:.....	101
6.4 Impact of pore pressure:.....	102
6.4.1 Repeatability tests:.....	107
6.6 Impact of temperature:.....	111
6.6 Wider implications:	114
6.6 Evaluation of experimental measurements:	115
6.7 Discussion:.....	115
Chapter 7	117
Dispersion and diffusion mechanisms	117
7.1 Introduction:.....	117
7.2 Review of gas displacement in porous media:	117
7.3 Theory of dispersion:.....	120
7.4 New Model:.....	121
7.5 Results and discussion:	123
7.6 Discussion:.....	128

Chapter 8	129
Steady state tests.....	129
8.1 <i>Introduction:</i>	129
8.2 <i>Experimental procedure:</i>	129
8.3 <i>Steady state relative permeability:</i>	131
8.3.1 <i>Sample S_V_1:</i>	131
8.3.2 <i>Sample S_C_1A:</i>	134
8.3.3 <i>Sample S_C_2A and S_C_3A:</i>	135
Chapter 9	137
Simulation	137
9.1 <i>Introduction:</i>	137
9.2 <i>Tempest simulator:</i>	137
9.3 <i>Geo-model:</i>	140
9.4 <i>Simulation case studies:</i>	143
9.4.1 <i>Base case:</i>	143
9.4.2 <i>Case-1:</i>	144
9.4.3 <i>Case-2:</i>	148
9.4.4 <i>Case-3:</i>	150
Chapter 10	152
Conclusion and Recommendations.....	152
10.1 <i>Conclusions and discussions:</i>	152
10.2 <i>Recommendation:</i>	156
Appendix	168
Appendix A:	169
Appendix B:	170
Appendix C:.....	176
Appendix D:.....	177
Appendix E:	190

List of Figures

Figure 1.1: Density and viscosity of Carbon dioxide and Methane at 40 °C and different pressure and composition. After Oldenburg and Benson (2002).	2
Figure 1.2: (a) Mass fraction of CO ₂ (b) Gas density after 10 years of CO ₂ injection with a constant pressure from upper left hand. After Oldenburg and Benson (2002).	3
Figure 1.3: Schematic of gas relative permeability trapping model for water-wet porous media. After Land (1968).	6
Figure 2.1: Three phase H-L _w -V equilibrium curves of pore hydrates from CO ₂ -methane phase equilibria. After Seo, Lee, and Uchida (2002).	12
Figure 2.2: CO ₂ -methane physical properties at different conditions of pressure and temperature. After Oldenburg, Pruess, and Benson (2001).	14
Figure 2.3: CO ₂ -H ₂ S breakthrough from well 06-23. After Darvish et al. (2008).	16
Figure 2.4: Pore level schematic of foam in porous media. After Tanzil (2001).	20
Figure 2.5: Gas relative permeability as a function of liquid saturation. After Muskat et al (1937).	25
Figure 2.6: Ideal Gas relative permeability for two miscible fluids.	27
Figure 2.7: Interface between SCO ₂ and methane, the bubble is SCO ₂ and the ambient is methane at 3000 psia and 95 °C.	30
Figure 2.8: Schematic explanation of wetting phase and non-wetting phase contact angles that forms with a solid surface. (a) Partially wetting the solid $\theta > 0$, (b) completely wetting the solid ($\theta = 0$).	34
Figure 2.9: Schematic explanation of wetting and non-wetting phase distribution over pore network during displacement process.	36
Figure 3.1: Sketch of apparatus used in investigating methane-SCO ₂ interface.	42
Figure 3.2: Sketch of the experiment apparatus designed for the tests up to 95 °C and 6000 psia.	44
Figure 3.3: Samples of O-rings damaged during the experimental runs.	45
Figure 3.4: Modified Sketch of the experiment apparatus designed to stand up to 160 °C and 6000 psia.	46
Figure 3.5: Bubbles and Melting appearing on the inner layer of the sleeve after a run.	47
Figure 3.6: Sketch illustrating the technique of calibrating pressure transducers in a coupling connection.	48
Figure 3.7: Differential pressure between P1 and P2 when connected to one source of pressure from 6000 psia to 5700 psia.	48
Figure 4.1: CO ₂ -Methane densities at various temperatures and pressures.	52
Figure 4.2: Shows denser phase CO ₂ flows downward at low injection rate.	53
Figure 4.3: A thermodynamic stable interface between SCO ₂ -methane at 95 °C and 3000 psia.	53

Figure 4.4: Schematic illustrating the dimensions used in IFT measurements. The ambient is methane and the bubble on the tip of needle is CO ₂	55
Figure 4.5: Diagram illustrating the structure of SCO ₂ -methane interface from the bubble produced on the tip of the capillary needle.	56
Figure 4.6: CO ₂ -Methane interfacial tensions as a function of pressure and temperature.....	58
Figure 4.7: Effect of SCO ₂ injection speed on CO ₂ -methane interface formation.	61
Figure 4.8: Effect of N ₂ injection speed on N ₂ -methane interface formation at 95 °C and 1750 psia.	62
Figure 4.9: Effect of SCO ₂ injection speed on CO ₂ -N ₂ interface formation at 95 °C and 2000 psia.	62
Figure 5.1: Image Samples from Pre-test CT scan.	67
Figure 5.2: Image samples from Post-test CT scan.....	68
Figure 5.3: Δp of stimulated brine at 1cc/min versus injected Pore volume.....	71
Figure 5.4: Δp of stimulated brine at 1cc/min versus injected Pore volume.....	72
Figure 5.5: Δp of 90% methane displacing brine at 0.365 cc/min versus injected Pore volume.	73
Figure 5.6: Back pressure regulators used in the experiments. (a) Initial BBR, (b) New BBR	75
Figure 5.7: Δp of CO ₂ 90% displacing methane 90% in the short samples for almost 8 hours.	76
Figure 5.8: Drainage gas-brine relative permeability of core sample S_C_1A obtained from the displacement test conducted at 95 °C and 5900 psia, using Darcy's law.	79
Figure 5.9: Drainage gas-brine relative permeability of core sample S_C_1A obtained from the displacement test conducted at 95 °C and 5900 psia, using JBN method.....	82
Figure 5.10: Drainage gas-brine relative permeability of core sample S_C_1A obtained from the displacement test conducted at 95 °C and 5900 psia, using JBN and Hassler methods.	83
Figure 5.11: Drainage gas-brine relative permeability of core sample S_C_2A obtained from the displacement test conducted at 95 °C and 5900 psia, using JBN and Hassler methods.	85
Figure 5.12: Drainage gas-brine relative permeability of core sample S_V_1 obtained from the displacement test conducted at 95 °C and 5900 psia, using JBN and Hassler methods.	86
Figure 5.13: Drainage gas-brine relative permeability of core sample S_1_V obtained from the displacement test conducted at 95 °C and 5900 psia, using JBN and Hassler methods.	87
Figure 5.14: Relationship between absolute permeability and breakthrough.....	88
Figure 6.1: Mole percent CO ₂ production vs. injection pore volume.....	90

Figure 6.2: CO ₂ breakthrough PV vs. CO ₂ percent saturation within the in situ gas (methane).	92
Figure 6.3: Relative permeability curves vs. CO ₂ saturation calculated from displacing methane 90% by SCO ₂ 98% at 5900 psia, 160 °C and 10 cm/hr.....	93
Figure 6.4: Relative permeability curves vs. CO ₂ saturation calculated from displacing methane 90% by SCO ₂ 98% at 5900 psia, 160 °C and 10 cm/hr.....	94
Figure 6.5: Relative permeability curves vs. CO ₂ saturation calculated from displacing methane 90% and 75% by SCO ₂ 98% at 5900 psia, 160 °C and 10 cm/hr.	95
Figure 6.6: Relative permeability curves vs. CO ₂ saturation calculated from displacing methane 25% and 50% by SCO ₂ 98% at 5900 psia, 160 °C and 10 cm/hr.	96
Figure 6.7: Displacement rate tests of sample S_V_1.	97
Figure 6.8: SCO ₂ and methane relative permeability vs. CO ₂ saturation at 10 cm/hr, 160 °C and 5900 psia.	100
Figure 6.9: SCO ₂ and methane relative permeability vs. CO ₂ saturation at 1 cm/hr, 160 °C and 5900 psia.	101
Figure 6.10: Initial and repeatability tests of 1cm/hr of sample S_V_1.	102
Figure 6.11: Pore pressure tests for sample S_V_1, 5900 pisa and 4500 pisa. Temperature 160 °C and displacement rate of 10 cm/hr.....	104
Figure 6.12: Initial Pore pressure tests of sample S_V_1, 3500 pisa, 2500 pisa and 1500 pisa.	104
Figure 6.13: SCO ₂ and methane relative permeability vs. CO ₂ saturation at pore pressure 5900 psia and 4500 psia and displacement rate of 10 cm/hr, temperature of 160 °C.	105
Figure 6.14: SCO ₂ and methane relative permeability vs. CO ₂ saturation at pore pressure 1500 psia and displacement rate of 10 cm/hr, temperature of 160 °C.....	106
Figure 6.15: Initial and repeatability tests at 3500 psia of sample S_V_1.....	107
Figure 6.16: SCO ₂ breakthrough versus injected pore volumes for the short and long core samples. Test condition; pore pressure 5900 psia, temperature of 160 °C and displacement rate of 10 cm/hr.	109
Figure 6.17: SCO ₂ –methane relative permeability curves versus SCO ₂ saturation for the three short core samples. Test condition; pore pressure of 5900 psia, temperature of 160 °C and displacement rate of 10 cm/hr.....	110
Figure 6.18: SCO ₂ –methane relative permeability curves versus SCO ₂ saturation for core samples S_V_1 (vertically mounted) and S_C_3A (horizontally mounted). Test condition; pore pressure of 5900 psia, temperature of 160 °C and displacement rate of 10 cm/hr.	111
Figure 6.19: SCO ₂ –viscosity versus pressure at two different temperatures.	112
Figure 6.20: SCO ₂ breakthrough versus injected pore volumes for the short core samples at two temperatures. Test condition; pore pressure of 5900 psia, temperature of 95 °C and 160 °C and displacement rate of 10 cm/hr.....	113

Figure 6.21: SCO ₂ -methane relative permeability curves versus SCO ₂ saturation for sample S_C_1A. Test condition; pore pressure of 5900 psia, temperature 95 °C and 160 °C and displacement rate 10 cm/hr.....	114
Figure 7. 1: Interface between SCO ₂ and methane. The bubble is SCO ₂ and the ambient is methane at 3000 psia and 95 °C.	118
Figure 7. 2: Schematic illustration on SCO ₂ dispersion while displacing methane. At point A, diameter of the chamber is small enough to form an interface, at point B the chamber has a bigger diameter therefore a weak or no interface can form.....	119
Figure 7. 3: Experimental and simulated viscosities of SCO ₂ and methane at 160 °C and 725 psia to 7250 psia.	120
Figure 7. 4: Dispersion coefficient of SCO ₂ as a function of CO ₂ percentage. Solid line experimental (Eq.7.1 to 7.5) and dashed line calculated (Eq.7.8 to 7.12)	124
Figure 7. 5: Dispersion coefficient of SCO ₂ as a function of injected pressure. Solid line experimental (Eq.7.1 to 7.5) and dashed line calculated (Eq.7.8 to 7.12)....	125
Figure 7. 6: Dispersion coefficient of SCO ₂ as a function of injection rate. Solid line experimental (Eq.7.1 to 7.5) and dashed line calculated (Eq.7.8 to 7.12)	126
Figure 8.1: Pressure drop versus injected pore volume from the simultaneous injection of SCO ₂ -methane through S_V_1 at 160 °C, 5900 psia and 10 cm/hr. SCO ₂ concentration 20%.....	131
Figure 8.2: Steady state relative permeability of sample S_V_1.....	132
Figure 8.3: Steady and unsteady state relative permeability of sample S_V_1.....	134
Figure 8.4: Steady state relative permeability of sample S_V_1A.....	135
Figure 8.5: Steady state relative permeability curves of sample S_C_2A.....	136
Figure 8.6: Steady state relative permeability curves of sample S_C_3A.....	136
Figure 9.1: Critical water saturation distribution in the geo-model.....	140
Figure 9.2: Permeability distribution in the geo-model.....	141
Figure 9.3: Methane phase saturation distribution in the geo-mole and GWC.....	142
Figure 9.4: Methane cumulative production and pressure depletion in the base case.....	143
Figure 9.5: CO ₂ profile at wells P-1, P-2, P3 and P4. Case-1, injection target is 500K sm ³ /day.....	144
Figure 9.6: CO ₂ -methane displacement front in the case of no aquifer.....	145
Figure 9.7: CO ₂ profile at wells P-1, P-2, P3 and P4. Case-1, injection target is 500K sm ³ /day. Solid dots indicate no aquifer while blank dots refer to CO ₂ profile with the presence of aquifer.....	146
Figure 9.8: CO ₂ -methane displacement front in the presence of the aquifer.....	146
Figure 9.9: Methane cumulative production (case-1, no aquifer) from well P-1, P-2, P-3 and P4 at injection rate of 500K, 1500K and 3000K sm ³ /day.....	147
Figure 9.10: Methane cumulative production (case-2, no aquifer) from well P-1, P-2, P-3 and P4 at injection rate of 500K, 1500K and 3000K sm ³ /day.....	149
Figure 9.11: Methane cumulative production (case-3, no aquifer) from well P-1, P-2, P-3 and P4 at injection rate of 500K, 1500K and 3000K sm ³ /day.....	151

List of Tables

Table 3.1: Dimensions of the core plugs tested.	44
Table 4.1: SCO ₂ -Methane interfacial tension data for tests conducted at 95 °C.....	58
Table 4.2: Supercritical CO ₂ Methane Interfacial Tension Data.	59
Table 5.1: Basic macroscopic measurements for the short and long core samples.	63
Table 5.2: Basic macroscopic measurements for the short and long core samples.	64
Table 5.3: Basic test sequences.....	66
Table 5.4: Flow rate in (cc/min) at ambient and reservoir condition.....	70
Table 5.5: Basic data measurement at reservoir condition.	71
Table 5.6: Ka and Swi before and after dean stark.	74
Table 5.7: CO ₂ permeability at Swi after 8 hours.	77
Table 5.8: Gas-water brine relative permeability.....	80
Table 5.9: Gas-water brine relative permeability (JBN method).....	84
Table 6.1: Test conditions and CO ₂ breakthrough at various in situ gas compositions.	91
Table 6.2: CO ₂ breakthrough and end point permeability of five injection rates.	98
Table 6.3: CO ₂ breakthrough and end point relative permeability at five pore pressure.	103
Table 6.4: CO ₂ breakthrough and absolute permeability of the cores were examined.	108
Table 6.5: CO ₂ breakthrough and ultimum recovery at two different temperature.	113
Table 6.6: The value of a, b and c variables that were used in Eq 1 and 2.....	116
Table 8.1: End point relative permeability from displacement tests.....	130
Table 9.1: General petro-physical characteristic of the layers.....	141
Table 9.2: Wells completion and trajectories.....	141
Table 9.3: Case-1 ultimate cumulative gas production and recovery factor at all injection targets.	148
Table 9.4: Case-2 ultimate cumulative gas production and recovery factor at all injection targets.	149
Table 9.5: Case-2 ultimate cumulative gas production and recovery factor at all injection targets.	150

Appendix Figures:

Figure D-1: Initial and repeatability tests at 2500 psia of sample S_V_1.....	188
Figure D-2: SCO ₂ -methane relative permeability curves versus SCO ₂ saturation for sample S_C_2A. Test condition; pore pressure 5900 psia, temperature 95 °C and 160 °C and displacement rate 10 cm/hr.....	188
Figure D-3: SCO ₂ -methane relative permeability curves versus SCO ₂ saturation for sample S_C_3A. Test condition; pore pressure 5900 psia, temperature 95 °C and 160 °C and displacement rate 10 cm/hr.....	189
Figure E-1: Pressure drop versus injected pore volume from the simultaneous injection of SCO ₂ -methane through S_V_1 at 160 °C, 5900 psia and 10 cm/hr. SCO ₂ concentration 10%.....	192
Figure E-2: Pressure drop versus injected pore volume from the simultaneous injection of SCO ₂ -methane through S_V_1 at 160 °C, 5900 psia and 10 cm/hr. SCO ₂ concentration 50%.....	192
Figure E-3: Pressure drop versus injected pore volume from the simultaneous injection of SCO ₂ -methane through S_V_1 at 160 °C, 5900 psia and 10 cm/hr. SCO ₂ concentration 20%.....	193

Appendix tables:

Table A-1: Equipment types and specifications.....	169
Table B-1: Decane-Brine relative permeability for sample S_C_1A at ambient condition by centrifuge.	170
Table B-2: Decane-Brine relative permeability for sample S_C_1B at ambient condition by centrifuge.	171
Table B-3: Decane-Brine relative permeability for sample S_C_2A at ambient condition by centrifuge.	172
Table B-4: Decane-Brine relative permeability for sample S_C_2B at ambient condition by centrifuge.	173
Table B- 5: Decane-Brine relative permeability for sample S_C_3A at ambient condition by centrifuge.	174
Table B-6: Decane-Brine relative permeability for sample S_C_3B at ambient condition by centrifuge.	175
Table C-1: Endpoint relative permeability calculated from brine displacement by 90C ₁	176
Table C-2: Endpoint relative permeability calculated from 90C ₁ displacement by SCO ₂	176
Table C-3: Endpoint relative permeability obtained from displacement tests at different injection rates.	176
Table C-4: Endpoint relative permeability calculated from displacement tests at different pore-pressures.....	176

Table D-1: Gas-water relative permeability by using JBN method and Darcy's law...	177
Table D-2: Gas-water relative permeability by using JBN method and Darcy's law...	177
Table D-3: Gas-water relative permeability by using JBN method and Darcy's law...	178
Table D-4: SCO ₂ -methane relative permeability for sample S_V_1 by using JBN method and Darcy's law.	178
Table D-5: SCO ₂ -methane relative permeability for sample S_V_1 by using JBN.	179
Table D-6: SCO ₂ -methane relative permeability for sample S_V_1 by using JBN.	179
Table D-7: SCO ₂ -methane relative permeability for sample S_V_1 by using JBN.	180
Table D-8: SCO ₂ -methane relative permeability at speed 7 cm/hr using JBN method.	180
Table D-9: SCO ₂ -methane relative permeability at speed 5 cm/hr using JBN method.	181
Table D-10: SCO ₂ -methane relative permeability at speed 2 cm/hr using JBN method.....	181
Table D-11: SCO ₂ -methane relative permeability at speed 1 cm/hr using JBN method.....	182
Table D-12: SCO ₂ -methane relative permeability at speed 10 cm/hr using JBN method.....	182
Table D-13: SCO ₂ -methane relative permeability at speed 10 cm/hr using JBN method.....	183
Table D-14: SCO ₂ -methane relative permeability at speed 10 cm/hr using JBN method.....	183
Table D-15: SCO ₂ -methane relative permeability at speed 10 cm/hr using JBN method.....	184
Table D-16: SCO ₂ -methane relative permeability at speed 10 cm/hr for sample S_C_1A using JBN method.	184
Table D-17: SCO ₂ -methane relative permeability at speed 10 cm/hr for sample S_C_2A using JBN method.	185
Table D-18: SCO ₂ -methane relative permeability at speed 10 cm/hr for sample S_C_3A using JBN method sample.....	185
Table D-19: SCO ₂ -methane relative permeability at speed 10 cm/hr using JBN method sample S_C_1A.....	186
Table D-20: SCO ₂ -methane relative permeability at speed 10 cm/hr using JBN method sample S_C_2A.....	186
Table D-21: SCO ₂ -methane relative permeability at speed 10 cm/hr using JBN method sample S_C_3A.....	187
Table E-1: Steady state relperm calculation for sample S_V_1.	190
Table E-2: Steady state relperm calculation for sample S_C_1A.....	191
Table E- 3: Steady state relperm calculation for sample S_C_2A.....	191
Table E-4: Steady state relperm calculation for sample S_C_3A.....	191

Chapter 1

Introduction

Natural gas reservoirs can be a perfect place for carbon dioxide sequestration by direct carbon dioxide injection. This is because the ability of such reservoirs to permeate gas during production and their proven integrity to seal the gas against future escape. Carbon dioxide sequestration in newly discovered natural gas reservoirs can be coupled with enhanced gas production by injecting CO₂ into one end, or lower part, of the reservoir. This process is called Carbon Sequestration with Enhanced Gas Recovery (CSEGR) (Oldenburg 2003). However CSEGR has yet to be implemented commercially and tested in the field. The high density and viscosity of CO₂ at reservoir conditions, in comparison to methane, make it favorable to this process (Oldenburg and Benson 2002). The greater density of CO₂, relative to methane, makes CO₂ migrate downward relative to methane, whilst the greater viscosity of CO₂ will result in the displacement of methane by CO₂ having a favorable mobility ratio with less tendency to inter-fingering (Oldenburg, Pruess, and Benson 2001).

However carbon dioxide undergoes a large change in density in the gas phase as it passes through the critical pressure at temperatures near the critical temperature. In such conditions the CO₂ physical properties (viscosity and density) in comparison to methane are greater by a factor of about three times, as shown in Figure 1.1. Thus the concern about excessive mixing resulting in possible degradation of the value of the remaining gas should be less as methane's viscosity and density are considerably lower than the displacing phase at the supercritical condition.

The active injection of supercritical carbon dioxide (SCO₂) causes re-pressurization and displacement, whilst it permits the acceleration and enhancement of gas recovery. This injection is analogous to water-drive or depletion-drive reservoir operations. Several authors (Al-Hashami, Ren, and Tohidi 2005; Clements and Wit 2002; Jikich et al. 2003; Oldenburg and Benson 2002; Oldenburg, Pruess, and Benson 2001; Seo and Mamora 2003) have studied intensively the possibility of the CSEGR project in their simulation works.

The simulation results suggested that an incremental of about 10% of OGIP (original gas in place) of natural gas can be recovered after the conventional depletion by the means of CO₂ injection.

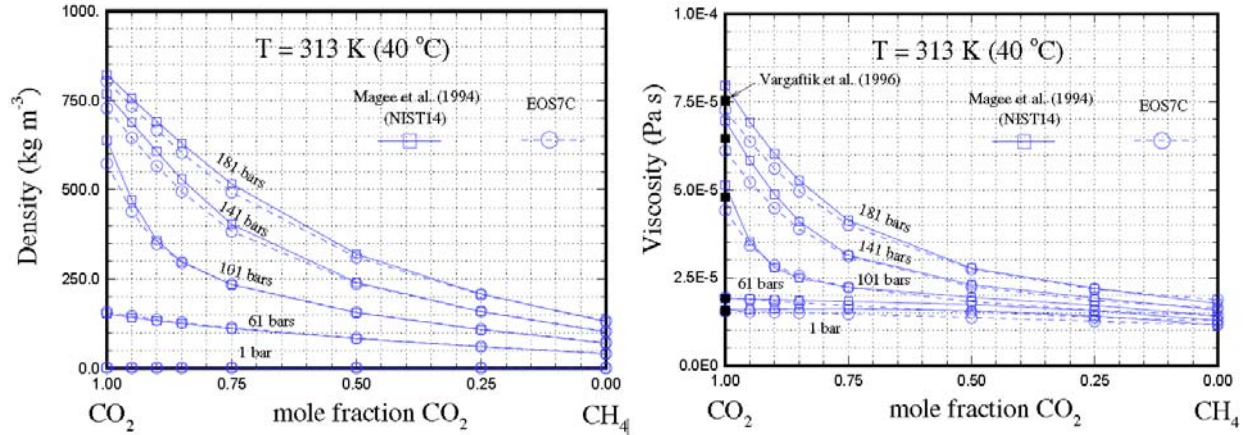


Figure 1.1: Density and viscosity of Carbon dioxide and Methane at 40 °C and different pressure and composition. After Oldenburg and Benson (2002).

The enhanced gas produced as the result of SCO₂ sequestration can moderately offset the cost that is associated with the CO₂ capturing, transporting and re-injection into the reservoir. Furthermore, Gaspar et al., (2005) state that “increasing level of knowledge and experience ‘learning by doing’, and contribution of new technologies in the field of CO₂ sequestration will probably reduce these costs”. Sengul (2006) believes that the technologies required for CO₂ capturing, injecting, and monitoring of the reservoir are widely available today. It seems there is not any real obstacle to implementing CO₂ sequestration for enhanced gas recovery at field scale.

Throughout this research the factors that have an effect on gas-gas relative permeability and CSEGR process will be investigated in detail. The optimum conditions of the displacement process through temperature, pressure, and injection rate on CSEGR are determined. Moreover, effects of composition, permeability heterogeneity and displacement front on SCO₂ breakthrough has been investigated in detail. In addition, interfacial tension between SCO₂-methane phases has been measured successfully through this research. A simple mathematical model is developed for SCO₂-methane relative permeability and SCO₂ dispersion coefficient is presented. Motivation behind this work, together with the specific goal and scope of the thesis, is described at the conclusion of this chapter.

1.1 Statement of the Problem:

The central issue in the physical processes of injecting CO₂ in a gas reservoir is the extent to which the natural gas will mix with the injected CO₂ and reduce the calorific value of the natural gas. Experimental studies have demonstrated that diffusion and dispersion processes are the same for supercritical fluids as for normal gases and liquids, (Wei and Sadus 1996), so there should not be any unexpected penalty at supercritical conditions in this regard. Recent experimental results focused on CO₂ storage in combination with enhanced gas recovery show limited mixing for methane displaced by CO₂ in carbonate rock cores (Mamora and Seo 2002).

In simulations performed by Oldenburg and Benson (2002), using a reservoir with a relatively thin vertical dimension (22 m), the gas flow was noted to be predominantly horizontal. This configuration leads to gravity override and a broadening of the interfacial area between the gases and, correspondingly, more mixing will occur particularly within a high permeable layer (See Figure 1.2). Thus heterogeneity in the reservoir rock permeability will accelerate early carbon dioxide breakthrough.

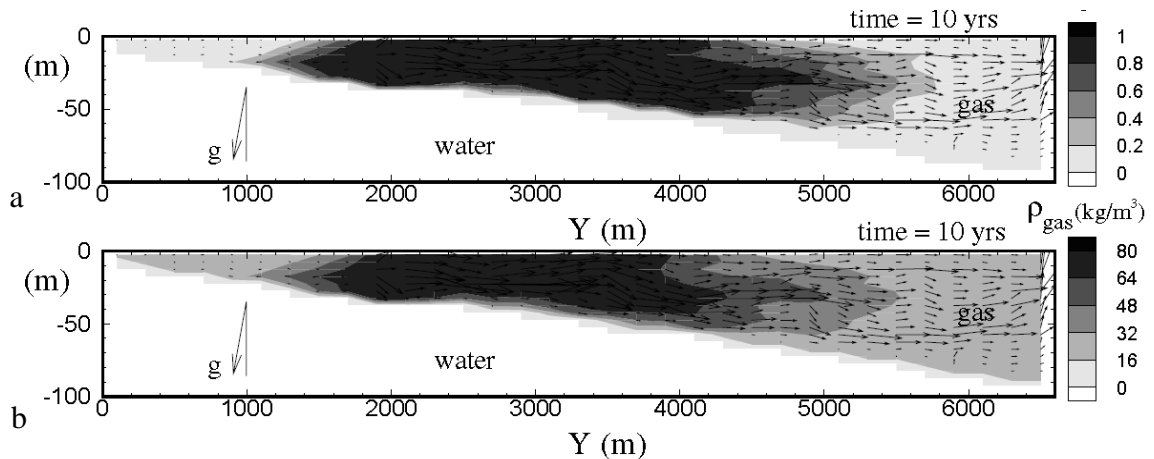


Figure 1.2: (a) Mass fraction of CO₂ (b) Gas density after 10 years of CO₂ injection with a constant pressure from upper left hand. After Oldenburg and Benson (2002).

In gas reservoirs with a large vertical extent, relative to lateral extent, the density effects of CO₂ could be exploited by placing the CO₂ deep in the reservoir and producing the natural gas from near the top. In all, the degree to which reservoir gases mix is subject to considerable variability depending on reservoir geometry, anisotropy, heterogeneity, fracturing, and other rock or fluid properties. Jikich et al (2003) have investigated two injection scenarios: (1) simultaneous CO₂ sequestration

and methane recovery from the very beginning of the project, and (2) primary production to the economic limit, followed by injection of carbon dioxide for secondary gas recovery. Although these authors conclude that more methane can be recovered if CO₂ is injected after primary production, the reason for this feature has been left unexplained. It is well known that carbon dioxide's viscosity and density decreases with decreasing pressure, therefore excessive mixing is expected to have been resulted in their second scenario because both phases exhibit less physical properties differences at low pressure.

In short, careful reservoir selection and active strategy development can limit the extent of gas mixing in particular gas reservoirs, but clearly the extent and rate of gas mixing in the subsurface is uncertain. However limited mixing has been observed during this research project in laboratory scale studies. Field gas mixing needs to be investigated further.

1.2 Relative permeability model of a gas-gas system:

Relative permeability plays a main role in determining ultimate recovery (Jerauld 1997). The attempt to establish a model for gas-gas relative permeability is of great importance to help design, optimize, and analyse the gas-displacement process. Although relative permeability engages the main role in the recovery scenario; petrophysical characterization, gravitational effects, gas phase behaviour, and mass transfer by molecular diffusion and dispersion processes are among other factors that determine the amount of gas that can be recovered economically (Jerauld 1997). The resistance to fluid flow in a porous medium determines total fluid capacity and has the main impact on injectivity. The fractional flows and molecular diffusion determine methane/CO₂ production ratio, breakthrough timing, and the incremental and ultimate recovery. This may cause dissipation of the miscible fluid through heterogeneity and resulting early breakthrough. The key descriptions of multiphase flow in porous media are usually modeled as relative permeabilities to each flowing phase. The concept of relative permeability is derived from the absolute permeability of a porous medium normally ascribed as Darcy-type formulation.

$$u = -\frac{K}{\mu}(\nabla p + \rho g) \quad (1.1)$$

Where u is the volumetric flux per unit cross-sectional flow area, superficial velocity, K is the permeability of the medium, and μ is the viscosity of the fluid.

Eq.1.1 can be generalized to describe flow of two phases if the fluids flow through different paths in the porous media, provided both phases are immiscible. Hence relative permeability to a phase will be a function of that fraction of pore spaces contributing to its cross-sectional flow. This means that the overall effective permeability of a medium that contains two fluids will be lower than its absolute permeability, under at the same pressure drop (Richards 1931).

$$u = -\frac{KK_{r\alpha}}{\mu_{\alpha}}(\nabla p_{\alpha} + \rho_{\alpha}g) \quad (1.2)$$

Where $K_{r\alpha}$ is the α -phase relative permeability, defined as the fractional reduction in the effective permeability to phase α due to the presence of the second phase.

Relative permeability is normally obtained from dynamic fluid displacement and it is generally calculated indirectly for the purpose of simulation based on the displacement process. There are two distinct methods for relative permeability calculation, the implicit and the explicit methods. The explicit method was developed based on the Buckley-Leverett (1942) representation of the displacement process (Johnson, Bossler, and Naumann 1959; Jones and Rozelle 1978). Thus calculated relative permeability is an empirical quantity that adds the effects of the complex interaction between the flowing fluids and the porous medium.

Therefore some researchers believed that by using the explicit method such physical properties relating to pore-geometry and capillary pressure cannot easily be taken into account (Tao and Watson 1984a; Kerig and Watson 1987; Watson et al. 1988). Furthermore, as the method is developed from a mathematical derivation process it will magnify any errors associated with the experimental data (Tao and Watson 1984b). Consequently the implicit method has been introduced to overcome the problems that are associated with the explicit models. Many models have been introduced to predict the shape of the relative permeability curves of the wetting phase and non-wetting phase during imbibition and drainage flowing cycles.

For instance the Land (1968) model, which is known as the most used empirical trapping model, and most relative permeability models, have been assimilated with hysteresis functions by Killough (1976) and Larsen and Skauge (1998). Land's model was developed to predict trapped gas saturation as a function of the initial gas saturation in water-wet sandstone cores (See Figure 1.3). While for the mixed wet rocks Jerauld (1997) has initiated a new model which was dependent on the observation of initial residual curves of the non-wetting phase in a mixed wet medium.

Hence modeling relative permeability curves for a gas-gas system in a reservoir porous medium has been a great challenge to this research as it has not knowingly been carried out before. One may argue fluid flow in gaseous state through a porous media, such as SCO_2 -methane, cannot be modeled in term of relative permeability because both phases are miscible and thus marginally influenced by the morphology of the porous medium. In a recent study by Amin et al. (2010), a thermodynamic stable interface between SCO_2 and methane is documented and measured. This finding allows the process of natural gas displacement by SCO_2 to be modeled in terms of relative permeability. However the stability of the interface was concluded to be time dependant and coexisted with molecular diffusion. Hence relative permeability of the gaseous phase at pore scale can be a function of pore morphology and dispersion and molecular diffusion mechanisms.

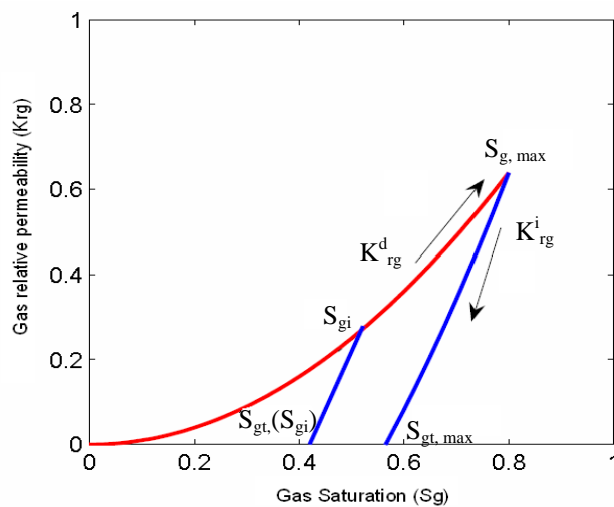


Figure 1.3: Schematic of gas relative permeability trapping model for water-wet porous media. After Land (1968).

Modeling gas-gas relative permeability through this research has been completely independent of the parameters that other researchers have used in developing their models, as the gas phases undergo a series of changes at different pressures and temperatures while propagating in porous media. Thus at the transition zone, miscible fluid will occur between pure injected SCO_2 and pure methane and will have a great influence on the shape of the relative permeability because it is mainly dependent on phase behavior; dispersion and molecular diffusion; and rock morphology.

1.3 Objective and Significance:

The main objective of this research is to explore the mechanisms by which SCO_2 displaces in situ gas in porous media, as well as investigating the effects of several parameters such as composition, injection rate, pressure, temperature, and permeability heterogeneity on the recovery efficiency. Eventually, the research tries to determine the optimum condition of SCO_2 injection for enhanced gas recovery.

The implication of this research is crucial in environmental terms as it attempts to sequester the greenhouse gas CO_2 for enhanced gas recovery. Since the industrialization era began the concentration of CO_2 has increased in the atmosphere from 270 ppm to 370 ppm, and most scientists believe that burning fossil fuel is a principal reason for this increase, (Al-Hashami, Ren, and Tohidi 2005). Therefore to moderate the effect of greenhouse gas emissions on climate change, many countries have pledged to reduce carbon emissions by up to 8% by 2010 relative to the level approved in 1990 (Gale and Freund 2000). Furthermore, the European Commission in 1993 initiated the Joule II Non-nuclear Research Program for investigating the possibility of CO_2 sequestration in depleted gas/oil reservoirs, (Holloway 1996). Due to their proven integrity against gas escape over geological time periods these reservoirs become an attractive target for CO_2 sequestration. The Joule II programme concludes:

- In order to sequester larger quantities of CO_2 , shallow reservoirs are not recommended because CO_2 will be in the gaseous phase.

- For maximum storage capacity, CO₂ has to be injected as a supercritical fluid, at a temperature and pressure greater than 31 °C and 1071 psi, respectively.
- The cost associated with CO₂ separation from flue gas is considerably higher than that of transporting and injecting CO₂ into the reservoir.

The estimated underground volume that would be available for CO₂ disposal worldwide has been studied constantly by the International Energy Agency (IEA), with latest estimates stating that 1,000-10,000 Gt (Giga tonnes) of CO₂ can be sequestered in the depleted gas and oil reservoirs, saline aquifers and un-minable coal seams (Haefeli, Bosi, and Philibert 2004). Lawal and Frailey (2004) stated that because gas is more compressible than oil, depleted gas and gas condensate reservoirs can store more gas than a depleted oil reservoir despite each reservoir having identical hydrocarbon pore volume (HCPV).

Briefly the significance of this research is illustrated in the following points;

- Improving recovery efficiency and controlling pressure decline in the reservoir and thus preventing excessive water production which is normally concurrent with pressure decline in water-drive gas reservoirs.
- Environmentally, the separated CO₂ that is associated with the natural gas stream can be injected back into the reservoir instead of being emitted into the atmosphere as a conceivable cause of global warming.
- Economically, the fraction of additional gas that can be recovered will help offset the costs associated with CO₂ capturing, compressing and re-injection into the reservoir.
- It will contribute to future research works that are attempting to model gas-gas systems flow in the reservoir porous medium, enhanced gas recovery, condensate gas recovery and CO₂-foam regime flow studies.

1.4 Thesis outline:

The details of the ten chapters are:

Chapter One: Introduction to the topic, describing the feasibility of modeling gas-gas relative permeability and the challenges associated with the SCO_2 -methane relative permeability model. Also discussed is the impact of excessive gas mixing that may occur during gas-gas displacement on the recovery process by CSEGR, both economically and physically in the reservoir performance. Finally, the advantages and motivation beyond this research are briefly presented.

Chapter Two: Includes an extensive literature review on gas phase behavior, dispersion and molecular diffusion, and relative permeability. Furthermore, the factors affecting relative permeability between two immiscible or near miscible fluids are reviewed in detail with evaluation of their possible impacts on SCO_2 -methane relative permeability through a porous medium.

Chapter Three: Presents the sequence of the experimental process and the design of the equipment that is used in the SCO_2 -methane displacement tests, as well as in the interfacial tension measurements. Problems associated with the experimental equipment, particularly with o-rings, Teflon seals and stainless steel tubes are described in detail. The modifications which were performed on the initial design of the apparatus used in the core-flooding tests are discussed together with the factors that led to carrying out the adjustments.

Chapter Four: Explains the methodology and the procedure for measuring interfacial-tension between SCO_2 -methane and N_2 -methane systems. The SCO_2 -methane interface was measured successfully at pressure from 1100-5900 psi and temperature $95\text{ }^\circ\text{C}$ to $160\text{ }^\circ\text{C}$. Attempts to measure a distinctive N_2 -methane interface were unsuccessful.

Chapter five: Presents the results from linear core-flooding test carried out on the reservoir plugs in the CGTA laboratory.

Chapter six: The gas propagation through the cores is modeled in terms of relative permeability which is derived by the explicit methods. The factors that profoundly affected the shape of relative permeability curves are given in details. These factors were mainly related to test conditions such as pore pressure, injection rate, temperature, and gas composition. Moreover, effects of the analyzed heterogeneity are given for the test carried out in plugs from high to low quality.

Chapter seven: A straightforward method is presented for calculating the dispersion coefficient of supercritical carbon dioxide (SCO₂) displacing methane in a linear porous reservoir. The dispersivity of SCO₂ has been identified to be a function of injected pressure, in situ gas composition and injection rate. It was found to vary proportionally to changes in purity of the displaced phase and injection rate, while inversely varying with the injected pressure.

Chapter eight: Presents the steady state methodology and procedure of injecting both phases simultaneously through the plugs. The objective was to determine SCO₂ permeability relative to methane due to its intrinsic gas properties, dissolution and potential mobilization of formation water, miscibility with methane, or reactions with the rock mineral.

Chapter nine: Simulation of the laboratory results investigated in an example gas field. Several case scenarios were executed with the aim of determining the optimum injection strategy for a specific gas field as well as illustrating the effects of CO₂ injection on the recovery efficiency in different stages of pressure depletion.

Chapter ten: This Chapter provides the conclusions from this research work as well as the recommendation to design an optimum enhanced gas recovery by SCO₂ injection project.

Chapter 2

Background History

2.1 Introduction:

This chapter describes the fundamental background of the CO₂-enhance gas recovery project. A summary is presented of the parameters that would affect the feasibility of such a displacement process in a porous medium at extreme reservoir conditions. The main parameters are the phase behaviour and physical properties of methane-CO₂. Previous studies that have been conducted on sequestering supercritical carbon dioxide for enhanced gas, oil, and coal-bed methane recovery are also broadly described. As well, the chemical and physical reactions that are concurrent with the SCO₂ sequestration process are investigated and their possible effects on injectivity impairment considered. Fluid flow of two immiscible and near-miscible fluids through porous medium are investigated with the aim of understanding their conceivable impacts on methane-SCO₂-relative permeability and recovery efficiency.

2.2 Methane-CO₂ phase behaviour:

Predicting phase behaviour of a binary methane-CO₂ system at reservoir conditions of high temperatures and pressures has been crucial in defining the process by which CO₂ displaces methane at pore scale. It is known that CO₂ at a temperature of 31 °C and pressure of 1071 psi reaches critical condition. However, in the vicinity of the critical condition, with increasing pressure and temperature, CO₂ undergoes a large change in viscosity and density, in comparison with methane. To this author's knowledge no prior attempt has been made to investigate the phase behaviour of methane-CO₂ systems at these conditions because it is considered that both phases will remain in the gaseous state regardless of operational conditions. Only a study by Amin et al. (2010) explored the phase behaviour of a binary SCO₂-methane system at high pressures and temperatures. The experimental results indicated there is a distinct interface between the two phases and states "All interfaces cannot be treated in the same theoretical or experimental frame-work since the mechanism governing interaction and motion of the different phases is different because of physical properties, mobility and stability of the phases". A modified reverse pendant drop technique was used to capture the interface between methane and SCO₂ phases. For

the IFT measurement a mathematical model was formulated based on the contact angle that both phases have made with the needle-wall. The tests were conducted at temperatures ranging from 95 °C to 160 °C and pressures from 1500 psia to 6000 psia.

At temperatures below the critical point of CO₂, researchers chiefly focused on hydrate formation from binary methane-CO₂ systems because in gas plants hydrate precipitation is sporadically a common problem that causes pipe-clogging. A substantial amount of literature can be found addressing hydrate formation for various systems. For instance Thiéry, Van den Kerkhof AM, and Dubessy (1994) accurately calculated vX properties through their model for the entire ranges of composition and molar volume of CO₂-methane and CO₂-N₂ systems at temperature < 31 °C and pressure < 400 bar. Zhu et al. (2005) developed a numerical model to calculate and predict hydrate phase equilibria at hydrate formation temperature and pressure conditions for pure gas (methane-CO₂) and water. The results obtained from their model is in close agreement with experimental data from Sloan (1998). In addition, the effect of pore size on hydrate formation from binary system methane-water and CO₂-water has been studied by Seo, Lee, and Uchida (2002). At a specified temperature, three phase H-L_w-V equilibrium curves of pore hydrates were noticed by these authors to shift to the higher pressure region depending on pore sizes of the medium when compared with bulk hydrate formation (See Figure 2.1). This phenomenon is considered to be the result of the water mobility reduction due to the geometrical constraints of the medium.

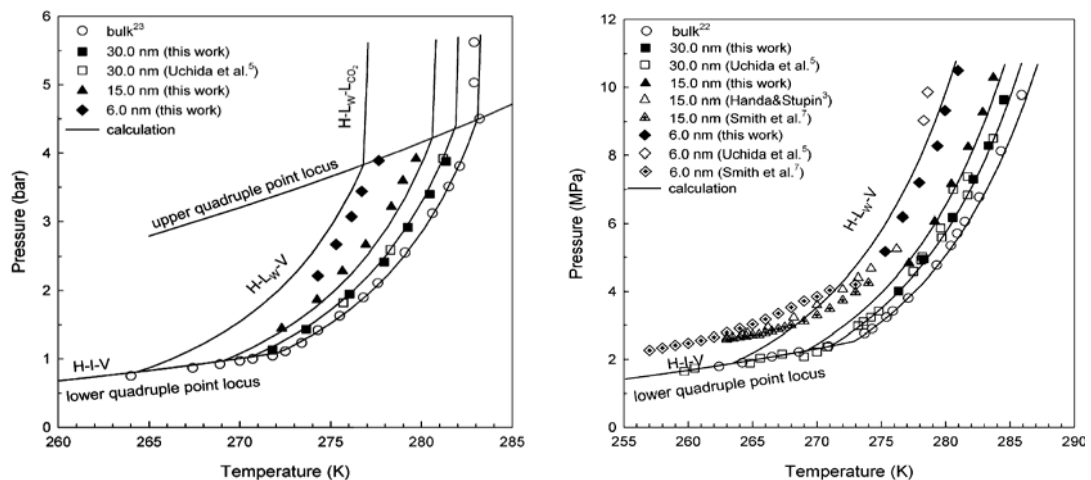


Figure 2.1: Three phase H-L_w-V equilibrium curves of pore hydrates from CO₂-methane phase equilibria. After Seo, Lee, and Uchida (2002).

The problems associated with hydrate precipitation are of increasing importance for CO₂ sequestration for enhanced gas recovery, because in such projects CO₂ injection not only involves the flow at extreme reservoir conditions. It also involves the separation, transportation and compression processes, which normally are executed at ambient temperature; hydrate precipitation is anticipated to be associated with impurities and subsequently affects the flow rate of CO₂.

2.3 Physical properties of methane-CO₂:

The main objective of this research was to investigate enhanced gas recovery by CO₂ injection at high pressure and temperature, 6000 psia and 160 °C, and to ascertain an observed interface at these conditions. It is known that gas mixing will effectively depend on the physical properties, viscosity and density, in a homogeneous medium. In a reservoir porous medium, in addition to the physical properties of both phases, heterogeneity will greatly impact on the displacement front as well as the rate of mixing. At the set research conditions, CO₂ will exhibit greater viscosity and density than methane, therefore as it is injected it will tend to spread downward in the reservoir region while displacing methane.

Oldenburg et al (2001) studied the effect of pressures, temperatures and compositions on CO₂ and methane viscosity and density. Their results demonstrate that CO₂'s density and viscosity increases with increasing pressure and temperature while decreasing with increasing methane in the mixture. Thus the greater density of CO₂, relative to methane, makes CO₂ migrate downward relative to methane, whilst the greater viscosity of CO₂ will cause the displacement of methane by CO₂ having a favorable mobility ratio with less tendency to inter-fingering.

Figure 2.2 shows density and viscosity of CO₂ and methane at different temperatures and pressures, 40 °C to 80 °C and 1 bar to 200 bars respectively. It is apparent that the CO₂ physical properties will be superior to methane upon increasing its mole fraction in the mixture and its pressure (Oldenburg, Pruess, and Benson 2001).

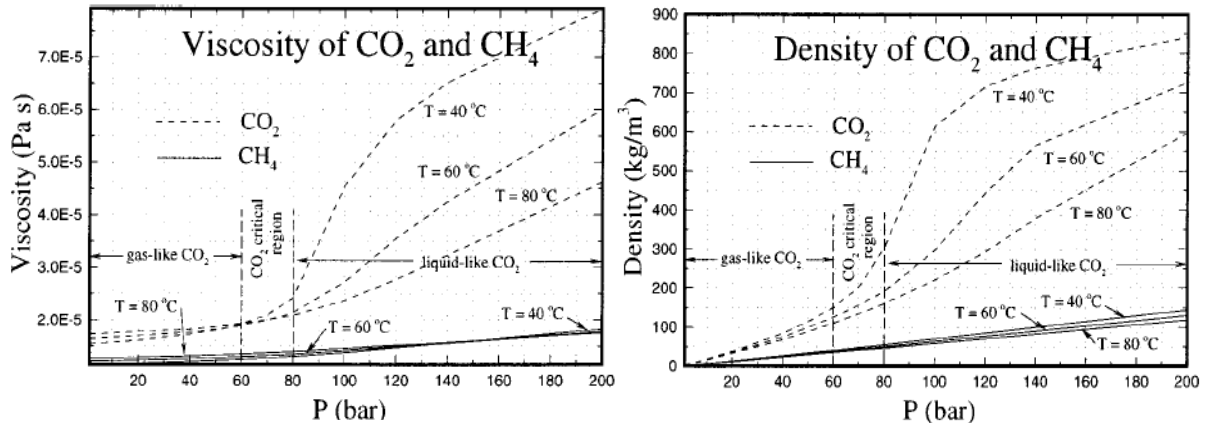


Figure 2.2: CO₂–methane physical properties at different conditions of pressure and temperature.

After Oldenburg, Pruess, and Benson (2001).

2.4 CO₂ for enhanced gas recovery:

Although there are plenty of studies that have been carried out to comprehend by which process CO₂ sequestration in a depleted gas reservoir could lead to enhanced gas recovery, none of these studies has ever attempted to explain the effect of gas-gas (CO₂–methane) flow in porous media, particularly relative permeability, on the recovery process. These studies were mainly aimed at reducing greenhouse gas emission in the atmosphere and sequestering in a depleted gas-oil reservoir or in an aquifer. A number of these studies were limited to the economic analysis of CO₂ enhanced gas recovery from CO₂ capturing, transporting, compressing, and re-injecting in to a reservoir formation.

Through simulation software, the impact of permeability heterogeneity, injection rate, injection pressure and vertical stratification on enhanced gas recovery can be investigated. Van der Burgt, Cantle, and Boutkan (1992) were the first group who studied and simulated the possibility of injecting CO₂ with enhanced gas recovery in one of the Dutch gas reservoirs. Three base case scenarios were studied, first; after primary production, using the existing production wells for CO₂ injection, no additional methane recovery was noticed, second; after primary production, drilling a new well down-dip of the reservoir, as a result of CO₂ injection an approximate increment of 1.7×10^9 m³ of methane was recovered, and third; injecting CO₂ while methane produced at primary phase.

However, in the beginning of injection the methane production rate remained high but after CO₂ breakthrough the total amount of methane recovered was less than that produced after primary production with or without CO₂ injection.

On the other hand, other researchers (Al-Hashami, Ren, and Tohidi 2005; Clements and Wit 2002; Jikich et al. 2003; Oldenburg and Benson 2002; Oldenburg, Pruess, and Benson 2001; Seo and Mamora 2003) have come to almost the same conclusion, for the above scenarios to that of (Van der Burgt, Cattle, and Boutkan 1992) in their simulations. Although the incremental amount of natural gas that was expected to be recovered as a result of CO₂ injection only comprised 10% of the OGIP (original gas in place). Van der Burgt et al., (1992) had not expected such incremental recovery. The divergence in the result between the Van der Burgt et al., study and the others might be related to advances that have occurred in the simulation programs by increasing more functional inputs as well as considering reservoir structure, petrophysical properties, and gas phase behavior more specifically.

The first large scale gas-gas (methane-inert gas) injection was carried out in France for storing natural gas in the Saint-Clair-Sur-Epte underground storage facility. Initially the project started by injecting 20% of inert gas as a cushion for the natural gas that followed the inert gas injection. Laille, Molinard, and Wents (1988) had explored in detail the miscibility of the gases by analyzing gas composition at different locations of the storage. By using surveying tools and geophysical methods, both phase distribution and the gradual compositional contact in the storage were continuously monitored. As a result, for several years no compatibility problems were observed during the storage of natural gas in contact with its cushion of 20% inert gas. This result encouraged the concept that SCO₂-methane may not mix excessively during the displacement process because the differences in the physical properties (viscosity and density) between natural gas and the inert gas (which is mainly N₂) are considerably smaller than the difference between SCO₂-methane at supercritical conditions. Further more, the first pilot enhanced gas recovery using CO₂ (98%) and H₂S (2%) injection at reservoir scale, was carried out in a depleted gas reservoir in Long Coulee Glauconite F Pool in Alberta, Canada (Darvish et al. 2008). Although the breakthrough of CO₂ was noted within one to three years from the producing wells, an incremental amount of natural gas recovered as a result of the

CO₂ sequestration (See Figure 2.3). The early CO₂ breakthrough at the effluent point was examined thoroughly; the gaseous state of CO₂ was expected to be the major reason for that CO₂ breakthrough timing. CO₂ injection was performed when the reservoir pressure was almost at abandonment level of around 140 psi at a temperature of 68 °C. Therefore formation volume factor and density of CO₂ appeared to be close to that of the in situ gas. Consequently CO₂ was accelerated to propagate and diffuse instantaneously into the in situ natural gas due to similar physical properties.

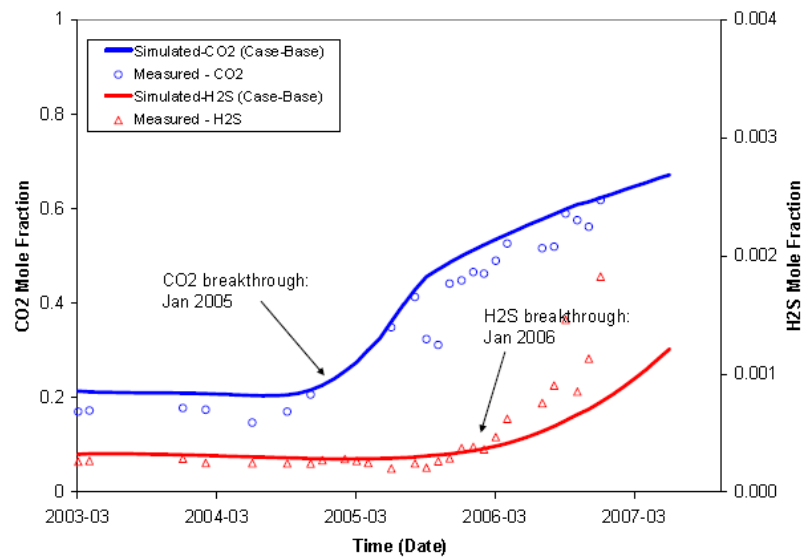


Figure 2.3: CO₂-H₂S breakthrough from well 06-23. After Darvish et al. (2008).

Accordingly, the optimum reservoir (pressure and temperature) conditions for enhanced gas recovery by CO₂ injection must be conspicuously greater than the condition referenced in the Long Coulee Glauconite F Pool project. The test conditions investigated in this research are in favor of enhanced gas recovery by SCO₂ as the physical properties of the injected gas are about three times greater than the in situ gas at a temperature of 160 °C and pressure of 6000 psia.

2.4.1 Mixing gas-gas by dispersion:

When a fluid is miscibly displacing another in a liner porous medium, where the fluids are initially distinguished by a sharp interface, they will slowly diffuse into each other. With the passage of time the displacement becomes stable and dissipation of the miscible fluid does not occur. The sharp interface will gradually diffuse into a mixed grade zone ranging from one pure fluid to other.

The resulting miscible zone is due to random motion of molecules of both phases. If the diffusion does not change the volume of the miscible fluids, the transport of the molecules in any arbitrary plane is often represented by the Fick diffusion equation (Collins 1963).

$$\frac{\partial G}{\partial t} = -D_o \cdot A \cdot \frac{\partial C}{\partial X} \quad (2.0)$$

Where:

G quantity of material diffused across a plane.

t time, sec.

D_o molecular diffusion, cm^2/sec .

A cross-sectional area, cm^2 .

C concentration.

X distance, cm.

The most well known form of the above equation is:

$$\frac{\partial C}{\partial t} = K_i \frac{\partial^2 C}{\partial X^2} - u \frac{\partial C}{\partial X} \quad (2.1)$$

Where:

K_i dispersion coefficient.

u interstitial velocity, cm/sec .

X distance, cm.

Essentially the dispersion coefficient calculated from Eq.2.1 is a function of concentration. Consequently K_i changes while the concentration of injected phase continuously changes with time because of miscibility. Therefore using various K_i to reproduce the effluent profile mathematically is quite a complicated process. Perkins and Johnston (1963), having comprehensively reviewed gas-gas diffusion issues, suggested that a simplifying calculation can be made by determining a single value for K_i - the effective average diffusion coefficient. Hence the dispersion coefficient is rendered constant and independent of concentration, and thus the effluent profile can be easily generated mathematically.

Furthermore, a well determined boundary is essential to mathematically retrace the displaced composition profile. Using Eq.2.1 will be a reasonable match with an experimental effluent profile. Most of the developed mathematical models that have been derived to represent a profile of the displaced fluid composition have used error functions such as given in Eq.2.2.

$$C = 1/2 \left\{ \operatorname{erfc} \left(\frac{X_D - t_D}{2\sqrt{t_D/P_e}} \right) + e^{PeX_D} \operatorname{erfc} \left(\frac{X_D + t_D}{2\sqrt{t_D/P_e}} \right) \right\} \quad (2.2)$$

Due to the intrinsic behaviour of SCO₂ at supercritical conditions mixing between displacing and displaced phase (SCO₂-methane) in porous media will not only be governed in the main direction of the convective flux, it is also controlled by other mechanisms such as molecular diffusion, Taylor dispersion, viscosity ratio, gravity force, capillary pressure and permeability heterogeneities.

The dispersion coefficients of CO₂ were calculated from the tests conducted by Mamora and Seo (2002) and Seo (2004) at different conditions ranging between 0.01-0.12 cm²/min. In this research the impact of injection pressure, flow rate, in situ gas composition and permeability heterogeneity on the dispersion coefficient of SCO₂ in porous media have been studied thoroughly.

Experimental results from different core plugs have revealed that the dispersion coefficient is proportionally changing with changes in purity of the displaced phase, injection rate and absolute permeability, while inversely changing with injected pressure. Furthermore, Oldenburg and Benson (2002) in a simulation study concluded that permeability heterogeneity tends to accelerate CO₂ breakthrough by creating a faster flow path to the producing well. The dispersion coefficient determined in this study was greater for the high quality rock and smaller for the low quality rock.

2.5 CO₂ for enhanced oil recovery:

Enhanced oil recovery (EOR) by CO₂ solvent flooding is one of the most successful recovery methods worldwide (Moritis 2000; Lake 1989). Approximately 300,000 bbl/day of oil is produced as a result of CO₂ injection and comes as a second method

of EOR (Clements and Wit 2002). Although considerable oil can be recovered via CO₂ sequestration, miscible CO₂-flooding cannot sweep the entire oil in place because of the gravity effects. The light viscous and dense phase (CO₂) when displacing the heavier phase (oil) will tend to override the oil zone and cause CO₂ premature breakthrough at the producing wells (Bondor 1992). In porous media the displacement of oil by SCO₂ will be governed by the mobility ratio, gravity segregation and reservoir heterogeneity. Accordingly all the oil reservoir types cannot be an appropriate target for CO₂-EOR.

The optimum requirements for successful EOR by CO₂ injection is for at least the dynamic miscibility and favourable mobility ratio to be attained during the displacement process. Accordingly the candidate reservoirs should have a pore pressure of 1450 psia to 2175 psia or above (Mathews 1989) and the effective permeability has to be greater than 5 md (Martin 1992). Sometimes CO₂ injection may alter the permeability of the medium if the irreducible water saturation (S_{wi}) is highly saturated with dissolved salts. Because during the CO₂ flooding brine becomes supersaturated as the S_{wi} is continuously evaporated into the injected phase, as a result salt precipitation will occur in the pores. This causes injectivity impairment which results in unfavourable displacement type.

Several points outlined by Bachu, Shaw, and Pearson (2004) for selecting and screening oil reservoirs that would be suitable for the CO₂-EOR process are given below. The outlines are based on the studies reviewed in the literature by these authors.

Parameters for selecting candidate oil reservoirs for EOR by CO₂ injection are:

- Oil (density) between 788 and 893 kg/m³ (27^o API and 48^o API),
- Temperature between 32 °C and 121 °C,
- Reservoir pressure should be greater than 1100 psia,
- Injection pressure should be at least by 200 psia more than the minimum miscibility pressure, and
- Oil saturation should be greater than 0.25 of the original oil in place.

The increment in oil estimated to be recovered from the candidate reservoirs by CO₂ flooding ranged from 7% to 23% (average 13%) of the original oil in place (Martin 1992; Todd and Grand 1993; Taber, Martin, and Seright 1997).

Due to an unfavourable viscosity ratio ($\frac{\mu_{CO_2}}{\mu_{oil}}$) CO₂ always tends to bypass the in situ reservoir fluid because of gravity segregation during the displacement process resulting in poor sweep efficiency. Therefore to mitigate the tendency of CO₂ to channelling and gravity overriding, dispersion of CO₂ in a liquid phase (foam) has been studied constantly since the 1970s (Bikerman 1973). (See Figure 2.4)

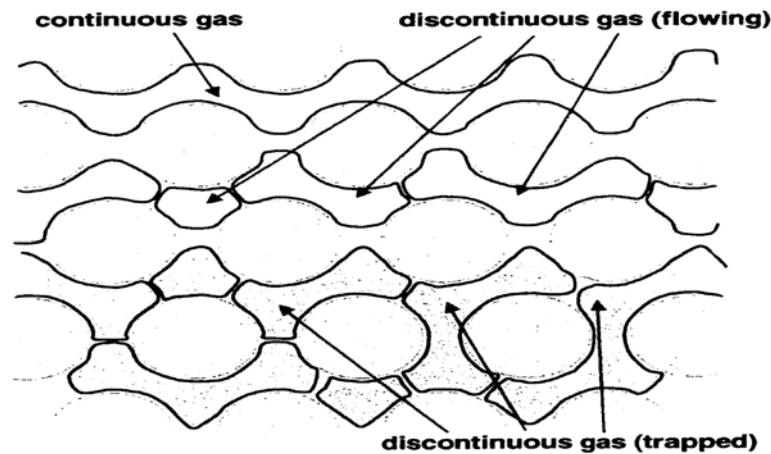


Figure 2.4: Pore level schematic of foam in porous media. After Tanzil (2001).

This was first, to control the high mobility of CO₂ when it passes through the porous medium that have been filled with liquid phase (foam) and second, to divert CO₂ to the unswept region to maximize recovery efficiency (Martinz 1998). Laboratory investigations indicate that gas mobility can be reduced conspicuously by a factor greater than 10,000 when it is dispersed through a foam in a porous media (Rossen and Zhou 1995). Results from field trials have revealed that foam would reduce gas mobility only by a much smaller factor (Ligthelm, van Eijden, and Gronsveld 2000). Furthermore, foam has been studied and applied for enhancing oil-steam flooding because steam flooding alone has been noted to suffer from poor sweep efficiency (Djabbarah et al. 1990) particularly in a reservoir characterized by permeability heterogeneity and multi zone layers (Hiraski 1989). The petroleum industry began to investigate the application of foam for EOR in the early 1960s and since then many field trials have been implemented by injecting the surfactant being assimilated with

gas to the subsurface to generate foam. The results have shown that CO₂ mobility was noticeably reduced, sweep efficiency was enhanced and hence improved oil recovery (Tanzil 2001). In extreme reservoir conditions of high temperature and pressure, the foam would be less effective and even destroyed, particularly in a region where fluid flow is specifically affected by capillary pressure and brine saturation (Khatib, Hirasaki, and Fall 1988; Rossen and Lu 1997). In addition, to divert CO₂ foam into unswept areas of the reservoir, the concept of gel-foam has been proposed by (Friedmann et al. 1997; Hughes et al. 1999). This process is performed by dissipating gas into a distinctive foam type which would form gel and propagate into the reservoir.

Results indicated reduced foam mobility has been achieved with the gel concept; the CO₂ that is released from the break-up of the foam-gel would be forced to propagate and flow in other directions to the main injection stream. Consequently CO₂ mobility is decreased and diverted to an unswept location from which improved sweep efficiency is observed. Moreover, CO₂ gel-foam has been used to control fluid flow from the high streak of the permeable zone, as well as from fractures and joints. The gel foam technology conserves the amount of gelant required to form the flow barrier compared to conventional non-foam gel treatment. This results in significant cost reductions.

2.6 CO₂ for enhanced coal bed methane recovery:

Coal-bed gas is a form of natural gas that can be extracted from coal beds by pressure depletion that causes methane to desorb from the coal-bed. It is characterized by dual primary and secondary porosity systems. The primary system that contains the majority of gas-in-place is characterized by a network of micro pores. Fluid flow through this zone can be represented by mass transfer and diffusion due to its moderate impermeability (Mazumder and Wolf 2008). For the secondary system, which is characterized by macro pores and natural fractures, fluids can flow under a pressure gradient and thus can be represented by Darcy's law. Recovery of methane from a coal bed is regarded as being mainly controlled by the permeability of the coal bed and porosity distribution (Syahrial 2005). As carbon dioxide is injected to displace methane it is preferentially adsorbed by the coal causing desorption and thus methane will be produced (Busch et al. 2004). Upon

adsorption CO₂ displaces methane from the primary porosity into the secondary porosity system so that the pressure of the secondary porosity system will increase and force the methane to flow to the production wells (Shi and Durucan 2003).

The first large scale pilot CO₂ injection for coal-bed enhanced gas recovery started in 1995, in the San Juan Basin, New Mexico (Stevens and Riemer 1998). This project consisted of a 4-injector and 7-producer well pattern. Injected CO₂ was supplied from a nearby pipeline that transports CO₂ at pressure of 2000 psi from a carbon dioxide-enhanced oil recovery field in Colorado. Approximately 85×10^3 m³/day (3 MMSCF/D) of carbon dioxide was injected resulting in enhanced gas production by up to 150% in comparison to production under the conventional pressure-depletion method. During 1998, the amount of CO₂ that had been sequestered at the pilot project was considered to be more than 57×10^6 m³ (2 BSCF). Primary results indicated that CO₂-ECBM project would be cost-effective in the San Juan Basin at wellhead gas prices of above 6.18 cents/m³ (\$1.75/MSCF), with possible enhanced production of methane at 3.7×10^{11} m³ (13 TSCF) adding a resource value as much as \$22.8 billion. Coal-bed methane development in the San Juan basin accounts for 75% of world coal-bed methane production (Seo 2004).

2.7 SCO₂ disposal into aquifer:

With the purpose of reducing green house emissions, geological aquifers have been a subject of intense studies for CO₂ sequestration. The trapping mechanisms of CO₂ in an aquifer were considered to be controlled by the following factor (Kumar et al. 2005; Noh et al. 2007)

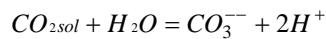
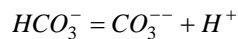
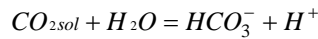
- In a gaseous phase or supercritical phase CO₂ can be trapped near the low permeable sealed cap rock,
- Dissolution into the aqueous phase,
- Mineralization due to the interaction of dissolute CO₂ with the minerals and organic matter of the host rock, and
- As a residual gas saturation that is trapped by capillary pressure.

As the CO₂ is injected to displace brine in an aquifer, the mobility of CO₂ is dominated by drainage relative permeability, which is wetting phase relative

permeability. After injection, due to viscosity differences and hydrodynamic flow through the aquifer, the CO₂ is more buoyant than the brine and tends to move upward in the reservoir. The migration of the CO₂ plume is dominated by both drainage and imbibition relative permeability. At the head of the plume where the CO₂ displaces brine, trapping of CO₂ depends on drainage relative permeability, while at the tail where the drained brine displaces CO₂ it depends on imbibition relative permeability (Flett, Gurton, and Taggart 2004). Over a period of time with continual, drainage-imbibitions, displacements between CO₂-brine, the mobility of the CO₂ diminishes substantially through dissolving in the aqueous phase and imbibing as a gaseous phase as residual gas saturation in the pores media. In addition, pore size distribution, capillary pressure, IFT CO₂-Brine, salinity, pressure and temperature are recognised as being able to affect CO₂-brine relative permeability (Bennion and Bachu 2006b; Bennion and Bachu 2006a).

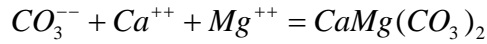
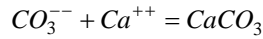
2.7.1 Chemical process during CO₂ injection:

When SCO₂ propagates in a porous medium to displace methane that was initially saturated with connate water, part of the gas will react with the aqueous phase. The mechanism that is causing SCO₂ to dissolve in the aqueous phase is of great importance, particularly to predict mineral dissolution and precipitation. Impacts of mineral dissolution and precipitation can be seen through the injectivity impairment throughout the reservoir. The main chemical reactions occur while SCO₂ is dissolving into connate water and can be represented by the following equations according to Xu, Apps, and Pruess (2000):



The above reactions are homogeneous and involve only aqueous components. If ions are freed into the aqueous phase from the dissolving minerals of the host rocks, carbonate will react with these ions and possibly minerals precipitation will occur. The precipitation of minerals depends on the mineral composition of the host rock

(Gunter, Perkins, and McCann 1993; Gunter et al. 1996). For example if it is carbonate or dolomite rock the following reactions could occur:



In a simulation study by Pruess et al. (2003) it was demonstrated that SCO_2 injection results in a decreased porosity in the reservoir that can generate a large decrease in permeability. The medium of reaction is observed to be acidic as the pH is considerably reduced due to dissolution of SCO_2 in an aqueous phase. This change in pH leads to chemical interaction between the acidic aqueous phase and the rock minerals. Calcite and dolomites in general are the most reactive minerals and tend to precipitate. In another study by Calabrese and Masserano (2005) the estimated time that was required for precipitating various minerals due to SCO_2 injection into the reservoir formation was analysed. It was noted that for calcite, approximately 20 years is anticipated while for quartz about 10,000 years is required.

Injectivity impairment due to mineral precipitation should be taken into consideration in such a project. For instance in a northern German Basin where the reservoir is saturated with highly saline brine, SCO_2 injection caused injectivity impairment. In this case, the brine becomes supersaturated as the water consistently evaporates into the SCO_2 phase and halite precipitates in the pores.

2.8 Relative Permeability:

Conventionally, relative permeability is used to describe and model the multiphase-flow of the immiscible fluids through porous medium. The analysis of such complex multiphase flow in porous media is normally ascribed as a Darcy-type formulation. The extension of Darcy's law to include the phase relative permeability concept appears to have been first suggested by Muskat and Meres (1936) and co-workers Wyckoff and Botset (1936). Relative permeability of a phase was presented as a function of the phase saturation and a fraction of the pore volume that is occupied by the phase. At unit phase saturation, where the phase occupies all the pores, the intrinsic permeability is exactly equal to the single-phase permeability. Therefore, relative permeability to the phase will be equal to unity at maximum phase

saturation. On the other hand, relative permeability to the phase approaches zero when the saturation is so low the phase is isolated and no longer connected in the porous medium. Any further reduction in saturation of the residual phase saturation the phase becomes stagnant. Disconnected droplets can build up significant resistance to flow and cannot be dragged along by the continuous flowing of the phase because of Jamin's effect (Calhoun 1953).

At a given saturation, fluid flow in porous media could be the function of several macroscopic transport properties such as relative permeability, capillary pressure and dispersivity. Experimentally determined, these properties depend on fluid saturations, saturation history, fluid properties (viscosity, density and composition) and pore space morphology. The preference of the porous material is different for being covered or wet by one of the phases and the interaction between the fluid phases and the pore wall engages capillary forces and ultimately influences the fluid distribution in the medium. The wetting phases tend to distribute over a high capillary region (the small pores) thus minimizing the contact angle with the pore wall. By contrast, the non wetting phases that have a preference to occupy the space in the middle of the larger pores maximize the contact angle with the wall. The difference in fluid distribution causes dissimilarity in relative permeability to the wetting and the non-wetting phase. This may be seen in Figure 2.5 which shows the results of the earliest measurements of relative permeability as a function of liquid saturation.

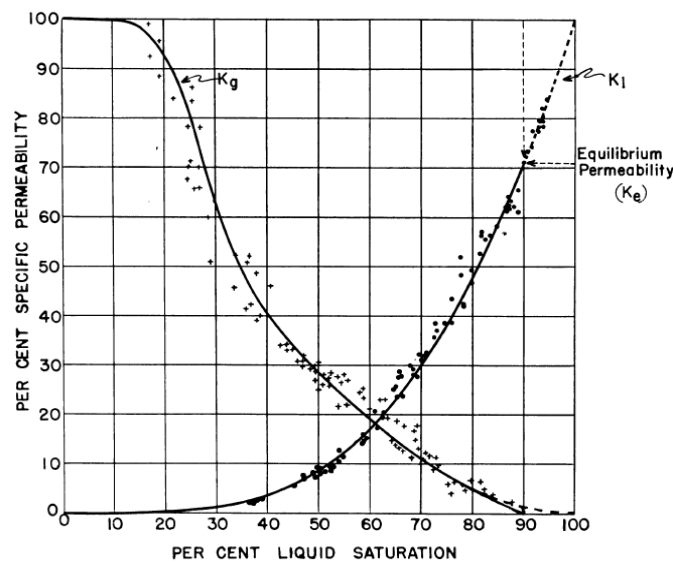


Figure 2.5: Gas relative permeability as a function of liquid saturation. After Muskat et al (1937).

These results were obtained by Muskat et al. (1937) from experiments conducted on sand columns measuring the simultaneous flow of water and carbon dioxide gas. A point to be noted is that when the sand column was equally saturated with both phases (corresponding to saturation 50%), relative permeability of the wetting phase (water) was much lower in comparison to the non-wetting phase (gas) relative permeability. This is because the friction encountered with the pore walls for the wetting phase was more than for the non-wetting phase. Accordingly the non-wetting phase tends to flow in channels connecting the larger pores (low capillary regions), which makes flow with ease through the medium in contrast to the wetting phase.

In the case of two gases flowing (SCO₂ – methane) simultaneously through a porous medium, researchers interpret the flows behaviour in terms of gas dispersion and molecular diffusion. The displacement front in such gas-gas systems in porous media has been considered as a gradational zone ranging from one pure phase to another. Hence, effects of capillary force on the phases' distribution are expected to be diminished because gas phases cannot create a finite contact angle with the pore walls. Initially both phases, as injected, tend to saturate the larger pore and then smaller pores if the viscous force is great enough to overcome capillary forces that are produced by morphology of the porous media. As a result, recovery efficiency will not be affected by the phase's relative permeability.

Recovery efficiency of a phase in gas-gas displacement will be a function of gas properties, morphology of the pores, mobility ratio, injection rate, composition and permeability heterogeneity. On the other hand, some researchers believe first contact miscible in a reservoir porous medium may not be occurring due to the intrinsic nature of the process, as well as the reservoir macroscopic and microscopic properties. Therefore the near-miscible phase term or multi-contact miscible behaviour considered for two phases is recognized by a low or fragile interface. Consequently the recovery efficiency of one of the phases will be a function of relative permeability effects. Many experimental studies that have been carried out at low interfacial tension have indicated relative permeability of the fluids was enhanced if compared to the relative permeability of two phases corresponding to high interfacial tension (Bardon and Longeron 1980; Haniff and Ali 1990; Schechter and Haynes 1992; Jerauld 1997).

The enhancement in the relative permeability curves was seen in terms of weakening the capillary forces as the interfacial tension decreased. For instance, if a case of zero interfacial tension is expected, like single-phase flow, relative permeability arguably increases because the medium will have the same affinity for the flowing phases. The relative permeability can be represented as two identical curves that intersect at 50% of phase saturation in the porous medium. As wettability would not have any effects on phase distribution, there will be no preference for one of the phases to take the faster path. Therefore, relative permeability is linearly proportional to the pore space occupied by the phase in question. Moreover, the hypothetical relative permeability curves should approach to unity and the fluid flow should be described in terms of diffusion and dispersion. The ideal relative permeability curves if representing the flowing phases would be unit-slope straight lines as shown in Figure 2.6.

When the interfacial tension between two phases becomes sufficiently low, the capillary forces that would be formed would be weak and can be neglected with regard to the viscous forces caused by friction within the flowing fluids. As a result, the ratio of the viscous forces to the capillary forces induces a change in flow regime and thus relative permeability curves approach the trends in Figure 2.6.

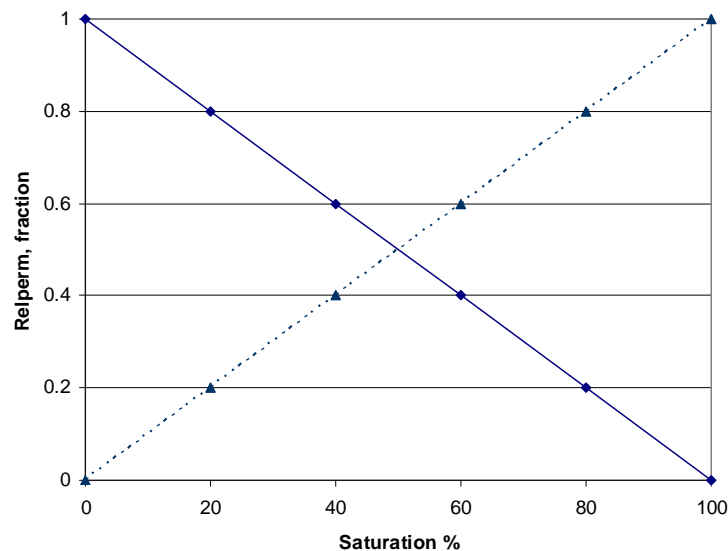


Figure 2.6: Ideal Gas relative permeability for two miscible fluids.

This type of displacement, which corresponds to low interfacial tension, is considered as dynamic miscibility contact or a near-miscible process. The wetting

state in this condition will be a possible cause affecting relative permeability curves. If the interfacial tension is reduced below a certain value, an incipient layer of the wetting phase will be formed inbetween the non-wetting phase and wetting phase or solid phase. This phenomenon in the wetting state was predicted by Cahn (1977). Accordingly wetting alteration by transition can influence the relative permeability curves at a certain value of the interfacial tension, rather than at a certain ratio of the viscous forces to the capillary forces on the pore scale.

From the literature there is no consensus on which mechanisms relative permeability curves at near-miscibility condition are affected and which parameters are controlling the trend of the curves. Several investigators have found non-wetting phase relative permeability has been easily affected at near miscible condition rather than wetting phase (Ameafule and Handy 1982; Harbert 1983; Henderson et al. 1996). Whereas others have observed wetting phase relative permeability as being significantly increased if compared to the non-wetting phase relative permeability (Asar and Handy 1988; Schechter and Haynes 1992).

Moreover, some authors concluded that establishing a weak interface between both phases would not affect the trend of their relative permeability (Delclaud, Rochon, and Nectoux 1987; Kalaydjian, Bourbiaux, and Lombard 1996). This indicates that the mechanisms that affect the relative permeability of the two phases are not well understood and appears to be arguable. Wetting transitions that occur between the phases at this condition are considered to be responsible for the changes that appeared in relative permeability (Teletzke, Scriven, and Davis 1981; Schechter 1988; Haniff and Ali 1990) whereas, on the other hand, several researchers expected that the controlling parameter would be a ratio between the strength of the viscous forces relative to that of the capillary forces on the pore scale (Leverett 1939; Bardon and Longeron 1980; Ameafule and Handy 1982; Boom et al. 1995; Henderson et al. 1996; Pope et al. 1998).

The transition zone will occur between miscible fluids during displacement tests, particularly when the fluids are in a gaseous state and will be different from the transition zone that would appear between near-miscible fluids.

Because in a gas-gas system this zone consists of compositional gradation from one pure gas phase to another and its length depends on the dispersion and molecular diffusion mechanisms with time.

2.8.1 Fluid distribution on the pore scale:

When two fluids are flowing through a porous medium their distribution over the pores is strongly influenced by capillarity, which is a result of the interaction between the porous medium, the wettability of the flowing fluids, and the cohesion within the fluids (interfacial tension).

If the interfacial tension between the two immiscible fluids is noticeably high, the preference of the porous medium for one of the phases will, undoubtedly, have an influence on the distribution of the phases over the pore space. For this reason, the distribution is scarcely influenced by the increase in viscous forces. Thus, capillary forces relative to viscous forces on the pore scale dominate immiscible multi-phase flow. Consequently, macroscopic flow quantities such as relative permeability can be seen independent of interstitial velocity and interfacial tension. At this condition relative permeability of both phases will be a function of the fluid saturation, saturation history and properties of the porous medium.

For the gas-gas system where the interfacial tension is weak, the main parameters that influence the stability of the interface are dispersion and molecular diffusion mechanisms. These are significantly affected at pore scale by heterogeneity, gas composition, viscous forces, and gas properties (viscosity and density). Therefore relative permeability in a gas-gas system will be a function of the parameters mentioned. However a distinct interface captured between SCO_2 and methane by Amin et al. (2010) (See Figure 2.7). Relative permeability should not be seen as only being affected by the interfacial tension and phase saturation in a gas-gas system, because of dispersion and molecular diffusion parameters.

The steadiness of the interface, at very low rate, was time dependant and vanished with time due to molecular diffusion and compositional equilibration. This has been noticed as a cloudy layer which formed around the SCO_2 -methane interface on top of the needle and is explained as a compositional gradient.

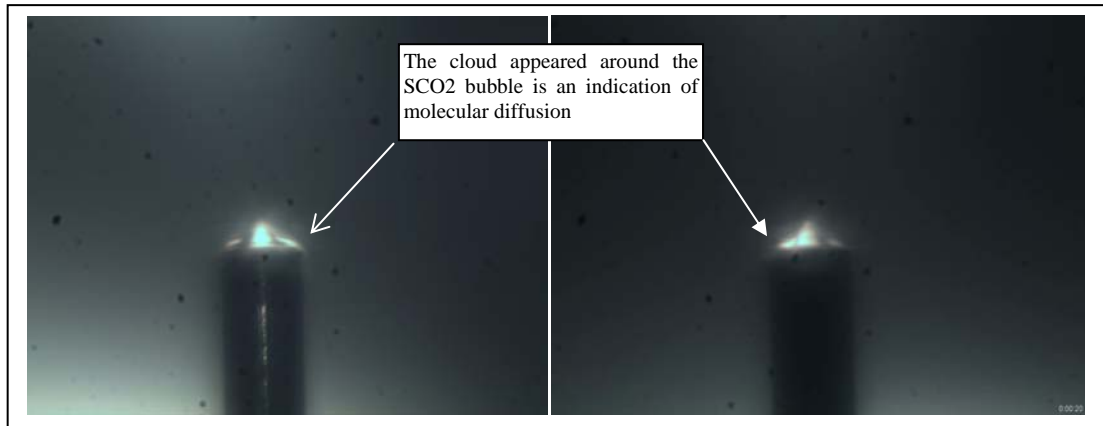


Figure 2.7: Interface between SCO_2 and methane, the bubble is SCO_2 and the ambient is methane at 3000 psia and 95°C .

To the author's knowledge there is not any literature focuses on simultaneous flow of supercritical and natural gas fluids in porous media in terms of relative permeability. Reviewing the parameters that are considered as having a significant effect on the near-miscible fluids' relative permeabilities will provide a substantial understanding to predict which factors can be chiefly influencing the relative permeability between supercritical fluids and natural gases. Because natural gas displacement by supercritical gases in porous medium will exhibit approximately the same behaviour as fluids displaced at near-miscible conditions such as IFT and the viscosity ratio. For example, interfacial tension measurement and viscosity ratio between SCO_2 -methane that has been published recently (Amin et al. 2010; Sidiq and Amin 2009) are comparable of that between two near-miscible phases (Bardon and Longeron 1980; Harbert 1983; Boom et al. 1995).

2.8.2 Effect of miscibility:

Some of fluids are mutually immiscible and separated by a distinguished interface. However any attempt to diffuse this interface by mixing the fluids employed will not work as the interface will remain visible and clear. Since the molecules of the phases have the ability to share a combined lesser orbit upon the external effort applied, the interface will remain clear. On the other hand, most gases' molecule cannot share definite orbits in their phases therefore they mix with ease and have no distinctive interface and become miscible in all proportions. In-between these extremes there are some fluids partially miscible or incompletely miscible. Their molecules have the

ability to mix and share less room but only partially and not in all proportions. The degree to which partially miscible fluids mix depends on the fluids chemical composition, temperature and pressure.

The impacts of miscibility on recovery efficiency have been studied comprehensively since early last century. Achieving absolute miscibility between injected and in situ fluid in the reservoir is important to reduce residual phase saturation that is held by wettability and capillary forces. Most researchers believe ideal sweepout can only be obtained in the case of miscible displacement because miscibility can alter wettability and reduce capillary forces. Therefore, any applicable means that can lead to the reduction of capillary forces and interfacial tension between the phases have been studied constantly for fluid-gas systems in reservoirs. For example, interfacial tension between two phases may also be reduced by an increase in viscous forces or the addition of a surface-active agent like soap. The surfactant molecules are attracted to the interface so that a fragile intermediate interface phase will form, resulting in low effective interfacial tension between the original phases.

When a gas is displacing another gas within reservoir pores, the approaches made to achieve improved recovery for a gas-gas system will be completely opposite to that considered for liquid-gas system. Miscibility in such systems adversely affects the amount of in situ gas that can economically be recovered. This is because the length of the miscible phase would not be constant as it is growing with time by means of dispersion and molecular diffusion. These factors will lead to earlier breakthrough and reduce the potential value of the in situ gas. To achieve a better recovery factor the length of the miscibility zone should be controlled.

2.8.3 Effect of interfacial tension:

Interfacial tension can be defined as the tendency of liquids to reduce their exposed surface to the smallest possible area which causes it to behave as if it is a stretched elastic membrane. The strength of the interface depends on the forces of attraction among the particles of the liquid itself, and with the particles of the gas, solid, or liquid with which it comes in contact.

Moreover, interfacial tension may be seen as the amount of energy required to create a unit area of interface (White 1972; Gennes et al. 2004) or as the force per unit length acting along an arbitrary line on the interface.

Due to the shrinkage tendency, the curved interface can only exist when there is a pressure difference between the two phases. For example, for two phases α and β that are separated by an interface, their particles inside are forced to share less space until the internal pressure across the interface exceeds the pressure outside by a sufficient amount. Laplace (1806) measured the pressure difference over a curved interface depending on principal radii R_1 and R_2 :

$$p_\alpha - p_\beta = \sigma^{\alpha,\beta} \left(\frac{1}{R_1} + \frac{1}{R_2} \right) \quad (2.3)$$

Where p_α and p_β are the pressures in the α phase and the β phase, respectively, and $\sigma^{\alpha,\beta}$ is the interfacial tension between the two phases.

An extreme interface between the injected and in situ fluid in a fluid-fluid or gas-fluid system will influence the economics of flooding, particularly when associated with an unfavourable mobility ratio. Poor sweep efficiency will result because the injected fluid in this condition will have a tendency to viscous fingering, gravity overriding or underriding, and channelling through the in situ fluid. On the other hand, the presence of an interface in a gas-gas system will be of benefit to the enhanced gas recovery project. This is because it will reduce the arbitrary motion of molecules at the interface, resulting in less contamination between the injected and produced gas during displacement process. This makes the displacement process at pore scale being more likely to be piston type.

2.8.4 Effect of wettability:

Wettability can be defined as the affinity of a solid surface to be wetted by a liquid phase for a wetting phase. The surface tension of the liquid is reduced so that it spreads over the solid phase. In general, the attraction of a solid surface to liquid phases will vary from one fluid to another. Assume phase β is attracted more strongly than phase α to a solid phase S . Establishing a unit area of an interface between the β -phase and the solid S requires less energy in comparison with the

same area of interface between the α -phase and the solid phase. This means the surface tension between the β -phase and the solid ($\sigma^{\beta,s}$) is lower than that between the α -phase and the solid ($\sigma^{\alpha,s}$). Accordingly the β -phase is then called the wetting phase and the solid phase is called β -phase wet.

While the wetting phase creeps over the solid phase a contact angle will form between the phases and its value depends on the nature of the solid surface and physical properties of the fluids. Researchers have indicated that if the contact angle ranges between 0 and 90⁰ (or others believe between 0 and 75⁰), the solid surfaces would be water wetted. On the other hand, if the angle becomes greater than 105⁰ the surface will be oil-wetted. The range lies between these two extremes is considered to be the intermediate wetted phase. Figure 2.8 shows the contact angle of a drop of the wetting phase β that is surrounded by a non-wetting fluid phase α with the solid phase. The contact angle created on the solid surface with both fluids can be used to analyse the wettability of the solid phase. Young (1805) derived a relation for calculating the angle from the surface tension forms between the fluids and the solid surface.

$$\cos \theta = \frac{\sigma^{\alpha,s} - \sigma^{\beta,s}}{\sigma^{\alpha,\beta}} \quad (2.4)$$

Where θ is the contact angle formed between the wetting phase and the solid surface. According to Adamson (1997) the contact angle generally would not be the same when the wetting phase is advancing or receding from the solid phase because of the irregularities in the solid surface and thus being subject to hysteresis.

Wettability has significant consequences on recovery efficiency especially in oil-wetted reservoirs. At laboratory scale study high residual oil saturation for oil-wetted core plugs was noticed in comparison to water-wetted plugs. The same situation is recognized where a reservoir is strongly oil-wetted. Therefore to reduce residual oil saturation after primary recovery, other methods such as hot steam, CO₂, surfactant and alcohol injection have been investigated for secondary and tertiary recovery methods.

If the fluids were gaseous, such as enhanced gas recovery by SCO_2 , both phases are acting as the more non-wetting phase because gas has not the ability to form a definite thermodynamic stable interface with the solid surfaces. Therefore the preference of the solid surface being wetted by the flowing phases (SCO_2 and methane) will most likely be the same. On the other hand, if the residual water saturation appeared as a thin film coating the surface of the porous grains, the preference of the medium of being wetted will be attracting injected phase, because CO_2 has the ability to interact with water either through dissolution or evaporation. This will add a resistance to the CO_2 dispersion relative to methane, hence the rate of mixing between the injected and displaced phase will be controlled.

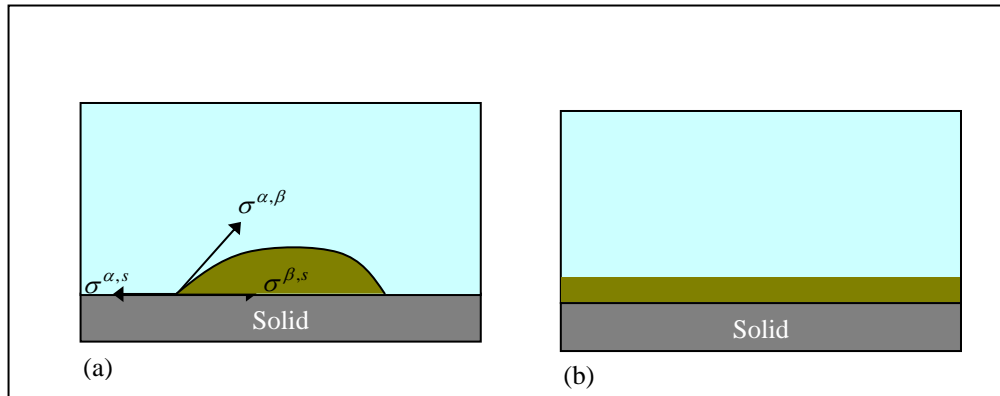


Figure 2.8: Schematic explanation of wetting phase and non-wetting phase contact angles that forms with a solid surface. (a) Partially wetting the solid $\theta > 0$, (b) completely wetting the solid ($\theta = 0$).

2.8.5 Effect of capillarity:

The interaction between the surface tension of a fluid and a solid that distorts the fluid interface to form a planer shape is known as a capillary force. This phenomenon occurs when the pressure inside the wetting phase β is lower than in the non-wetting α phase in a capillary regime. Thus capillarity at pore scale induces spontaneous flow of the wetting phase into the medium (imbibition), whereas it resists the drainage of the wetting phase from the medium.

For example, when a porous medium is fully saturated with the preferentially wetting phase β , the non-wetting phase α can only move into the medium if its pressure exceeds the capillary pressure that imbibed the wetting phase. If the pressure difference applies between the two phases over a distance L through the medium it will be balanced by capillary forces. Flow in this condition where the steady state is

reached, will be controlled by capillary pressure. The magnitude of pressure across the porous medium depends on the volume of the wetting phase that can be drained in the medium.

Leverett (1941) measured the macroscopic capillary pressure as a function of saturation from experiments conducted on different porous medium and fluids. Leverett eventually suggested that capillary pressure can be expressed in terms of the interfacial tension and the macroscopic properties of the porous medium:

$$P_c = P_{nw} - P_w = \sigma \sqrt{\frac{\phi}{K}} J(S) \quad (2.5)$$

Where n_w and w refer to the non-wetting and wetting phase, respectively, ϕ is the porosity of the porous medium, K is the permeability of the medium and $J(S)$ is a dimensionless capillary pressure, this is known as the Leverett function.

According to Stegemeier (1977) Eq.2.4 reasonably represents the capillary pressure for a condition when the wetting phase is completely wets the solid phase, meaning $\theta=0$. To generalize the applicability of Leverett (Eq.2.5), the right-hand side of the equation should be multiplied by a factor that weakly depends on the contact angle. Nonetheless capillary pressure partially depends on the contact angle as it is subject to hysteresis. This is because the hysteresis is somewhat influenced by the difference in the receding and advancing contact angle (Van Lingen 1998).

However it is a fact that when the wetting phase is drained it will be restricted by locally narrower pores than by the wider pores, whereas the opposite is true for imbibition that is restricted by the locally wider pores than the narrower ones. For instance when the non-wetting phase is forced into a porous medium, before the wetting phase actually moves, the pressure difference will rise. Thus the curvature of the interfaces increases as the pressure difference increases between the phases. At this stage the non-wetting phase is not able to occupy any pores until the interface yields to the increased pressure, which is most likely to occur in the widest pores. The corresponding configuration on the pore scale is schematically represented in Figure 2.9.

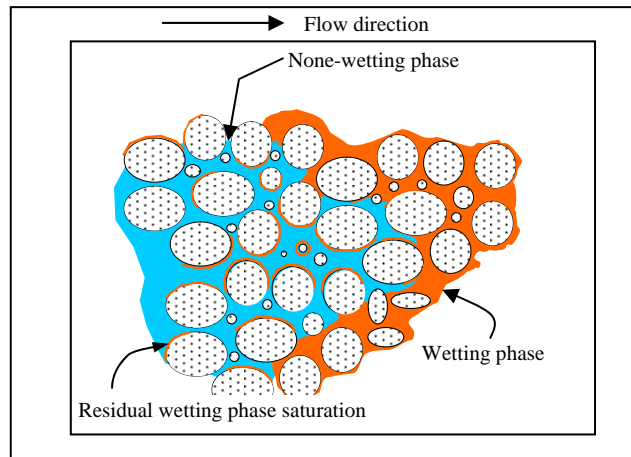


Figure 2.9: Schematic explanation of wetting and non-wetting phase distribution over pore network during displacement process.

As the saturation of a wetting phase approaches residual saturation the capillary pressure increases noticeably, and the wetting phase tends to cease flowing. The wetting phase will be in a pendular state and no longer connected; whilst in the case of complete wetting it is connected through a very thin film coating of the inner part of the pores. Any increase in pressure difference will cause compression of the pendular drops to concave shapes which are resident in small corners of the pore space.

In a similar way, the non-wetting phase can be trapped in the pore as isolated blobs resident in the centre of the pores. Capillary forces appear to have a significant impact on the fluid distribution and entrapment of the phases in the liquid-gas or liquid-liquid systems. For gas-gas (SCO_2 -methane) a capillarity effect is noticeable only when the core is heterogeneous. According to the Sidiq and Amin (2009) experiments, an immiscible interface exists only if the inner diameter of the needle is less than 0.22 mm, which means a high capillary region. However, gas cannot retain another gas in the porous media; the difference in the pores morphology in the direction of convective flux (flow gross) will increase the rate of mixing between SCO_2 and methane. Consequently only a smaller amount of methane can be economically recovered due to contamination.

2.8.6 Effect of high capillary number:

The phase distribution inside the porous medium has been a subject of many studies in terms of the ratio of the viscous forces relative to the capillary forces. As well the influence of this ratio on the reduction of non-wetting residual saturation level has been studied in the context of increasing injectivity, viscous forces, and adding surfactant to the injected fluid for the purpose of enhanced oil recovery (Stegemeier 1977). Results indicate that the residual oil saturation decreases if the viscous forces increase relative to the capillary forces.

From a dimensional analysis, Prey (1973) concluded that relative permeability might depend on the viscosity ratio of the fluids and on the ratio of the capillary forces to the viscous forces on the pore scale. This ratio is expressed by a dimensionless group, the capillary number, $N_C (N_C = \frac{\mu v}{\sigma})$. Although there is no consensus on the definition of capillary number from the literature (Larson, Davis, and Scriven 1981; Taber 1981), many have represented it in terms of a viscous pressure gradient. It has been known that viscous forces are the product of the viscosity and the velocity of the phase while capillary force is the product of interfacial tension and wettability. If the viscous forces overcome the capillary forces, the fluid distribution is altered in a way that the flow resistance is decreased and results in less residual phase entrapment. Therefore, achieving a high capillary number will result in enhanced relative permeability for both phases.

On the other hand, for a gas-gas (SCO₂-methane) system high capillary number will enhance relative permeability for both phases as well as result in less mixing. However to author knowledge there is not any published paper on this respect. The effect of capillary number on relative permeability and recovery efficiency will be discussed in detail in the following chapters.

2.8.7 Effect of Bond number:

The Bond number is a dimensionless group and can be seen as the ratio of gravitational forces relative to capillary forces on the pore scale. This dimensionless group was first defined by Bond and Newton (1928) to explain the motion of drops surrounded by a high viscous fluid. If one of the phases is much denser than the

other, the capillary force might be neglected, particularly if the interfacial tension was low and the pore size was relatively big. At this condition, segregation of a denser phase due to gravity will occur. This facilitates the denser fluid to flow in the lower part of the pore whilst the lighter fluid will flow in the upper part. The phase relative permeability curves at high Bond numbers, in a homogeneous medium, would approach the straight line as that shown in Figure 2.6.

When the fluid distribution is governed by the capillary forces in a given flow system, relative permeability curves will retrace the same trend regardless of the experimental conditions. If either viscous forces or gravitational forces control the flow regime, the three-dimensional channel flow system may be changed through which the separate phases flow. Subsequently this will influence the macroscopic properties of the flow regime. In that case, the described flow system may be well formulated through using apparent relative permeability functions that depend on the coupled properties and the flow conditions.

The effects of the Bond number in a gas-gas (SCO₂-methane) system have not been studied yet. As the SCO₂ density changes with pressure and temperature, especially at pressure >3000 psia and temperature >95 °C, the magnitude is about three times greater than methane density. In Figure 2.7, the denser SCO₂ moves downward like a fountain and then disappear by mixing with the methane. This suggests that gravity segregation does not occur in such systems and the propagation of the phases at pores scale could not be affected by the Bond number.

2.8.8 Effect of viscosity contrast:

The impact of viscosity contrast on gas-gas (SCO₂-methane) relative permeability has been studied. Referring to the IFT experiments, surface tension will be low if the viscosity contrast is small and thus result in greater mixing. For other systems if the capillary number is high the viscosity ratio between the coupled phases may influence the relative permeability. For instance, according to Vizika, Avraam, and Payatakes (1994) high viscosity contrast affects the stability of the fluid interface at pore scale during displacement. As a result flow channels may be arbitrarily formed as a highly viscous phase is being displaced by a less viscous phase.

The apparent relative permeability to the highly viscous phase was observed to decrease, while for the less viscous phase increased because of the high viscosity contrast (Peters and Khataniar 1987).

The conclusion is that relative permeability to the creeping flow of the coupled phases will be a function of saturation, saturation history, wetting state, and pore morphology. Outside the capillary-dominated flow regime, it will also depend on the viscosity contrast ($\frac{\mu_\alpha}{\mu_\beta}$), the capillary Nc and the Bond number.

2.8.9 Effect of pores morphology:

Since early in the last century, the effects of porous morphology on fluids flow in reservoir formation have been widely studied by numerous researchers. The fluids' permeability for a phase is found to be specific to the porous medium so that it can be correlated with macroscopic features of the pore geometry, porosity, tortuosity, and specific surface (Kozeny 1927; Carman 1937). In brief, pore geometry is found to significantly affect permeability for the phase through the pore size of the flow area. Tortuosity impact on permeability can be seen through the pressure gradient obtained over the length of the porous medium. If the medium is considered as high tortuous, it means average pressure gradients on the pore scale are lower than the measured gradient and consequently resulting to a lower permeability. Finally, the specific surface affects permeability through the surface of the pore wall; fluid flows through smaller pores encounter more friction with the wall surface of the pore therefore a larger specific surface corresponds to a lower permeability.

Darcy's equation is valid if the pressure drop is entirely due to viscous dissipation. This means that Darcy's equation ignores the pressure drop caused by changes in direction and magnitude of the momentum of the fluid particles that is known by inertial effects.

Reynolds in 1883 defined a dimensionless group that denotes the ratio of the inertial forces to the viscous forces. It is proportional to the characteristic size of the flow problem. For porous media, this size is given by the characteristic pore scale length, which may be estimated by the square root of permeability divided by porosity, this gives an expression for the Reynolds number of the form (Collins 1963);

$$\text{Re} = \frac{\rho \|u\| \sqrt{K}}{\mu \phi} \quad (2.6)$$

The critical Reynolds number is where fluid flow deviates from a Newtonian flow system to a turbulent type. Experiments indicated that if the Reynolds number demonstrates a value greater than the normal range 0.1-75, fluid flow deviates from a laminar flow type (Scheidegger 1974). The analysis of experimental results along with various literature data indicates that the critical value for the Reynolds number is approximately equal to 10.

The creeping flow regime corresponds to values below the specific critical Reynolds number. At higher values, the relation between pressure drop and flow velocity becomes non-linear. This does not necessarily indicate a turbulent flow regime; the non-linearity already arises when the flow is simply laminar.

Chapter 3

Experiments and Equipment Set-up

3.1 Introduction:

The experimental procedures and equipment setup for the interfacial tension and core-flooding experiments are described in detail in this chapter. The calibration methods that were performed to calibrate the facility equipment, such as pressure transducers, back pressure-regulator, flow meters, air bath temperature and CO₂ analyser, are explained and assessed. Results from the calibration tests indicated that there were variations in the readings of the instruments which were employed in the core-flooding and surface tension facilities. For the pressure transducer this variation was about 0.2-0.6 psi, back pressure regulator ± 5 psi, flow rate $< 1\%$, temperature ± 1 °C, and CO₂ analyser $\pm 3\%$. On the other hand, during the experimental runs many unexpected obstacles occurred, with most relating to the failure of the O-ring seals, stainless steel tubes (microscopic holes) and core-sleeves damage. SCO₂ was also recognized as behaving corrosively at the extreme test condition.

3.2 Equipment set-up for IFT measurements:

In the experiment a SCO₂ drop within the methane phase is formed at the tip of a capillary needle. Its digital image is then acquired, using a digital image acquisition system. Figure 3.1 shows a schematic diagram of the reverse pendant drop equipment used in this study. The major components of this system are a high-pressure chamber with two see-through windows (ST-Technology, France), an air bath and a precision injection system. The temperature during the test was maintained by the climatic air bath. The pressure cell was placed inside the air bath. The injection system composed of a syringe pump and two titanium cylinders, each containing a piston used for pressure increase in the system (See Figure 3.1). There are a total of 3 ports around the pressure chamber, each controlled through the very fine metering valves. In this study, the bottom port is used to introduce the SCO₂ into the methane phase, and the top port served as a pressure monitoring point. In order to obtain high resolution images of SCO₂ drop, the see-through windowed high-pressure chamber was placed between a light source and a microscope digital camera, with the entire experimental setup being mounted on a vibration-free table.

When the SCO_2 was injected through the bottom port, which was controlled via a very fine metering valve, a drop is formed in the methane phase at the tip of a stainless-steel capillary needle. The process of SCO_2 drop image capturing, analysis, digitization, and computation was carried out through a desktop computer that was attached to the system. Pressure in the chamber was monitored constantly and recorded in temporary memory in the data taker. After the completion of the test the data was downloaded directly onto the computer. In summary the system is designed in away to duplicate the interfacial interactions of the reservoir SCO_2 -methane system at high pressures and temperatures.

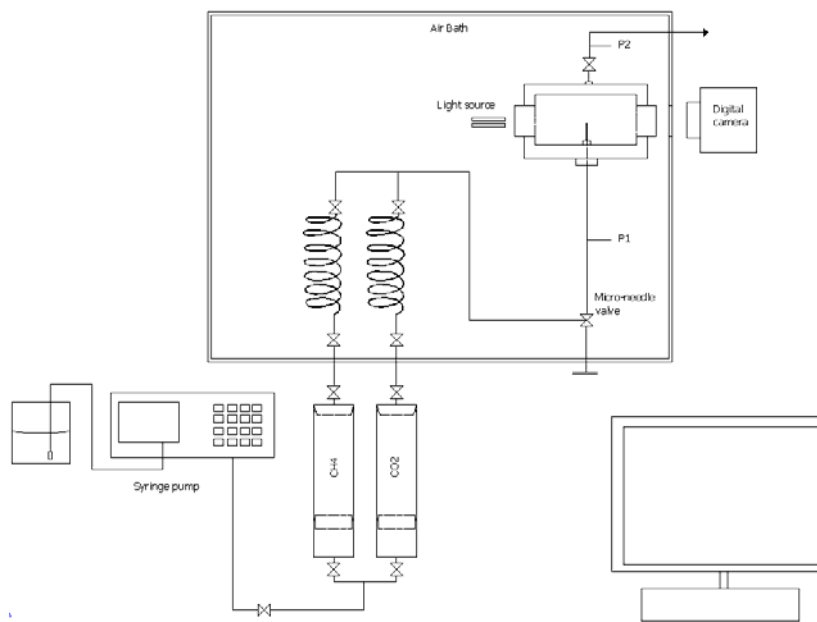


Figure 3.1: Sketch of apparatus used in investigating methane- SCO_2 interface.

3.2.1 Test producers:

The general experimental procedure for the IFT measurements and visual observations is briefly described as follows. The SCO_2 is introduced from the CO_2 coil placed inside the air bath, with pressure maintained by a positive displacement pump from the external cylinder. The flow of SCO_2 was controlled via a micro-needle valve until a SCO_2 bubble was formed at the tip of the stainless-steel needle. After the SCO_2 bubble has formed in the methane phase, its digital image was precisely-focused, acquired sequentially, and stored automatically in the computer memory. For each digital image, a standard grid image is used to calibrate the drop image and correct for possible optical distortion. The output data also include the radius of the curvature at the apex point, and the volume and surface area of the

SCO₂ bubble. The local gravitational acceleration and the density difference between the methane phase and SCO₂ were used as the input data for the IFT calculation. The IFT measurements were conducted at least twice to ensure satisfactory repeatability at the specified pressure and temperature. After each test, the IFT cell and the entire tubing system were evacuated to vacuum conditions and then flushed with methane. Through the application of computer digital image analysis and processing techniques, an accurate interfacial profile of the SCO₂ bubble was obtained. Finally, the IFT of the SCO₂ bubble surrounded by the methane phase was determined by solving the Laplace equation and finding the best fit for the numerically calculated interfacial profile to the physically observed bubble profile.

3.3 Core-flooding setup and apparatus:

Since the experiments commenced, the apparatus of the core-flooding facility was modified three times due to the variations in the required values for pressure and temperature. Initially the equipment was designed to withstand the tests to be conducted at a temperature of 95 °C and pressure up to 3000 psia. Second, to investigate pressure effects on recovery efficiency, the system apparatus was modified again, particularly the tubes and valves in order to be certain that the facility would yield accurate results at 6000 psia and 95 °C. Finally, as temperature was increased to 160 °C nearly all of the apparatus, such as tubes, back pressure regulators and valves had to be changed because SCO₂ at this condition demonstrated as a strong corrosive fluid even on the stainless steel tubes. In a few points the core-flooding facility units are described as follow:

The system consists of five main components:

- 1- Injection system,
- 2- Core-flood cell,
- 3- CT scan, performed before and after the run.
- 4- Data recording system, and
- 5- Confining pressure unit, back pressure regulator (BBR), flow meter, CO₂ analyzer and local designed flow rate check unit.

Two core-flood cells have been used in this study, the application of either depending on the dimension of the core plugs investigated; Table 3.1 shows the dimensions of the core plugs. For the longer core plugs, a cell about 100 cm long with an outer diameter of (13.38 cm) (5.3 in) was used. Whereas for the shorter core plugs a cell of about 25 cm long with an outer diameter of 12 cm was employed. The core plugs inserted individually into a Viton sleeve with both ends secured to plungers in the cell. Thereafter the cell is placed inside the core holder and fixed in a horizontal position, while vertically positioned when the gravitational impact on the displacement efficiency was examined.

Table 3.1: Dimensions of the core plugs tested.

S.N.	Samples Code	Length (cm)	Diameter (cm)	Area (cm ²)
1	S_C_1A	5	3.95	12.25
2	S_C_2A	5.05	3.89	11.89
3	S_C_3A	5.1	3.91	12.01
4	S_V_1	19.41	3.9	11.95

Figure 3.2 shows the schematic sketch of the experimental apparatus designed for the tests that were carried out at a temperature of 95 °C and pressure of 6000 psia. In this stage, the titanium cylinders were left inside the bath and connected to a syringe pump for the pore pressure maintenance during the tests.

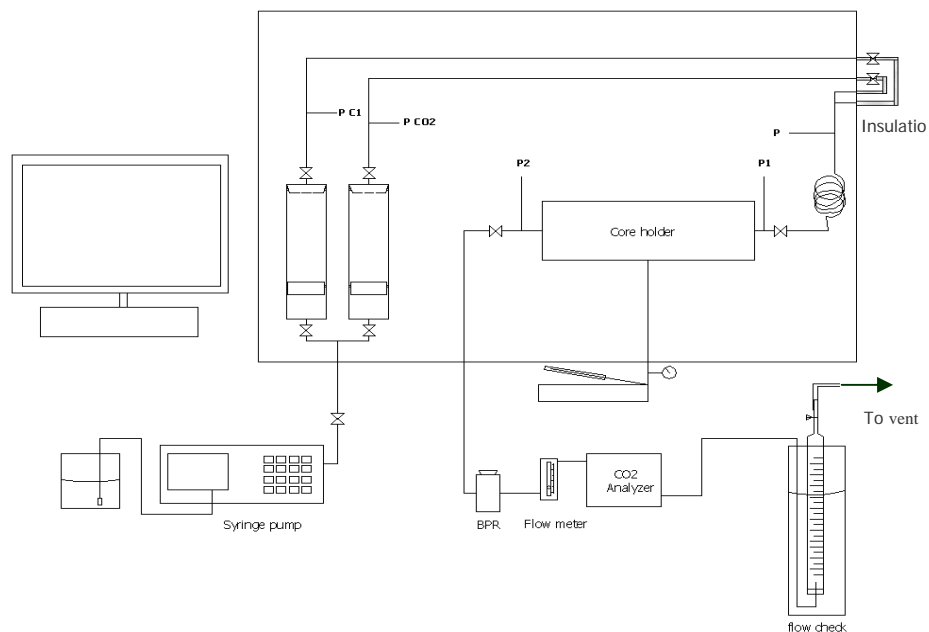


Figure 3.2: Sketch of the experiment apparatus designed for the tests up to 95 °C and 6000 psia.

The main constraint of this design was the Viton and Teflon O-rings damage. These O-rings were placed around the pistons as well as around the top and bottom lid of the cylinders. Although these O-rings are designed to withstand high temperatures (up to 250 °C), they were frequently replaced because of ruptures and melting. Supercritical CO₂ was considered to be the key factor for the failure of the seals. The friction of the piston's O-ring with the titanium cylinder-wall was also regarded as a contributing factor. However, high temperature lubrication was used for minimizing the friction impacts.

The worst case of the experimental phase was when the temperature increased from 95 °C to 160 °C. All the seals (O-rings at top and bottom lid, and around the piston in the CO₂ cylinder) were promptly destroyed as the temperature of the bath reached 160 °C. The O-rings could not even withstand this temperature for 10 minutes and SCO₂ gushed into the air-bath from the cylinder. Figure 3.3 shows samples of the damaged O-rings collected during and after the experimental runs.



Figure 3.3: Samples of O-rings damaged during the experimental runs.

To overcome the seals operation limitation, the core-flooding facility was modified by replacing the titanium cylinders with two stainless-steel tube coils, each having a volume of 110 cm³. These coils were connected directly to the cylinders and placed outside of the air bath to maintain the desired pore pressure. (See Figure 3.4)

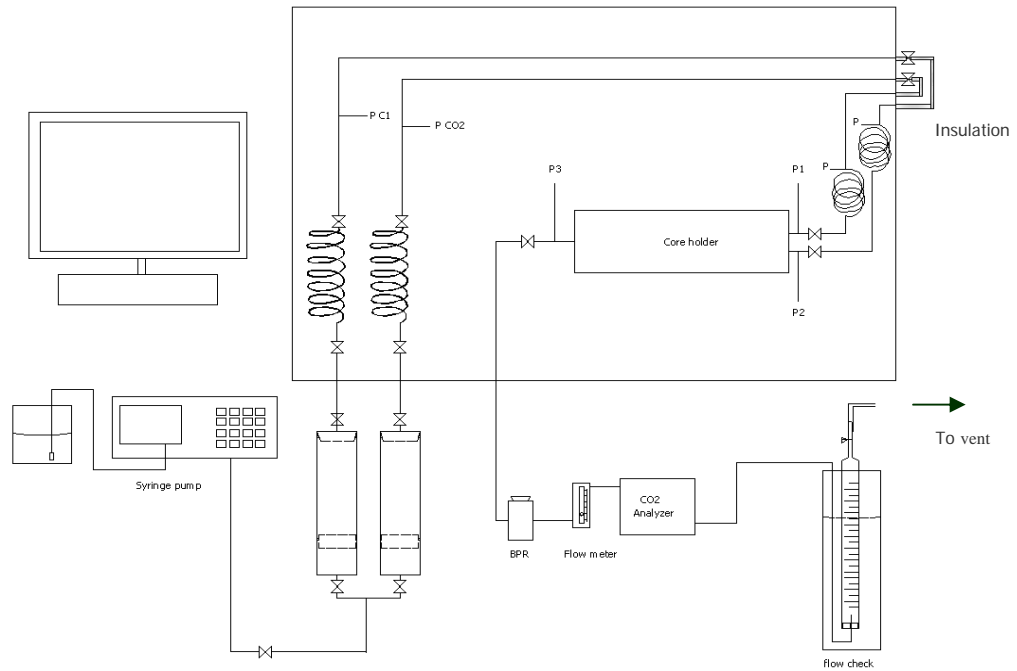


Figure 3.4: Modified Sketch of the experiment apparatus designed to stand up to 160 °C and 6000 psia.

Another unexpected limitation of the tests that were carried out at 160 °C and 5900 psia was the constant stainless steel tube damage. These tubes were supplied by Swagelok, and according to their manual have operational specifications of 11,000 psia at 250 °C. Although the burst pressure of the tubes is three times higher at the given temperature 250 °C, at several locations along the tube lengths inside the air bath, tiny holes appeared.

The experimental conditions were considerably lower than the manufacturer's specification, the Swagelok stainless tubes could not withstand the severe conditions of the tests. This damage to the tubing was detected when some inconsistent results were obtained when constantly observing pressure drops in the system.

Experimentally these tiny holes were located by shutting all the valves in the system and monitoring the pressure drop through the system. While, no leakage was seen at the tube-tube and tube-valves connections, the continuous pressure drop required the author to check the entire length of the tubes in the system for leakage, particularly in the air bath. Eventually the tiny holes that caused the problem were detected. This matter was reported to the supplier on three occasions for tube replacement. The tube failure caused considerable delays.

The corrosive nature of SCO_2 under the test conditions was the major source for the tube damage. Therefore, before deploying SCO_2 re-injection at the field operators are recommended to take this observation into account.

The core-sleeves used in the experiments were supplied by Ergo-tech (UK). These are high quality sleeves designed to fully function under the referenced conditions. Even though, the operating specifications of the sleeves is much higher than the test conditions applied in this study, these sleeves started melting and rarely could they be extracted safely from the core plugs. Throughout the experiments almost three meters of core sleeves were consumed because once the system shut down the inner layer of the sleeves either melted or swelled as bubbles, this can be seen clearly in Figure 3.5.

Again the SCO_2 dissolving into the sleeve (polymer) was considered to be behind the damage observed on the sleeves. It is recommend taking this matter into account in designing an SCO_2 re-injection that may deploy seals, o-rings or any polymers in an enhanced gas recovery project.



Figure 3.5: Bubbles and Melting appearing on the inner layer of the sleeve after a run.

3.4 Calibrations producers:

As reliable and accurate data is of prime importance for any experiment, the calibration of the test equipment is an inevitable necessity in order to assess the magnitude of any errors that may impact the measured data. A series of calibration tests were carefully performed for the experimental apparatus utilized in this study, particularly before and after each run for the pressure transducers, flow meters and temperature transducers.

The permeability calculation is fully dependent on the measured pressure differences across the core plugs (See Figure 3.4). Although the pressure transducers were calibrated individually by a legitimate third party, calibrating them as a coupled pair, for example P1-P2 then P2-P3, was a crucial requirement to investigate the error that might occur in their readings for the same pressure value. Thus P1 and P2 then P2 and P3 were connected together to one source of pressure, as shown in Figure 3.6. Steadily the pressure was increased to 6000 psia and then gradually the pressure was allowed to drop. The coupled pressure transducers readings were recorded over the span of 10 sec, their readings and variations plotted against time (See Figure 3.7).

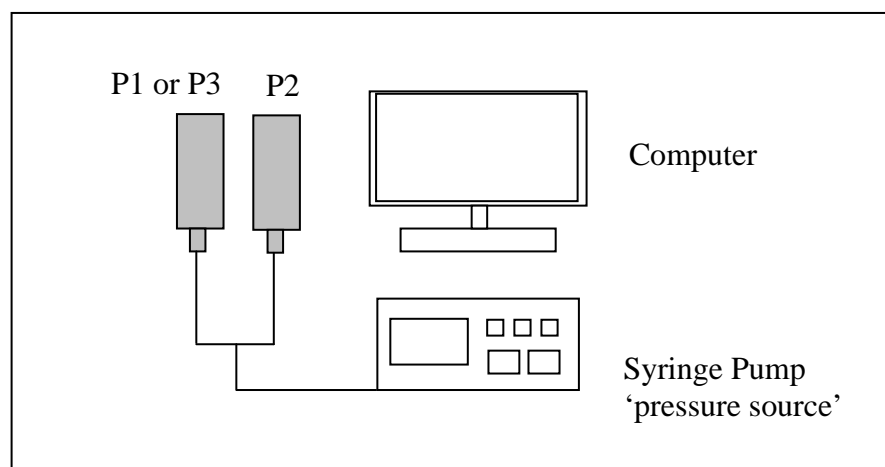


Figure 3.6: Sketch illustrating the technique of calibrating pressure transducers in a coupling connection.

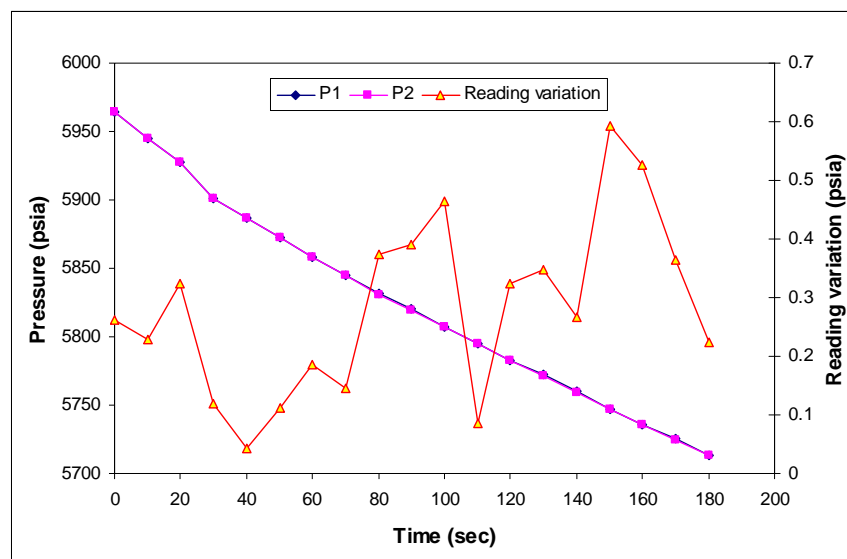


Figure 3.7: Differential pressure between P1 and P2 when connected to one source of pressure from 6000 psia to 5700 psia.

Results indicated that there were errors in transducers readings, between two consecutive readings a divergence of about 0.2-0.6 psi existed for the calibrated span. Furthermore, this distortion in transducer readings between two points had been noticed from the data obtained during experiments.

Three different types of flow meter were used during the experimental run; a digital, a rotameter and a locally designed flow rate check unit. Although the digital and rotameter flow meters were calibrated by their supplier, during the double check runs the measured rate was constantly calibrated and compared with a third independent local flow meter's data (refer to Figure 3.4). This unit consists of a titration tube placed upside down inside a 1 litre flask of water. The flow rate was checked frequently over the duration of a 10-20 minute period during each test. This was done by shutting the titration tube valve, allowing the gas to accumulate in the tube displacing water with time. This method is a very accurate way to measure flow rates as the displaced volume and time are known throughout the test. By the same method, before starting the run, the flow rate of the injected gas at the inlet of the core plugs was also checked.

The temperature of the air bath was calibrated against a K, J type thermometer reading at equilibrium conditions, the temperature variation was about 0.5-1 °C. The temperature of the injected gas was regularly checked by the same instrument, especially at the inlet of the core samples, the temperature fluctuated between 158 °C and 159.5 °C.

The manufacture, type, model, and specifications of all the equipment used in this study can be found in Appendix A-1.

Chapter 4

Interfacial Tension Measurements

4.1 Introduction:

A thermodynamically stable interface can only exist between two immiscible fluids; nonetheless, in this work an “immiscible interface” between two gases (SCO₂-methane) has been observed and is documented within this thesis. This chapter presents the first ever attempt to measure the interfacial tension (IFT) in a Gas-Gas system, the interfacial tension of supercritical carbon dioxide-methane was measured at temperatures of 95 °C and 160 °C and pressures range from 1000 to 6000 psia, using a modified reverse pendant drop method.

It was noted that the IFT decreased linearly with both temperature and pressure in the low-pressure range, but was less sensitive at higher pressures. There was a zone in the vicinity of 1500 psia and above that was noted to be independent of temperature where IFT increased very sharply. The IFT was almost three fold higher at 3000 psia, for the same temperature, compared with 1000 psia. This is attributed to the density of SCO₂ at 1000 psia being less than 1/3 the density at 3000 psia, at the same temperature.

It was also evident that the SCO₂-methane IFT was relatively lower at higher temperatures; a behaviour seen in density and viscosity of SCO₂ measured and in a simulation study by Oldenburg (2003). The IFT results at 6000 psia and 160 °C were very close to the 3000 psia and 95 °C. The increase in temperature slightly influenced IFT and was matched by the pressure effect on IFT. Hence the overall impact remained almost the same.

4.2 Theory back ground:

The immiscibility between gas phases at an equilibrium state can occur in some fluids at high pressure and temperature. Although this behaviour was initially predicted by Van Der Waals in 1894, the first experimentally measured interface between N₂-NH₃ was released by Krichevskii (1940). However no attempts were carried out to verify the CO₂ ability to form an interface with other gases. In this work the immiscible interface of CO₂ with methane is documented at various

reservoir conditions. Therefore all interfaces should not be assessed from the same theoretical or experimental frame-work while the mechanism governing the interaction and motion of the molecules from different phases are different because of the intricacy of the physical properties, mobility and stability of the phases. The gas-gas interfacial tension in a motion state has never been measured previously because it is conceived and reported in the literature as non-existent (Butt, Graf, and Kappl 2003). On the other hand, the IFT measurements between the miscible fluids (liquid phase e.g Isobutyric acid (IBA) and water) are reported by Pojman et al (2006) and Zoltowski et al (2007). The spinning drop tensiometry (SDT) technique was used and results indicated effective interfacial tension was insensitive to changes in temperature and always larger than the equilibrium interfacial tension.

Measuring gas-gas IFT experimentally has presented many challenges, the greatest of which is preparation of the initial stable interface before the mixture is too contaminated with the incoming gas, which will alter the IFT as concentration of the mixture changes with time by means of dispersion. In order for the clear interface between the SCO_2 and methane to be seen, the mixing process had to be meticulously managed. This process was noted to be dependent upon pressure, temperature and total composition. The interface was discerned to have been strongly influenced by the injecting flow velocity. The detail of the rate of mixing of CO_2 with methane across the interface at various conditions is also included in this chapter.

4.2.1 Properties of supercritical CO_2 -methane:

It is well known that interfacial tension is the main driving force in the phase separation of multiphase blends; thus the interfacial tension can have crucial significance in the formation or mixing of the phases, including the formation of a gradient in miscible systems (Yasuhiko et al. 2004). In order to understand the behaviour, the influence of the gas density of each gas at the measured conditions and subsequently the influence of that on the formation of the interface, has to be properly comprehended. In the SCO_2 -methane system the lighter component, methane, has a molecular weight of about 0.38 that of CO_2 , and density 1/3 of CO_2 over most regions of the pressure-temperature (P-T) range beyond critical conditions.

Supercritical fluids have liquid-like densities and gas-like diffusivities (McHugh and Krukoniš 1986). Experimental water-saturated Methane-CO₂ mixture densities as a function of pressure and temperature were used by Dewitt and Thodos (1966), Nieva and Barragán (2003) and Li, Ji, and Yan (2005).

The density profiles for CO₂ and methane measured in this work are shown in Figure 4.1. If the trend of the average change (Δ) in gas density is compared to the IFT, a proportional relationship will be perceived. With increasing IFT the average Δ gas density increases and vice versa.

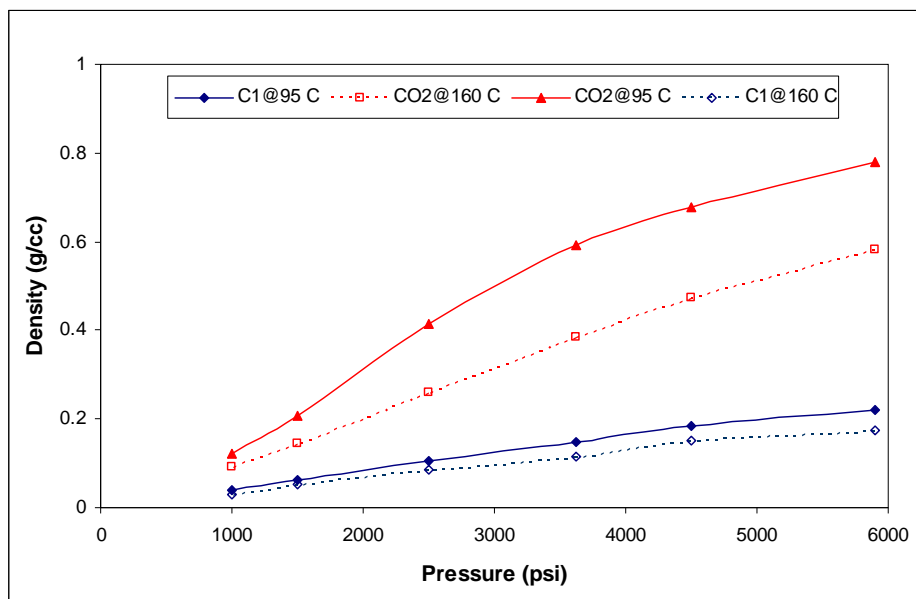


Figure 4.1: CO₂-Methane densities at various temperatures and pressures.

The gradient phase that occurs between the two miscible gases at pore scale can be controlled. When relating the effect of interfacial tension between the injected and displaced phases on the formation of the gradient phase in front of the mixture. Therefore in this set-up CO₂ and methane gases are placed in contact with methane on top of the CO₂ and allowed to interface by controlling the flow rate of the injected CO₂ at between 1200 psia and 6000 psia, and at 95 °C and 160 °C.

At the low injection rate the mixing in the system was limited to gradient formation because, as expected, the denser gas (CO₂) flowed down to the bottom of the cell and disappeared as it mixed with methane by molecular diffusion (See Figure 4.2). At the capillary needle, the lighter gas methane was pushed to the top forming a clear

interface that developed into a gradient. As more CO₂ was injected continually into the limited volume of methane, steadily the interface was reduced noticeably and gradually vanished by dispersion and molecular diffusion. For calculating IFT a stable interface is required, however the gradient zone incorporated with CO₂ injection, a stable drop was able to form through reducing the injection rate to the lowest possible limit rate via controlling the micro-meter valve (See Figure 4.3).

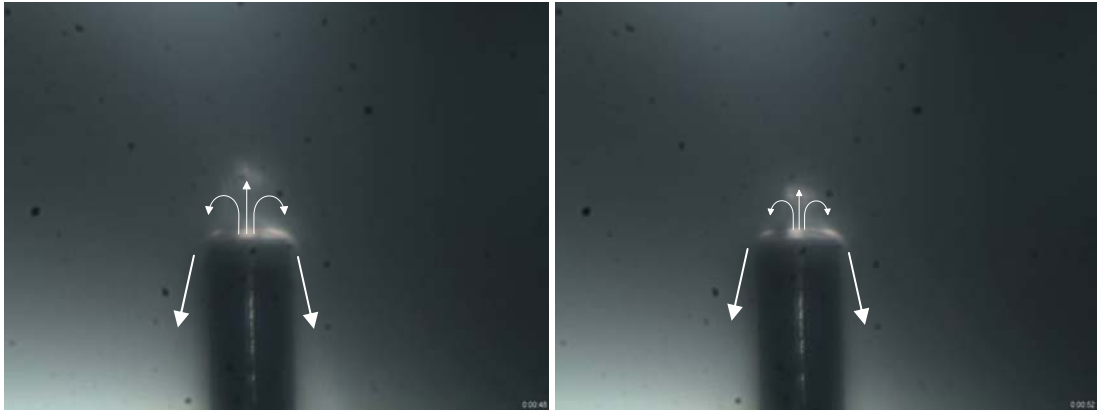


Figure 4.2: Shows denser phase CO₂ flows downward at low injection rate.



Figure 4.3: A thermodynamic stable interface between SCO₂-methane at 95 °C and 3000 psia.

4.3 Methodology:

To the author's knowledge gas-gas interfacial tension measurements by means of the reverse pendant drop method have not been carried out previously. Therefore reviewing the interface measurement technique of two immiscible fluids in a capillary tube is of great importance to develop a method for calculating a gas-gas interface.

The surface tension between two immiscible fluids, for example gas and liquid, is usually variable, depending upon the physical properties of the phases and the solid surface. A greater value of surface tension is acquired from the interface between the immiscible fluids rather than their interface with the solid surface. As a rule of thumb, the geometry of the interface must balance all the forces applying on it. When the two immiscible fluids meet in a capillary tube a contact angle, θ , will form where the phases' interface meets with the solid surface. If the interface between the immiscible fluids is known, the gas-solid and liquid-solid interfaces can be calculated by means of the contact angle, see Eq.4.1.

$$\gamma_{ls} - \gamma_{sa} = -\gamma_{la} \cos \theta \quad (4.1)$$

Where:

- γ_{ls} liquid-solid surface tension,
- γ_{la} liquid-air surface tension,
- γ_{sa} solid-air surface tension,
- θ contact angle, where a concave meniscus has contact angle less than 90° and a convex meniscus has contact angle of greater than 90° .

For the SCO_2 -methane interface measurements, a capillary needle has been employed in comparison to the standard needles used in the pendant drop method. The interfacial tension was determined by measuring the radius of curvature of the interface in the tip of the capillary pipe.

As the SCO_2 is injected into the methane phase through the capillary needle into the cell, it was noted that a bubble formed at the tip of the needle. This was monitored as the pressure increased due to the injected SCO_2 . Obviously the shape of the gas bubble was affected as the injecting fluid (CO_2) pressure was changed. The images were subsequently processed by image analysis with respect to the spatial characteristics of area, width, length, perimeter and contact-angle (See Figure 4.4). In light of the limitations of a gas-gas interface in terms of clarity, stability and durability, it would be advantageous to have a method of measuring equilibrium and dynamic interfacial tensions in which the clean interface is rapidly replenished and equilibration times are relatively short. More specifically the geometry of the

interface created between SCO_2 -methane is conspicuously different from that forming between two immiscible fluids. At the point where the three phases, (SCO_2 , methane gas and solid) meet, a horizontal interface is formed and then a convex like shape appeared (See Figure 4.4.). This is evident when the gases-solid contact angle is 0° and indicates no surface tension is in existence because the gas phase cannot make a distinctive interface with the solid phase as it is the most non-wetting phase.

The diagram in Figure 4.5 is a magnified version of the SCO_2 bubble that is shown in Figure 4.4. It illustrates all the forces that equilibrate the interface. Surface, tension forces are shown for the CO_2 -methane, CO_2 -solid, and solid-methane interfaces. The difference between the CO_2 -solid and methane-solid surface tension, $\gamma_{c_1s} - \gamma_{c_2s}$, is obviously less than the CO_2 -methane surface tension, $\gamma_{c_2c_1}$. This is because CO_2 -solid and methane-solid contact angles are almost zero. But at a minute distance away from the needle's wall, (solid phase), a hemisphere shape SCO_2 bubble was created where the tension forces are normalized at the intersection point between the imaginary dashed line with CO_2 -methane interface (See, Figure 4.5). The vertical and horizontal forces at the intersection point cancel each other and the horizontal vector of $\gamma_{c_2c_1}$ will be cancelled by adhesive force (See Figure 4.5).

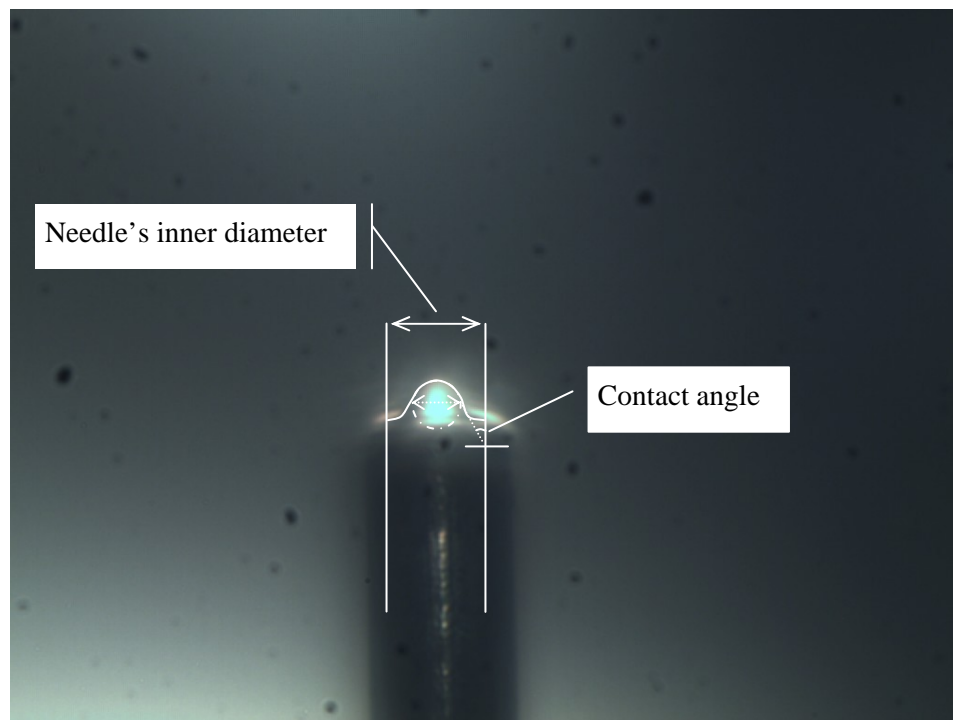


Figure 4.4: Schematic illustrating the dimensions used in IFT measurements. The ambient is methane and the bubble on the tip of needle is CO_2 .

The force generated in the direction of γ_{CO_2S} is a combination of the gravity force and molecular friction with the needle's wall. Its magnitude will be compensated by arbitrary motion of the SCO_2 -methane molecules particularly in the direction of γ_{C_1S} as CO_2 molecules have greater momentum than methane molecules.

The inter-molecular frictions that result in the horizontal direction, together with the balanced effect of the gravity force and arbitrary molecules motion, have resulted in creating a horizontal plane up to the point where all the forces are in equilibrium. Eventually the tangential vector of the $\gamma_{CO_2C_1}$ force has formed a dome like bubble which permits surface tension to be calculated from the current computational methods using iterative approximations. This permits a solution to the Young–Laplace equation for shape factor to be performed.

$$\gamma = \frac{\Delta\rho g R_0^2}{\beta} \quad (4.2)$$

Where:

- $\Delta\rho$ density difference.
- γ surface tension.
- g gravitational constant.
- β shape factor.

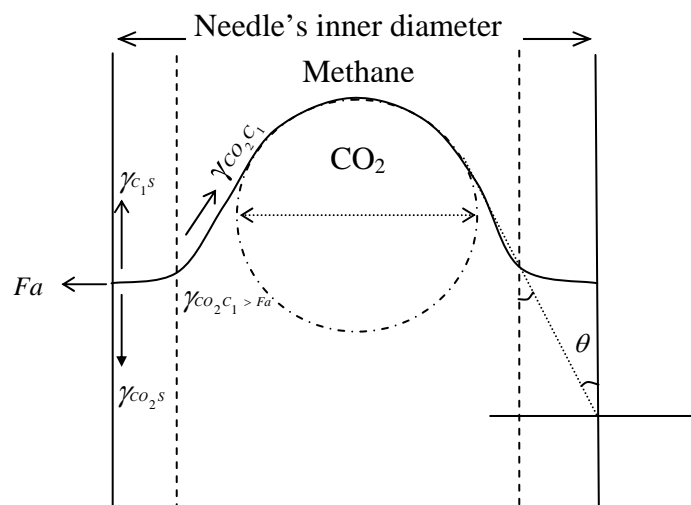


Figure 4.5: Diagram illustrating the structure of SCO_2 -methane interface from the bubble produced on the tip of the capillary needle.

The justification used was that the SCO₂-methane interface is characterised by a single radius of curvature that is equivalent to the 70% pipe radius when the interface is a hemispherical cap in the tip of the pipe. This suggests the existence of IFT between SCO₂ and surrounding methane, especially as explained the contact angle at the pipe wall is zero because of no gas phase wettability effect.

For this reason, the interfacial tension determined by measuring the radius of curvature was assumed to be suitable. The accuracy of this method has been verified by making equilibrium interfacial tension measurements of various miscible systems where interfacial tension is already reported in the literature.

Sequential digital images were obtained of the SCO₂ bubble formed in the methane phase with a standard image analysis and reverse pendant drop calculation software used to calculate the IFT.

4.4 Experimental results:

4.4.1 Results of tests conducted at 95 °C.

Table 4.1 shows results of interfacial tension that is carried out at a temperature 95 °C and pressures from 1300 to 3600 psia. The results show the interfacial tension of a supercritical CO₂ (98%)-methane system decreases when the mutual miscibility of the two gases increase, or as the two become totally miscible approaches zero at around 1100 psia (See Figure 4.6). It was obvious that the interface was not as sharp as observed in the case of liquid-liquid or gas-liquid. In this case the interface is slightly “cloudy” suggesting some compositional gradient via molecular diffusion across the interface, though the process seems to be significantly slower than was anticipated.

This cloudy phenomenon can be seen more clearly at higher injection rates when the heavier and denser phase CO₂ starts to flow downwards and the interface is much more dispersed. However, this may not be the case at reservoir conditions because of the flow ratio between the injected and displaced phase.

Table 4.1: SCO₂-Methane interfacial tension data for tests conducted at 95 °C.

S.N.	Pressure psia	IFT (Dyne/cm)@ 95°C
1	1300	0.00036
2	1590	0.00373
3	1890	0.0068
4	2370	0.00937
5	2720	0.01068
6	3360	0.01211

Mixing of fluids in porous media during a displacement is a diffusion-like process and the dispersion coefficient depends on the velocity and direction of the dispersion flux with respect to the main convective flux (Adolf, Tirrell, and Davis 2004). In addition, the stability of the SCO₂-methane miscible zone in porous media is influenced by several mechanisms such as molecular diffusion, Taylor dispersion, convective dispersion, permeability heterogeneities, and adsorption mechanisms. (Kempers and Haas 1994).

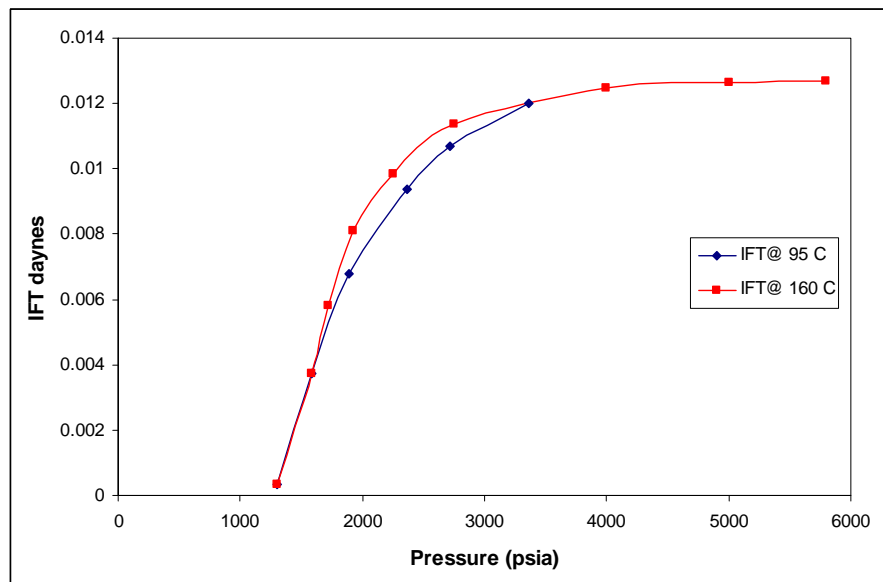


Figure 4.6: CO₂-Methane interfacial tensions as a function of pressure and temperature.

4.4.1 Results of tests conducted at 160 °C.

Table 4.2 shows results of interfacial tension that is performed at 160 °C and pressures from 1300 to 5800 psia. The results demonstrate almost the same trends of

the interfacial tension measurements that were carried out at 95 °C. Initially a dramatic increase in the surface tension, for pressures of 1300-3000 psia, was noted with a further slight increase in interfacial tension up to a pressure of 5800 psia observed.

A variation of note was that at a pressure of 1590 psia the interfacial tension at 160 °C displayed a higher trend when compared with the surface tension measured at 95 °C. This behaviour continued until the pressure approached 3000 psia. Above this pressure reading the trend only modestly increased up to a pressure of 5800 psia at both tested temperatures. Apparently the measured surface tension between SCO₂-methane reflects the physical properties behavior of both phases at the referenced test conditions.

Besides SCO₂-methane interfacial measurements being made within this study, several attempts were made to measure surface tension between CO₂-N₂ and N₂-methane systems at different pressures and temperatures. Results confirmed that the measurements relating to the IFT of the CO₂-methane system are definitely different from that obtained from the N₂-CO₂, methane-N₂ systems. Figures 4.8 and 4.9 show experimental images taken from the N₂-CO₂ and methane-N₂ surface tension measurements. Clearly there are not any distinctive interfaces distinguished.

Table 4.2: Supercritical CO₂ Methane Interfacial Tension Data.

S.N.	Pressure psia	IFT (Dyne/cm) @ 160°C
1	1300	0.00036
2	1590	0.00373
3	1720	0.00581
4	1920	0.00812
5	2250	0.00983
6	2750	0.0114
7	4000	0.0124
8	5000	0.0126
9	5800	0.0124

4.5 Evolution of Gas-Gas Gradient Zone:

With reference to Figure 4.7, images 1-4, the evolution of the SCO₂-methane gradient zone can be seen versus the injection rates. The most obvious interface at higher injection rates gradually became faint because the diffusion of SCO₂ into the

methane was accelerated over time. It will be noted that the gradient zone is dependent on the flow velocity of the CO₂ injected into the methane phase. Mixing of fluids at reduced flow velocity is more intensively affected by molecular diffusion than it is at high flow rates. This can be noted from Image 1 where the SCO₂ interface at high flow rate was clearly seen in the methane phase. This suggests mixing of SCO₂ with methane at pore scale will be hastened by the diffusion process at low injection rates which may result in an early breakthrough. The brightness of the SCO₂ interface at the very high injection rates was an interesting phenomenon to observe. If the SCO₂ injection rate is reduced, the injected SCO₂ immediately begins to mix diffusively across the concentration front (Images 2 and 3). As a result the composition in homogeneities further reduced the IFT between the fluids and made the front of the interface much more miscible.

When the flow rate is reduced successively (Images 3 and 4) the SCO₂ flows downwards driven by gravity forces (like a fountain) mixing with the fluid (methane) beneath the needle and gradually disappearing at the lower end. For a further reduction in flow rate (Images 4 and 5) this phenomenon continues, but at a slower rate of mixing with the front and being relatively more stable. Finally when the lowest flow rate possible is reached a perfectly stable SCO₂ bubble is noted to be sitting in the methane ambient (Image 6) with mixing only at the interface with methane via dispersion and molecular diffusion mechanisms.

This behavior is a result of combined molecular diffusion and dispersion depending on the direction of the flux, however in the reservoir the dispersion will be the dominant parameter because it depends on the permeability heterogeneity rather than inter-molecular forces of diffusion.

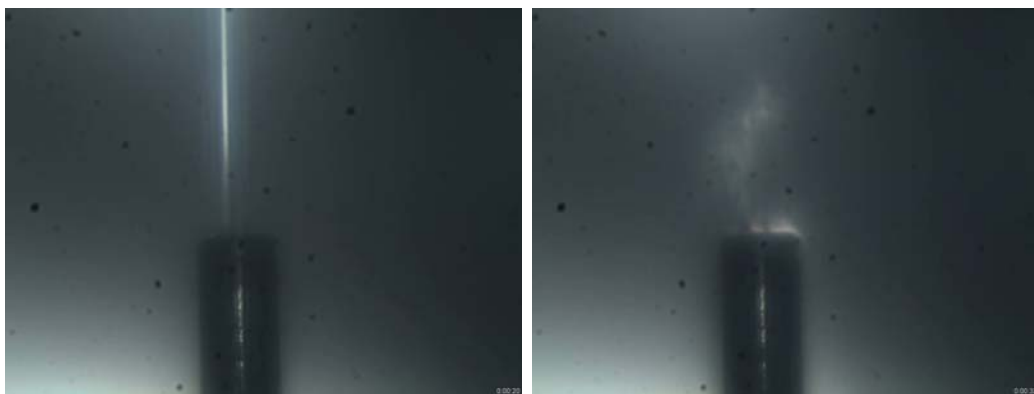


Image (1) High injection rate

Image (2)

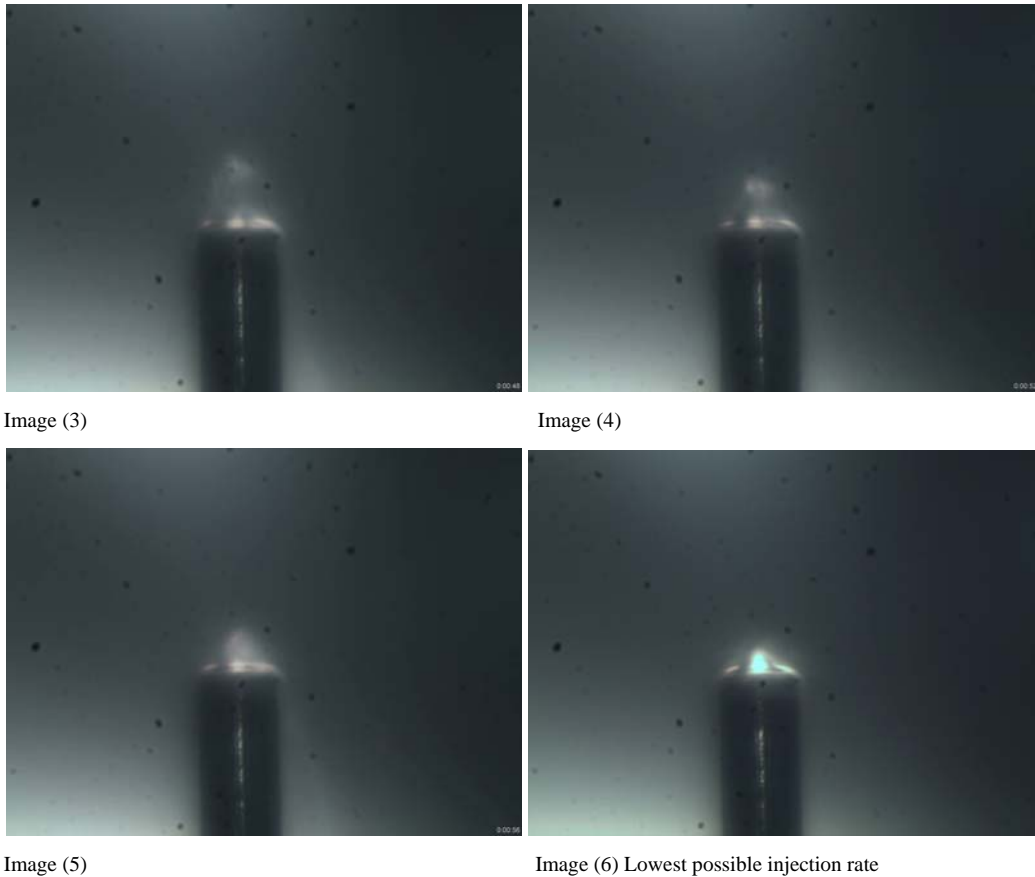


Figure 4.7: Effect of SCO_2 injection speed on CO_2 -methane interface formation.

4.6 Discussion:

Interfacial tension, being a property of the interface between two fluids, is strongly dependent on mass transfer interactions occurring between the two fluid phases. In the relevant literature there is often a mix between the role of IFT in miscibility, solubility and mass transfer. It is quite clear that IFT plays a significant role in all these phenomena including the gas-gas interfaces which has not been mentioned in any literature or referenced as being zero and implies immediate miscibility, which is first contact miscibility.

All interfaces cannot be treated in the same theoretical or experimental frame-work since the mechanism governing the motion of the different phases is different because of the physical properties, mobility and stability of the phases (Moegen and Giouse 1989). The gas-gas interfacial tension in motion was reported in the literature as non-existent in that it has never been measured. Here, the rate of mixing between CO_2 and methane across the interface does exist but is not perfectly defined. This presents many challenges to the experimental measurements, the greatest of which is

preparation of the initial interface. In this work the interface was observed and the details documented.

The interface, which largely depended on the temperature and pressure, was also noted to be strongly influenced by the CO₂ injection flow velocity. The rate of mixing of CO₂ with methane across the interface at various conditions is also included in this report.

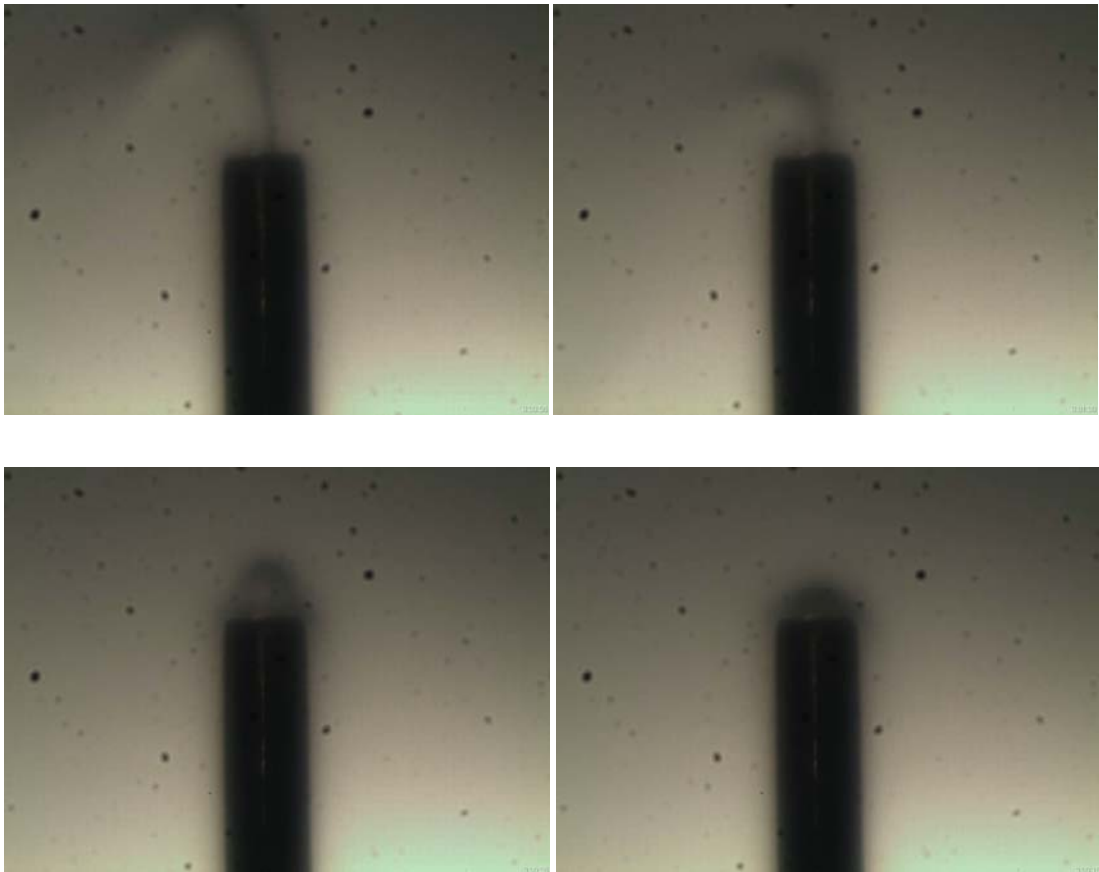


Figure 4.8: Effect of N₂ injection speed on N₂-methane interface formation at 95 °C and 1750 psia.



Figure 4.9: Effect of SCO₂ injection speed on CO₂-N₂ interface formation at 95 °C and 2000 psia.

Chapter 5

Unsteady state experiments

5.1 Introduction:

To investigate the effect of CO₂ injection on enhanced gas recovery, six short (horizontal) and one long (vertical) reservoir core plugs were prepared and used in this study. Preliminary tests indicated that the horizontal short core samples comprised three identical twins from the point view of absolute permeability, porosity and grain density (See Table 5.1). Therefore only three of the short core samples, with the vertical long sample, were selected for further investigation of the SCO₂-methane core flooding experiments.

The test conditions applied were to simulate the initial reservoir conditions of pore pressure of about 6000 psia and temperature of 160 °C. Although the initial test condition was to explore the effect of P-T parameters on the displacement efficiency, running experiments at various pressures and temperatures were crucial to conclude the optimum condition for implementing CO₂-enhanced gas recovery.

The results show that the recovery factor at CO₂ breakthrough was relatively high, ranging from 60% - 80% of original gas in place, depending on the CO₂ content in the injecting gas, injection rate, pressure and temperature. With decreasing injection rates and pore pressures, CO₂ breakthrough occurred earlier. This coincided with the IFT measurement as pressure and injection speed resulted in a reduction in the IFT. Moreover, a model for SCO₂-methane relative permeability was developed from the existing explicit models.

Table 5.1: Basic macroscopic measurements for the short and long core samples.

S.N.	Sample Code	Depth (m)	K air (md)	Porosity (%)	Pore volume (cc)
1	S_C_1A	4144.28	391	17.9	9.818
2	S_C_1B	4144.33	421	17.6	7.958
3	S_C_2A	4160.68	115	14.1	9.793
4	S_C_2B	4160.75	123	14.1	7.929
5	S_C_3A	4184.37	8.37	9.9	5.726
6	S_C_3B	4184.42	7.50	9.9	5.555
7	S_V_1	---	92	14.3	32.95

5.2 Preliminary tests:

The preliminary tests that were carried out on the six short samples at Core Laboratories Australia were to reveal the initial macroscopic properties of the core samples. These tests were performed at ambient conditions by using a centrifuge. The aim was to investigate basic measurements and decane-brine relative permeability for the core samples. A point to be noted is that for identical samples (S_C_1A/S_C_1B and S_C_3A/S_C_3B) both retained higher residual decane in comparison to S_C_2A and S_C_2B. Table 5.2 shows the summary of the tests for the short samples. For further details refer to Appendix B.

Thereafter the core plugs were cleaned in toluene and methanol in case they retained pore fluids from the previous tests. After drying the cores in a non-humidified oven at 160 °C, air permeability (Ka), helium porosity and grain (matrix) density values were calculated and compared with historical values generated from the samples. All data was found to be close to the original values, and so the samples were deemed to be suitable for testing.

After the preliminary tests, as all samples were determined to be appropriate for further investigation, three short core plugs were chosen (S_C_1A, S_C_2A, and S_C_3A) together with the long core plug (S_V_1) for the CO₂-methane core flooding experiments.

Table 5.2: Basic macroscopic measurements for the short and long core samples.

Initial Conditions			End Conditions					
Samples	Initial Water Sat. (%pv)	Kdecane at Swi (md)	Water Displacing Decane				Decane Displacing Water	
			Residual decane (%pv)	Kw at Sdr (md)	Decane Recovery		Kdec at Swr (md)	Final water sat. (% pv)
					(% pv)	(% DIP)		
S_C_1A	7.2	364	34.3	98.6	58.5	63.1	106	12.5
S_C_1B	8.3	390	36.0	98.7	55.7	60.7	170	10.4
S_C_2A	9.6	105	27.5	47.7	62.9	69.6	42.8	8.3
S-C_2B	7.1	114	23.0	57.3	69.9	75.2	59.5	12.5
S_C_3A	12.8	6.95	41.8	0.98	45.4	52.1	7.70	10.0
S_C_3B	12.4	6.29	41.7	0.77	45.9	52.4	6.92	11.7

5.3 Test sequences:

The core plugs were inserted into a Viton Hassler sleeve and placed inside the core holder which was then evacuated before being pressure saturated with connate water. Progressively the temperature of the air bath was increased to the desired reservoir conditions and the pore pressure controlled through the back pressure in the system. When the equilibrium state was achieved, the core samples were flushed for almost 10 PV until 100% brine saturation was considered to be achieved in the core plugs.

Thereafter, effective gas permeability at irreducible water saturation was measured ($K_{ge@Swi}$). This was performed by displacing brine by methane (90% concentration with CO₂ being the remaining 10% as recommended by the operator), to irreducible water saturation and then aged overnight. Eventually the in situ gas (methane) was displaced by CO₂ at a pore pressure of 5900 psia and 7500 psia as an overburden pressure with the given flooding rate (velocity). In this way, the relative permeability of SCO₂ could be calculated from the unsteady state displacement tests for all the core plugs. The basic summary of the test steps can be found in Table 5.3.

For evaluating the effect of SCO₂ passage on permeability alteration through mineral precipitation, several screening tests were conducted on the three short core samples. This was implemented by flushing the core samples with SCO₂ for almost 8 hours with the pressure difference across the core samples monitored constantly. Results showed that none of the short samples were affected by SCO₂ passage as the pressure difference had not demonstrated any significant variations. On the other hand, the impacts of the displacement rates, pore pressures, and gas composition on the recovery efficiency were investigated only on the long core after step 3 in Table 5.3.

The composition of the produced gas at the effluent point was monitored continuously online via a SCO₂ gas analyzer (PEM tech gas analyser) and recorded on an integrator. The volume of produced gas was also measured by the flow meters that were connected in series. From these data, the recovery of methane at SCO₂ breakthrough was obtained.

Table 5.3: Basic test sequences.

<ul style="list-style-type: none">• Stabilize temperature of air bath and equipment at 160 °C for 24 hours.
<ul style="list-style-type: none">• Measure permeability to air on clean, dry core samples. <i>K_a</i><ol style="list-style-type: none">1. Saturate samples with 25,000 mg/ℓ brine.<ul style="list-style-type: none">○ Measure water permeability at 100% brine saturation. <i>K_w</i>2. Flush samples with Methane 90% to immobile water saturation,<ul style="list-style-type: none">○ Measure gas permeability at immobile water saturation. <i>K_{Cl@Swi}</i>3. Flood samples with supercritical CO₂ 98%.<ul style="list-style-type: none">○ Measure CO₂ permeability and monitor CO₂ breakthrough versus methane recovery. <i>K_{CO2@Swi}</i>4. Dean Stark extraction5. Steady state tests.

Three more steps were performed on the long core sample (19.41 cm long by 3.8 cm diameter) for estimating the impact of displacement rate, pore pressures, and gas composition on the methane recovery. Each step included of series of tests, carried out as follows:

- After displacing methane by SCO₂ at a certain flow rate and constant pore pressure, the core was re-saturated with methane so as to be ready for the next cycle of displacement at the lower flow rate except pore pressure was maintained at 5900 psia for all the rates investigated. The displacement speed ranged from 1-10 cm/hr.
- In the same way pore pressure tests were carried out. The composition of the in situ gas (90% methane) and the injected gas velocity were kept constant while only pore pressures were changed from 1500 - 5900 psia.
- For studying the effect of composition, a series of tests were executed by displacing different SCO₂-methane mixtures by SCO₂ at a constant flow velocity of 10 cm/hr and pore pressure of 5900 psia. The in situ gas mixtures were studied with SCO₂ content ratio ranging between 10% and 75%.

The dry sample S_V_1 (long core plug) was studied by CT scan before the commencement of the core-flooding experiments. Although the scan images were not conclusive on the homogeneity of the core sample, no cracks, fractures or high permeable streaks were observed. Figure 5.1 shows sample cross-sectional images, each taken 1 cm apart over one longitudinal section. The bright dots are considered to be pyrite minerals. Other than this mineral observation nothing else is of note.

Repeated CT scans were conducted after the SCO_2 flooding experiments to perceive the effects of fluid rock interaction. Only cross-sectional scans were attained for the post-test as the CT scanner could not take longitudinal section images. Post scan images displayed no major changes when compared to pre-test scan images (See Figure 5.2)

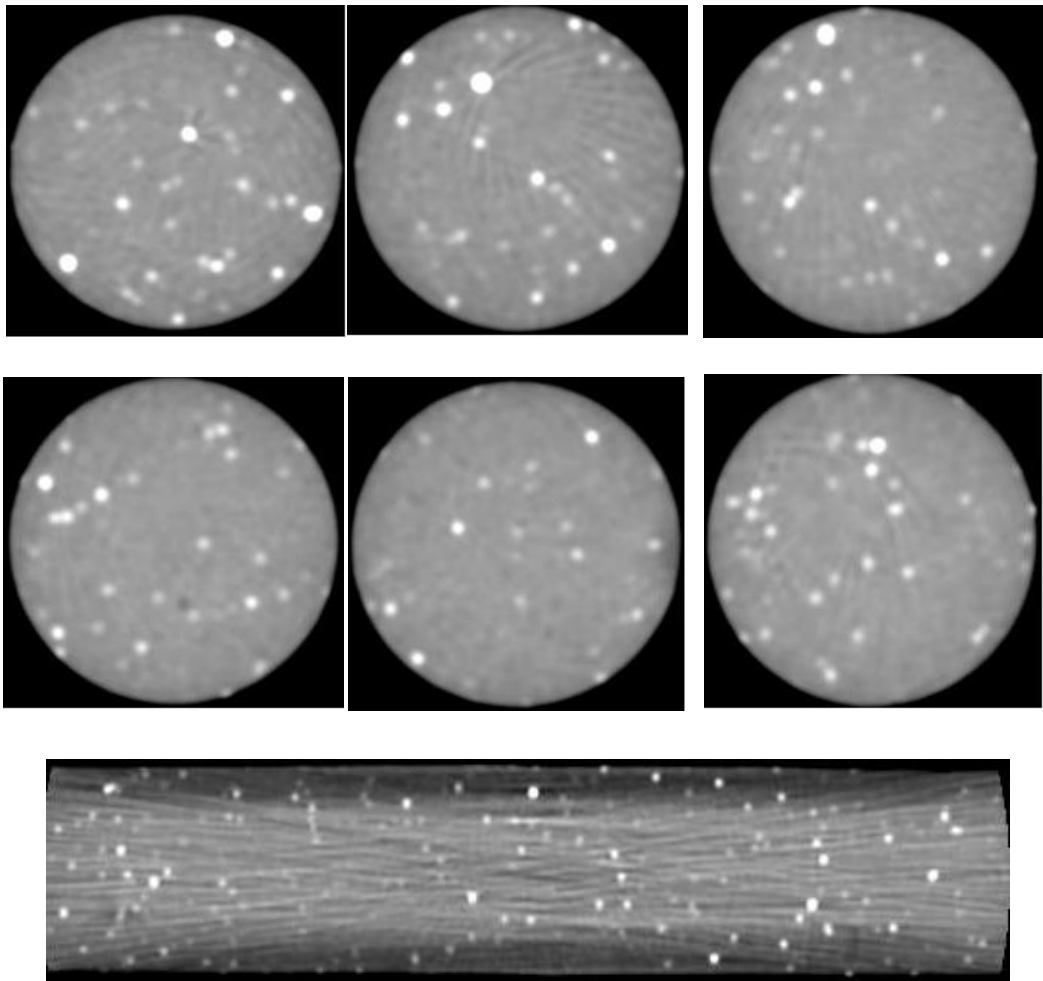


Figure 5.1: Image Samples from Pre-test CT scan.

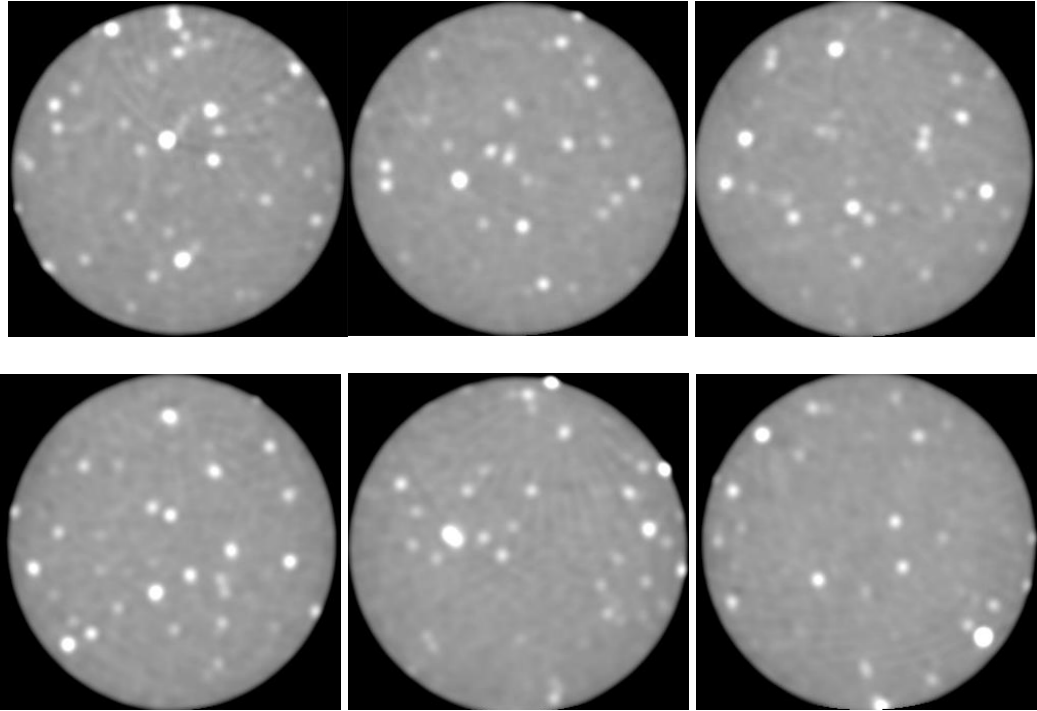


Figure 5.2: Image samples from Post-test CT scan.

5.4 Fluid flow in porous media:

5.4.1 Permeability calculation:

Throughout this work permeability of the core samples for different fluids are calculated by using the Darcy equation. From the experimental work the normalized pressure drop and measured fractional flow rate at the end of each run were used for the permeability calculation.

$$K = \frac{Q \cdot \mu \cdot L}{\Delta p \cdot A} \quad (5.1)$$

Where:

K permeability to liquid, Darcies,

L sample length, cm,

Q flow rate, cm³ per second,

Δp pressure difference across the core sample, atmospheres, μ =Viscosity, centipoise, A cross sectional area, cm².

The speed gradient is anticipated to occur at field scale during CO₂ injection. The gas speed was estimated to reduce from 10 cm/hr to 1 cm/hr at one kilometre distance away from the injector well. The conversion of gas speed unit to a flow rate in cc/min was made using the following equation.

$$Flowrate(cc/min) = speed(cm/min) * A * \phi \quad (5.2)$$

Where:

A cross sectional area, cm²

ϕ porosity, volume fraction.

The flow meters employed in the facility could only measure flow rates at ambient conditions. Although many attempts were made to find flow meters that would operate at a high pressure of 5900 psi and temperature 160 °C whilst being compatible with the system. To the author's knowledge no suitable flow meters are available.

Table 5.4 shows calculated flow rates in cc/min from the speed of 10 cm/hr for the samples studied. The desired gas velocity, which was converted into a flow rate by using Eq.5.2, is at reservoir condition (160 °C and 5900 psia). Therefore to convert flow rates from reservoir condition to atmospheric conditions and also considering the gas composition, a PVT equation has been used. The effect of gas composition on flow rate has been taken into account for the core samples studied. (See Table 5.4)

$$\frac{P_1 V_1}{T_1 Z_1} = \frac{P_2 V_2}{T_2 Z_2} \quad (5.3)$$

For instance, to achieve a gas speed of 10 cm/hr through the sample S_C_1 during the displacement test at 160 °C and 5900 psia, if the injected gas has a composition of 90% methane and 10% CO₂, the produced gas must be allowed to have a flow rate at ambient conditions of 95 cc/min, which is equivalent to 0.365 cc/min at reservoir conditions. The reservoir flow rates during the experiments have been checked continuously via the linear flow meters which were attached to the system with their value maintained through the micro-meter valves.

Table 5.4: Flow rate in (cc/min) at ambient and reservoir condition.

Sample	A Cm ²	Porosity (%)	Speed (cm/hr)	Flow rate					
				reservoir cc/min	Atmospheric condition cc/min				
					CO ₂ 10%	CO ₂ 20%	CO ₂ 50%	CO ₂ 75%	CO ₂ 98%
S_C_1A	12.255	0.179	10	0.365	95.28	96.5	101.5	106.97	110.2
S_C_2A	12.255	0.141	10	0.295	77.01	77.99	82.08	87.26	93.1
S_C_3A	12.255	0.099	10	0.212	55.34	56.05	58.99	62.71	65.3
S_V_1	12.125	0.143	10	0.289	75.18	76.14	80.14	85.19	89.4

The following steps were required for calculating permeability in millidarcies (md);

1. Flow rate has to be converted to cc/sec.
2. Pressure differential is experimentally measured in psi - so has to be changed to atmospheric pressure.
3. To convert to (md) the right hand of the Eq.5.1 has to be multiplied by 1000 as one Darcy is equal to 1000 md.

Viscosities of the phases used in the permeability calculation were obtained from an in-house modified PVT-Sim EOS and experimental data from Core Laboratories Australia. The results were in good agreement with the published experimental viscosity data of both SCO₂ and methane. Details of the permeability calculation can be found in Appendix C.

5.4.2 Basic permeability measurements:

These tests were conducted at 160 °C and 5900 psia. The simulated brine used in the tests was prepared by dissolving 25 g of NaCl 80% and KCl 20% each in one litre of fresh water. The resulting 25000 mg/l salinity approximated the salinity of the reservoir formation brine. The brine injected into the core with a rate of 1cc/min and the pressure differences (Δp) across the core were monitored and plotted against the injected PV. Figure 5.3 shows Δp across the short core samples (S_C_1A, S_C_2A and S_C_3A), the distribution of Δp trend emphasised the initial test results that were implemented at ambient conditions at Core Laboratories Australia. Core sample S_C_1A was considered to be high quality rock and displayed the lowest Δp

(average 3.5 psi), with the high permeable rock, sample S_C_3A demonstrating the highest Δp (average 14 psi) which means low permeable rock and poor quality. Furthermore, the intermediate rock quality S_C_2A Δp trend was distributed between the lowest and highest quality rock and its average value at the end of the run was approximately 3.6 psi.

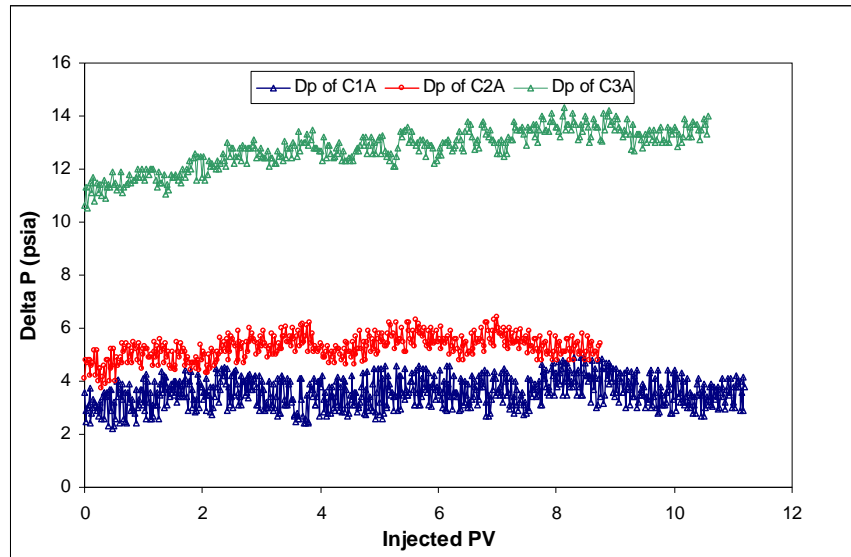


Figure 5.3: Δp of stimulated brine at 1cc/min versus injected Pore volume.

Figure 5.4 shows pressure difference across the long sample S_V_1 with the value normalized at around 6.4 psi at the end of test. The achieved Δp across sample S_V_1 was around the value of Δp that was obtained with the intermediate rock quality S_C_2A but slightly higher by 1 psi. Table 5.5 shows absolute water permeability measurement for the three short samples and the long sample at reservoir conditions.

Table 5.5: Basic data measurement at reservoir condition.

S.N.	Sample no.	K air (md)	Porosity (%)	Test Condition		kw
				Temp.	Pressure	1cc/min
				(°C)	(PSI)	(md)
1	S_C_1A	391	17.9	160	5900	9.25
2	S_C_2A	115	14.1	160	5900	7.02
3	S_C_3A	8.37	9.9	160	5900	2.75
4	S_V_1	92.1	14.3	160	5900	3.54

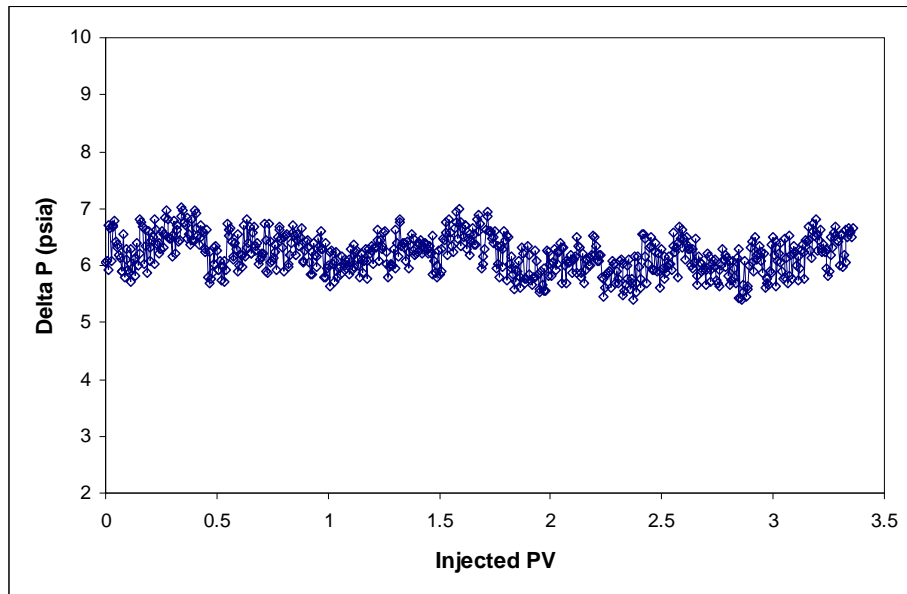


Figure 5.4: Δp of stimulated brine at 1cc/min versus injected Pore volume.

The next step was the gas effective permeability (K_{ge}) measurement. This is achieved by displacing the water saturated core with 90% methane to immobilized water saturation Sw_i . Obviously when the low viscous phase is displaced, the higher viscous phase (brine) pressure difference across the samples drops until gas breakthrough, it then gradually stabilizes.

This behaviour was noticed from the tested core samples which satisfied the Buckley-Leverett theory. For example, Figure 5.5 shows pressure differences across sample S_C_1A versus the injected pore volume during brine displacement by 90% methane. The pressure difference is seen to decline at around 0.3-0.4 PV before peak again. This may be an indicator for flowing gas breakthrough followed by some less intense peaks between 1.8 to 2.3 PV which may be related to the additional water recovery.

The cumulative brine production curve showed a steep slope pattern. This is an indication of two possibilities. First, the medium is oil wet, or intermediate wet, which facilitated water to flow with ease through the porous medium. Second, because sample S_C_1A was noted to have high permeability, lower capillary pressure was expected and thus a piston like displacement front achieved.

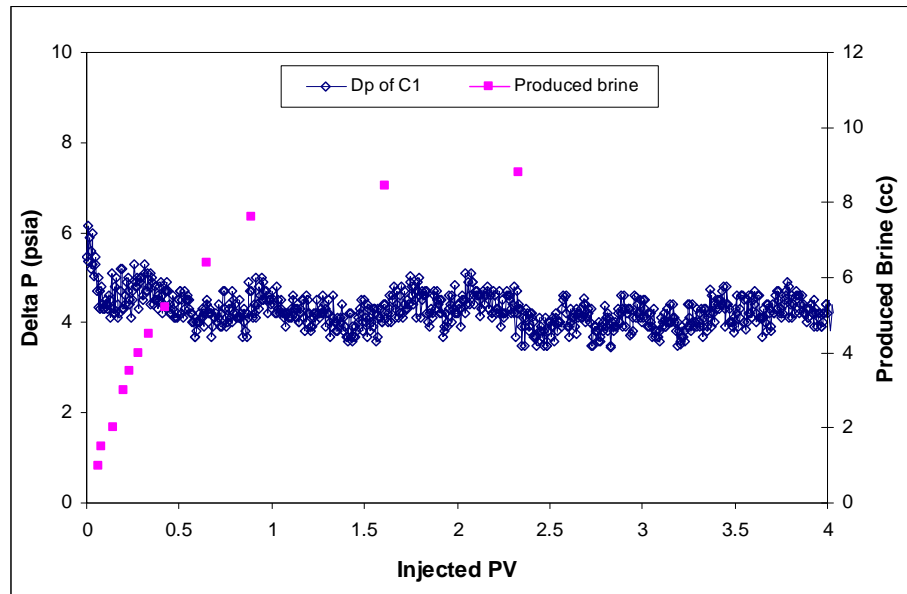


Figure 5.5: Δp of 90% methane displacing brine at 0.365 cc/min versus injected Pore volume.

All samples were subjected to Dean Stark extraction when the test sequences were completed. The purpose of Dean Stark was to evaluate the amount of irreducible water saturation remaining in the core after the samples underwent a constant flushing with SCO_2 at high temperature and pressure. Results indicated S_{wi} measured by Dean Stark extraction for all core samples was considerably lower than the S_{wi} experimentally obtained from the displacement of brine by 90% methane (90%) at reservoir conditions. However, during the experiments the injected gas, SCO_2 , was saturated with brine in order not to influence the volume of the inherited connate water saturation in the core samples. Lower S_{wi} accentuates the fact that some S_{wi} was evaporated due to SCO_2 flooding.

Table 5.6 shows the Dean Stark extraction and air permeability measurement results for all four samples tested before and after the completion of the experiments. Air permeability results demonstrated that the short samples remained unaffected as their value after Dean Stark displayed almost the same as pre-test values. In contrast the long sample, S_V_1, seemed to have been affected by SCO_2 flooding and a reduction of about 35% in its K_{air} resulted in comparison to its initial K_{air} measurement. Nevertheless, when the sample was re-loaded for the steady state tests after the Dean Stark test, the effect of lower K_{air} was not discernible on the SCO_2 Δp at 5900 psi and 160 °C.

This possibly happened because the gas compressibility factor and extreme pore-pressure favoured the flowing phase to overcome the capillarity of the medium. As the flow met with less resistance across the sample S_V_1, the Δp before and after the Dean Stark test for SCO₂ flooding was observed to be almost the same.

Table 5.6: Ka and Swi before and after dean stark.

Sample No.	Ka (md)		Swi %PV	
	Before	After	Before	After
S_C_1A	391	390	11.3	1.2
S_C_2A	115	104	14.5	1.1
S_C_3A	8.4	9.4	9.6	3.6
S_V_1	92.1	32.5	14.7	2.2

The lower value of *Swi* could be due to one or both of the following reasons:

1. The injected gas was saturated with water at reservoir condition before injecting it into the core sample, evaporation of *Swi* took place because of the high temperature and pressure of the test condition. Fine sand particles that were saturated with water were noticed in the filter at the inlet of BPR, and this could be evidence of *Swi* evaporation.
2. As all core samples were sent in one consignment to Core Lab for Dean Stark extraction, the time difference between testing for the first and last core sample was about two months. This could have resulted of some *Swi* evaporation; however the core plugs were securely wrapped with plastic cling wrap after completing the runs.

5.4.3 Screening test:

The aim of these tests was to find out whether or not the passage of CO₂ will cause an increase or decrease in permeability of the samples, either by mineral dissolution or precipitation. The screening tests were conducted only for the short samples by injecting SCO₂ continuously at a speed of 10 cm/hr at 95 °C and 1100 psia for almost 8 hours.

This step was performed after the core samples had reached irreducible water saturation level and aged overnight. Two repeatability tests were conducted to illustrate the uncertainties that resulted in the initial tests of the S_C_2A and S_C_1A samples, particularly in S_C_2A. This is because the initial screening tests of sample S_C_2A demonstrated a lower Δp compared to S_C_1A, which was the highest quality rock.

This result was inconsistent as S_C_2A from the preliminary tests displayed as intermediate rock quality and should have demonstrated a higher Δp than the S_C_1A sample. A repeatability test was therefore conducted with the aim to ascertain whether the CO₂ passage made this permeability alteration or if the result lies within the experimental uncertainty band. Before the repeatability test was conducted, the back pressure regulator in the core facility was changed because during the initial tests flow at the outlet was interrupted several times.

Figure 5.6 shows both the initial (the replaced) and the new back pressure regulator images. The initial BBR worked by applying pressure on a Teflon plate from the back port. Once the pressure of the flowing gas stream became greater than the applied pressure, flow would be initiated. Due to the corrosive nature of CO₂ this Teflon plate was found to be damaged and resulted in Δp variations through the readings. When the repeatability tests were conducted the Δp trend across S_C_2A was noted to lie between the highest and lowest quality rock. Accordingly the variation in Δp appeared to be mostly associated within experimental uncertainties.

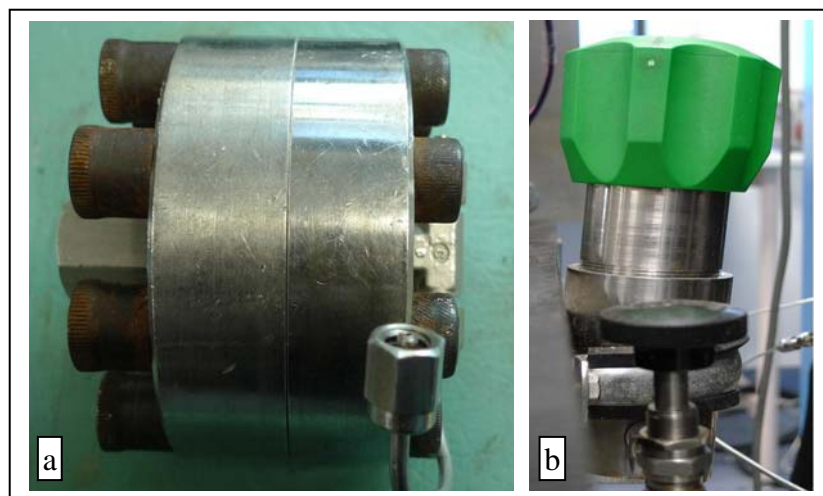


Figure 5.6: Back pressure regulators used in the experiments. (a) Initial BBR, (b) New BBR

Results obtained from the screening tests are shown in Figure 5.7. In the beginning of the SCO_2 injection, pressure differences across the short samples increased until SCO_2 had breakthrough. This increase in Δp was due to the two phase flow through the porous media. Subsequently the Δp started to gradually normalize as more of the saturating phase was recovered resulting in only one phase flowing through the sample. No significant changes were observed after flooding the core samples continuously with SCO_2 for approximately 16 PV as SCO_2 Δp stabilized after the two phase flow had displayed similar patterns. Any minor variations in Δp could fall within the experimental uncertainty.

End point relative permeability of SCO_2 was calculated when the pressure difference was normalized and single phase flow achieved at the end for each run. Average Δp was selected through the measured pressure points recorded on a span of 10 sec for each core sample during the experiments. Table 5.7 shows end relative permeability of CO_2 after 8 hours of flushing through the short samples at 90°C and 1100 psia. Higher SCO_2 permeability is obtained with the higher quality rock sample S_C_1A and lower permeability with low quality rock S_C_3A, with results being 30.9 md and 6.9 md, respectively.

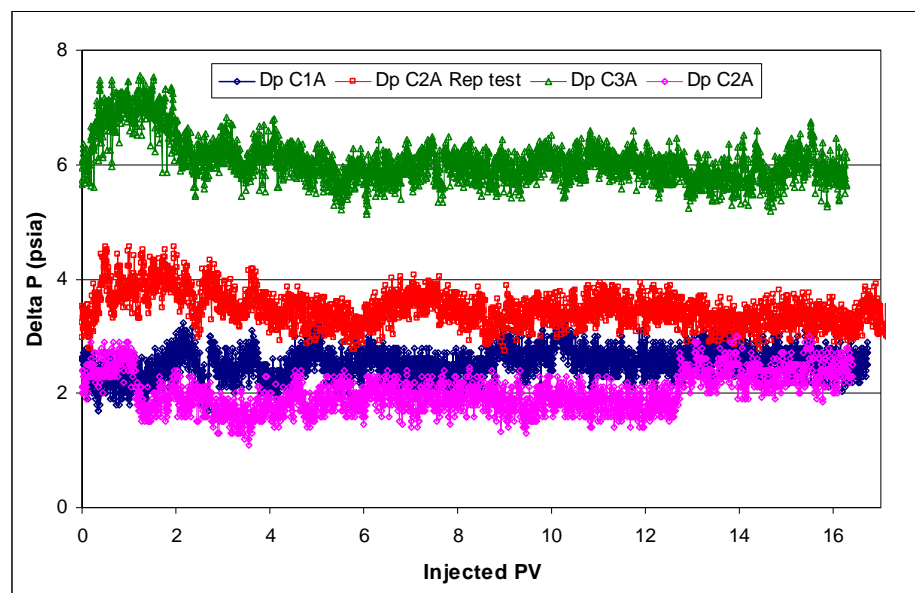


Figure 5.7: Δp of CO_2 90% displacing methane 90% in the short samples for almost 8 hours.

The evidence on permeability changes was not conclusive because of SCO_2 injection. Further investigation of the time dependant nature of permeability variation is essential. It can provide the basis for determining variations in methane production rate and SCO_2 injectivity with time.

Table 5.7: CO_2 permeability at S_{wi} after 8 hours.

Sample no.	Note	Test Condition		Kg CO_2 8 Hours
		Temp. ($^{\circ}\text{C}$)	Pressure (psia)	
S_C_1A	Rep test	95	1000	30.9
S_C_2A		95	1100	27.2
S_C_2A		95	1100	16.8
S_C_3A		95	1100	6.9

5.5 Relative permeability:

5.5.1 Gas-water relative permeability:

The Generation of gas-water relative permeability has been studied by numerous researchers through displacement experiments. In this work, explicit methods such as Hassler, JBN (Johnson, Bossler, and Naumann 1959) and (Jones and Rozelle 1978) are used for calculating the gas-water relative permeability. These methods are based on the Buckley and Leverett (1942) frontal advance solution and applicable within the Darcy's flow regime. The effect of hysteresis was not targeted, as the main purpose of this study is to explore the impact of SCO_2 injection into a natural gas reservoir, as well as developing a method for gas-gas flow at pore scale in terms of relative permeability and the diffusion mechanism.

The limitations of the explicit methods of generating relative permeability are circumvented using implicit methods. These methods of calculating relative permeability depend on applying a series of continuous mathematical formulae. The generated relative permeability data are adjusted until the displacement data produced from the Buckley and Leverett frontal advance theory. The advantage of these methods over explicit methods is that the relative permeability can be estimated over the entire saturation range, not only for saturation greater than the frontal saturation.

In this work the calculated gas-water relative permeability using the Hassler method is compared with the most common models that have been used by industry, for example JBN. This method is straight forward in generating relative permeability and depends on the direct application of Darcy's law (refer to Eq.5.4). If the compressibility factor is considered the generated relative permeability from the JBN method displays an excellent match with the direct measurement of gas-water relative permeability by using Darcy's law (Hassler method). But for the lowest quality rock, gas-water relative permeability curves that were calculated from the JBN method have demonstrated a smaller value in comparison to the Hassler method measured data.

$$K K_{ri} = \frac{u_i \cdot \mu_i \cdot L}{\Delta p \cdot A} \quad (5.4)$$

Where:

K_{ri} relative permeability of the phase

K absolute or effective permeability of the phase.

u_i fractional flow of the phase

From the displacement experiments relative permeability values were generated by using the Hassler method for the 90% methane-brine system in the core samples tested. Figure 5.8 shows drainage gas-brine relative permeability curves generated for the core sample S_C_1A from a displacement test conducted at 5900 psia and 160 °C. The distributed points represent experimental data while the continuous solid lines are the best fit of the experimental data using power and polynomial equations. A gas saturation profile was obtained from the assumed average saturation change in the core by using Eq.5.5.

$$S_2 = S_{av} - W_i \times d(S_{av})/d(W_i) \quad (5.5)$$

Where:

S_{av} average saturation

W_i cumulative injection per V_p

As the imbibition tests have not been performed, residual gas phase saturation and endpoint relative permeability are hypothetically assumed through Land's model (Land 1968), refer to Eq.5.6.

$$\frac{1}{S_{nwr}} - \frac{1}{S_{nwi}} = C^* \quad (5.6)$$

Where:

S_{nwr} residual non-wetting saturation

S_{nwi} initial wetting saturation

C^* trapping characteristic constant

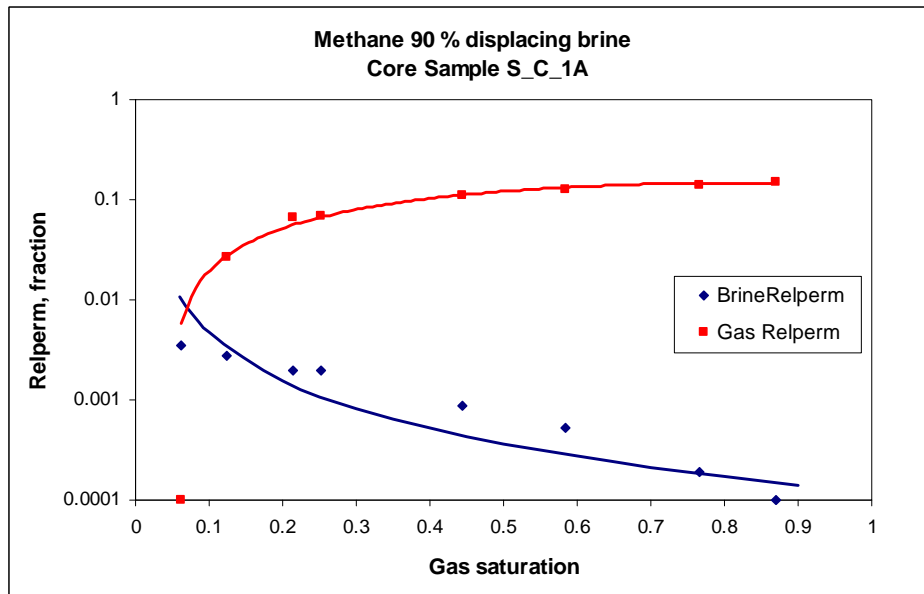


Figure 5.8: Drainage gas-brine relative permeability of core sample S_C_1A obtained from the displacement test conducted at 95 °C and 5900 psia, using Darcy's law.

An appropriate C^* factor was chosen to reproduce the drainage gas-water relative permeability and then applied in Eq.5.6 to calculate residual gas saturation and endpoint relative permeability from Eq.5.7.

$$K_{nwr}^I(S_{nw}) = K_{nwr}^D(S_{mf}) \quad (5.7)$$

Where:

K_{nwr}^I imbibition non-wetting phase relative permeability

K_{nwr}^D drainage non-wetting phase relative permeability

The generated relative permeability data in Figure 5.8 demonstrates variation, particularly within the brine relative permeability, as the data poorly matches the power representation values (solid curve). This may be due to the complexity of the

experiments, as the experiments were conducted at extremely high pressure and temperature. A point to be noted is that the gas relative permeability will be greater than the brine relative permeability, when gas saturation had reached 0.1 PV in the core pores. The breakthrough of methane was observed at 0.28 pore volume of gas injection. This early breakthrough of gas strongly suggests the fact that viscous fingering had occurred during the displacement test because the viscosity ratio μ_{gas}/μ_{water} was considerably small and equals to 0.0345.

Table 5.8 shows data required for generating gas-water relative permeability for the core sample S_C_1A. Both phase relative permeabilities are generated relative to the absolute permeability (K_{air}) before the tests. The interstitial velocity inside the core was about 10 cm/hr. Measured viscosity at test conditions for 90% methane was 0.0258 cp while brine was 0.1929 cp.

Table 5.8: Gas-water brine relative permeability.

$\frac{W_i}{V_{gas}/P_v}$	$N_p \frac{V_{wat}}{P_v}$	Δp psia	$S_{w_{av}}$	S_{w2}	Brine fractional flow (cc/min)	Gas fractional flow (cc/min)	$K_{r_{water}}$	$K_{r_{c1}}$
0	0		0.0626					
0.361	0.361	4.8	0.424	0.062	0.341	0.0001	0.00358	0.0001
0.421	0.411	4.9	0.473	0.123	0.27	19.155	0.00278	0.02671
0.502	0.461	4.7	0.523	0.213	0.177	44.246	0.00190	0.06431
0.742	0.591	4.9	0.653	0.251	0.174	45.055	0.00179	0.06282
1.025	0.671	4.8	0.733	0.443	0.075	71.765	0.00078	0.10214
1.848	0.791	4.7	0.854	0.584	0.044	80.129	0.00047	0.11647
2.685	0.831	4.4	0.894	0.765	0.016	87.683	0.00018	0.13614
5.11	0.852	4	0.915	0.871	0.011	89.032	0.0001	0.15206

With the aim of comparing Hassler and JBN methods, gas-water relative permeability data have been generated from both methods. Eq.5.8 to Eq.5.12 were used for calculating relative permeability using JBN method.

Average gas saturation obtained from the sum of the irreducible gas saturation and produced brine from the displacement tests shown in Eq.5.8.

$$S_{av} = S_{ir} + N_p / V_p \quad (5.8)$$

Flowing phase (brine) is achieved from the changes that occur in the average saturation to the changes in the injected gas pore volume, Eq.5.9.

$$f_w = d(S_{av}) / d(W_i) \quad (5.9)$$

When the injected gas displaces brine in the core sample, its saturation can be estimated from the difference between the average water saturation and the injected pore volume of the displacing phase, Eq.5.10.

$$S_2 = S_{av} - W_i.(f_w) \quad (5.10)$$

If the porous medium is considered to be completely saturated with the in situ fluid, gas fractional flow will be the product of the difference between the unity saturation and the fractional flow of water, Eq.5.11.

$$f_g = 1 - f_w \quad (5.11)$$

Hence water relative permeability can be obtained through Eq.5.12 and gas relative permeability through Eq.5.13.

$$K_{rw} = f_w / (1/W_i I_r) / (1/W_i) \quad (5.12)$$

$$K_{rg} = (f_g / f_w) * (\mu_g / \mu_w) * K_{rw} \quad (5.13)$$

Where:

S_{av} average saturation,

S_{ir} irreducible saturation,

N_p cumulative production,

V_p pore volume,

W_i cumulative injection per V_p ,

f_w water fractional flow,

f_g gas fractional flow,

I_r relative injectivity $= u / \Delta p / (\text{initial } u / \Delta p)$, and $u = Q / \Delta p$

Figure 5.9 shows relative permeability of the gas-brine system for the same core sample S_C_1A. The gas relative permeability demonstrates almost the same value of gas relative permeability to that calculated from Darcy's law. On the other hand,

water relative permeability appeared to have been amplified if compared to the brine trend displayed in Figure 5.8. This difference in brine relative permeability values from applying two different methods to the same experimental data was considered to be related to the compressibility of the gas. Accordingly, a gas volume correction factor is required to be used in the JBN method; this is carried out through Eq.5.14.

$$F_{comp} = \frac{V_{ambient}}{V_{reservoir}} \quad (5.14)$$

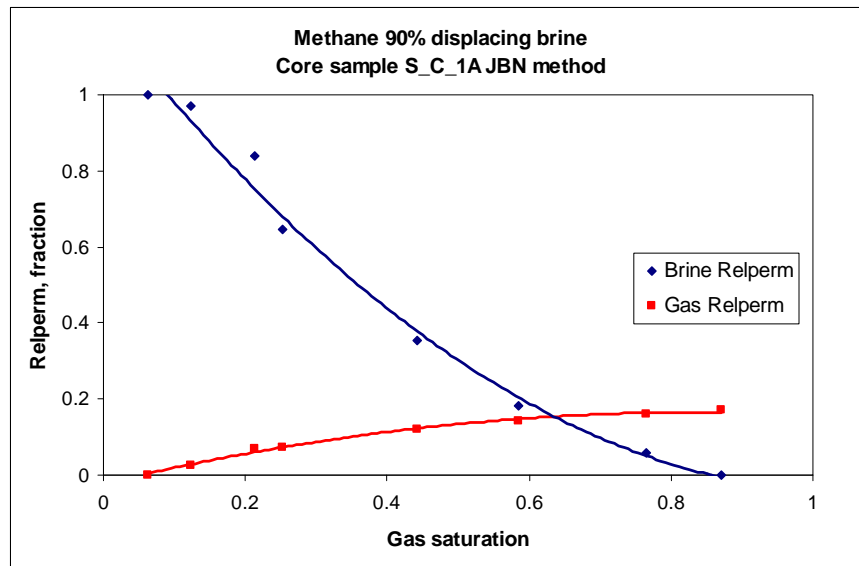


Figure 5.9: Drainage gas-brine relative permeability of core sample S_C_1A obtained from the displacement test conducted at 95 °C and 5900 psia, using JBN method.

The interstitial velocity of the injected gas was investigated and found to be 10 cm/hr. To achieve the designed displacement velocity through sample S_C_1A at reservoir condition, the injection rate must be set at 0.365 cc/min. Because of the gas compressibility, for the effluent of the core to achieve this rate of 0.365 cc/min through the core, 90% methane should produce at a rate of 92 cc/min. The gas volume correction factor was obtained from Eq.5.14 and is equal to 256. Brine relative permeability calculated from the JBN method for sample S_C_1A, was then divided by this factor and plotted in Figure 5.10 together with the relative permeability values generated from Darcy's law.

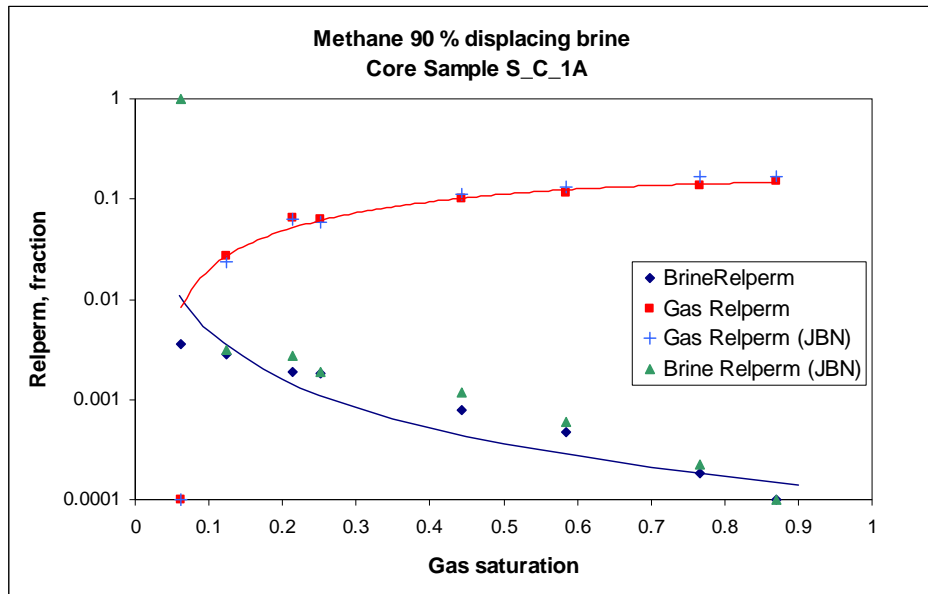


Figure 5.10: Drainage gas-brine relative permeability of core sample S_C_1A obtained from the displacement test conducted at 95 °C and 5900 psia, using JBN and Hassler methods.

Gas relative permeability measurements that were acquired from both methods interestingly virtually coincide, with only a very minor variation noted in the data, see Figure 5.10. Similarly brine relative permeability, after the correction process was made, was noted to match with the direct representation of relative permeability that was generated from Darcy’s law, although there are some variations especially at saturation ranging between 0.2-0.6.

In summary, for the JBN method to apply correctly to a gas-water system, at such harsh conditions, the gas volume correction factor must be taken into account. Table 5.9 shows data that were required for generating the gas-water relative permeability for the core sample S_C_1A by using the JBN method. Measured viscosity at test condition of 90% methane was 0.0258 cp while for brine it was 0.1929 cp.

Initial injection rate was 85 cc/min and pressure difference was 4.9 psi. This value was used in determining the subsequent values of the relative injectivity column that is shown in Table 5.9.

Table 5.9: Gas-water brine relative permeability (JBN method).

$\frac{W_i}{V_{gas/Pv}}$	$\frac{N_p}{V_{wat/Pv}}$	$\frac{\Delta p}{psia}$	$Swav$	$Sw2$	I_r	f_w	f_g	$WiIr$	$\frac{d}{(1/WiIr)}$	$\frac{d}{(1/Wi)}$	K_{rw}	k_{rgas}
0	0		0.0626									
0.361	0.361	4.8	0.424	0.062	1.021	1	0	0.369	2.708	2.764	1.021	0.0001
0.421	0.411	4.9	0.473	0.123	1.023	0.831	0.169	0.431	16.26	16.91	0.863	0.023
0.502	0.461	4.7	0.523	0.213	1.054	0.617	0.382	0.529	10.12	12.321	0.751	0.063
0.742	0.591	4.9	0.653	0.251	1.023	0.541	0.458	0.759	4.339	4.158	0.519	0.059
1.025	0.671	4.8	0.733	0.443	1.056	0.283	0.716	1.083	3.092	3.539	0.324	0.111
1.848	0.791	4.7	0.854	0.584	1.091	0.145	0.854	2.018	1.061	1.214	0.165	0.131
2.685	0.831	4.4	0.894	0.765	1.152	0.047	0.952	3.096	0.927	1.195	0.061	0.166
5.11	0.852	4	0.915	0.871	1.268	0	1	6.481	0.295	0.412	0.0001	0.17

In fact, in the JBN method, flow for the phases at the endpoint is equal to one and at their residual saturation equal to zero, where the phases were trapped and no longer formed a continuous phase inside the porous medium. Endpoints for the phases that appear in grey in Table 5.6 are obtained from the extrapolation of the main trend of the phases' relative permeability. The purpose of the extrapolation producer is to display all the relative permeability measurements on a Log-Cartesian scale. This means that the zero value cannot be plotted on the log scale. Following the same producer of the relative permeability calculation, the gas-brine relative permeabilities are generated for other core samples were tested throughout this study and displayed in Figures 5.11 to 5.13.

Figure 5.11 shows drainage gas brine relative permeability for core sample S_C_2A generated from both methods, as detailed previously. Measured data from the JBN method are scattered under the Darcy's relative permeability points in most of the saturation units. Smaller values of relative permeabilities that were acquired from JBN presumably related to the ratio of pressure differences to the absolute permeability of the core sample S_C_2A. Because pressure differences that were measured during the displacement experiments for sample S_C_2A, having absolute permeability of 115 md, are comparatively small when compared to the pressure differences that were obtained for sample S_C_1A with absolute permeability of 391 md, See Appendix D (Table D-1).

The erratic relationship between pressure difference and absolute permeability may relate to the pore size of the sample S_C_2A. However, it has lower absolute permeability than S_C_1A, but the mean pressure difference across the sample S_C_2A is almost 1 psi greater than the mean of the pressure difference across S_C_1A while its absolute permeability is almost three times smaller than S_C_1A. Hence the best match of the data for both methods would be achieved if the pressure differences were double that of the measured experimental values. This phenomenon indicates that the flow could be laminar through the core sample.

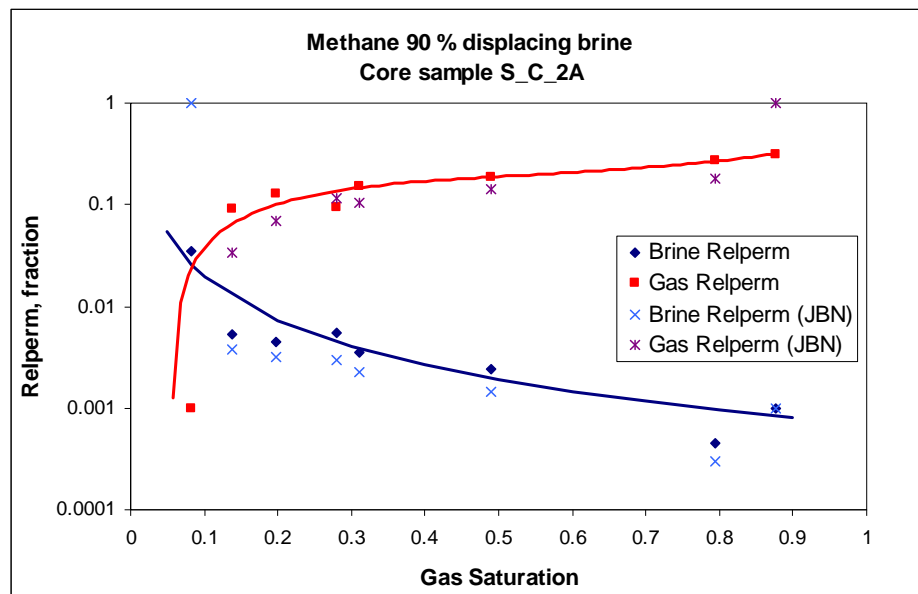


Figure 5.11: Drainage gas-brine relative permeability of core sample S_C_2A obtained from the displacement test conducted at 95 °C and 5900 psia, using JBN and Hassler methods.

The Reynolds number was calculated for all core samples and was noted to lie within the Newtonian flow regime. Wettability and tortuosity of the porous media were considered as being the main cause of the observed erratic relationship. The medium of the intermediate quality rock S_C_2A appeared to be moderately tortuous and had less affinity to being water wetted. Support for the referenced reasons can be through; first, the gas flow through sample S_C_2A had a later breakthrough if compared to S_C_1A. This means gas had passed a greater distance to the outlet of the core sample, and second, brine flow exhibits less resistance to being displaced by gas, due to wettability, and thus the pressure drop across the displaced length was reduced.

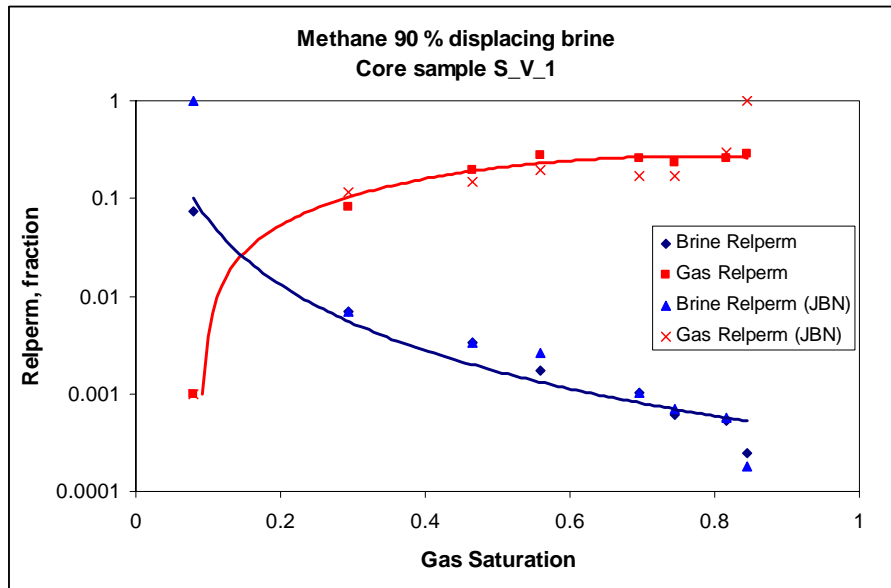


Figure 5.12: Drainage gas-brine relative permeability of core sample S_V_1 obtained from the displacement test conducted at 95 °C and 5900 psia, using JBN and Hassler methods.

Figure 5.12 shows drainage gas-brine relative permeability for the long core S_V_1, the test conducted in gravity stable mode (core holder vertically mounted) with the gas injected in the lower part. The calculated data from both methods are reasonably matched with only some minor variations. The patterns of the curves demonstrate the same behaviour as described for the intermediate rock quality. Referring to the graph, gas relative permeability had succeeded brine relative permeability after the saturation of gas in the core sample approached 0.18 PV while the short samples ranged between 0.07-0.1 PV saturation, see Table D-1 to D3 in Appendix D.

It seems the length and position of the cores had influenced the efficiency of the displacement process because a better recovery of brine was observed with the longer core rather than with the shorter cores. The significant divergence of the measured relative permeabilities was observed for the poor quality rock sample S_C_3A. JBN relative permeabilities data are distributed with nearly the same trend under the relative permeabilities measured by using Darcy's law. However pressure difference values across S_C_3A were reasonably higher than for the other core samples but it was not sufficient to compensate for the increase that occurs in relative permeability data determined by Darcy's law, due to the lowest absolute permeability of 8.4 md of the medium. The mean of the pressure drop was about 9.5

psi while to yield the matched relative permeability curves that were generated from both methods a mean of 40 psi is required; see Table D-2 in Appendix D.

Consequently, the gas and brine flows across S_C_3A are considered to be affected by the tortuosity, wettability, and pore morphology of the medium. In addition, the severity of test conditions that were applied during the experiments could have resulted in a massive reduction in the capillary forces relative to the viscous forces. Accordingly, gas and brine appeared to have flowed with ease through the S_C_3A porous medium. Further reduction in the pressure drop could have been caused by the tortuosity.

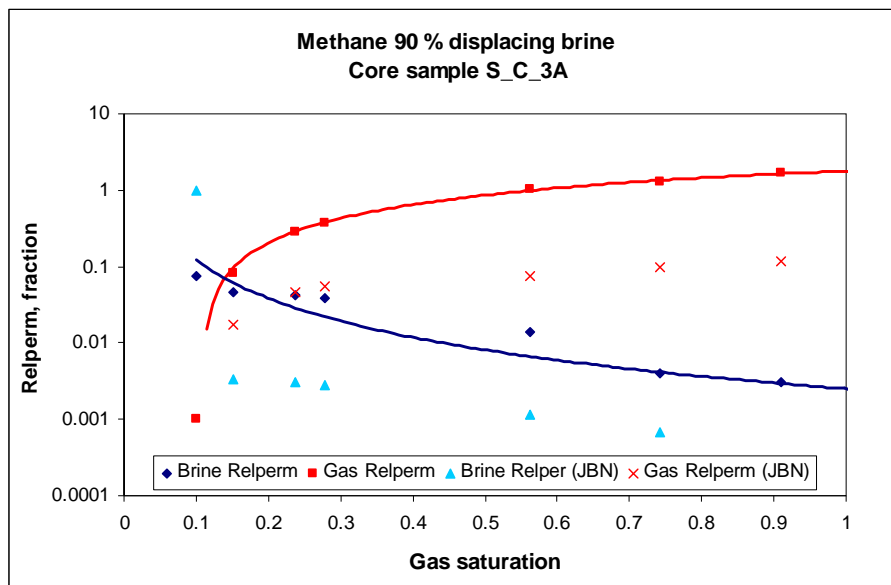


Figure 5.13: Drainage gas-brine relative permeability of core sample S_1_V obtained from the displacement test conducted at 95 °C and 5900 psia, using JBN and Hassler methods.

5.5.2 Effect of permeability heterogeneity:

For the gas-brine displacement tests conducted on various rock qualities, different recovery and gas breakthrough values were observed. These data collectively can be used to investigate the effect of permeability heterogeneity on recovery efficiency and multiphase flow through the cores that were studied. Figure 5.14 shows a relationship between absolute permeability of the cores and displaced brine in pore volume. Clearly the shorter cores, which were mounted horizontally with decreasing absolute permeability, gas had an earlier breakthrough. This means less volume of brine displaced. Thus inter-fingering and channelling was anticipated resulting in an

unfavourable displacement front. This is because less viscous and dense fluid displacing the more viscous and denser fluid. Earlier breakthrough with decreasing absolute permeability of the core was assumed to be associated with the wettability and pore morphology of the rocks.

Wettability acts in favour of capillary forces relative to the viscous forces as a result the pore wall will have an affinity to retain more brine for water wet rock, and consequently an early breakthrough occurs. In the same way, pore morphology and the surface of the wall behave to keep more water in the pore structure if the small pore size and irregular wall surface are distributed abundantly in the porous medium. This indicated, with reducing absolute permeability, higher capillary pressure is predicted and thus smaller pore sizes are considered to be spread dominantly. On the other hand, the length and the position of the core plugs have been demonstrated to profoundly impact the fluids flow in a porous medium. This can be seen through the late gas breakthrough in the long sample S_V_1 if compared to other core plugs' gas breakthrough, being shorter in length and mounted horizontally (See Figure 5.14).

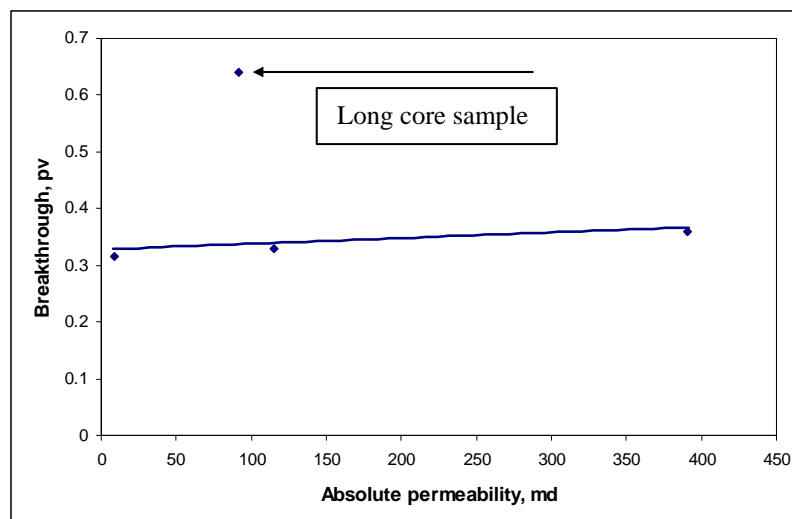


Figure 5.14: Relationship between absolute permeability and breakthrough.

Chapter 6

Gas-Gas displacement

6.1 Introduction:

The displacement process of SCO_2 -methane in porous media can be explained in terms of relative permeability since the immiscible interface between SCO_2 and methane is confirmed in this study. The medium through which the fluid flows can only influence the relative permeability of the flowing phases through its pore morphology and permeability heterogeneity. Whereas it cannot influence the gas multiphase flow through its wettability as the gases are well acknowledged for being mostly in the non-wetting phase.

The displacement experiments were conducted on the three short samples and the vertical long core sample for the SCO_2 -methane core flooding experiments. The impact of the various test conditions on the recovery efficiency and gas multiphase flow at pore scale were extensively studied. The parameters which were selected for investigation in this study were predicted to have significant influence on the ultimate recovery; these parameters were pressure, temperature, composition, injection rate and heterogeneity of the medium.

The methodologies used for generating relative permeability curves are the JBN and Hassler methods. The acquired results from both methods were compared to ensure accuracy. A nearly perfect match of the relative permeability curves was observed through applying these methods to the displacement experiments data. The results gathered from studying the mentioned (referenced) parameters was used to syntheses a new model for gas-gas relative permeability, which would accurately account for subsequent gas compositional changes during the displacement process. Generally the recovery factor at CO_2 breakthrough was relatively high, ranging from 70% to 80% of original gas in place. It is a function of CO_2 content in the injected gas, injection rate, pressure, temperature and absolute permeability. Mainly injection rates, in situ gas compositions and pore pressures will severely impact methane recovery. In contrast, temperature, permeability heterogeneity and core position will moderately affect the recovery efficiency.

6.2 Impact of composition:

The impact of gas composition on the recovery factor and multiphase gas flow were studied extensively. This was conducted by displacing the in situ gas at four different compositions of SCO_2 -methane mixture by almost 98% pure SCO_2 . The objective of these tests was to determine the intensity of the compositional effect on gases mixing by diffusion mechanism. These series of tests were conducted in a gravity stable mode, by injecting SCO_2 from the bottom of the core plug to displace methane to explore the impact of composition on the recovery factor as well as to investigate SCO_2 miscibility and gravity separation effects. All the compositional experiments were carried out on the long core sample due to sufficient pore volumes and minimizing experimental artefacts.

The test condition applied simulated the initial reservoir condition, with pressure of about 6000 psia, temperature 160°C and interstitial velocity of 10 cm/hr. Figure 6.1 shows four in situ gas composition profiles that were displaced by 98% CO_2 and CO_2 breakthrough versus injected pore volumes. Subsequent to the CO_2 injection into core sample S_V_1, methane production rate was almost instantaneous, with the methane production profile indicating piston like displacement until the SCO_2 breakthrough occurred.

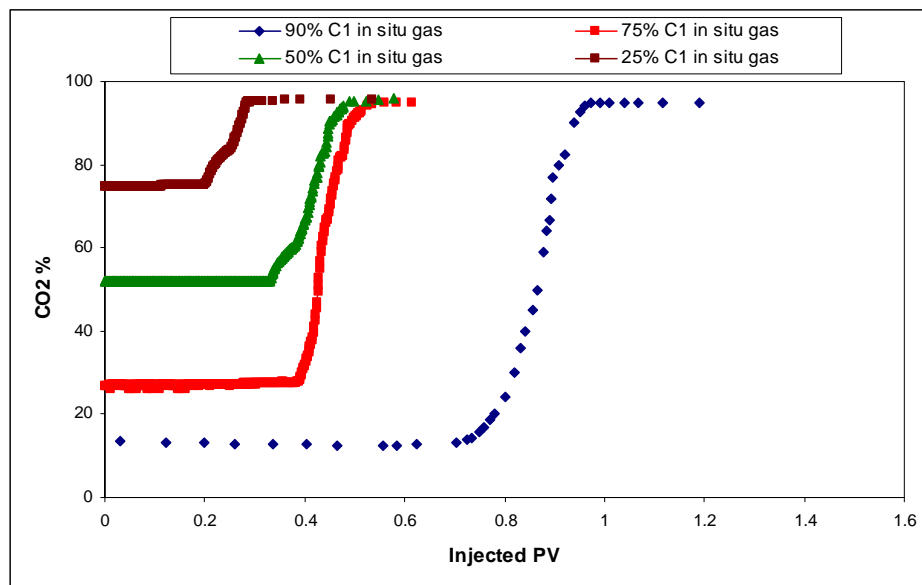


Figure 6.1: Mole percent CO_2 production vs. injection pore volume.

Obviously recovery of methane at SCO₂ breakthrough is higher for the highest methane concentration in the in situ gas. Breakthrough of SCO₂ was observed from the four displacement tests 0.7 PV, 0.4 PV, 0.33 PV, and 0.2 PV for CO₂ concentration 10%, 25%, 50%, and 75% in the methane, respectively. As a result, the SCO₂ dispersion coefficient was anticipated to increase with increasing SCO₂ contaminant of the in situ gas. In the same way, SCO₂ relative permeability was also predicted to increase with increasingly in situ gas contamination. Details of experimental data can be seen in Table 6.1 for the compositions investigated.

The CO₂ breakthrough as a function of CO₂ concentration can be represented through a continuous mathematical form which can interpolate the entire composition within the test limit. Figure 6.2 shows the best fit of experimental breakthrough versus concentration, a third order polynomial graph appeared to be well matched with the experimental data. When SCO₂ passes through a core plugs having 19.41 cm in length, 12.255 cm² diameter, Ka 92 md, speed of 10 cm/hr, and reservoir condition of 5900 psi and 160 °C, SCO₂ can be expected to breakthrough via Eq.6.1.

$$\text{CO}_2 \text{ BT} = 3 \times 10^{-6} C^3 + 5 \times 10^{-4} C^2 - 0.0328C + 0.966 \quad (6.1)$$

Where 'C' is CO₂ concentration.

Table 6.1: Test conditions and CO₂ breakthrough at various in situ gas compositions.

SCO ₂ Content Mole %	Test Condition			Displacement	CO ₂ Break thro PV	CO ₂ BT min:ss
	Injection Rate (cm/hr)	Temp. (°C)	Pressure (psia)			
0.10	10	160	5900	98% CO ₂ @90 CH ₄	0.72	71:28
0.25	10	160	5900	98% CO ₂ @75 CH ₄	0.42	42:52
0.50	10	160	5900	98% CO ₂ @50 CH ₄	0.33	33:41
0.75	10	160	5900	98% CO ₂ @25 CH ₄	0.22	22:27

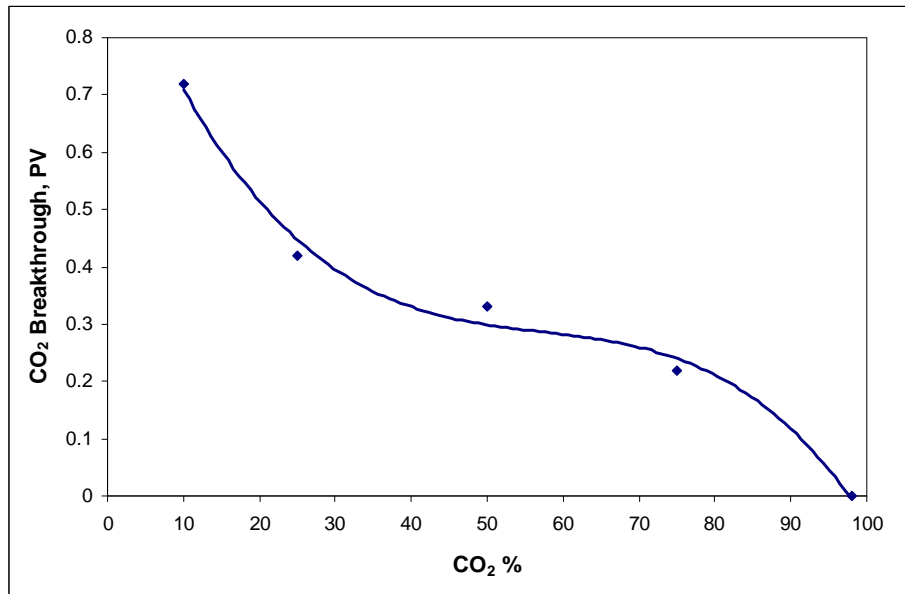


Figure 6.2: CO₂ breakthrough PV vs. CO₂ percent saturation within the in situ gas (methane).

From the displacement tests of various compositions in S_V_1, relative permeability curves are generated for each phase at successive in situ gas compositions. Moreover the impact of in situ gas compositions on relative permeability was determined. Relative permeability for the injected SCO₂ unexpectedly increased as the CO₂ concentration increased in the in situ gas. Both injected and displaced phases exhibited less physical property differences that resulted in the accelerated miscibility, earlier breakthrough and enhanced relative permeability for SCO₂ being noticed.

The methods that were used for generating relative permeability in the SCO₂-methane system are the JBN and Darcy's methods. A reasonable fit of the measured relative permeability via both methods was observed. For instance, Figure 6.3 shows relative permeability of CO₂ and methane as a function of 'S₂' that was calculated by both methods. For the other compositions the same approximation between the relative permeability curves was found. This facilitates the conclusion that the JBN method is an applicable technique for generating relative permeability curves for SCO₂-methane systems in porous media. Consequently only JBN relative permeabilities are shown in the succeeding Figures.

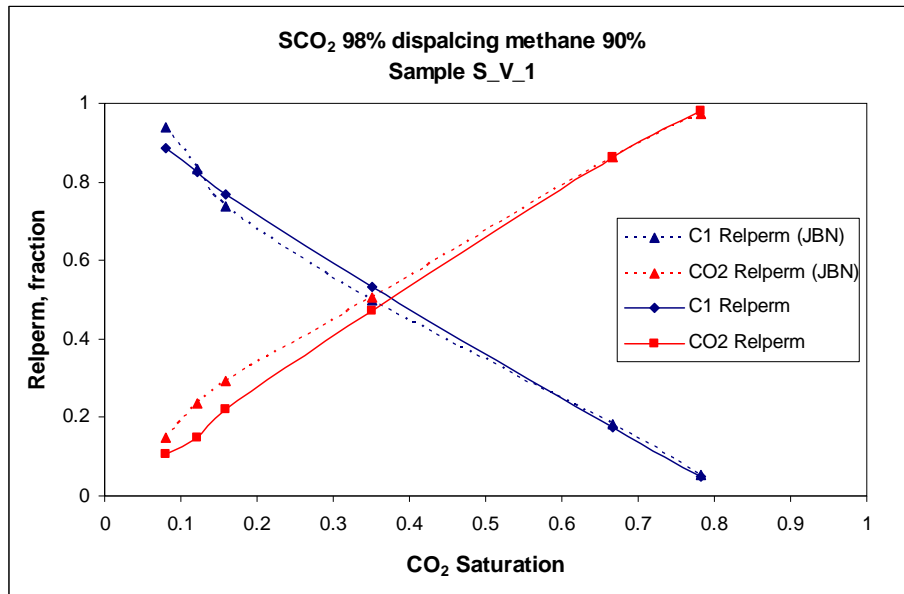


Figure 6.3: Relative permeability curves vs. CO₂ saturation calculated from displacing methane 90% by SCO₂ 98% at 5900 psia, 160 °C and 10 cm/hr.

From the study of the relative permeabilities curves two unique, almost straight lines can be seen, approaching to the ideal gas relative permeabilities. Although Kerig and Watson (1987) consider a power relative permeability model would not provide sufficient flexibility to reproduce the observed field results, the nearly straight SCO₂-methane relative permeability lines are considered to conveniently be modelled as a power-law. For example, Figure 6.4 shows generated relative permeability for both phases from the JBN and power models. The power relative permeability model for the gas-gas phase was obtained from the best fit of the experimental data by applying the following equations.

$$Kr_{CO_2} = a \times (S_{CO_2})^b \quad (6.2)$$

$$Kr_{C_1} = Kr_{CO_2}^c \times [(1 - S_{CO_2}) \times f_c] \quad (6.3)$$

Where:

Kr_{CO_2} SCO₂ relative permeability

Kr_{C_1} methane relative permeability

S_{CO_2} fractional saturation of SCO₂

f_c fractional composition of in situ gas

The power relative permeability curve for SCO_2 that was generated from Eq.6.2 gives a practical fit with the experimental data, which is in contrast to the methane relative permeability data where only a fair match was achieved by applying Eq.6.3 (See Figure 6.4). Overall, achieving this result from the power model will permit relative permeability curves to be modelled accurately for a gas-gas system.

Furthermore, the impact of the parameters that are predicted to undeniably affect the SCO_2 -methane flow in porous media, such as pressure, temperature, injection rate, and gas composition, can be simply taken into consideration by the power model. Details of the calculation can be found in Table D-4 in Appendix D.

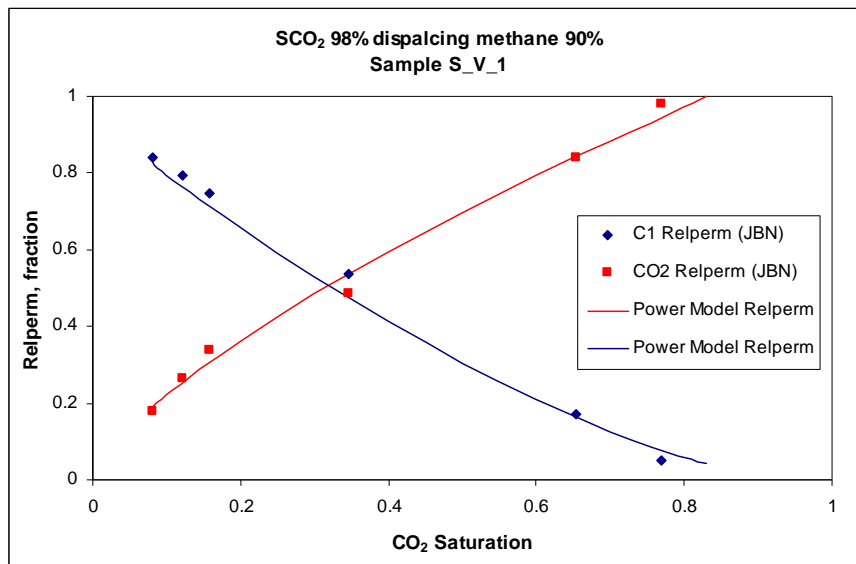


Figure 6.4: Relative permeability curves vs. CO_2 saturation calculated from displacing methane 90% by SCO_2 98% at 5900 psia, 160 °C and 10 cm/hr.

In the same way, relative permeability curves are calculated and compared for other compositions. Figure 6.5 shows relative permeability curves that are plotted against saturation ' S_2 '. These curves are generated from the displacement of methane at SCO_2 content of 10% and 25% by 98% SCO_2 . The relative permeability of CO_2 , if analysed in terms of saturation, will be noted to have improved when displacing in situ gas at a higher CO_2 concentration.

Moreover its shape and magnitude, if compared to lower CO_2 content relative permeability, become steeper and the improved methane relative permeability can be observed to increase by factor of 20%.

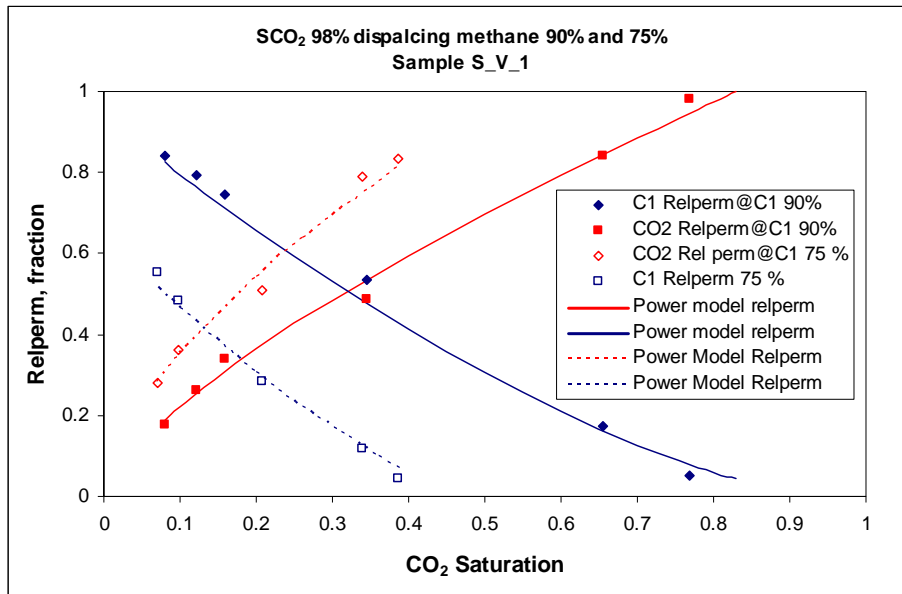


Figure 6.5: Relative permeability curves vs. CO₂ saturation calculated from displacing methane 90% and 75% by SCO₂ 98% at 5900 psia, 160 °C and 10 cm/hr.

The entrapment of methane by injected SCO₂ can only occur through it dissolving in the connate water saturation and interacting with the porous grains. Although a piston like displacement is predicted until the CO₂ breakthrough, the amount of methane left as residual saturation after SCO₂ breakthrough is produced in a small fraction in the produced gas at the effluent of the core sample. The concentration of CO₂ in the produced gas only reached 94%; nevertheless at the inlet of the core concentration of CO₂ in the displacing phase was 98%. After CO₂ breakthrough, the core plug was continually flooded for almost 10 pore volumes. In the case where in situ gas had a composition of 90% methane, only after 3 pore volumes of injection the CO₂ concentration in the effluent had reached the same concentration as CO₂ observed at the inlet of the core. It can be interpreted from this phenomenon that the displaced phase, which is methane in the direction of the main convective, will be produced much faster to the fraction that would be perpendicular to the main convective passes, as observed by Hagoort (1998).

Figure 6.6 shows relative permeability of both SCO₂ and methane in the case where the in situ gases contained 50% and 75% of CO₂, respectively. Interestingly relative permeability of SCO₂ at the beginning of the displacement process was greater than the displaced phase. Because the fractional flow of methane was considerably lower, greater mixing resulted as the in situ gas was displaced by 98% SCO₂. This is why

the curves do not intersect each other, see Figure 6.6. Indicatively SCO_2 relative permeability will surpass the methane relative permeability whenever its concentration reaches about 40% of the in situ gas.

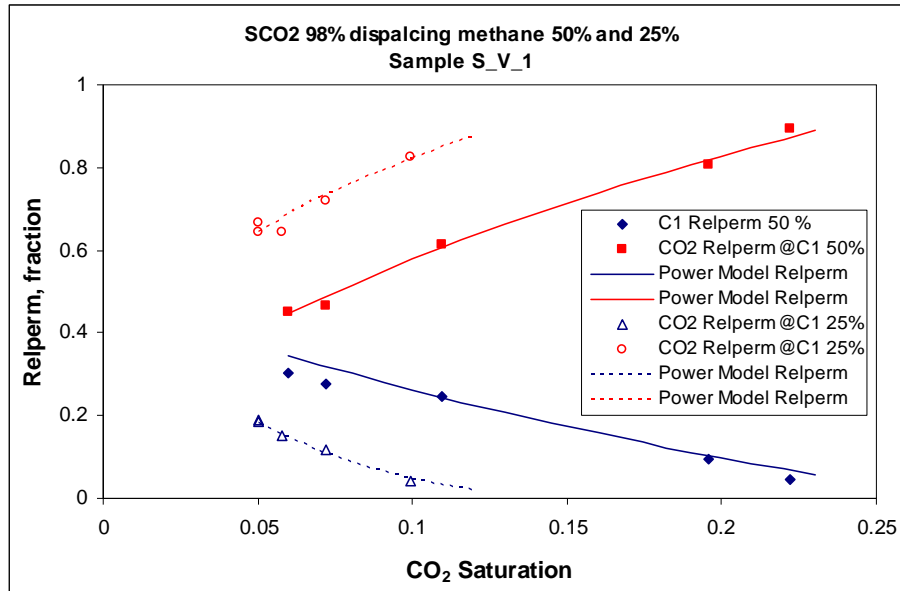


Figure 6.6: Relative permeability curves vs. CO_2 saturation calculated from displacing methane 25% and 50% by SCO_2 98% at 5900 psia, 160 °C and 10 cm/hr.

6.3 Impact of displacement rate:

When two miscible fluids are in contact in the dynamic state in a linear porous medium, recovery efficiency depends on the extent to which these phases are miscible. The less difference there is in their physical properties (i.e. viscosity and density) the bigger the miscible zone becomes, and thus poor recovery efficiency results. Therefore, relative permeability curves in such a system (gas-gas displacements) are conspicuously affected by the injection velocity because the flow of both the phases has been associated with dispersion and molecular diffusion. The purpose of these tests was to determine the effect of displacement rates on the recovery factor as well as investigate SCO_2 miscibility and gravity separation effects. In order to emphasize the gravity separation effects on multi phase gas flow, the runs were conducted in a gravity stable mode, which was injecting CO_2 from the bottom to displace methane.

Five displacement rates were examined, starting from the initial reservoir velocity of 10 cm/hr to 1 cm/hr. The descending arrangement was to duplicate the reduction that would occur to the injection speed at the unit distance away from the injection well due to SCO_2 friction with the porous wall. The gas speed is predicted to approximately result in a decrease by a factor of 10 at 1 km away from the injection well when compared to its initial velocity near the source of injection. The decision to implement pilot SCO_2 injection to enhance gas recovery will be appropriately estimated if the effects of the displacement rate on the ultimate recovery are determined.

The SCO_2 profile from the rate-sensitivity tests are plotted in Figure 6.7 for the rate-sensitivity displacements conducted on the long core S_V_1 plug at flooding pressure of 5900 psia and temperature of 160 °C. The breakthrough of CO_2 at methane recovery was surprisingly varied and ranged from 0.16 PV to 0.7 PV of initial gas in place. With decreasing displacement rate CO_2 had an unexpectedly earlier breakthrough. Nonetheless lower displacement rates, as comprehended, typically provide improved recovery when the phases are either near, or at immiscible conditions. This phenomenon of accelerated breakthrough with decreasing displacement speed was not anticipated originally. This is because to the author's knowledge, tests in such sever conditions have not been performed or documented in the literature.

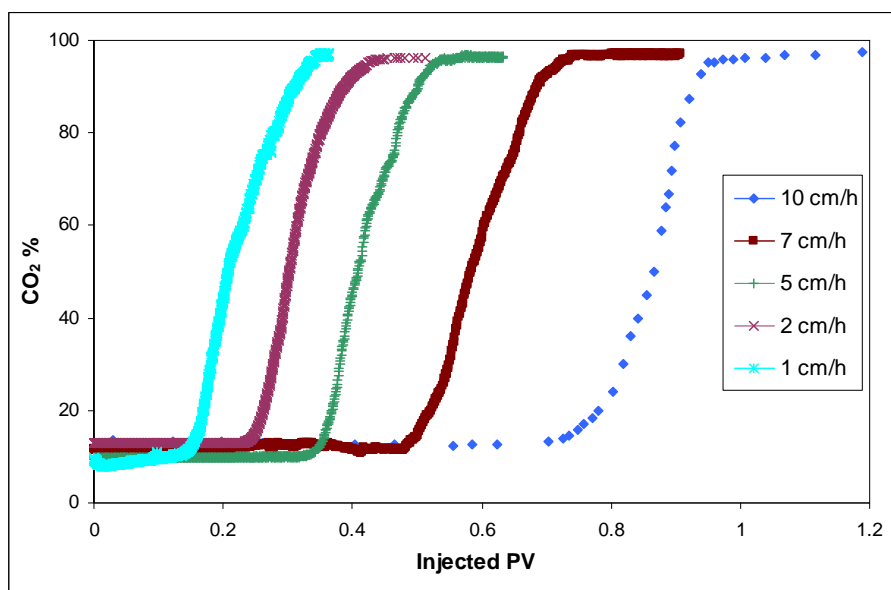


Figure 6.7: Displacement rate tests of sample S_V_1.

Therefore two more repeatability tests were conducted to weigh the initial test results that were obtained with applying the two lower injection rates (1 cm/hr and 2 cm/hr). Results from the repeatability tests confirmed the initial results and do not lie within the experimental artifact.

The displacement rates investigated corresponded to displacement velocities of 10, 7, 5, 2 and 1 cm/hr. However, SCO_2 at the referenced test conditions has greater viscosity and density about three times that of methane. With decreasing injection velocity from 10 cm/hr to 1 cm/hr, SCO_2 showed accelerated breakthrough from 0.7 PV to 0.16 PV, respectively (See Table 6.2).

The reason for the earlier breakthrough of SCO_2 as the injection rates decreased, could be either through dissipating the miscible fluid or channelling due to heterogeneity of the medium (Perkins and Johnston 1963). The authors considers that dispersion and diffusion mechanisms are the major cause of channelling and dissipating of miscible fluids, which usually results in facilitating the displacing phase to an earlier breakthrough. In addition, the SCO_2 -methane phase will be in the gaseous phase at the referenced test condition. Hence dispersion and molecular diffusion have a noticeable effect on methane recovery.

Further illustration of the earlier SCO_2 breakthrough that corresponded with decreasing the flow rates, can be clearly explained through the SCO_2 -methane IFT measurements. The occurrence of a cloud was noticed in the IFT tests. This cloud formed above the CO_2 bubble at the lowest possible injection rates. This phenomenon was interpreted as the molecular interaction between both phases via a molecular diffusion mechanism.

Table 6.2: CO_2 breakthrough and end point permeability of five injection rates.

Injection Rate cm/hr	Test Condition		Displacement	CO ₂ BT PV	CO ₂ BT mm:ss
	Temp. (°C)	Pressure (psia)			
1	160	5900	98% CO ₂ @90 CH ₄	0.16	173:35
2	160	5900	98% CO ₂ @90 CH ₄	0.24	116:48
5	160	5900	98% CO ₂ @90 CH ₄	0.35	71:58
7	160	5900	98% CO ₂ @90 CH ₄	0.49	71:24
10	160	5900	98% CO ₂ @90 CH ₄	0.72	72:14

At the pore level, the displacement front can be reasonably assumed to be a partial or near miscible front. Since the interfacial tension forces, which have been measured, were proportional to the viscous forces on a reservoir scale. Accordingly at low flooding rates, which permit greater time for the miscibility between CO₂ and methane by molecular diffusion, the recovery rate is much higher than the recovery by re-pressurization. As a result, supercritical CO₂ at this condition may form a separate channel through the porous medium of S_V_1 resulting in earlier breakthrough. This is because of its intrinsic properties and molecular diffusion at low flow rates.

With reference to Figure 6.7 it can be noted that the residual in situ gas remained in the core after CO₂ breakthrough was gradually produced with continual injection, as small fractions at the effluent. The same occurrence was also noted from the series compositional tests. Analysed effluent concentration always showed less SCO₂ percentage than the known injection gas SCO₂ content, despite the continual SCO₂ flooding for several injected pore volumes. The fraction of methane produced after breakthrough was about 5% at an injection velocity of 10 cm/hr. This value remained more or less the same for almost 3 pore volumes of injection. As the flooding rate was reduced in steps of 1 cm/hr, more pore volumes of injection were required to displace the entrapped gas that remained in the core after the breakthrough. This means that as SCO₂ was injected to displace methane, greater mixing occurred in the direction of gross fluid movement (parallel to flux direction) rather than perpendicular to the main convective direction. Several researchers have stated that the greatest dispersion coefficient in porous media can be obtained in the main flow direction (longitudinal dispersion), while the smallest value of dispersion acquired is in the perpendicular direction (Hagoort 1998; Blackwell 1962; Perkins and Johnston 1963).

The JBN method was used in generating relative permeability for both phases at each sub-sequential injection rate. Figure 6.8 shows relative permeability curves for SCO₂-methane system versus SCO₂ saturation for the injection rates of 10 cm/hr and 7 cm/hr. The generated power model relative permeability curves from Eq.6.2 to Eq.6.3 likely agree with the experimental data. SCO₂ relative permeability was enhanced in terms of velocity reduction.

As the saturation of SCO_2 approaches 36% and 24% of pore volume in the core, SCO_2 relative permeability succeeded that of methane at 10 cm/hr and 7 cm/hr, respectively. Successively reducing the rates to the lowest level of 1 cm/hr, SCO_2 breakthrough was accelerated and at the lowest displacement rate its breakthrough was about 4 times quicker than its breakthrough at 10 cm/hr. Details of the data can be seen in Tables D-4 and D-8 in Appendix D.

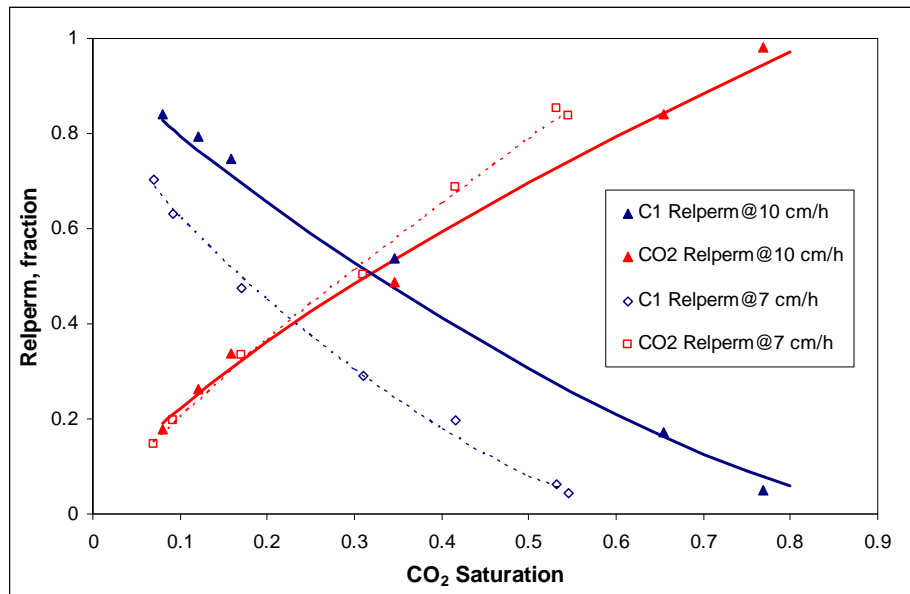


Figure 6.8: SCO_2 and methane relative permeability vs. CO_2 saturation at 10 cm/hr, 160 °C and 5900 psia.

Figure 6.9 shows relative permeability curves for SCO_2 –methane system versus SCO_2 saturation at the lowest injection rate of 1cm/hr. Methane relative permeability was considerably decreased to about 80% in comparison to its relative permeabilities at the injection rate of 10 cm/hr. The substantial reduction in methane relative permeability could be due to dissipation of the miscible fluid and channelling. The first factor is a result of molecular diffusion and dispersion. While channelling is more likely to be occur because of heterogeneity of the rock.

For instance at the field scale, if the impacts of displacement rate are taken into account, the scenario of SCO_2 injection can be described as follow; the speed of the injected SCO_2 , initially, has the same magnitude inside as at the adjacent area of the injector well. Thereafter, at a distance away from the injector well, the rate will be

reduced by friction. Thus SCO_2 is accelerated to disperse, contaminating the in situ natural gas by molecular diffusion and compositional equilibration over time.

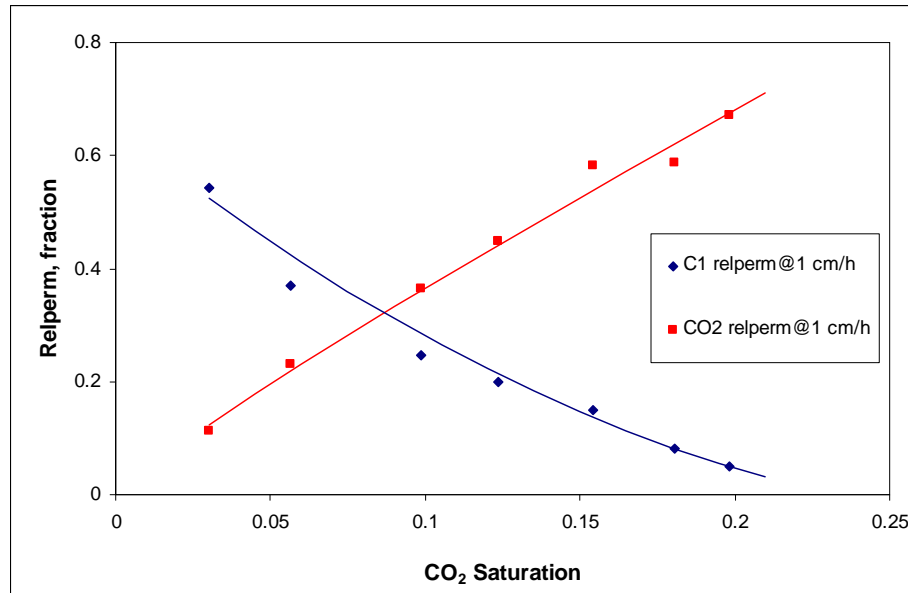


Figure 6.9: SCO_2 and methane relative permeability vs. CO_2 saturation at 1 cm/hr, 160 °C and 5900 psia.

On the other hand the impact of interfacial tension, capillary pressure, permeability heterogeneity, and morphology of pores are known parameters that significantly influence the recovery efficiency from two immiscible fluids. Possibly these parameters will have the same, or less, effect on natural gas recovery.

6.3.1 Repeatability tests:

The proportionality between the accelerated SCO_2 breakthrough and decreased displacement rates was investigated further with respect to methane recovery rate sensitivity (dependence). This is achieved through repetitive tests, especially for the two lowest injection velocities. Marginal differences between the initial tests and the repeatability tests were observed and only the trend of the displacement front and breakthrough time was noted to be affected.

This minor variation was probably either related to the continuous adjustment of the SCO_2 injection rate during the run or in situ gas leakage through the tiny fracture that occurred in the tube. This is mentioned in detail in Chapter 3. The variation in

displacement rate was caused by maintaining the pore pressure constantly via a back pressure regulator. The initial pore pressure was set to 6000 psia and the core pressure was varied during the experiment. This pressure fluctuation caused minor injection rate fluctuations which may have affected the displacement front. Since the volume, flow rate and composition of the produced gas is measured, it is possible to compare and calibrate the CO₂ injection rate in the core, based on methane volume produced at CO₂ breakthrough.

Figure 6.10 shows the SCO₂ profile for the repeatability and initial tests that were carried out at 1 cm/hr. In general the breakthrough of SCO₂ in the initial test occurred slightly earlier when compared to the repeatability test result. Specifically the trends are in good agreement with the total amount of methane recovered.

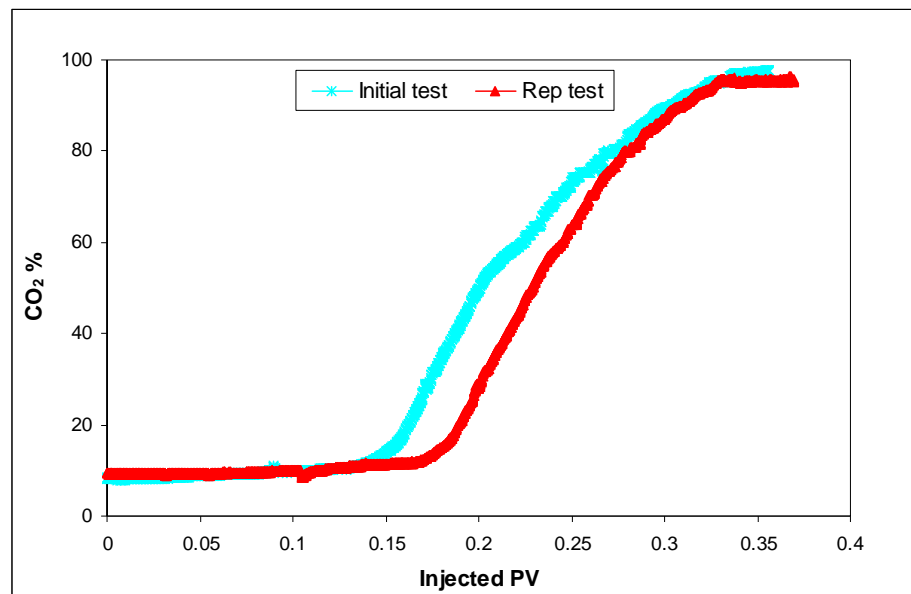


Figure 6.10: Initial and repeatability tests of 1cm/hr of sample S_V_1.

6.4 Impact of pore pressure:

The aim of these tests was to explore the effect of pore pressure on SCO₂ breakthrough, and ultimate recovery. Pore pressures investigated ranged from the current reservoir pressure of 5900 psia to abandonment pressure of 1500 psia. Throughout these tests five pore-pressures were studied in a descending manner, from the initial to abandonment pressure. Essentially these tests were carried out in a similar manner to the previous tests, being displacement rate tests. This was done in a way to study the effect of SCO₂ miscibility and gravity separation.

The pore pressures studied were successively decreased from 5900 to 4500, 3500, 2500, and 1500 psia. Throughout the tests a temperature of 160 °C and injection speed of 10 cm/hr were sustained. With decreasing pore-pressure the difference in physical properties between SCO₂-methane was observed to decrease noticeably. Thus SCO₂ will disperse and mix with methane with ease and consequently resulting in earlier breakthrough. Ultimate recovery of methane from initial to abandonment pressures were 0.7 and 0.43 of pore volume of initial gas in place (See Table 6.3).

Table 6.3: CO₂ breakthrough and end point relative permeability at five pore pressure.

Pore Pressure (psia)	Test Condition		Displacement	CO ₂	Kg CO ₂
	Temp. (°C)	Pressure (psia)		BT PV	md
1500	160	1500	98% CO ₂ @90 CH ₄	0.40	53.3
2500	160	2500	98% CO ₂ @90 CH ₄	0.45	109.4
3500	160	3500	98% CO ₂ @90 CH ₄	0.54	171.1
4500	160	4500	98% CO ₂ @90 CH ₄	0.6	222.3
5900	160	5900	98% CO ₂ @90 CH ₄	0.72	270

The impact of a low flow rate of 1 cm/hr was severe on the recovery factor when compared with the methane recovery that was measured at the low pore pressure test of 1500 psia. The recovery of methane at SCO₂ breakthrough for the lowest injection speed was 0.16 PV of original gas in place (OGIP), whereas at abandonment pressure of 1500 psia, recovery was considerable at about 0.40 PV.

Figure 6.11 shows SCO₂ profile versus injected pore volume at the effluent for the two highest pore pressure (5900 and 4500 psia). Obviously with decreasing pore pressure SCO₂ would breakthrough earlier, from 0.72 PV to 0.6 PV. The effect of pressure was clearly apparent if referred to the IFT measurements, which was IFT decrease with reducing cell-pressure. At lower pressure, miscibility between SCO₂-methane phases was significantly speeded up due to less variation in the physical properties between both phases. (See Figure 6.11)

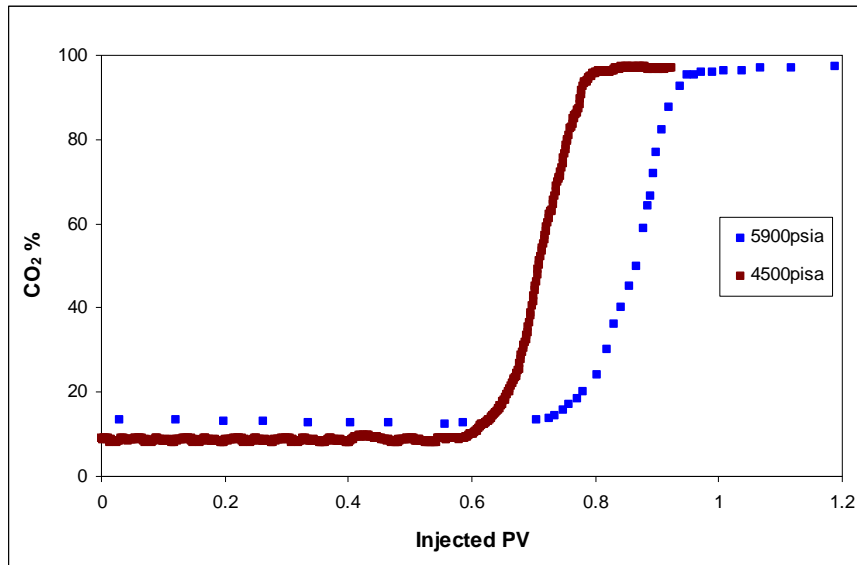


Figure 6.11: Pore pressure tests for sample S_V_1, 5900 pisa and 4500 pisa. Temperature 160 °C and displacement rate of 10 cm/hr.

Figure 6.12 shows the SCO₂ produced trend at the effluent of the core versus injected pore volumes at the three lowest pore pressures of 3500, 2500, and 1500 psia. Their displacement front, if compared to the SCO₂ trends in Figure 6.11, demonstrates a gentle slope front suggesting a greater miscible zone has been formed as SCO₂ displaces methane. Steeper slope displacement fronts at higher pore pressures agrees to the previous discussion that supercritical CO₂ behaves as a more viscose and denser fluid at high pressures, and thus it will be less miscible with methane.

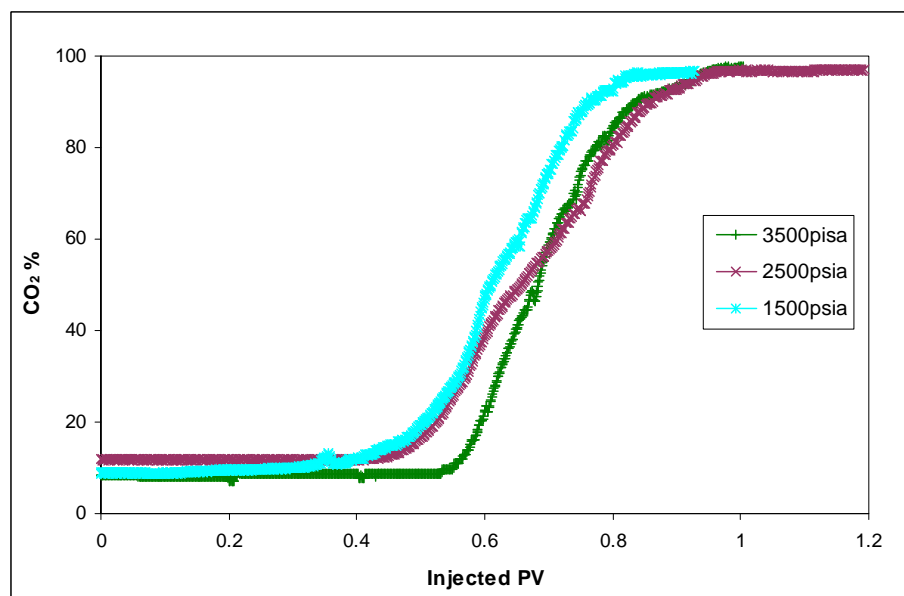


Figure 6.12: Initial Pore pressure tests of sample S_V_1, 3500 pisa, 2500 pisa and 1500 pisa.

The influences of pore pressure on SCO_2 -methane relative permeability are analysed and studied in detail. Relative permeability curves for the two highest pore pressures of 5900 and 4500 psia versus SCO_2 saturation are shown in Figure 6.13. With decreasing pore pressure relative permeability for both phases was affected. When the saturation of SCO_2 reached 0.36 and 0.3 pore volumes in core sample S_V_1, its fractional flow overcame methane at 5900 and 4500 psia, respectively.

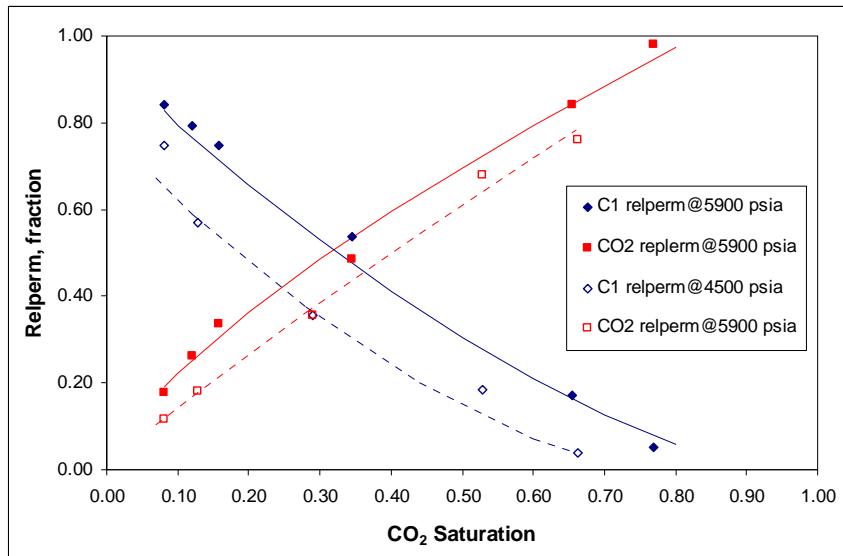


Figure 6.13: SCO_2 and methane relative permeability vs. CO_2 saturation at pore pressure 5900 psia and 4500 psia and displacement rate of 10 cm/hr, temperature of 160 °C.

Successively reducing pore pressure to the minimum level (1500 psia) from the initial reservoir pressure, breakthrough of SCO_2 was hastened by a factor of 1.7 if compared to its breakthrough at 5900 psia. This means SCO_2 miscibility with methane has been increased but with the lower velocity test, the magnitude was much greater. Since the flow rate during pore pressure tests was maintained at 10 cm/hr, mixing has been limited due to the time that was required for methane displacement at the lower pressure test. Details of the data can be seen in Tables D-11 and D-15 in Appendix D.

Figure 6.14 shows relative permeability curves for both phases at a pressure of 1500 psia. Methane relative permeability was considerably decreased by about 17% compared to its relative permeability when the pore pressure applied was 5900 psia. The noticeable reduction in methane relative permeability could be due to physical properties of the gases rather than dissipation of miscible fluid or channelling.

Injecting SCO_2 at abandonment pressure appeared to be an ideal period for the pilot enhanced gas recovery project rather than at the initial pressure of the reservoir. However an encouraging improved recovery was obtained with applying the initial pressure.

With reduced gas speed away from the injector well and the passage of time, SCO_2 tended to display extensive dispersion into the methane phase, resulting into a dissipating miscible zone through the heterogeneity of the rock and thus early breakthrough. The fraction of the residual methane saturation left after CO_2 breakthrough was produced with continual SCO_2 injection as a small fraction of only 5-6%. From an economic point of view, it is unrealistic to inject a corrosive gas like SCO_2 to displace methane and only harvest 5-6% of the injected phase.

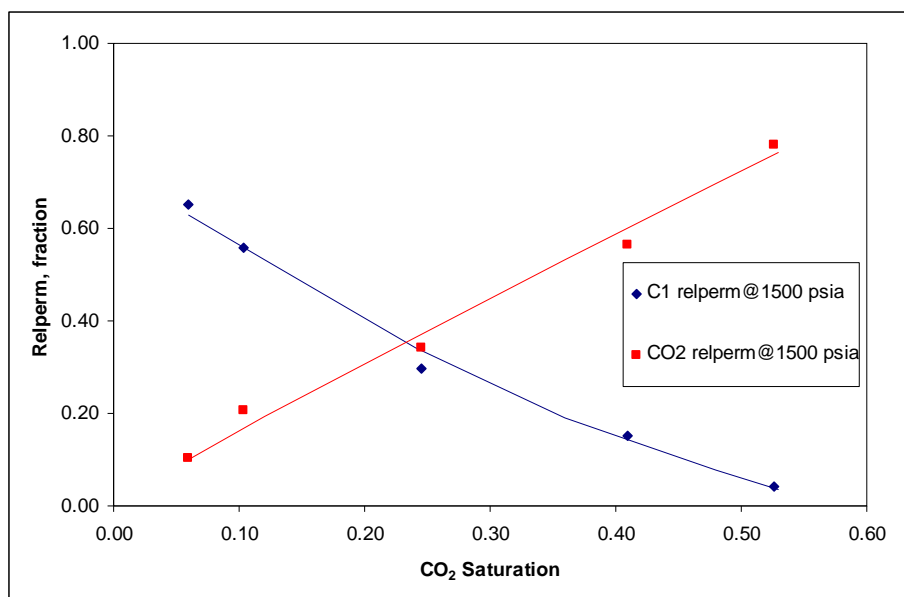


Figure 6.14: SCO_2 and methane relative permeability vs. CO_2 saturation at pore pressure 1500 psia and displacement rate of 10 cm/hr, temperature of 160 °C.

If CO_2 injection is ceased at its breakthrough, the in situ gas will gradually mix with the SCO_2 fraction that has been injected to displace natural gas through molecular diffusion. Consequently it will reduce the calorific value of the in situ gas and extra cost will be associated with separating the produced SCO_2 . Several researchers have noticed this outcome in their simulation studies (Oldenburg and Benson 2002; Clements and Wit 2002). Less natural gas was observed to be recovered if SCO_2

injection was started in the primary stage of production rather than the recovery at tertiary stage, and would normally be achieved by means of natural pressure depletion without SCO_2 injection.

6.4.1 Repeatability tests:

Several repeatability tests were conducted after the initial tests for the purpose of validating the initial results. The first was performed at a pore pressure of 3500 psia and the second was at 2500 psia. Results from the repeatability test at 3500 psia almost approximated the initial test result with minor variation in the frontal displacement. SCO_2 had advanced by only 0.03 PV from the initial breakthrough in the repeatability test.

This minor difference in SCO_2 breakthrough could be due to constantly maintaining the pore pressure via the BPR unit. Figure 6.15 shows the result of both initial and repeatability test of sample S_V_1 which were conducted at 160°C and 3500 psia. Details of the pore-pressure test and other repeatability test results can be found in the Tables D-12 to D-15 and Figure D-1 in the Appendix D.

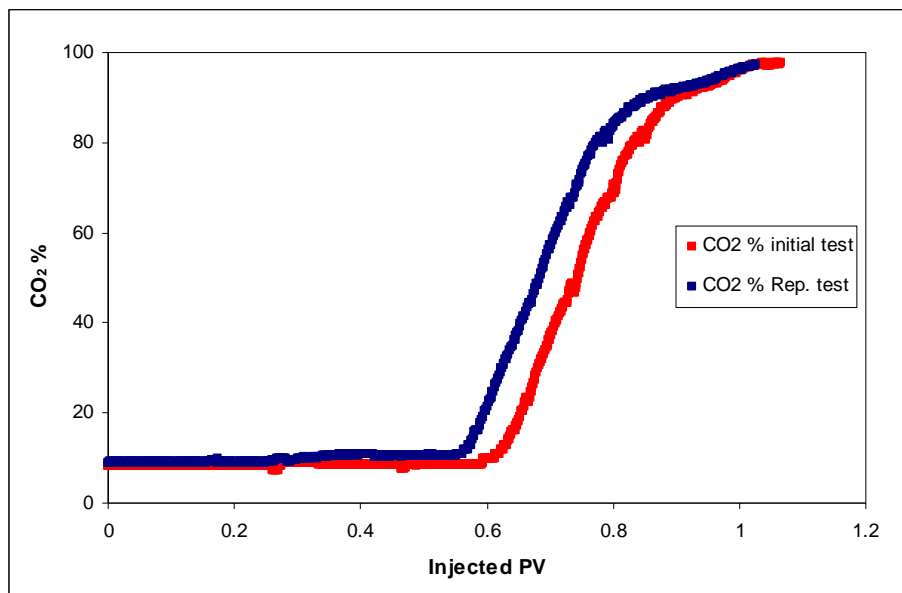


Figure 6.15: Initial and repeatability tests at 3500 psia of sample S_V_1.

6.5 Impact of permeability heterogeneity:

One of the main parameters that has been recognized and considered to adversely impact the recovery efficiency of natural gas from a CO₂-enhanced gas recovery project is permeability heterogeneity. With the aim of experimentally determining the effect of the permeability heterogeneity on recovery efficiency in a gas-gas system, a series of laboratory experiments were carried out on methane displacement by SCO₂ in various reservoir core plugs. The test conditions applied throughout the experiments were a pressure of 5900 psia and temperature of 160 °C.

Since the constant test conditions were applied on various rock qualities, results of different recoveries and gas breakthrough are definitely an indication of the effects of the permeability heterogeneity on the gas-gas displacement process in a porous medium. These data collectively can lead to investigating the impact of permeability heterogeneity on recovery efficiency and gas multiphase flow through the studied cores. Figure 6.16 shows SCO₂ breakthrough versus injected pore volumes for the core plugs that were tested in this work at the initial reservoir conditions.

The relation between absolute permeability of the cores and relative permeabilities of the phases are highlighted in Chapter 5. Clearly the shorter cores were horizontally mounted, with decreasing absolute permeabilities SCO₂ breakthrough being delayed by 15% compared to breakthrough obtained with the high quality rock (See Table 6.4). The disproportional relation between breakthrough and absolute permeability of the core can be interpreted precisely through the pore morphology of the rocks. Since the wettability of the medium can only marginally affect the propagation of the multi-gas, pore size and morphology of the medium should significantly impact the gas multiphase flow.

Table 6.4: CO₂ breakthrough and absolute permeability of the cores were examined.

Core samples	Ka	Test Condition		Displacement	Core Position	CO ₂ BT PV
		Temp.(°C)	Pres. (PSI)			
S_C_1A	391	160	5900	98% CO ₂ @90 CH ₄	Horizontal	0.49
S_C_2A	115	160	5900	98% CO ₂ @90 CH ₄	Horizontal	0.55
S_C_3A	8.7	160	5900	98% CO ₂ @90 CH ₄	Horizontal	0.64
S_V_1	92	160	5900	98% CO ₂ @90 CH ₄	Vertical	0.72

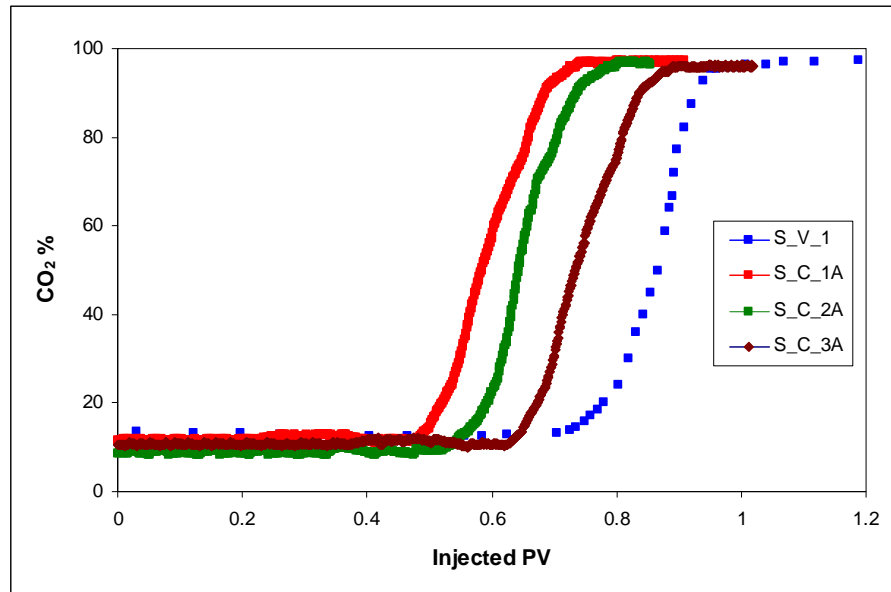


Figure 6.16: SCO₂ breakthrough versus injected pore volumes for the short and long core samples. Test condition; pore pressure 5900 psia, temperature of 160 °C and displacement rate of 10 cm/hr.

Referring to the IFT measurements, surface tension would only exist when the capillary needle was used. If in the porous medium wider pores were dominant, surface tension will approach zero, and subsequently the gas phases can mix easily. Observing late SCO₂ breakthrough with decreasing absolute permeability of the core plug suggests the fact that smaller pore sizes are widely distributed in the core.

Smaller pore size distribution in the gas-brine displacement is also concluded as greater residual brine saturation was observed with poor quality rock. This is indicated that with reducing absolute permeability of the core plugs, the smaller pore size distribution is expected to be dominant in the core plugs. Furthermore the length of the core plugs and position of the core holder crucially impacted the fluids flow in a porous medium. This can be seen through the enhanced gas recovery that was obtained with the long sample S_V_1 in comparison with the shorter cores for the same test condition.

Figure 6.17 shows relative permeability curves that were generated by using the JBN method. The solid and dashed lines represent the best fit of experimental data that were developed from the power model. However, as these tests were carried out horizontally at the constant reservoir conditions, the effect of permeability heterogeneity can be clearly noticed from the relative permeability curves.

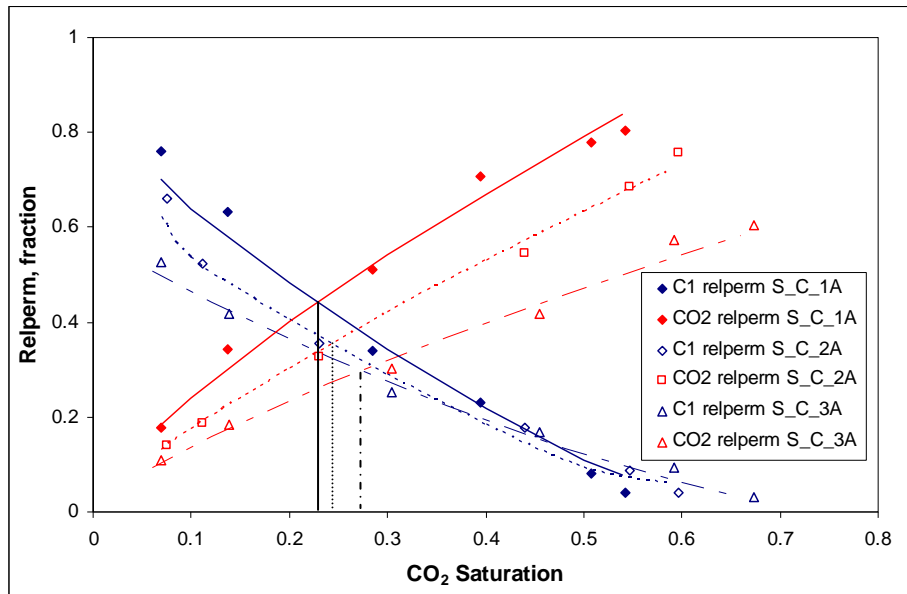


Figure 6.17: SCO_2 -methane relative permeability curves versus SCO_2 saturation for the three short core samples. Test condition; pore pressure of 5900 psia, temperature of 160 °C and displacement rate of 10 cm/hr.

With decreasing absolute permeability of the medium, from high quality rock to low quality rock, relative permeability of methane was increased by 3% of unit pore volume saturation. This enhancement only occurred due to the permeability variation of the short core plugs because other parameters of the test remained constant. The interaction of the flowing phases with the rock medium, which will affect the multiphase gas flow, will be diminished. This is because the predicted time length for mineral precipitation, such as calcite or quartz, to take place is assumed to be around 20 and 10000 years, respectively (Calabrese and Masserano 2005). The displacement experiments for the short core plugs spanned approximately 25 minutes of injecting one pore volume. As a result these outcomes will only an indication of the impact of permeability heterogeneity on SCO_2 -methane displacement.

In order to reveal the influence of injection direction and length of the core, relative permeability curves are plotted in Figure 6.18 for the long sample S_V_1 (vertically flooded) and short core S_C_3A (horizontally flooded). Although the core sample S_V_1 had almost the same absolute permeability as the intermediate core plug S_C_2A, its methane relative permeability was improved by 11% of unit saturation if compared to S_C_3A. The length and direction of the test certainly contributed to the observed outcome. All other parameters were kept constant during the tests.

The effect of gravity is considered to be greater on multi-gas flow and SCO_2 breakthrough rather than the length of the core. SCO_2 at this condition is approximately three times denser and is more viscous than methane. Therefore the expansion of frontal displacement (miscible zone) was limited by gravitational forces and later breakthrough resulted. Furthermore, to exclusively determine the impact of gravitational force, one vertical run was performed in S_C_2A. Results indicated improved recovery efficiency was achieved with the vertical test by a fraction of nearly 0.05 of pore volume of OGIP (See Tables D-4 and D-18 Appendix D).

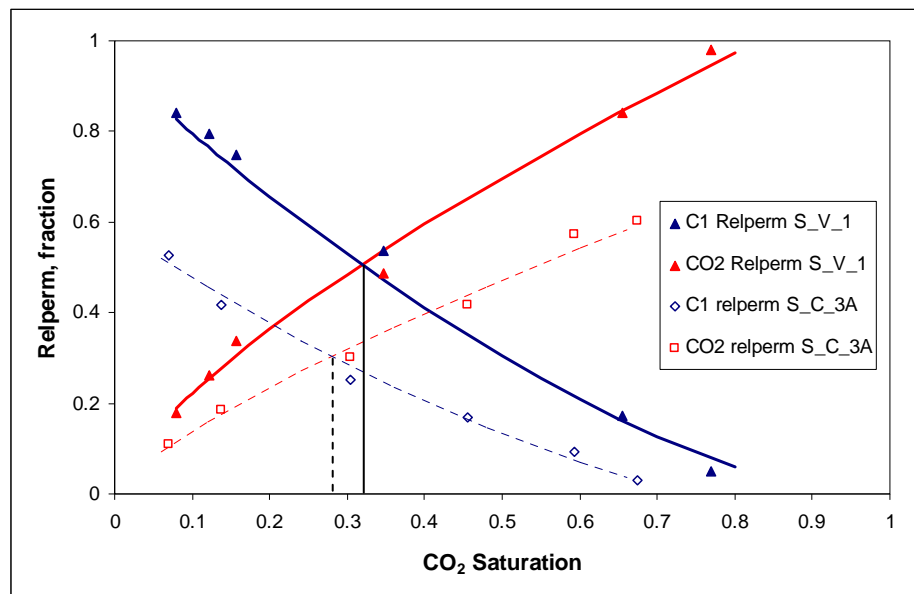
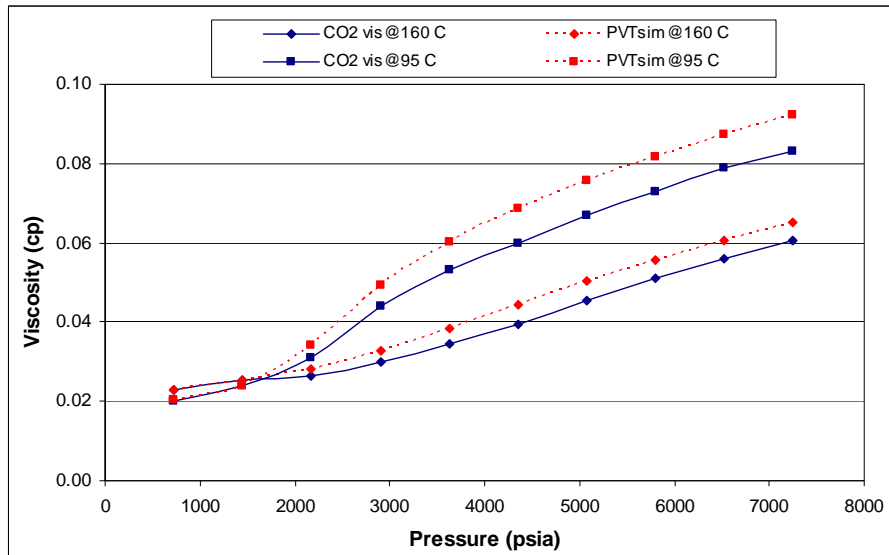


Figure 6.18: SCO_2 –methane relative permeability curves versus SCO_2 saturation for core samples S_V_1 (vertically mounted) and S_C_3A (horizontally mounted). Test condition; pore pressure of 5900 psia, temperature of 160 °C and displacement rate of 10 cm/hr.

6.6 Impact of temperature:

Temperature can affect the fractional flow of the gases by changing the physical properties of the flowing gases. However, SCO_2 viscosity reduces noticeably when temperature increases from 95 °C to 160 °C, see Figure 6.19. Methane viscosity was moderately influenced within this range of temperature variation. Briefly the objective of the tests was to discern the extent to which the temperature can influence the recovery efficiency and the gas multiphase flow in a porous medium. In addition, a further objective was to analyse its severity and compare its effect with other parameters that are described in detail in the preceding sections.



*Continuous line is experimental while dashed line is simulation.

Figure 6.19: SCO₂–viscosity versus pressure at two different temperatures.

Two high temperatures were studied in this work, namely 95 °C and 160 °C. Only the short samples underwent the displacement tests at low temperature. Results revealed the trend of the displacement fronts is noticeably affected by applying various temperatures after SCO₂ breakthrough. Although the breakthrough timing of the SCO₂ shows less sensitivity to the changes in temperature, the trend of the frontal displacement appeared to be more miscible at 95 °C when compared to the fronts that were obtained with the higher temperature. This can be seen clearly in Figure 6.20, in which the SCO₂ profile behaves differently in the short core samples when different temperatures were applied. This was not expected because temperature increase causes a reduction in viscosity and density for SCO₂ more effectively than for methane. Therefore the establishment of a greater miscible zone would have been anticipated with higher temperature rather than low temperature.

On the other hand, the trend of the SCO₂ profile at high temperature was similar to the production profile of two immiscible fluids. Moreover, residual gas saturation was increased with increasing temperature up to one pore volume of injection. A higher miscibility ratio was predicted at high temperature due to the physical properties differences between the phases being reduced. This permitted SCO₂ to disperse rapidly in the core and heterogeneity of the rocks facilitated SCO₂ to breakthrough earlier.

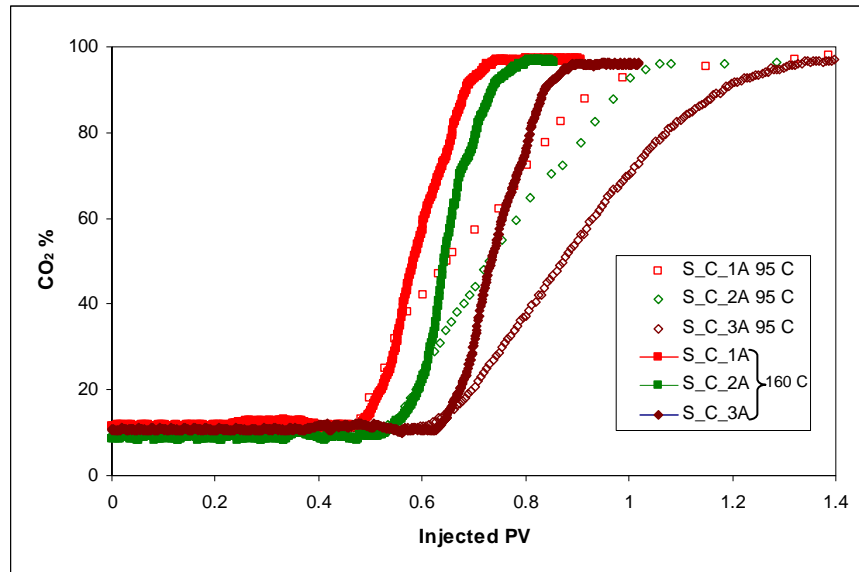


Figure 6.20: SCO_2 breakthrough versus injected pore volumes for the short core samples at two temperatures. Test condition; pore pressure of 5900 psia, temperature of 95 °C and 160 °C and displacement rate of 10 cm/hr.

Table 6.5 shows the ultimate recovery of methane at two different temperatures and up to 1.4 pore volume of injection. With continual injection, approximately all residual gas saturation can be produced as a small fraction after SCO_2 breakthrough. Since gases are considered as being the most non-wetting phase inside the porous medium, they can easily mix by dispersion and molecular diffusion mechanisms.

Table 6.5: CO_2 breakthrough and ultimate recovery at two different temperatures.

Sample	SCO_2 BT	Ultimate recovery @95 °C	Ultimate recovery @160 °C
S_C_1A	0.48	0.59	0.52
S_C_2A	0.53	0.58	0.55
S_C_3A	0.63	0.79	0.63

Figure 6.21 shows relative permeability curves at two different temperatures that were calculated by using the JBN method for the SCO_2 -methane system in core sample S_C_1A. The solid and dashed lines represent the best fit of experimental data and the data developed from the power model. Because the breakthrough timing was the same for both temperatures, the relative permeability curves for the displaced and displacing phase remained roughly alike. The differences can be noticed through the enhancement in relative permeability curves for both flowing phases at 95 °C in comparison to relative permeabilities at 160 °C. Impact of temperature is obviously

apparent on SCO_2 relative permeability rather than methane. This confirms that temperature alteration severely impacts SCO_2 physical properties more than methane. Graphs and details of other sample can be found in Tables D-16 to D18 and Figures D2 to D3 in Appendix D.

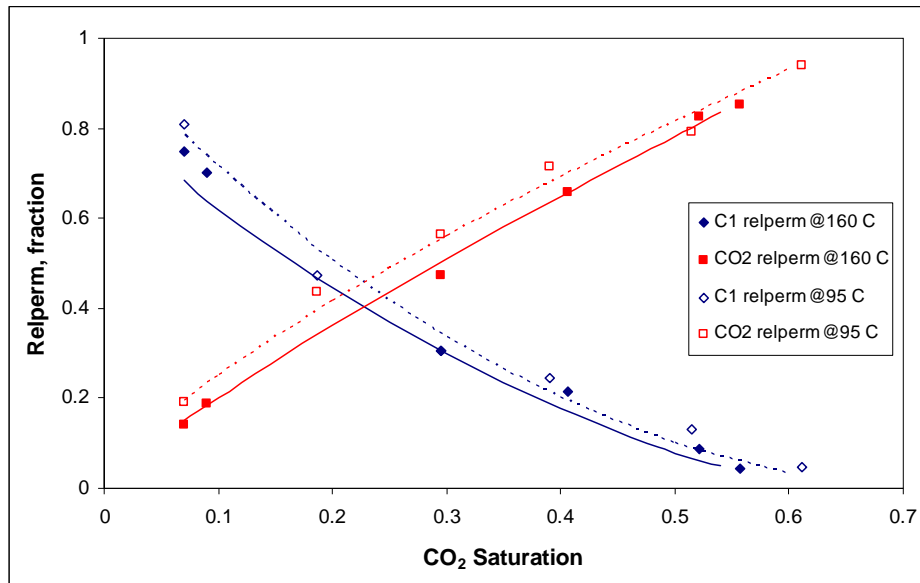


Figure 6.21: SCO_2 –methane relative permeability curves versus SCO_2 saturation for sample S_C_1A. Test condition; pore pressure of 5900 psia, temperature 95 °C and 160 °C and displacement rate 10 cm/hr.

6.6 Wider implications:

The results reported by Al-Abri, Sidiq, and Amin (2009) suggested that enhanced condensate recovery can be obtained with a decreased injection velocity, whereas poor recovery was observed for methane with a decreased displacement rate. The residual saturation in both cases always exists following measured miscible SCO_2 injection. This un-displaced condensate and natural gas that is left behind in the given volumes of examined rocks is analogous to the microscopic residual hydrocarbons left after water-flooding.

In addition, the residual phases possibly decrease the SCO_2 injectivity below the rate that would be anticipated for complete displacement away from the injection well. The amount of residual saturation depends on the dispersivity of dead-end pores and low permeability occlusions. More explicitly, due to the heterogeneity of the medium, and/or hydrocarbons phase separation, all the pores cannot be flushed. As a result of mixing with SCO_2 a multiphase region displacement is anticipated.

6.6 Evaluation of experimental measurements:

Relative permeability data can play a key role in the design, optimization and execution of CSEGR projects through the understanding of fluid mobility, fractional flows, and breakthrough and ultimate recovery. This provides insights into how crucial the accuracy of the laboratory measurements to reproduce the production profile. This major issue was given due attention to ensure that the precision of the relative permeability measurements were good enough to match historical data when applied to full field applications.

The aim was to investigate the parameters in detail so as to provide a clear vision of the feasibility carbon sequestration enhanced gas recovery (CSEGR) project in all aspects. The relative permeability curves that were obtained by applying different test conditions can be scaled up for field purposes.

6.7 Discussion:

The impacts of different parameters on SCO_2 -methane relative permeabilities have been accurately determined in a reservoir porous medium. Relative permeability of the injected phase, being SCO_2 , is identified to vary proportionally to changes in impurity of the displaced phase while inversely varying with injection speed, pressure, and permeability heterogeneity of the media.

The influences of injection speed and in situ gas composition on multiphase gas flow are obvious if compared to the impact of the other parameters on gas-gas relative permeability. Methane relative permeability was observed to have been considerably affected when the displacement speed rate decreased from 10 cm/hr to 1.0 cm/hr. Almost 80% of its relative permeability decreased as a result of speed alteration. In addition when the SCO_2 -contamination of the in situ gas reached 75%, methane relative permeability was reduced noticeably by a factor of 67%. In contrast the severity of other parameters on gas-gas relative permeability was seen to be moderate in comparison to injection speed and composition impacts. With changes in pore pressure of about 40%, permeability heterogeneity of about 16%, and temperature of about 6% methane relative permeability was decreased.

The explicit methods were used in generating relative permeabilities for gas-gas system. It was found that the JBN method can be applied and used to re-produce gas-gas relative permeability curves. Furthermore, a power model was developed from the best match of the experimental data. The values of the variables a , b , and c from Eq.6.2 and Eq.6.3 that were used in generating the power model for the best fit with experimental data are shown in Table 6.6. The values of a , b and c variables range between (0.78-2.9), (0.35-0.93) and (0.8-7), respectively. For the first time a power model for gas-gas relative permeability has been developed, as given in this work. This model can be easily employed in a simulation program.

Table 6.6: The value of a , b and c variables that were used in Eq 1 and 2.

S.N.	Displacement	Pressure psia	Temperature C	Injection speed cm/hr	Core plugs	a	b	c
1	SCO ₂ @ 90 C ₁	5900	160	10	S_V_1	1.14	0.71	0.75
2	SCO ₂ @ 75 C ₁	5900	160	10	S_V_1	1.47	0.62	1.5
3	SCO ₂ @ 50 C ₁	5900	160	10	S_V_1	1.88	0.51	2.3
4	SCO ₂ @ 25 C ₁	5900	160	10	S_V_1	1.84	0.35	7
5	SCO ₂ @ 90 C ₁	5900	160	7	S_V_1	1.41	0.84	1.1
6	SCO ₂ @ 90 C ₁	5900	160	5	S_V_1	1.6	0.93	1.2
7	SCO ₂ @ 90 C ₁	5900	160	2	S_V_1	1.99	0.89	1.4
8	SCO ₂ @ 90 C ₁	5900	160	1	S_V_1	2.9	0.9	1.5
9	SCO ₂ @ 90 C ₁	4500	160	10	S_V_1	1.14	0.9	0.9
10	SCO ₂ @ 90 C ₁	3500	160	10	S_V_1	1.2	0.87	1.1
11	SCO ₂ @ 90 C ₁	2500	160	10	S_V_1	1.2	0.87	1.1
12	SCO ₂ @ 90 C ₁	1500	160	10	S_V_1	1.38	0.93	1.1
13	SCO ₂ @ 90 C ₁	5900	160	10	S_C_1A	1.32	0.74	1.0
14	SCO ₂ @ 90 C ₁	5900	160	10	S_C_2A	1.1	0.8	0.9
15	SCO ₂ @ 90 C ₁	5900	160	10	S_C_3A	0.8	0.75	0.95
17	SCO ₂ @ 90 C ₁	5900	95	10	S_C_1A	1.35	0.73	1.7
18	SCO ₂ @ 90 C ₁	5900	95	10	S_C_2A	1.17	0.66	1.2
19	SCO ₂ @ 90 C ₁	5900	95	10	S_C_3A	0.78	0.57	1.1

Chapter 7

Dispersion and diffusion mechanisms

7.1 Introduction:

A straightforward method is developed for calculating the average dispersion coefficient of supercritical carbon dioxide (SCO₂) displacing methane in a linear porous reservoir. The dispersivity of SCO₂ was identified to be a function of injection pressure, in situ gas composition and injection rate. It was found that the average dispersion coefficient of SCO₂ changes proportionally with changes in purity of the displaced phase and injection rate (from 1 to 5 cm/hr) while inversely changing with injected pressure and injection rate from 5 to 10 cm/hr.

This method was developed from the results of the unsteady state displacement laboratory experiments. Results of the three main parameters, namely displacement speed, pore pressure and composition, were used in the development of the new method.

7.2 Review of gas displacement in porous media:

The feasibility CO₂ sequestration in reservoirs has been widely studied for the purpose of greenhouse gas emission reduction, rather than for improving gas recovery. Relatively few studies have focused on the mechanisms of SCO₂ enhanced gas recovery (Oldenburg, Pruess, and Benson 2001; Oldenburg 2003; Seo 2004). The main mechanisms considered to influence the efficiency of methane recovery at pore scale are dispersion and molecular diffusion. However, in such a displacement process, recovery of methane depends on the stability of the miscible zone, where there is the possibility of the loss of this zone by dispersion and molecular diffusion. Experimental studies have demonstrated that dispersion and diffusion processes are the same for supercritical fluids as for normal gases and liquids (Wei and Sadus 1996). Nevertheless limited mixing for methane displaced by SCO₂ in carbonate rock cores was demonstrated by experiments conducted by Mamora and Seo (2002)

As it is known from displacement tests, a gas-gas interface can form a zone of miscibility, with the rock porous medium having the same affinity for both phases. Consequently, relative permeability would not influence the recovery of the

displaced phase. But in the case of SCO_2 , which undergoes a large change in density in the gas phase as it passes through the critical pressure at temperatures near the critical temperature, a thermodynamic stable interface is anticipated. For the first time, the surface tension has been successfully measured between SCO_2 and methane, as reported and documented by Amin et al. (2010). The stability of the interface was time dependent and concluded to be a function of the injection rate, composition, gas-physical properties and needle diameter (See Figure 7.1). This finding is crucial to further understanding the interaction occurring while both phases are in contact in a porous media.



Figure 7. 1: Interface between SCO_2 and methane. The bubble is SCO_2 and the ambient is methane at 3000 psia and 95 °C.

If pore media is considered as a series of small chambers having different diameters connected together, as shown in Figure 7.2, gas mixing can be explained through the conclusions made from IFT measurements. For instance, at point ‘A’ where the diameter of the chamber is small enough to allow a SCO_2 -methane interface to be formed, mixing of the gases will slow down due to the surface tension. But at point ‘B’ which has a greater diameter than ‘A’, gas mixing will be accelerated and the miscible fluid expands instantaneously. Because the interface that is formed at point ‘B’ is considerably weaker, mixing by molecular diffusion will be sped up as there is not any obstruction to molecular dispersion from either phase to mix and equilibrate the composition.

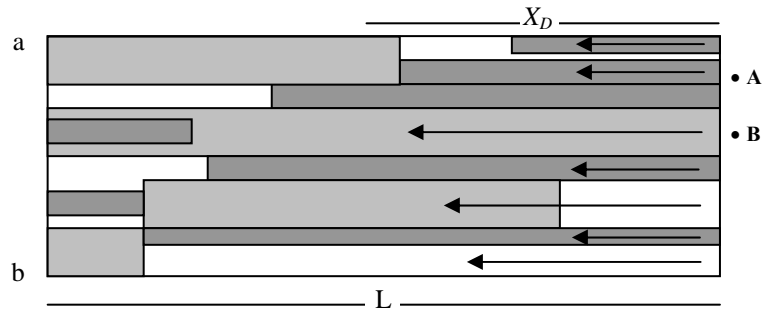


Figure 7. 2: Schematic illustration on SCO_2 dispersion while displacing methane. At point A, diameter of the chamber is small enough to form an interface, at point B the chamber has a bigger diameter therefore a weak or no interface can form.

Even the more stable interface at point ‘A’ vanishes with passing time because of the phase equilibration. This phenomenon can be seen clearly in Figure 7.1 through the cloud that surrounded the interface. This was interpreted to have been formed by molecular diffusion. Consequently, at low rates of displacement, which need longer times to displace in situ gas, recovery efficiency reduces. In contrast, many researchers argued that low flow rate test results improved recovery efficiency if a fluid immiscibly displaces another fluid. Therefore, the recovery of natural gas by SCO_2 injection will be governed not only by the miscibility zone. This is because the presence of an interface brings in the effects of gas-gas relative permeability and phase saturation.

This Chapter mainly focuses on the dispersion rate of SCO_2 from displacement tests conducted under various conditions. Pressures from 1500 psia to 5900 psia, composition from 0.1-0.75 mole percent of SCO_2 in the in situ gas, and injection rates (velocities) from 1-10 cm/hr (0.0166-0.166 cm/min) were investigated. Different test conditions (pressure and temperature) and injection rates were implemented in order to evaluate the impact of the intrinsic behaviour of SCO_2 at supercritical conditions on the dispersion coefficient (See Figure 7.3). Eventually, a straightforward model for calculating the dispersion coefficient at SCO_2 breakthrough was developed from the tests conducted on a consolidated core plug S_V_1.

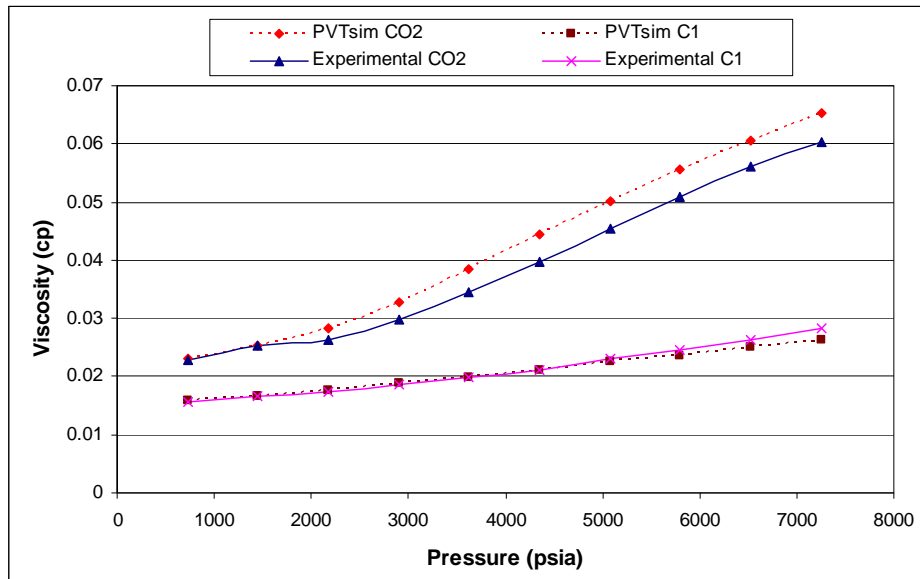


Figure 7. 3: Experimental and simulated viscosities of SCO_2 and methane at 160°C and 725 psia to 7250 psia.

7.3 Theory of dispersion:

The mixing of two miscible fluids in porous media in terms of dispersion and diffusion by the gas storage industry has been a subject of intense studies (Aronofsky and Heller 1957; Deans 1963; Donaldson, Kendall, and Manning 1976; Newberg 1988). As SCO_2 is injected to displace methane in a linear porous medium, initially both phases are separated by a sharp interface. With the passage of time, if the displacement becomes stable and dissipation of miscible fluid does not occur, the sharp interface will gradually diffuse into a mixed grade zone ranging from one pure fluid to the other. The resulting miscible zone is due to random motion of molecules in both phases. If the diffusion can not change the volume of the miscible fluids, the transport of the molecules in any arbitrary plane is often represented by the Fick diffusion equation (Collins 1963) as discussed in Chapter 2.

The dispersion coefficient that is calculated by the Fick diffusion equation is a function of concentration. Therefore the dispersion coefficient changes because the concentration of the injected phase continuously changes with time, due to miscibility. Using various dispersion coefficient values to reproduce effluent profiles mathematically is quite a complicated process. Perkins and Johnston (1963) suggested that a simplifying calculation can be made by determining a single value for the dispersion coefficient, the effective average diffusion coefficient. Hence the

dispersion coefficient is rendered constant and independent of concentration, and in this way effluent profiles can be generated mathematically with ease.

Furthermore, a well determined boundary is required to retrace the displaced composition profile by using the Fick diffusion equation, and to reasonably match an experimental effluent profile. Most of the developed mathematical models that have been derived to represent a profile of the displaced fluid composition have used error functions. Some researchers, such as Coats and Smith (1964) and Baker (1977) have noticed end an effect (capacitance impact), particularly from experiments conducted on consolidated cores. Simply applying the Fick diffusion equation may produce an asymmetrical composition profile, which means more fluid is produced than was originally in place. This error was seen to be a result of poor selection of the boundary limit. There they suggested a derivative capacitance model to solve the asymmetrically produced profile.

The Fick diffusion equation has been used for calculating diffusion coefficients of SCO_2 while displacing methane in carbonate rock at various conditions of temperature and pressure (Mamora and Seo 2002; Seo 2004). According to several researchers this equation is applicable only when both phases have the same density and viscosity, and are completely miscible and incompressible (Aronofaky and Heller 1957; Collins 1963).

It is apparent from the viscosity differences (See Figure 7.1) and the confirmed interface, this equation would not accurately predict dispersion between supercritical SCO_2 and methane. For that reason, a method is presented to calculate the dispersion coefficient directly from displacement tests.

7.4 New Model:

Assume SCO_2 is injected at a constant flow rate of 1 cc/min to displace methane in a porous medium that has the following specifications: pore volume 10 cm^3 , area 5 cm^2 and length 5 cm (See Figure 7.2). If molecular diffusion is neglected the SCO_2 will reach breakthrough at a time when the methane is completely displaced, at approximately 10 minutes. Thus the assumed displaced distance from the inlet of the core can be calculated by using Eq.7.1.

$$X_D = t_b * u \quad (7.1)$$

And

$$u = \frac{Q}{A * \phi} \quad (7.2)$$

Where:

X_D displaced distance from the inlet of the core in case no diffusion assumed,

t_b time to breakthrough, min.

u interstitial velocity, cm/min.

Q flow rate, cm³/min.

ϕ porosity, volume fraction.

A cross sectional area, cm²

However the rest of the distance through the core after X_D will be passed by molecular diffusion, so if the outlet plane (a-b in Figure 7.2) is moved to the X_D location, the dispersion coefficient (dispersion from injection rate and molecular diffusion) of SCO₂ across X_D can be expressed in Eq.7.3.

$$K_{it} = \frac{Q}{X_D * \phi} \quad (7.3)$$

To calculate the dispersion that resulted from the injection rate through the entire length of the core Eq.7.3 can be rewritten as follows:

$$K_{ir} = \frac{Q}{L * \phi} \quad (7.4)$$

Where:

K_{it} total SCO₂ dispersion coefficient, cm²/min.

K_{ir} dispersion coefficient caused by injection rate, cm²/min.

L sample length, cm.

Hence dispersivity of SCO₂ in the direction of gross fluid movement (parallel to flux direction) will be a function of dispersion resulting from the injection rate and molecular diffusion.

$$K_i = K_{ir} - K_{ir} \quad (7.5)$$

Where:

K_i average dispersion coefficient caused by molecular diffusion, cm^2/min .

It is of great importance to analyse the value of K_i that is calculated by Eq.7.5. Obviously the equation yields the length that is displaced by molecular diffusion, after X_D , to outlet of the core (See Figure 7.2). To calculate the length that is passed by molecular diffusion, the incremental flow rate that is produced as a result of molecular diffusion through the entire core can be calculated by Eq.7.6.

$$Q' = K_i * L * \phi \quad (7.6)$$

To reproduce the displaced length after X_D and correlate it to a difference between $L - X_D$, Eq.7.7 is used. The length that was calculated is found to match exactly the value calculated from the difference between L and X_D .

$$L = \frac{Q'}{A * \phi} * t_b \quad (7.7)$$

The value of dispersivity of SCO_2 calculated using Eq.7.1 to Eq.7.5 is a single value and independent of concentration. Moreover, the total length of the core can be attained with K_i and the dispersion from the injection rate.

7.5 Results and discussion:

Eq.7.1 to Eq.7.5 have been applied for calculating average dispersion of SCO_2 at breakthrough from the series of tests conducted on core plug S_V_1. While SCO_2 is displacing methane, the fraction of gas adjacent to the main convective flux has its calorific value reduced with time by dispersion and molecular diffusion. Therefore, SCO_2 was expected to accelerate through the contaminated fraction of gas, and the greater dispersion of SCO_2 would correspond to greater contamination of the in situ gas and thus early breakthrough.

Figure 7.4 shows SCO_2 dispersivity (solid line) versus in situ gas composition. The SCO_2 dispersion coefficient is clearly higher for increased concentrations of SCO_2 in

the in situ gas. This is because the viscosity and density of the displaced phase at a higher SCO₂ content will be nearly the same as that of the displacing phase. Therefore mixing has been hastened and corresponds to a higher dispersion coefficient.

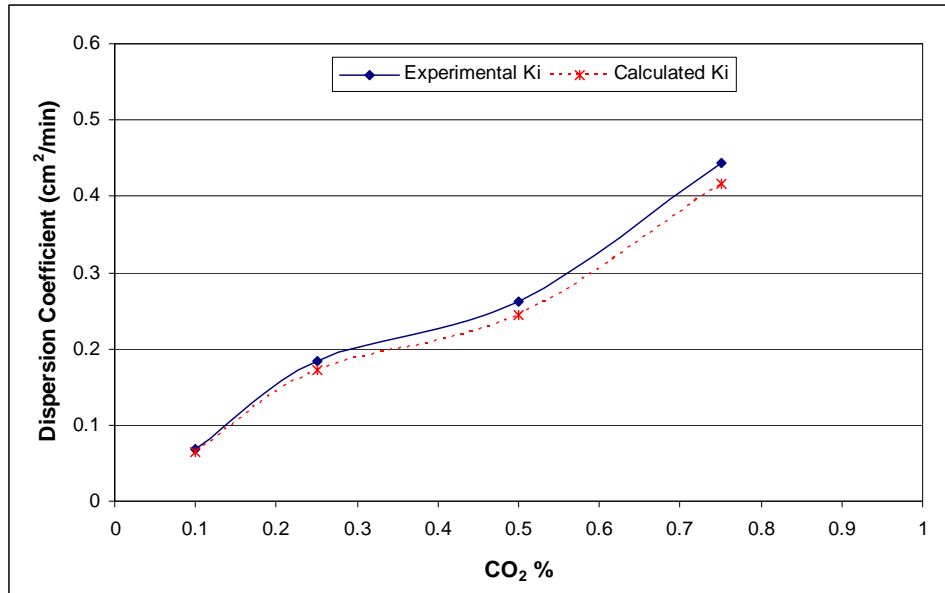


Figure 7. 4: Dispersion coefficient of SCO₂ as a function of CO₂ percentage. Solid line experimental (Eq.7.1 to 7.5) and dashed line calculated (Eq.7.8 to 7.12)

Dispersivity of SCO₂ can be considered as a function of in situ gas composition as it changes proportionally with the amount of SCO₂ contained in the displaced phase. The dispersion coefficient expressed mathematically is a function of in situ gas composition and can be represented through a polynomial line of best fit, as shown in Eq.7.8.

$$f(K_i)_c = 3.0118 C^3 - 3.6861 C^2 + 1.7587 C - 0.0728 \quad (7.8)$$

Where:

C SCO₂ mole fraction concentration in the in situ gas.

Figure 7.5 shows the dispersion coefficient of SCO₂ plotted against the injected pore pressure (solid line). Evidently, with increasing pore pressure SCO₂ dispersivity gradually decreases. This behaviour is consistent with SCO₂ physical properties as the difference in viscosity and density in comparison to methane is doubled or tripled when pressure is increased from 725 psia to 7250 psia at 160 °C (See Figure 7.3)

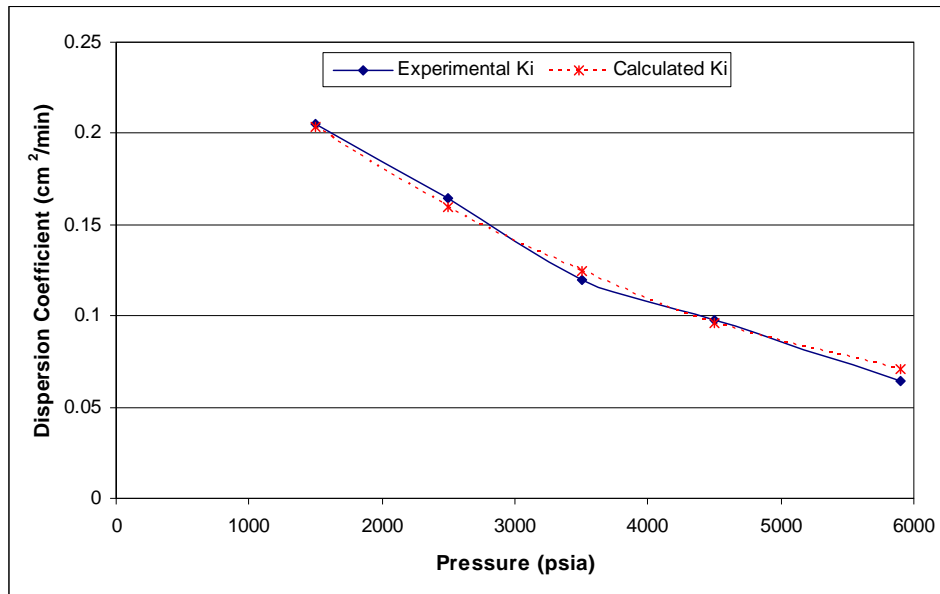


Figure 7. 5: Dispersion coefficient of SCO_2 as a function of injected pressure. Solid line experimental (Eq.7.1 to 7.5) and dashed line calculated (Eq.7.8 to 7.12).

The dispersion of SCO_2 can be seen as a function of pore pressure and it inversely changes with change in pressure. The best fit to the experimental data was through polynomial representation, which is displayed in Eq.7.9.

$$f(K_i)_p = 4*10^{-9} P^2 - 6*10^{-5} P + 0.2862 \quad (7.9)$$

Where:

P is pore pressure, psia.

Figure 7.6 displays K_i versus injection rate. Dispersivity of SCO_2 can be seen to be more sensitive to the injection rate (velocity) if compared to the trend of K_i from the previous tests, which were either proportional or inversely proportional. The K_i obtained from the rate tests has two trends, initially K_i is proportional to the rate increase from 1 cm/hr (0.0166 cm/min) to 5 cm/hr (0.083 cm/min), and second, it decreases at an increasing rate from 5 cm/hr to 10 cm/hr (0.166 cm/min). This means that at high rates the time required for mixing by diffusion was too short and thus higher recovery was achieved.

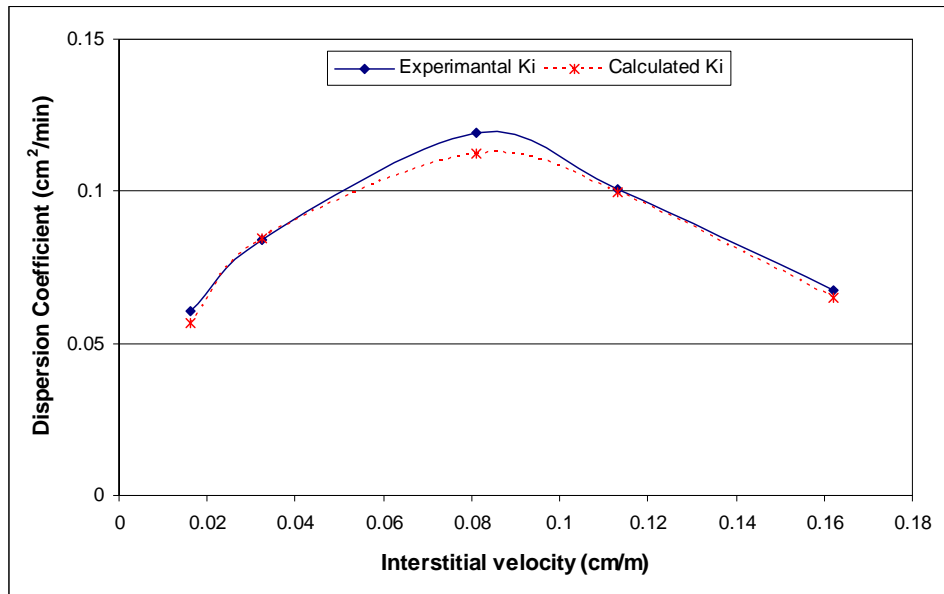


Figure 7. 6: Dispersion coefficient of SCO_2 as a function of injection rate. Solid line experimental (Eq.7.1 to 7.5) and dashed line calculated (Eq.7.8 to 7.12)

However, the dispersion coefficient at the lower rate (1 cm/hr) is almost the same as for the higher rate (10 cm/hr). Early breakthrough can be explained through the time associated with the displacement tests. For the lower rate the time required to put through 1 PV was about 10 times greater than the time needed at the higher rate. This means sufficient time was available for molecular diffusion at the lower rate test. Early breakthrough with a lower rate can be explained as dissipation of the miscible fluid may have been occurred because of rock heterogeneity and immiscibility of SCO_2 and methane. Therefore SCO_2 could disperse significantly in the direction of the main convective flux and resulting in earlier breakthrough.

The best fit to the experimental data (Figure 7.6) was through polynomial representation represented by Eq.7.10.

$$f(K_i)_{I_r} = 63.182I_r^3 - 26.565I_r^2 + 2.9513I_r + 0.0174 \quad (7.10)$$

Where:

I_r injection rate, cm/min.

In summary, the average dispersion coefficient of SCO_2 was found to change proportionally with injection rates (from 1 to 5 cm/hr) and the ratio of SCO_2 content in the composition of the in situ gas, while it is changed inversely with pore pressure

and rates from 5 to 10cm/hr. Therefore dispersivity of SCO₂ in sandstone core plugs can be represented in terms of pressure, composition, and injection rate, as shown in Eq.7.11.

$$K_i = \frac{f(K_i)_{Ir} * f(K_i)_c}{f(K_i)_p} \quad (7.11)$$

The dispersion coefficients calculated from Eq.7.11 are plotted as a dashed line in Figures 7.4 to 7.6. Best agreement was obtained between K_i , calculated by using Eq.7.11, and K_i obtained from experimental data using Eq.7.1 to 7.5 (solid line). Accordingly, dispersion of SCO₂ can be seen as a function of pressure, composition and injection rate.

For instance when values of K_i were generated for composition tests from Eq.7.11, both the values of $f(K_i)_{Ir}$ and $f(K_i)_p$ were constant because the tests were carried out at a constant injection rate and pore-pressure, only composition was changed. In the same way values of K_i were calculated from Eq.7.11 for injection speed where only $f(K_i)_{Ir}$ was changing. Since $f(K_i)_p$ inversely changes with K_i , the direct calculation of K_i from Eq.7.11 which only $f(K_i)_p$ changes would not produce comparable values to the K_i that were calculated from Eqs.7.1 to 7.5. A correction factor is required to produce comparable K_i values to those calculated by Eq.7.11. This was achieved through multiplying by a constant, as given in Eq.7.12.

$$K_i = \frac{1}{K_{ip(Eq-13)}} * 4.6^{-3} \quad (7.12)$$

By applying Eq.7.8 to Eq.7.12, the effective average dispersion coefficient of SCO₂ can be calculated for the entire range of pressure, composition and injection rates within the tests limit. These equations can be easily used in the simulation of enhanced gas recovery by SCO₂. For example, as SCO₂ is injected to displace natural gas at field scale conditions. Initially its injection rate near the injector well will be the same as the injection source, thereafter at a distance away from the injector, the rate (velocity) will reduce due to friction. Thus SCO₂ dispersion is accelerated by molecular diffusion and composition equilibration as time passes.

On the other hand, re-injecting SCO_2 causes a pore-pressure increase which leads to reduced SCO_2 dispersion. However, the dispersion is increased by molecular diffusion and in situ gas contamination. Therefore these equations can be used to represent the dispersion coefficient of SCO_2 while displacing methane in a sandstone reservoir at a constant temperature

7.6 Discussion:

This study has shown that the dispersion coefficient of SCO_2 can be empirically determined as a function of injected pressure, in situ gas composition and injection rate. Dispersivity of SCO_2 changes proportionally with changes in purity of the displaced phase and injection velocity (from 1 to 5 cm/hr) while inversely changing with injected pressure and injection rate from 5 to 10 cm/hr. SCO_2 injection rate (velocity), in situ gas composition and pore pressure were greatly affected by the displacement efficiency and the amounts of SCO_2 that can be sequestered.

The methane recovery factor at SCO_2 breakthrough for the various test conditions that were carried out has confirmed that the optimum recovery factor would be obtained at a pore pressure of 5900 psia and injection rate of 10 cm/hr (0.166 cm/min).

Chapter 8

Steady state tests

8.1 Introduction:

The objective of two phase flow relative permeability tests was to determine SCO_2 permeability relative to methane due to its intrinsic gas properties, dissolution and potential mobilization of formation water, miscibility with methane, or reactions with the rock mineral.

The steady state tests were performed by simultaneously injecting both SCO_2 and methane phases at a certain percentage and at a constant flow velocity of 10 cm/hr, pressure 5900 psia and temperature 160 °C. Results indicated that with decreasing absolute permeability, relative permeability of methane was improved in comparison to SCO_2 . All core plugs, which were subjected to unsteady state tests, were utilized for the steady state experiments.

8.2 Experimental procedure:

The procedure for the tests was conducted as; initially the core was saturated with methane and then SCO_2 was slowly added into the core up to the desired percentage. Each phase was injected through a dedicated port and at the inlet of the core plugs SCO_2 and methane were mixed. The percentages investigated were 10, 20, 50 and 75% of SCO_2 content in the flowing stream. At steady state conditions, the pressure drop across the core and SCO_2 percentage at the outlet was monitored constantly. In most of the test cases, for a certain percentage, relative permeability of SCO_2 to methane was calculated after approximately 10 pore-volumes of injection. This procedure was repeated at subsequent incremental percentages, measuring relative permeability of SCO_2 relative to methane. Eventually after about one week of continuous experiments, four points of steady state relative permeability were calculated for one core sample.

For the bounding points of the steady state curves, end point relative permeabilities were used. These points were achieved from the unsteady state displacement tests where 90% methane was displaced by 98% SCO_2 at reservoir condition of 160 °C, 5900 psia and flow velocity (10 cm/hr). End point relative permeability of SCO_2 was

measured once the outlet composition was normalized at around 98% of CO₂ concentration in the effluent stream, as well as when the stable pressure difference was reached across the core samples. Table 8.1 shows end point relative permeability measurement of supercritical SCO₂ for the core samples that were investigated.

Table 8.1: End point relative permeability from displacement tests.

Sample no.	Test Condition		Displacement	Kg CO ₂ End point Relperm (md)
	Temp. (°C)	Pressure (psia)		
S_C_1A	160	5900	98% CO ₂ @90 CH ₄	97.4
S_C_2A	160	5900	98% CO ₂ @90 CH ₄	67.4
S_C_3A	160	5900	98% CO ₂ @90 CH ₄	32.9
S_V_1	160	5900	98% CO ₂ @90 CH ₄	270

Steady state was achieved with difficulty for each subsequent percentage, even though both flowing phases were gaseous. The precision micro-needle valves were used to control flow rate (flow coefficient of 0.004 at 15000 psia). Generally steady state had been reached after injecting 3 pore volumes, in some cases up to 8 pore volumes or more were required to be injected to obtain steady state.

The SCO₂ end point permeability of sample S_C_1A, S_C_2A and S_C_3A were greater than their methane permeability at S_{wi} . This increase in permeability could be due to the stripping of connate water even though the S_{wi} asset at the end of the experiment showed 10% change. Another factor that might have contributed is the effect of the rock heterogeneity which caused the SCO₂ to channel through the rock to the outlet (See Table 8.1). Further investigation of the time dependant nature of the permeability change is essential. Details of relative permeability calculations for all samples are provided in Appendix C.

8.3 Steady state relative permeability:

8.3.1 Sample S_V_1:

Figure 8.1 shows pressure drop versus injected pore volume for the flowing phases through sample S_V_1. The effluent was composed of about 22% SCO_2 with 78%, after injecting 5 pore volumes. Steady state relative permeability was calculated for this percentage when the composition and pressure drop was stabilized after injecting 5 pore volumes. For example, only one point of relative permeability can be generated from this steady state experiment when the saturation of CO_2 reached approximately 20% in the core plug (See Figure 8.2). Details of other percentages tests data can be found in Figures E-1 to E3 in Appendix E.

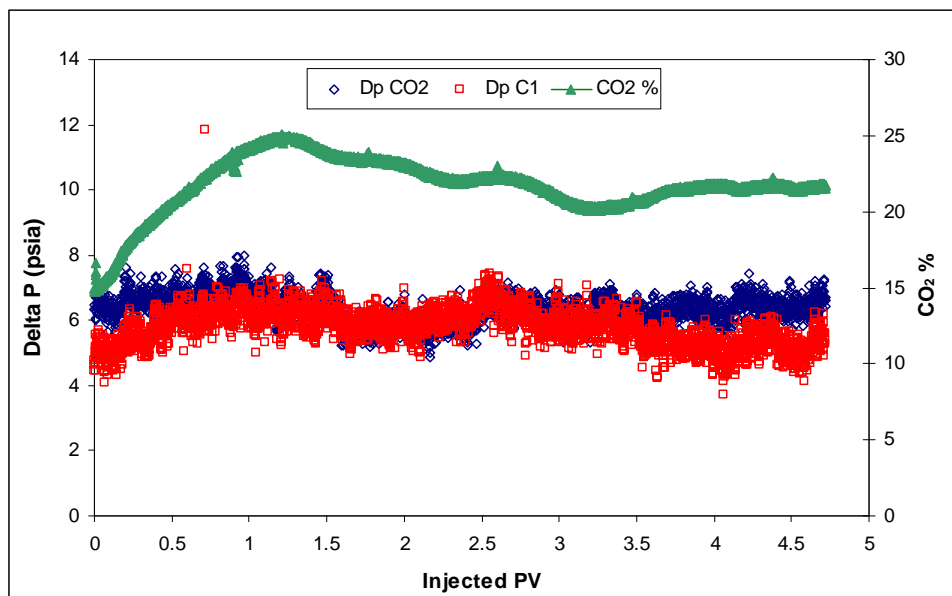


Figure 8.1: Pressure drop versus injected pore volume from the simultaneous injection of SCO_2 -methane through S_V_1 at 160°C , 5900 psia and 10 cm/hr. SCO_2 concentration 20%.

Figure 8.2 shows relative permeability curves for sample S_V_1 that are produced from the steady state experiments. When the saturation of SCO_2 in the core was increased to 50% its relative permeability increased dramatically. This indicated total miscibility had been reached. Such change can cause the formation of new flow pathways for each phase. This hypothesis is supported by the fact that the pathways may not have been accessible initially because of trapped methane.

This result confirms the unsteady state displacements in which SCO_2 breakthrough appears after 0.6-0.7 PV of methane was recovered. Nevertheless the difference is small. Still it is an indication that recovery by re-pressurization is much faster than miscibility by molecular diffusion.

Relative permeability is a multiplier (between 0 and 1) of intrinsic permeability which describes the relative ease of flow of two competing fluids, such as CO_2 and methane, through a porous medium. In this case the relative permeability of SCO_2 and methane can only be proportional with the saturation in the rock pores. Because both fluids are injected simultaneously, the partial mixing of SCO_2 and methane at the core inlet is almost certain, once a stable flow is attained. Mixing will start to take place and continue over a longer time scale (10 PV) by molecular diffusion. However, diffusive mixing of SCO_2 and methane can give rise to compositional gradients that can induce some saturation distribution variation of an individual flow path.

Understanding this coupled response of diffusion and flow to concentration gradients is important for predicting mixing times in stratified gas reservoirs that are used for SCO_2 sequestration.

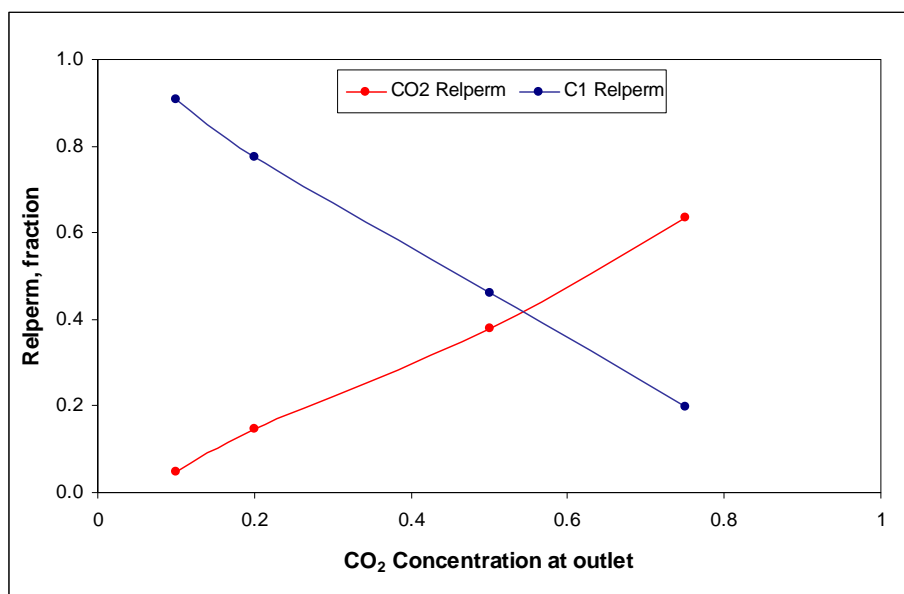


Figure 8.2: Steady state relative permeability of sample S_V_1.

As CO₂ concentration is increased to become 75% (methane comprised 25%) of the effluent gas, the relative permeability of CO₂ was enhanced noticeably. Accordingly methane recovery would not be expected to be greater than 0.7 PV of the original gas in the sample S_V_1.

Figure 8.3 shows relative permeability of sample S_V_1 from both steady state and unsteady state techniques. The relative permeability curves derived from both methods are significantly different. The greater relative permeability for methane was obtained with steady state methane rather than unsteady state, whereas for the SCO₂ phase the reverse conditions applied. This behaviour is a result of continuously injecting both phases at constant ratio for several pore volumes in case of steady state. This means both phases that were flowing through the sample have mixed at the inlet of the core. With steady state tests, the more viscous and denser phase will result in greater pressure drop across the core. Subsequently, poor relative permeability will be obtained. This is why SCO₂ has demonstrated lower relative permeability in steady state tests. Enhanced relative permeability with methane in steady state is an indication of the fact that methane's molecules had a greater momentum with continuous injection at a constant ratio. Hence SCO₂ cannot obscure methane fractional flow, and relative permeability of the medium will depend mainly on the measured pressure drop.

In the case of unsteady state tests, SCO₂ was injected to displace the methane. This resulted in the injected phase having a greater momentum than the residue gas. Therefore dissipation of the miscible zone occurred by molecular diffusion and heterogeneity. Thus the flowing fraction of the in situ gas was nearly disconnected in the pores at SCO₂ breakthrough, and the residual in situ gas saturation was produced gradually as a small fraction in the flowing SCO₂ phase. This resulted in the SCO₂ saturation of the majority of the pores.

In contrast, unsteady state SCO₂ has a greater momentum than the residue methane and therefore its relative permeability has advanced methane at its lower saturation. Details of the data can be found in Table E-1 in Appendix E.

Simultaneous flow of gases in pores media at field scale cannot be accomplished since the injected phase and displaced phase are nearly immiscible at the extreme reservoir conditions. Miscibility will increase with the time due to molecular diffusion, which results in a flowing phase representing a compositional gradient. With continual injection, each phase was barely able to form a different flow path through the medium. Accordingly, the displacement relative permeability represents the gas multiphase flow in porous media rather than simultaneous phase flow.

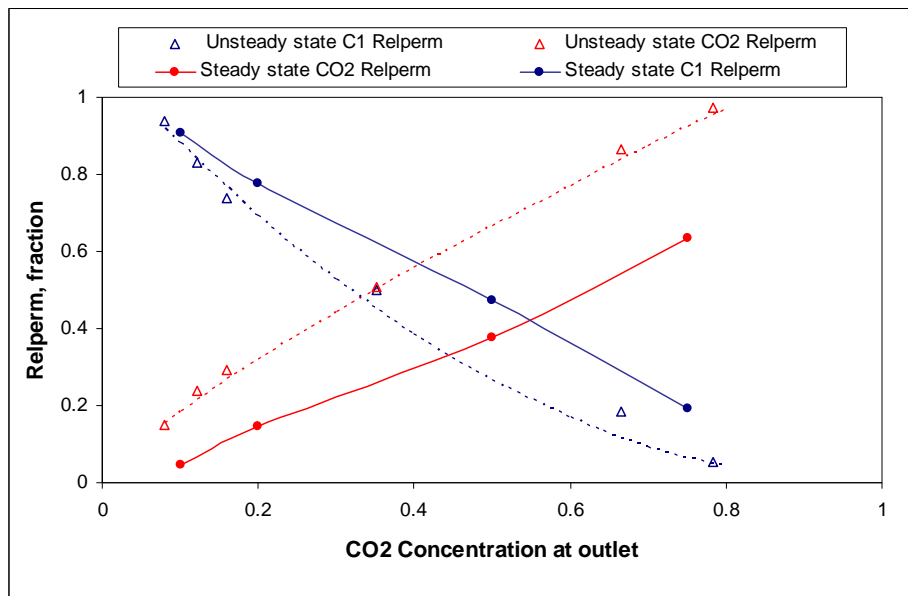


Figure 8.3: Steady and unsteady state relative permeability of sample S_V_1.

8.3.2 Sample S_C_1A:

Results of the steady state test of sample S_C_1A is shown in Figure 8.4. The curves display almost the same pattern as the steady state curves that were achieved with sample S_V_1. The key differences of the steady state curves of sample S_C_1A from other samples is that relative permeability of SCO_2 intercepted the methane relative permeability curve at a lower saturation of SCO_2 than for the other samples. This behaviour was noticed in the displacement tests in which SCO_2 had earlier breakthrough with sample S_C_1A than the other core samples. By increasing the absolute permeability of the medium, a low capillarity regime is expected.

Obviously in the displacement tests, with increasing absolute permeability, SCO_2 had earlier breakthrough by 15% when compared to the breakthrough obtained with low

quality rock S_C_3A. The disproportional relation between breakthrough and absolute permeability of the core plugs can be interpreted precisely through the pore morphology and size of the rocks. Since the wettability of the medium can only marginally affect the propagation of the gas flow, pore size, and its distribution in the medium will be considered to have significantly impacted the gases multiphase flow.

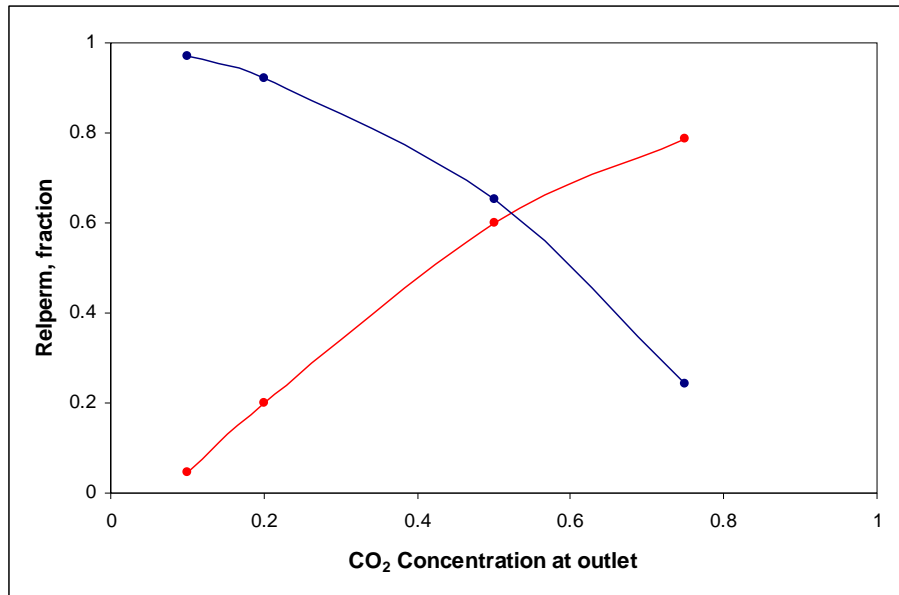


Figure 8.4: Steady state relative permeability of sample S_V_1A.

8.3.3 Sample S_C_2A and S_C_3A:

The steady state relative permeability curves of the core samples S_C_2A and S_C_3A are shown in Figures 8.5 and 8.6 respectively. For these cases the relative permeability curves experience similar characteristics. The difference can be seen as the SCO₂ relative permeability of sample S_C_3A advanced the methane relative permeability at greater saturation in comparison to intermediate rock quality S_C_2A. This has confirmed the above assumption, that high permeable rock is accompanied by a high capillarity regime and that larger pore distribution is abundant in the core plug.

In this way, dissipation of the miscible zone occurred and resulted in accelerated mixing by a molecular diffusion mechanism that led to earlier SCO₂ breakthrough. Again permeability heterogeneity had heavily impacted the multiphase flow of the gas in the porous medium.

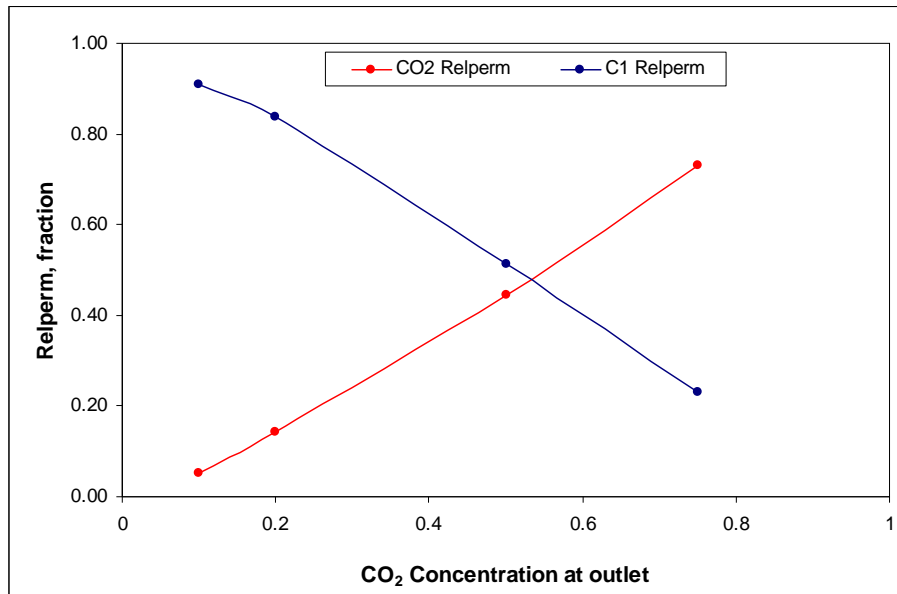


Figure 8.5: Steady state relative permeability curves of sample S_C_2A.

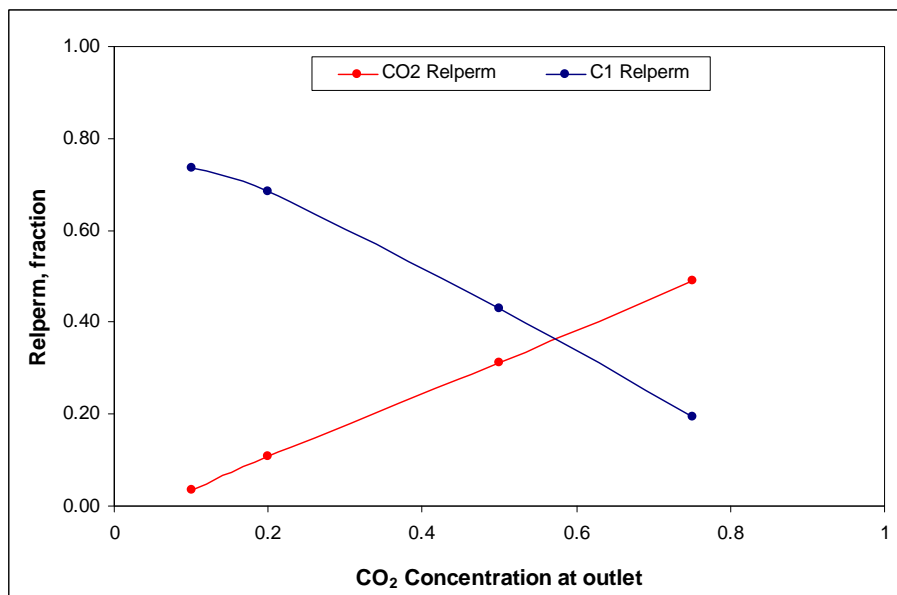


Figure 8.6: Steady state relative permeability curves of sample S_C_3A.

Chapter 9

Simulation

9.1 Introduction:

This chapter displays and analyses the simulation results that were obtained by executing different scenarios of injecting CO₂ for enhanced gas recovery. The key inputs of the simulation geo-model were acquired from the experimental data displayed in Chapters 5 and 6. To perceive their impact at field scale a comprehensive gas field example was developed using the Tempest simulator. The aim of running various scenarios was to determine the optimum injection strategy for a specific gas field as well as illustrating the effects of CO₂ injection on the recovery efficiency in different stages of pressure depletion.

Three scenario cases of CO₂ injection effects were studied on the ultimate recovery. For each case, three injection targets were examined. Although the first case aimed to investigate the effect of simultaneous CO₂ injection while producing methane, the other two cases were designed to investigate the combined effects of pressure depletion and injection rate on reservoir performance.

Results have shown that an accelerated gas production can be achieved with the highest injection rate in a shorter time. Nevertheless, ultimate gas recovery was marginally lower than the recovered gas attained with the two lowest injection strategies. The difference in recovery factor was only about 4% to 6%, therefore total sequestration of all CO₂ production from the example gas field appears to be a viable alternative.

9.2 Tempest simulator:

Simulating gas-gas displacement is a challenging task and requires a simulator equipped with compositional and pseudo multiphase flow capability. Two gases can be modelled using Tempest by using the Solvent option. This option is an extended black oil model in which two components exist. These are the reservoir gas (usually the original gas in place) and the solvent gas (usually injected gas). The aim is to simulate recovery processes in which injection gas and reservoir gases have different properties.

Such processes include vaporizing miscible drives, condensing miscible drives and low-pressure air injection. Fluid properties are changed by mass transfer between phases.

In this research work an immiscible interface between SCO_2 -methane is documented. Tempest integrated with the Todd-Longstaff (Todd and Longstaff 1972) model to control the miscible front expansion simply by viscosity mixing. Moreover, when the phase viscosities are obtained in the reservoir simulation, they are usually simply assigned to the appropriate phases. However, when a fluid is injected at an adverse mobility ratio, inter-fingering is expected. This results in the in situ fluid and the injected gas phase becoming intermingled. The Todd-Longstaff model sets the viscosities for the in situ fluid and the injected gas to a combination of the pure phase viscosity and a combined in situ fluid - the injected gas mixture viscosity.

The mixed viscosity is obtained by a one fourth power mixing law:

$$\left(\frac{1}{\mu_m}\right)^{1/4} = f_o \left(\frac{1}{\mu_o}\right)^{1/4} + f_g \left(\frac{1}{\mu_g}\right)^{1/4} \quad (9.1)$$

The phase viscosities are obtained as a combination of the mixed viscosity and the pure phase viscosity:

$$\mu_p = \mu_m \Omega + \mu_{pure} (1 - \Omega) \quad (9.2)$$

The mixing parameter is the Todd Longstaff omega parameter, $\Omega = 1$ corresponds to a totally mixed viscosity model, whilst $\Omega = 0$ corresponds to the original unmixed model. Tempest currently uses the viscosity mixing part of the Todd-Longstaff model. The relative permeability endpoint variation can be handled by using the surface tension model. It is possible to use the Todd-Longstaff model in black oil, solvent or compositional mode and it can be used without a surface tension relative permeability treatment.

In general this simulator solves a set of fluid conservation equations which presume there are (N_c) conserved components. In a compositional run these are hydrocarbon components such as methane, ethane and propane.

Mainly two sets of solution variables are used by Tempest. One possible set are *natural* variables, the pressure and one or two independent saturation variables.

Natural variables are used in fully implicit black oil mode and for steam injection when no hydrocarbon gas is present. The set of these for the Na active cells in the problem is the current solution $X = \{P_1..PNa, S_{o1}, \dots, S_{gNa}\}$.

The alternative variable set, used in all other cases, are *molar* variables. These comprise the pressure and molar densities per unit reference volume of each component present. Again, the set of all the active cells in the problem is the current solution $X = \{P_1..PNa, m_{11}, \dots, m_{NcNa}\}$.

Tempest uses the discretization system which is normally finite volume. The solution variable value is associated with the pore volume V_p of a cell, and the flow terms are obtained as functions of the solution values over a local stencil of cells. The actual pore volume of a cell is $V_p = b_r \cdot V_r$ where V_r is the pore volume of cell at reference pressure. The actual pore volume will vary as a function of pressure. A common simple form for b_r is:

$$b_r = (1 + Cr \cdot (P - P_{ref})) \quad (9.3)$$

Where Cr is commonly known as the rock compressibility, but is really pore-volume's expansivity. The mass conservation equation for active cell i for the time step T to $D = T + \Delta T$ is: $V_{ri} \cdot m_{ci}$

$$D - V_{ri} \cdot m_{ci} \quad (9.4)$$

$$T = \Delta T \cdot (Q_{ci} + \sum_j p F_{cpij}) \quad (9.5)$$

Where:

V_{ri} reference volume of cell i .

m_{ci} molar densities per unit reference volume of conserved component c in cell i .

Q_{ci} injection or production rate of component c in cell i due to wells.

F_{cpij} the flow rates of component c in phase p from cell i to its neighbour j .

In the molar variable case m_{ci} .

D primary variables; in the natural variable case m_{ci} . D may be obtained as functions of the natural variables.

9.3 Geo-model:

An asymmetrical double plunging anticline geo-model was prepared for simulating SCO₂-methane displacement at reservoir scale. The geo-model consists of four major gas compartments (layers) each represents the peterological characterization of one of the core plugs tested in this research work. The dimension of the geo-model is 1.7×2.2×0.3km. In the X-direction 34 cells while in Y-direction 44 are produced. The division of Z-direction was performed in accordance to the layers specification, 9, 5, 12, and 11 cells were produced for layers L1, L2, L3 and L4 respectively. The arrangement of the layers from top to bottom of the model was very low, high, medium and low quality rocks, their specification can be found in Table 9.1. Four wells were drilled in the geo-model, the injector I-1 lies at the syncline trough South of the producer well P-1. P-2, P-3 and P-4 wells were situated at the crest of the anticline at the North and Northwest of the injector I-1 (See Figure 9.1). The wells completion, trajectories and properties are illustrated in Table 9.2.

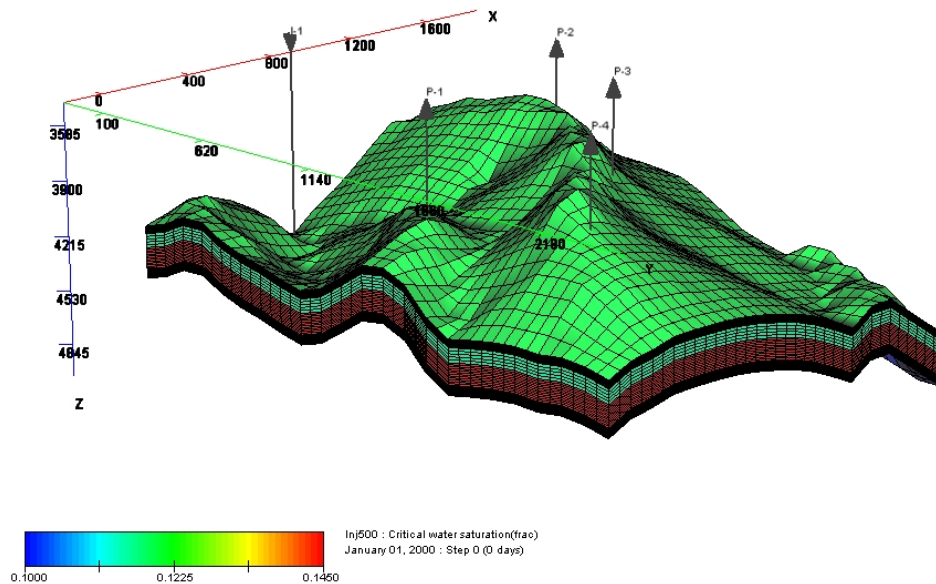


Figure 9.1: Critical water saturation distribution in the geo-model.

The initial reservoir condition pressure was 5900 psia, temperature was 160 °C and datum depth was set to 3650 m. Figure 9.2 shows the permeability distribution of the layers in the geo-model. The permeability data of the each zone was obtained from core plugs S_A_1, S_A_2 and S_A_3. For example layer L2 has almost the same peterophysical properties as core sample S_A_1, absolute permeability of 390 md, porosity of 0.175, Swc of 0.175, etc. Furthermore each layer has been given different

saturation tables so that four sets of SCO_2 -methane and methane-brine relative permeability curves have been supplied to the simulator in order to accurately perform the displacement process for all layers between gas-gas and gas-brine phases.

Table 9.1: General petro-physical characteristic of the layers.

Layers	Thickness m	Kx md	Ky md	Kz md	Porosity %	Sgr	Swcr	Core plugs
L1	50	6	6	4	0.04	0.05	0.12	S_A_3
L2	70	390	390	370	0.17	0.03	0.175	S_A_1
L3	120	115	115	100	0.14	0.04	0.145	S_A_2
L4	60	8.5	8.5	6	0.09	0.05	0.1	S_A_3

Table 9.2: Wells completion and trajectories.

Wells	Type	X	Y	MD m	Completion m	RAD m	Layers
I-1	Injector	675	125	4377-4690	4645-4690	0.5	L4
P-1	Producer	575	775	4050-4300	4100-4160	0.5	L2
P-2	Producer	975	1275	3605-3895	3650- 3715	0.5	L2
P-3	Producer	475	1825	3758-4043	3810-3865	0.5	L2
P-4	Producer	425	1825	3746-4026	3796-3857	0.5	L2

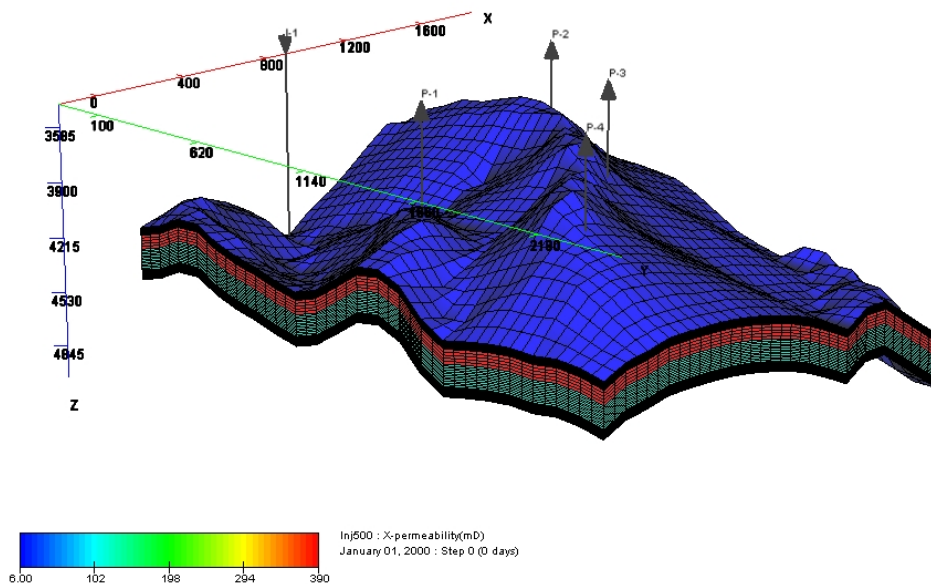


Figure 9.2: Permeability distribution in the geo-model.

Figure 9.3 shows in situ gas contact with the aquifer. All wells are perforated in layer L2 except the injector well I-1 that is perforated in layer L4. In the case of an

existing aquifer, the water gas contact (WGC) was assigned at depth 4400 m in which well I-1 perforated beneath WGC.

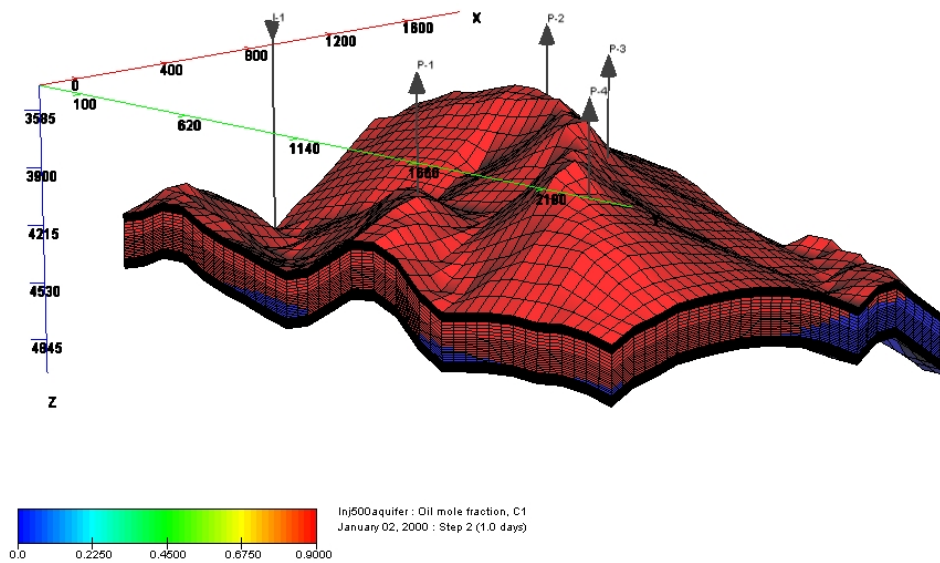


Figure 9.3: Methane phase saturation distribution in the geo-mole and GWC.

As the objective of the simulation study was to determine the optimum injection target and the time point of CO₂ injection, three case scenarios of CO₂ injection were studied in addition to the base case (conventional depletion). Although the first case aimed to investigate the impact of simultaneous CO₂ injection while producing methane at several injection rates, the other two cases were to study the combined effects of pressure depletion and injection rates on the recovery efficiency. Furthermore, the impact of direct CO₂ injection on the reservoir performance in the model was studied in two cases, first, in the present of an aquifer, second, in the absence of an aquifer. Injection of CO₂ early in the lifetime of the field in case-1 was used to achieve pressure maintenance. Case-2 and 3 are injection strategies after production had been established for a period of time in the lifetime of the gas reservoir to explore and determine the best possible condition of CO₂ injection results to achieve improved sweep efficiency.

The following paragraph describes the base case of conventional depletion of the model gas field. The paragraphs thereafter describe three scenarios of CO₂ injection, starting at different time frames for the lifetime of the gas field and investigating various injection targets for each case.

9.4 Simulation case studies:

9.4.1 Base case:

Gas production in the example reservoir covered the period from 2000 to 2032. In this case the injector well was shutoff while only the producer wells were allowed gas production to the economic limit. Pressure drop and production rate decline was monitored over a span of four months (See Figure 9.4). From the conventional pressure depletion three injection start points over the lifetime of the reservoir were determined. For Case-1, CO₂ injection starts in the beginning of gas production from the field, with the aim to maintain pressure drop. Case-2 and 3 CO₂ injection was initiated when the bottom-hole pressure declined to 2800 psia and 1350 psia, respectively.

As the in situ gas has 10% of CO₂ in its mixture, this study aimed to define the optimum fraction of the produced CO₂ to be re-injected back into the reservoir in order to achieve the best possible recovery factor. Hence three injection rates of 500K, 1500K and 3000K sm³/day were examined. These rates corresponded to 19%, 58% and 100% of total CO₂ production from the example gas field. Investigating several injection rates is crucial because experimental results confirmed that recovery efficiency from CO₂-methane displacement tests was severely affected with changes in injection rates, rather than with changes in other parameters such as in situ gas composition, pore-pressure, temperature, etc.

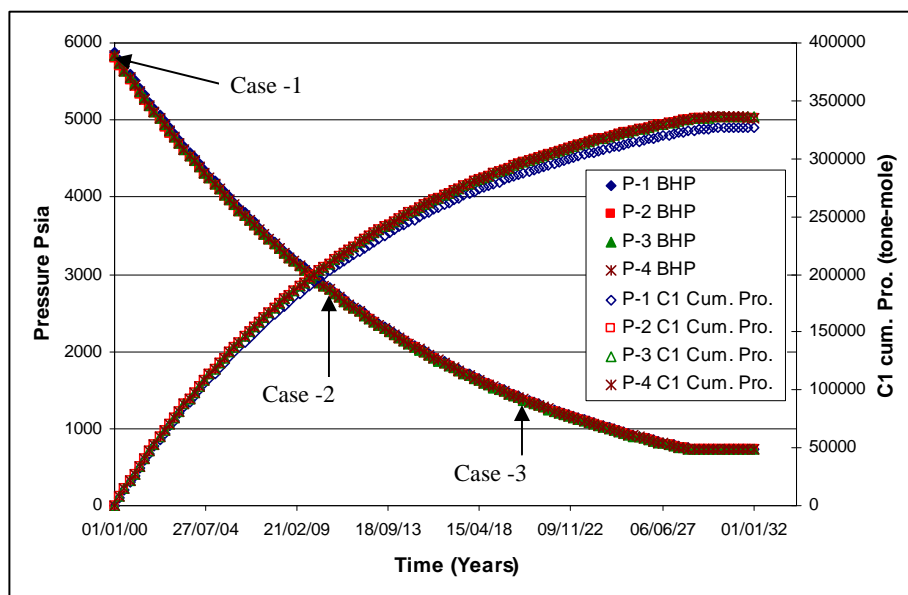


Figure 9.4: Methane cumulative production and pressure depletion in the base case.

9.4.2 Case-1:

Solubility of CO₂ in water is important to obtain reliable results when simulating CO₂-enhanced gas recovery projects. Solubility of CO₂ in water can be input into Tempest using keyword (Solu). The rate of CO₂ that would be soluble in the water phase at reservoir condition was calculated using Yih-Bor Chang's model (Chang, Coats, and Nolen 1998). Results from Yih-Bor model were compared with the experimental data published by Z. Duan and Rui Sun (2003) and a reasonable match was observed.

CO₂ injection starts at the beginning of gas production in the example gas field. Figure 9.5 shows CO₂ breakthrough of the producing wells in the absence of an aquifer. Since CO₂ has ability to dissolve in the connate water saturation, a fraction of injected CO₂ will be disappearing while displacing methane. When the brine is oversaturated partial displacement of brine by CO₂ is expected causing a reduction in connate water saturation. This means more pore volume will be available for CO₂ to be sequestered. Meanwhile three phase flow will occur and consequently the preferred phase will compete with others to breakthrough earlier. For example CO₂ profile at P-2 indicates three phase flow as its profile increases irregularly in comparison to the other wells CO₂ profiles. Connate water production has increased from 0 to 8 kg-mole/day in 2014, thereafter gradually reduced until the production at well P-2 stopped in 2027.

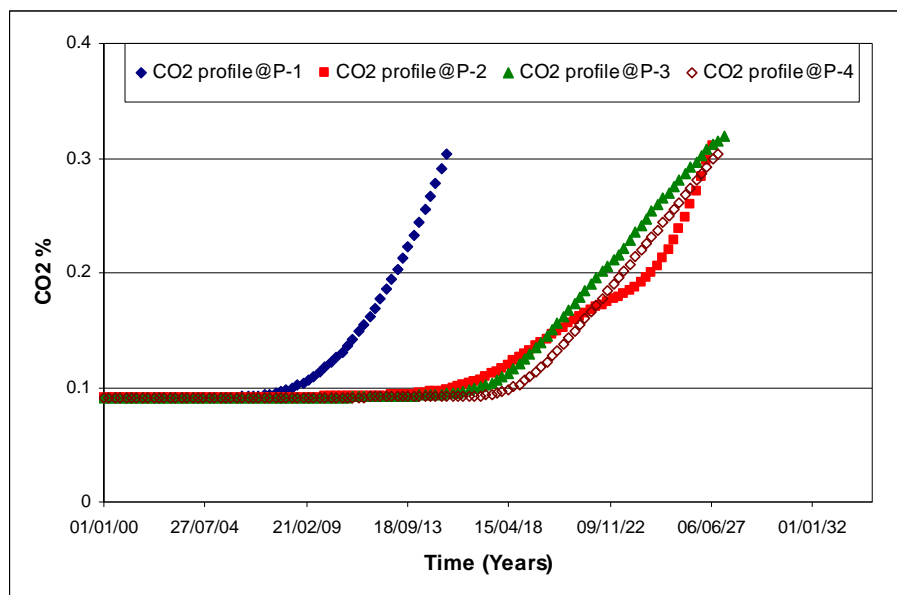


Figure 9.5: CO₂ profile at wells P-1, P-2, P3 and P4. Case-1, injection target is 500K sm³/day.

At each production well whenever CO₂ concentration reached 30% to 33% of the produced stream, production ceased due to the extra costs that would normally associate with CO₂ separation, compression and reinjection. Therefore it would be uneconomical to recover less than 70% of natural gas.

Figure 9.6 shows the cross-section between well I-1, P-1, P-4. It is apparent CO₂ inter-fingered with reservoir fluid, a meticulous look to layer L3, the medium quality rock. CO₂ appears to have been intermingled unsteadily with methane, having an unfavourable displacement front as CO₂ propagates much faster at the lower part of L3 then mixes with methane. This coincides to the hypothesis that the more viscous and denser the phase it tends to move downward.

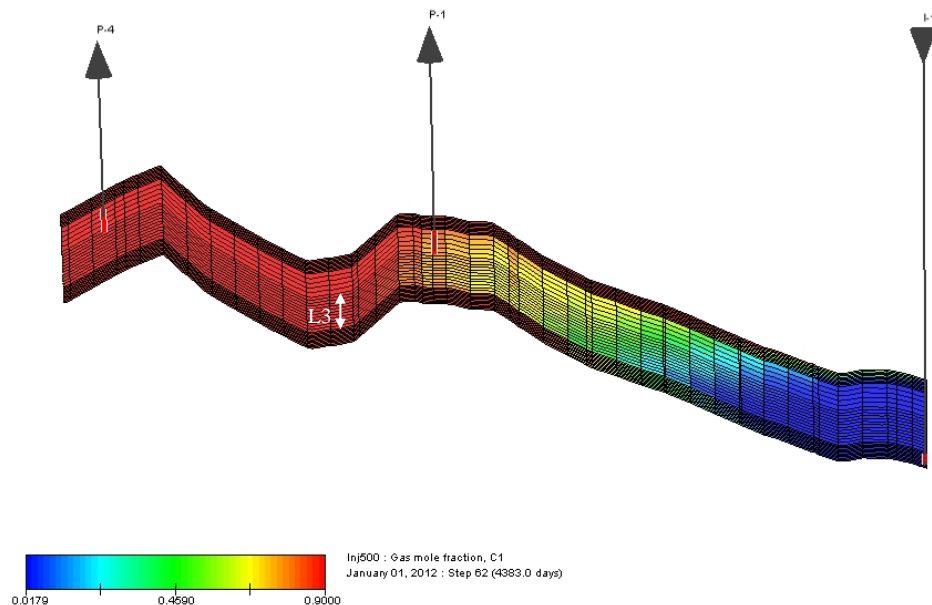


Figure 9.6: CO₂-methane displacement front in the case of no aquifer.

Figure 9.7 displays CO₂ breakthrough of the production wells in two different cases, namely in the existence of an aquifer and with no aquifer. It is obvious that CO₂ has broken through earlier with the existing aquifer. There are two reasons to illustrate and explain the cause of earlier breakthrough of CO₂ in the case of an existing aquifer. However poor transmissibility is anticipated for the injected phase because a greater fraction of CO₂ could be retained in the brine through its solubility and residual saturation. First, with the presence of an aquifer less pore volume will be available for in situ gas; consequently CO₂ will reach the producing well faster.

Second, CO₂ displacement of brine will be carried out adversely as the less viscous and denser phase displaces the brine, the poor mobility ratio will be achieved, and this causing the CO₂ to override the brine and subsequently gas mixing will be accelerated. Furthermore, the brine displacement by CO₂ originates methane displacement by brine on the other front, resulting in increased residual gas saturation. Figure 9.8 is a cross-section between I-1, P-1 and P-4 in the case of the existing aquifer. In layer L2 and L3 near the injector well greater residual methane saturation can be noticed.

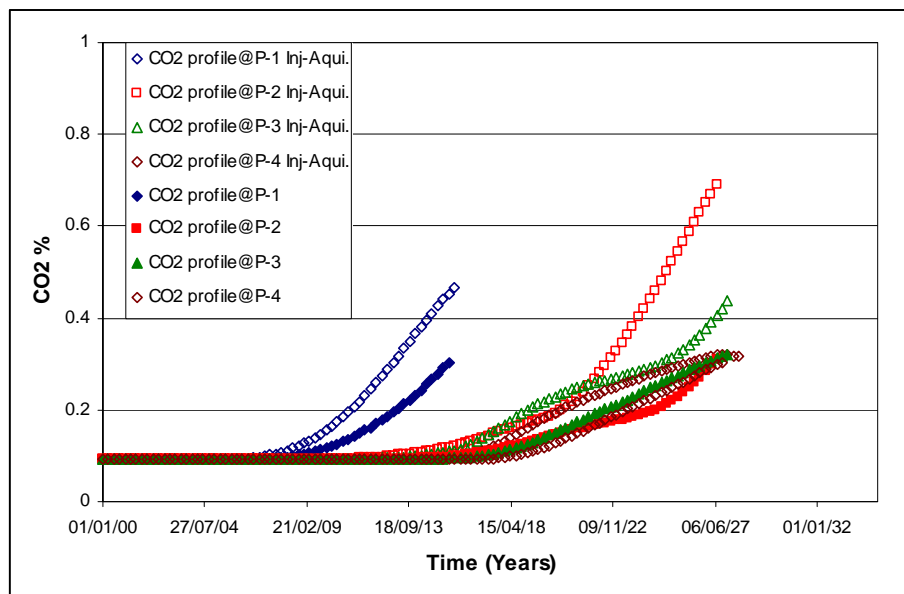


Figure 9.7: CO₂ profile at wells P-1, P-2, P3 and P4. Case-1, injection target is 500K sm³/day. Solid dots indicate no aquifer while blank dots refer to CO₂ profile with the presence of aquifer.

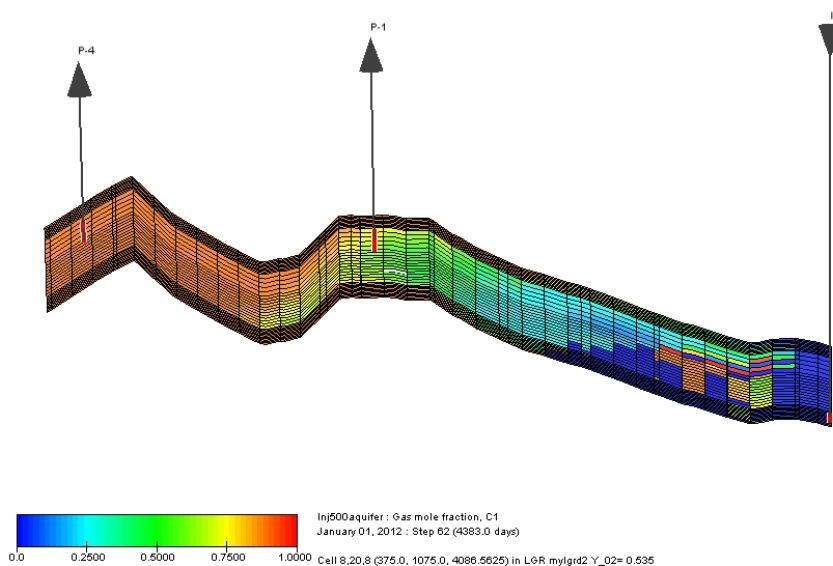


Figure 9.8: CO₂-methane displacement front in the presence of the aquifer.

The economic analysis of the outcomes that were achieved with running case-1 (CO₂ injection started at the beginning of the gas production at three different injection targets), was performed by generating the methane cumulative production in the example gas field for the three injection targets as shown in Figure 9.9. For the purpose of comparison of methane cumulative production with each of the three injection targets of 500K, 1500K and 3000k sm³/day, the results are examined against the base case which is conventional completion without CO₂ injection.

With a conventional depletion recovery factor, within a 32 year period the recovery factor was about 84.5% of OGIP in the example gas field. Whereas with CO₂ injections the ultimate recovery factor for the three injection rates of 500K, 1500K and 3000K sm³/day, was 87.1%, 81.1% and 78.6%, respectively. In spite of that fact improved recovery efficiency was achieved by applying the lowest injection rate. More precisely analysing the above recovery factor within the time frame, the two highest injection rates appear to the operator to be more practical rates. The ultimate recovery factor was attained in less time than the projected lifetime of the gas field, with dates being on October 2025 and July 2021, for injection rates of 1500K and 3000k sm³/day, respectively.

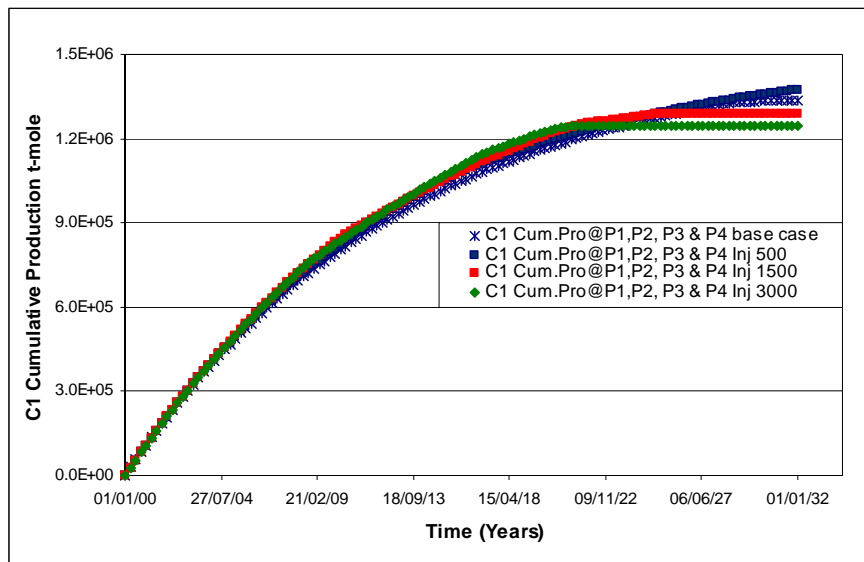


Figure 9.9: Methane cumulative production (case-1, no aquifer) from well P-1, P-2, P-3 and P4 at injection rate of 500K, 1500K and 3000K sm³/day.

The difference in recovery factor was less by only 4% to 6% in comparison to the recovery factor achieved with the base case. Accordingly the highest injection target may be attractive to the operator, because from July 2021 to January 2032 with conventional depletion only an extra 6% of OGIP will be recovered. Therefore total sequestration of CO₂ appears to be the optimum option for the CO₂-EGR project.

Applying the lowest injection target of 500k sm³/day resulted in the greater gas recovery within the span of 32 years. Nearly 2.6% extra natural gas was recovered by applying the lowest injection rate compared with the amount that was achieved with normal depletion strategy. The recovery factor and cumulative gas production in each stage of production for all injection target scenarios can be found in Table 9.3.

Table 9.3: Case-1 ultimate cumulative gas production and recovery factor at all injection targets.

Injection targets	Time years	Years and months	Total cumulative production (tone-mole C1)	Recovery factor %
Base case	Jan 00-Jan 32	32	1333511	84.5
500	Jan 00-Jan 32	32	1373467	87.1
1500	Jan 00-Oct 25	25y & 10m	1287982	81.1
3000	Jan 00-Jul 21	21y & 6m	1243658	78.6

9.4.3 Case-2:

Similar to the previous case the same injection targets were investigated in conjunction with the effect of pore-pressure. In this case CO₂ injection started in October 2010 when the pressure in the field drops to approximately 2800 psia. Approximately 62.3% of OGIP will be recovered in October 2010 before CO₂ injection starts. This scenario was designed to explore the possibility of improved recovery factor with CO₂ late injection. To conclude that and determining the optimal injection rate in case-2, gas cumulative production was plotted against time for all injection targets as well for the base case (See Figure 9.10). The recovery factor with injection targets of 500K, 1500K and 3000K sm³/day was 85.8%, 84.6% and 81.1%, respectively. Nonetheless, with decreasing pore-pressure the difference in physical properties between SCO₂-methane decreases dramatically. Consequently with the case-2 recovery factors were marginally lower for all injection rates than in the case-1.

Time appears to play a greater role in defining which of the injection rates is optimal. The 81.1% recovery factor was achieved in April 2024 with the highest injection rate. It is just 3.4% below that achieved with the base case of 32 years (See Table 9.4). For instance, if the other strategies were followed, in 8 years from 2024 only an additional 4.7% of OGIP would be recovered. Hence the highest injection rate appears to be an ideal option in this case too.

Table 9.4: Case-2 ultimate cumulative gas production and recovery factor at all injection targets.

Injection targets	Time years	Years & months	Total cumulative production (tone-mole C1)	Recovery factor %
Base case	Jan 00-Jan 32	32	1333511	84.5
500	Jan 00-Apr 31	31y & 4m	1354697	85.8
1500	Jan 00-Jan 29	29	1334449	84.6
3000	Jan 00-Apr 24	21y & 6m	1287982	81.1

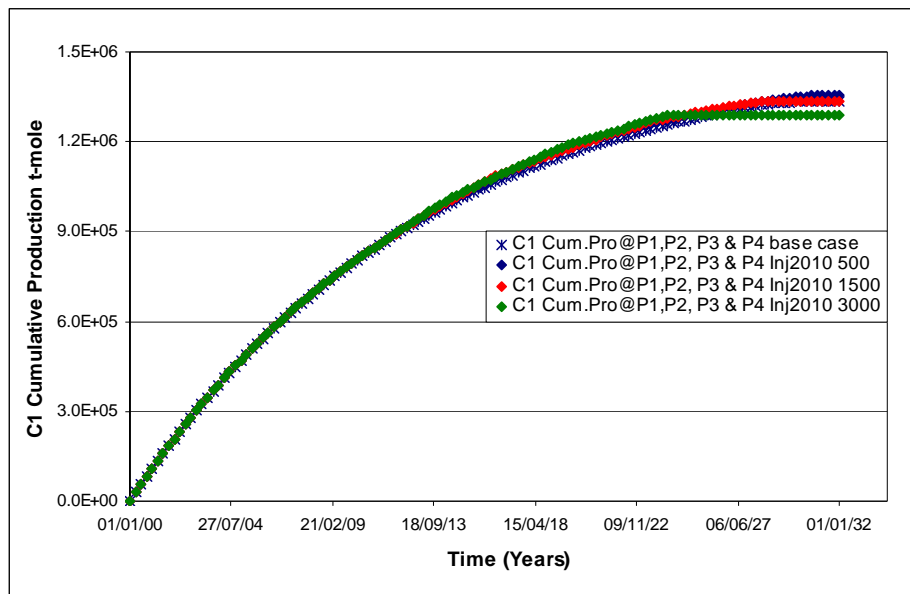


Figure 9.10: Methane cumulative production (case-2, no aquifer) from well P-1, P-2, P-3 and P4 at injection rate of 500K, 1500K and 3000K sm^3/day .

9.4.4 Case-3:

Experimentally reducing pore pressure to the minimum level (1500 psia) from the initial reservoir pressure, the recovery factor was decreased by about 40% if compared to the recovery factor at pore pressure of 5900 psia. The noticeable reduction in methane recovery efficiency could be due to the physical properties of the gases rather than the dissipation of miscible fluid or channelling. Case-3 was planned to explore the impact of near abandonment pressure on the recovery efficiency. In this case gas production was allowed without CO₂ injection until the lowest reservoir pore-pressure of about 1350 psia was attained in October 2021. Thereafter CO₂ injection commenced similar to other cases and at various rates. Figure 9.11 displays the results that were obtained with the three injection rates and the base case. The highest injection rate was considered to be the appropriate target for enhanced recovery, and resulted in moderate recovery efficiency in comparison to the previous cases. Since only an additional 2% of gas was recovered from October 2021 to July 2029, if compared with case-2. Recovery factor and cumulative gas production in each stage of production for all injection targets scenarios can be found in Table 9.5. In this case injection target 500k sm³/day appears to be the optimum injection rate for enhanced gas recovery.

Faster gas production has been achieved with the highest injection rates; nevertheless less gas was recovered at the closing stages of the simulation if compared to the base case. The difference is only about 4% to 6%, therefore total sequestration of all CO₂ production from the field could be a significant alternative for both case1 and 2. For case-3 the lowest injection rate, which corresponds to just 19% of total CO₂ production from the field, has been demonstrated to be a suitable choice for CO₂-EGR.

Table 9.5: Case-2 ultimate cumulative gas production and recovery factor at all injection targets.

Injection targets	Time years	Years & months	Total cumulative production (tone-mole C1)	Recovery factor %
Base case	Jan 00-Jan 32	32	1333511	84.5
500	Jan 00-Apr 32	32	1366659	86.6
1500	Jan 00-Jul 31	31y & 6m	1337065	84.8
3000	Jan 00-Jul 29	29y & 6m	1308039	82.9

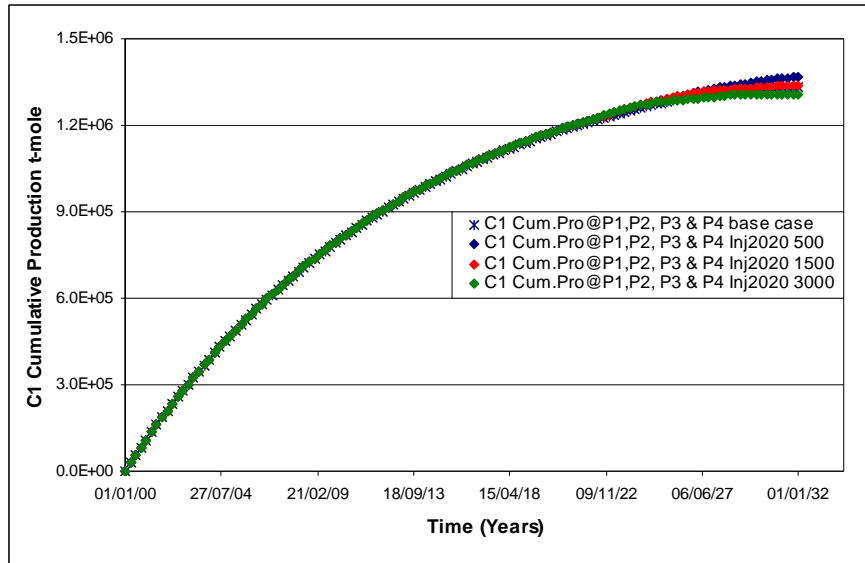


Figure 9.11: Methane cumulative production (case-3, no aquifer) from well P-1, P-2, P-3 and P4 at injection rate of 500K, 1500K and 3000K sm^3/day .

Chapter 10

Conclusion and Recommendations

10.1 Conclusions and discussions:

The results from this research work provide an analysis of enhanced gas recovery by CO₂ injection with the aim of CO₂ sequestration and increased sweep efficiency. From the experiments conducted the following conclusions have been made:

1. The corrosive nature of SCO₂ under the test conditions was the major reason of the tube, Viton and Teflon O-rings damage and therefore it is recommended that operators take this observation into account before deploying SCO₂ re-injection in the field.
2. The immiscibility of gases or gas-gas equilibrium can occur in some fluids at high pressure and temperature. The interfacial tension between SCO₂ and methane was measured at 95/160°C and pressures between 1000 to 6000 psia.
3. The interface between SCO₂ and methane at very low SCO₂ injection rate is much clearer than high rates. It was also obvious that the interface was not as sharp as in the case of liquid-liquid or gas-liquid phases. The interface is slightly “cloudy” suggesting some compositional gradient via molecular diffusion across the interface, though the process seems significantly slower than was anticipated
4. The results showed interfacial tension of the supercritical CO₂-methane system decreases when the mutual miscibility of the two gases increases, or as the two become totally miscible, approaching zero at around 1100 psia.
5. There was a zone in the vicinity of 1500 psia and above which is independent of temperature where IFT increased very sharply. The IFT was almost three times higher at 3000 psia than at 1000 psia for the same temperature. This is attributed to the density of SCO₂ at 1000 psia being less than 1/3 of the density at 3000 psia, at the same temperature.

6. Experimental results confirmed that the measurements related to IFT of the CO₂-methane system was absolutely different from those obtained from the N₂-CO₂, and methane-N₂ systems.
7. Dean Stark extraction results indicated considerably lower *Swi* than were obtained experimentally for all core plugs. As water is not very soluble in supercritical CO₂, continuous SCO₂ injection into a porous media will force the brine to continuously evaporate into the CO₂; however no evidence of zero limit of the irreducible water saturation has been reported or measured. In this work some enhanced injectivity is measured, which could be the result of this process assuming the brine is of low salinity.
8. In formations saturated with highly saline brine (e.g. Northern German Basin) the outcome is the opposite: injectivity is impaired. In this case, the brine becomes supersaturated as water continuously evaporates into the CO₂ phase and salt (halite) precipitates in the pores. The porosity and permeability diminishes, which can lead to the loss of a well.
9. Displacement experiments determined that SCO₂ injection is favourable for combined EGR and CO₂ sequestration via SCO₂ injection including re-pressurization without extensive SCO₂-methane mixing depending on the field development stage, CO₂ injecting point, rate/volume of injection, and purity of the SCO₂. An important practical issue for field application is the temperature and pressure of the gas at the injection point and temperature of the formation that are effecting on the mixing of CO₂.
10. Although methane production rate and CO₂ breakthrough might not permit continued production of methane beyond a certain point of mixing over the production time, the potential to sequester CO₂ is apparent at given pressure and re-injection rates. Continuous injection of CO₂ over time into one well can displace natural gas toward surrounding wells. Immediate surrounding wells will require monitoring for potential increases in gas production, pressures, or compositional changes.

11. It is apparent that recovery of methane at SCO₂ breakthrough is higher for the highest methane concentration in the in situ gas. The breakthroughs of SCO₂ was observed from the four displacement tests at 0.7 PV, 0.4 PV, 0.33 PV, and 0.2 PV for CO₂ concentration 10%, 25%, 50%, and 75%, respectively.
12. Subsequent to SCO₂ injection, methane production rate is almost instantaneous with (90% methane) production profile indicating piston like displacement until breakthrough. This was more obvious during the unsteady displacement experiments where the effect on permeability coming from segregation of the SCO₂ phase independent of the gravity and more flow rate dependent (velocity) which is forcing “viscous displacement” because the viscous forces of a displacing phase has greater momentum than that of the displaced phase adding to any permeability variation in the core. Better displacement efficiency was obtained at a higher rate.
13. A power relative permeability model for the gas-gas phase was developed from the best fit of the experimental data. An excellent match was observed with the experimental data.
14. This study shows SCO₂ injection velocity greatly affects the displacement efficiency and with it, the amount of SCO₂ sequestered. The methane recovery factor at SCO₂ breakthrough for various injection rates carried out confirmed that the recovery factor increased as the injection rate increased until a maximum recovery factor obtained at corresponding field injection rates of 10 cm/hr.
15. At a lower injection rate the displacement was less efficient. This was also observed visually during the IFT measurement where a compositional gradient developed over time. This mixing time could have been further accelerated in the core and the reservoirs because mixing porous media is caused by several mechanisms, such as molecular diffusion, Taylor dispersion, convective dispersion, and permeability heterogeneities.

16. Evidently for the shorter cores with decreasing absolute permeabilities, SCO_2 breakthrough was delayed by 15%. The disproportional relation between breakthrough and absolute permeability of the core can be interpreted precisely through the pore morphology of the rocks. Since the wettability of the medium can only marginally affect the propagation of the multi-gas.
17. The dispersivity of SCO_2 was identified to be a function of injected pressure, in situ gas composition and injection rate. It was found that a dispersion coefficient of SCO_2 changes proportionally with changes in purity of the displaced phase and injection rate (from 1 to 5 cm/hr) while inversely changing with injected pressure and injection rate from 5 to 10 cm/hr.
18. Relative permeability from both steady and unsteady state technique was found to be noticeably different. The greater relative permeability for methane was obtained with steady state methane rather than with unsteady state whereas for the SCO_2 phase the result was vice versa.
19. With steady state tests the more viscous and denser phase showed greater pressure drop across the core and subsequently poor relative permeability. For that reason SCO_2 demonstrated smaller relative permeability in steady state tests.
20. Three scenario cases of CO_2 injection were studied on the ultimate recovery. For each case three injection targets were examined, the injection rates were 500K, 1500K and 3000K sm^3/day and corresponded to 19%, 58% and 100% of total CO_2 production from the example gas field, respectively.
21. Results have showed that accelerated gas production can be achieved with the highest injection rate in less time, nevertheless ultimate gas recovery was marginally lower than the recovered gas attained with the two lowest injection strategies. The difference was only about 4% to 6%, therefore total sequestration of all CO_2 production from the example gas field appears to be a viable alternative.

10.2 Recommendation:

- Due to the corrosive nature of SCO_2 under the test conditions particularly at 160°C and 5900 psia, it is recommended to take this observation into account before deploying SCO_2 re-injection in the field.
- To avoid residual water saturation evaporation by CO_2 in the tested core samples CO_2 /water saturation should be carried out at reservoir temperature.
- The interfacial tension between SCO_2 and methane was measured at $95/160^\circ\text{C}$ and pressures between 1000 to 6000 psia by using a reverse pendant drop technique. Measuring by another technique at different pressure and temperature will add crucial knowledge to the concept of the presence of gas-gas IFT.
- The JBN method can be applied for generating gas-gas relative permeability curves. The power model that was developed from the best match of the experimental data has three variables a , b , and c . Further investigation is required to mathematically obtain the values of these variables to achieve a fully flexible approach in generating gas-gas relative permeability.
- To optimise the mathematical representation for SCO_2 -methane flow in porous media, an additional extensive laboratory investigation is required to explore the SCO_2 -methane phase flow under various conditions that have not been carried out within the scope of this research work.
- Further research is needed to investigate the significant differences in gas-gas relative permeability by employing different techniques to the steady and unsteady state. The greater relative permeability for methane was obtained with steady state rather than with unsteady state whereas for the SCO_2 phase it was vice versa.

References:

- Adamson, A. W. 1997. *Physical chemistry of surfaces*. 6 ed. New York, U.S.A.: Wiley-Interscience.
- Adolf, D., M. Tirrell, and H. T. Davis. 2004. Molecular theory of transport in fluid microstructures: Diffusion in interfaces and thin films *AIChE Journal* 31 (7): 1178 -1186.
- Al-Abri, A., H. Sidiq, and R. Amin. 2009. Experimental investigation of the velocity-dependent relative permeability and sweep efficiency of supercritical CO₂ injection into gas condensate reservoirs. *Journal of Natural Gas Science and Engineering* 1: 158-164.
- Al-Hashami, A., S. Ren, and B. Tohidi. 2005. *SPE Europec/EAGE Annual Conference, June 13-16, 2005: CO₂ Injection for Enhanced Gas Recover and Geo-Storage: Reservoir Simulation and Economics*. Madrid, Spain: SPE 94129. <http://www.spe.org/elibrary/app/newSearch.do> (accessed May 8, 2009).
- Ameafule, J. O., and L. L. Handy. 1982. The effect of interfacial tensions on relative oil/water permeabilities of consolidated porous media. *Society Petroleum Engineering Journal* 22 (3): 371-381.
- Amin, R., H. Sidiq, T. Kennaird, and E. Van der Steen. 2010. Gas-gas experimental interfacial tension measurement. *Fluid Phase Equilibria* 295 (2): 230-236.
- Aronofsky, J. W., and J. P. Heller. 1957. A Diffusion model to explain mixing of flowing miscible fluids in porous media. *Petroleum Transactions, AIME* 210: 345-349.
- Asar, H., and L. L. Handy. 1988. Influence of interfacial tension on gas/oil relative permeability in a gas-condensate system. *SPE Reservoir Engineering* 3 (1): 257-264.
- Bachu, S., J. Shaw, and R. Pearson. 2004. *SPE/DOE Fourteenth Symposium on Improved Oil Recovery, April 17-21 2004: Estimation of Oil Recovery and CO₂ Storage Capacity in CO₂ EOR Incorporating the Effect of Underlying Aquifers*. Tulsa, Oklahoma, U.S.A.: SPE 89340. <http://www.spe.org/elibrary/app/newSearch.do> (accessed April 10, 2008).
- Baker, L. E. 1977. Effects of dispersion and dead-end pore volume in miscible flooding. *Society Petroleum Engineering Journal* 17 (3): 219-227.
- Bardon, C., and D. G. Longeron. 1980. Influence of very low interfacial tensions on relative permeability. *SPE Journal* 20 (5): 391-401.
- Bennion, B., and S. Bachu. 2006a. *SPE Annual Technical Conference and Exhibition, September, 24-27 2006: Dependence on Temperature, Pressure,*

and Salinity of the IFT and Relative Permeability Displacement Characteristics of CO₂ Injected in Deep Saline Aquifers. San Antonio, Texas, U.S.A.: SPE 102138. www.onepetro.org (accessed May, 20 2009).

Bennion, B., and S. Bachu. 2006b. The Impact of Interfacial Tension and Pore Size Distribution/Capillary Pressure Character on CO₂ Relative Permeability at Reservoir Conditions in CO₂-Brine Systems In *SPE/DOE Symposium on Improved Oil Recovery*. Tulsa, Oklahoma, U.S.A. SPE 99325.

Bikerman, J. J. 1973. *Foams*. New York: Springer-Verlag.

Blackwell, R. J. 1962. Laboratory studies of micro-sopic dispersion phenomena. *Society Petroleum Engineering Journal* 2 (1): 1-8.

Bond, W. N., and D. A. Newton. 1928. Bubbles, drops and Stokes' law. *Philos. Mag.* 75 (31): 749-800.

Bondor, P. 1992. Applications of carbon dioxide in enhanced oil and gas recovery. *Energy CONversion and Management* 33: 579-586.

Boom, W., K. Wit, A. M. Schulte, S. Oedai, J. P. W. Zeelenberg, and J. G. Maas. 1995. *SPE Annual Technical Conference and Exhibition, October, 22-25 1995: Experimental Evidence for Improved Condensate Mobility at Near-wellbore Flow Conditions*. Dallas, Texas, U.S.A.: SPE 30766. <http://www.onepetro.org/> (accessed June, 22 2009).

Buckley, S. E., and M. C. Leverett. 1942. Mechanism of fluid displacement in sand. *Petroleum Transactions, AIME* 146: 107-116.

Busch, A., Y. Gensterblum, B. M. Krooss, and R. Littke. 2004. Methane and carbon dioxide adsorption-diffusion experiments on coal: upscaling and modeling. *International Journal of Coal Geology* 60: 151-168.

Butt, H.-J., K. Graf, and M. Kappl. 2003. *Physics and Chemistry of Interfaces*. Weinheim, Germany: WILEY-VCH verlag GmbH & Co. KGaA Weinheim.

Cahn, J. W. 1977. Critical point wetting *The Journal of Chemical Physics* 66 (8):

Calabrese, M., and F. Masserano. 2005. *SPE Annual Technical Conference and Exhibition October, 9-12 2005: Simulation of Physical-Chemical Processes During Carbon Dioxide Sequestration in Geological Structures*. Dallas, Texas, U.S.A.: SPE 95820. <http://www.spe.org/elibrary/app/newSearch.do> (accessed October, 20 2008).

Calhoun, J. C. 1953. *Fundamentals of Reservoir Engineering*. Norman, Oklahoma: University of Oklahoma Press.

Carman, P. C. 1937. Fluid flow through granular beds. *Transactions of the Institution of Chemical Engineering* 15: 150-167.

- Chang, Y.-B., B. K. Coats, and J. S. Nolen. 1998. A Compositional Model for CO₂ Floods Including CO₂ Solubility in Water *SPE Reservoir Evaluation & Engineering* 1 (2): 155-160.
- Clements, T., and K. Wit. 2002. *SPE Annual Technical Conference and Exhibition, September 29-October 2, 2002: CO₂ Enhanced Gas Recovery Studied for an Example Gas Reservoir*. San Antonio, Texas, U.S.A.: SPE 77348. <http://www.spe.org/elibrary/app/newSearch.do> (accessed April 9, 2008).
- Coats, K. H., and B. D. Smith. 1964. Dead-end pore volume and dispersion in porous media. *Society Petroleum Engineering Journal* 4 (1): 73-84.
- Collins, R. E. 1963. *Flow of fluids through porous materials*. Tulsa, OK, U.S.A.: Penn Well Books.
- Darvish, M., H. Hong, S. Theys, R. Stoker, S. Bachu, S. Dashtgard, and S. Fraser. 2008. *SPE Annual Technical Conference and Exhibition, September 21-24, 2008: CO₂ Injection for Enhanced Gas Recovery and Geological Storage of CO₂ in the Long Coulee Glauconite F Pool, Alberta*. Denver, Colorado, U.S.A.: SPE 115789. <http://www.spe.org/elibrary/app/newSearch.do> (accessed May 10, 2009).
- Delclaud, J., J. Rochon, and A. Nectoux. 1987. *SPE Annual Technical Conference and Exhibition, September, 27-30 1987: Investigation of Gas/Oil Relative Permeabilities: High-Permeability Oil Reservoir Application*. Dallas, Texas, U.S.A.: SPE 16966. <http://www.onepetro.org/> (accessed May, 30 2009).
- Dewitt, K. J., and G. Thodos. 1966. Viscosities of binary mixtures in the dense gaseous state: The methane-carbon dioxide system. *The Canadian Journal of Chemical Engineering* 44 (3): 148-151.
- Djabbarah, N. F., S. L. Weber, D. C. Freeman, J. A. Muscatello, J. P. Ashbaugh, and T. E. Covington. 1990. Laboratory Design and Field Demonstration of Steam Diversion With Foam. In *SPE California Regional Meeting*. California, U.S.A. SPE 20067.
- Flett, M., R. Gurton, and I. Taggart. 2004. *SPE Asia Pacific Oil and Gas Conference and Exhibition, October, 18-20 2004: The Function of Gas-Water Relative Permeability Hysteresis in the Sequestration of Carbon Dioxide in Saline Formations* Perth, Australia: SPE 88458. 18-20 October 2004 (accessed September, 20 2008).
- Friedmann, F., T. L. Hughes, M. E. Smith, G. P. Hild, A. Wilson, and S. N. Davies. 1997. *SPE Annual Technical Conference and Exhibition, October 5-8, 1997: Development and Testing of a New Foam-Gel Technology to Improve Conformance of the Rangely CO₂ Flood*. San Antonio, Texas, U.S.A.: SPE

- 38837-MS. <http://www.spe.org/elibrary/app/newSearch.do> (accessed May 15, 2009).
- Gale, J., and P. Freund. 2000. Coal Bed Methane Enhancement with CO₂ Sequestration: Worldwide Potential. In *21th World Gas Conference*. Nice, France.
- Gaspar, A. T. F. S., G. A. C. Lima, and S. B. Suslick. 2005. *SPE Europec/EAGE annual conference, June 13-16, 2005: CO₂ Capture and Storage in Mature Oil Reservoir: Physical Description, EOR and Economic Valuation of a Case of a Brazilian Mature Field*. Madrid, Spain: SPE 94181. <http://www.spe.org/elibrary/app/newSearch.do> (accessed April 3, 2008).
- Gennes, P., F. Brochard-Wyart, D. Quere, D. Quéré, F. Brochard-Wyart, and A. Reisinger. 2004. *Capillarity and wetting phenomena*. Berlin: Springer.
- Gunter, W. D., S. Bachu, D. H. Law, V. Marwaha, D. L. Drysdale, D. E. MacDonald, and T. J. McCann. 1996. Technical and economic feasibility of CO₂ disposal in aquifers within the Alberta sedimentary basin, Canada. *Energy Conversion and Management* 37 (6-8): 1135-1142.
- Gunter, W. D., E. H. Perkins, and T. J. McCann. 1993. Aquifer disposal of CO₂-reaction design for added capacity. *Energy Conversion and Management* 34 (9-11): 941-948.
- Haefeli, S., M. Bosi, and C. Philibert. 2004. Carbon Dioxide Capture and Storage Issues-Accounting and Baseline Under the United Nations Framework Convention on Climate Change. http://www.iea.org/Textbase/publications/free_new_Desc.asp?PUBS_ID=1023.
- Hagoort, J. 1998. *Fundamental of gas reservoir engineering*. New York: Elsevier Science Publishers.
- Haniff, M. S., and J. K. Ali. 1990. Relative Permeability and Low Tension Fluid Flow in Gas Condensate Systems In *European Petroleum Conference*. The Hague, Netherlands. SPE 20917.
- Harbert, L. W. 1983. *SPE Annual Technical Conference and Exhibition, October, 5-8 1983: Low Interfacial Tension Relative Permeability* San Francisco, California, U.S.A.: SPE 12171. <http://www.onepetro.org/> (accessed Jun, 8 2009).
- Henderson, G. D., A. Danesh, D. H. Tehrani, S. Ashaidi, and J. M. Penden. 1996. Measurement and correlation of gas condensate relative permeability by the steady-state method. *Society Petroleum Engineering Journal* 1 (2): 191-201.

- Hiraski, G. J. 1989. The steam-foam process. *Jouranl of Petroleum Technology* 41 (5): 449-456.
- Holloway, S. 1996. An overview of the Joule II project 'The underground disposal of carbon dioxide'. *Energy Convers.* 37 (6-8): 1149-1154.
- Hughes, T. L., F. Friedmann, D. Johnson, G. P. Hild, A. Wilson, and S. N. Davies. 1999. Large-volume foam-gel treatments to improve conformance of the rangely CO₂ flood *SPE Reservoir Evaluation & Engineering* 2 (11): 14-24.
- Jerauld, G. R. 1997. General three-phase relative permeability model for Prudhoe Bay. *SPE reservoir Engineering*, 12 (4): 255-263.
- Jikich, S., D. Smith, W. Sams, and G. Bromhal. 2003. Enhanced Gas Recovery (EGR) with Carbon Dioxide Sequestration: A Simulation Study of Effects of Injection Strategy and Operational Paraeters. In *SPE Eastern Regional/AAPG Eastern Section Joint Meeting*. Pittsburgh, Pennsylvania, U.S.A. SPE 84813.
- Johnson, E. F., D. P. Bossler, and O. V. Naumann. 1959. Calculation of relative permeability from displacement experiments. *Petroleum Transactions, AIME* 216: 370-372.
- Jones, S. C., and O. W. Rozelle. 1978. Graphical techniques for determining relative permeability from displacement experiments. *Jouranl of Petroleum Technology* 30 (5): 807-817.
- Kalaydjian, F. J.-M., B. J. Bourbiaux, and J.-M. Lombard. 1996. *SPE Annual Technical Conference and Exhibition, October, 6-9 1996: Predicting gas-condensate reservoir performance: how flow parameters are altered when approaching production wells*. Denver, Colorado, U.S.A.: SPE 36715. <http://www.onepetro.org/> (accessed July, 1 2009).
- Kempers, L. J. T. M., and H. Haas. 1994. The dispersion zone between fluids with different density and viscosity in a heterogeneous porous medium. *Journal of Fluid Mechanics* 267: 299-324.
- Kerig, P. D., and A. T. Watson. 1987. A new algorithm for estimating relative permeabilities from displacement experiments. *SPE Reservoir Engineering* 2 (1): 103-112.
- Khatib, Z. I., G. J. Hirasaki, and A. H. Fall. 1988. Effect of capillary pressure on coalescenes and phase mobilities in foam flowing through porous media. *SPE Reservoir Engineering* 3 (3): 919-926.
- Killough, J. E. 1976. Reservoir simulation with history dependent saturation functions. *SPE Journal* 11 (4): 37-48.

- Kozeny, J. 1927. Uber Kapillare Leitung Des Wassers in Boden. *Sitzungsberichte der Wiener Akademie des Wissenschaften* 136 (2a): 271-306.
- Krichevskii, I. R. 1940. Limited mutual solubility of gases at high pressures. *Acta Phys. Chem. U.S.S.R.* 12: 480.
- Kumar, A., R. Ozah, M. Noh, G. A. Pope, S. Bryant, K. Sepehrnoori, and L. W. Lake. 2005. Reservoir simulation of CO₂ storage in deep saline aquifers. *Jouranal of Petroleum Technology* 10 (3): 336-348.
- Laille, J. P., J. E. Molinard, and A. Wents. 1988. Inert Gas Injection as Part of the Cushion of the Underground Storage of Saint-Clair-Sur-Epte, France. In *SPE Gas Technology Symposium*. Dallas, Texas, U.S.A. SPE 17740.
- Lake, L. 1989. *Enhanced oil recovery*. Englewood Cliffs NJ: Prentice Hall.
- Land, C. S. 1968. Calculation of imbibition relative permeability for two and three phase flow from rock properties. *SPE Journal* 8 (2): 149-156.
- Larsen, J. A., and A. Skauge. 1998. Methodology for numerical simulation with cycle-dependent relative permeailities *SPE Journal* 3 (2): 163-173.
- Larson, R. G., H. T. Davis, and L. E. Scriven. 1981. Displacement of residual nonwetting fluid from porous media. *Chemical Engineering Science* 36 (1): 75-85.
- Lawal, A. S., and S. M. Frailey. 2004. *SPE Annual Technical Conference and Exhibition, September, 26-29 2004: Material Balance Reservoir Model for CO₂ Sequestration in Depleted Gas Reservoirs*. Houston, Texas, U.S.A.: SPE 90669-MS. <http://www.onepetro.org> (accessed May, 15 2009).
- Leverett, M. C. 1939. Flow of oil-water mixtures through unconsolidated sands. *Transactions, AIME* 139: 149-171.
- Leverett, M. C. 1941. Capillary bhavior in porous media. *Transactions, AIME* 142: 341-358.
- Li, H., X. Ji, and J. Yan. 2005. A new modification on RK EOS for gaseous CO₂ and gaseous mixtures of CO₂ and H₂O. *International Journal of Energy Research* 30 (3): 135-148.
- Ligthelm, D. J., G. J. M. van Eijden, and J. Gronsveld. 2000. Gas shut off using foam: The solution for unwanted gas production? In *SPE European Petroleum Conference*. Paris, France. SPE 65125-MS.
- Mamora, D., and G. Seo. 2002. *SPE Annual Technical Conference and Exihition, September 29-October 2, 2002: Enhanced Gas Recovery by Carbon Dioxide Sequestration in Depleted Gas Reservoirs*. San Antonio, Texas, U.S.A.: SPE

77347. <http://www.spe.org/elibrary/app/newSearch.do> (accessed February 19, 2008).
- Martin, F. D. 1992. Carbon dioxide flooding. *Journal of Petroleum Technology* 44 (4): 396-400.
- Martinez, J. 1998. Foam Flow Behavior in Porous Media: Effects of Flow Regime and Porous Medium Heterogeneity. PhD thesis, The University of Texas, Austin, Texas
- Mathews, C. S. 1989. *Carbon dioxide flooding, Chapter 6, Enhanced Oil Recovery, II Process and Operations*. Edited by E. C. Donaldson, G. V. Chilingraian and T. F. Yen. Amsterdam Elsevier.
- Mazumder, S., and K. H. Wolf. 2008. *SPE Asia Pacific Oil and Gas Conference and Exhibition, October, 20-22 2008: CO₂ and Flue Gas Coreflood Experiments for Enhanced Coalbed Methane*. Perth, Australia: SPE 114790. <http://www.onepetro.org> (accessed June, 15 2009).
- McHugh, M. A., and V. J. Krukoni. 1986. *Supercritical Fluid Extraction, Principles and Practice*. Boston, MA: Butterworths.
- Moegen, H. D., and H. Giouse. 1989. *SPE Annual Technical Conference and Exhibition, October, 8-11 1989: Long-Term Study of Cushion Gas Replacement by Inert Gas*. San Antonio, Texas, U.S.A.: SPE 19754. www.onepetro.org (accessed April, 22 2009).
- Moritis, G. 2000. EOR weathers low oil prices. *Oil and Gas Journal* 98 (12): 39-61.
- Muskat, M., and M. W. Meres. 1936. The flow of heterogeneous fluids through porous media. *Physics* 7: 346-363.
- Muskat, M., R. D. Wyckoff, H. G. Botset, and M. W. Meres. 1937. Flow of gas-liquid mixtures through sands. *Petroleum Transactions, AIME* 123: 69-96.
- Nieva, D., and R. M. Barragán. 2003. HCO-TERNARY: A FORTRAN code for calculating P-V-T-X properties and liquid vapor equilibria of fluids in the system H₂O-CO₂-CH₄. *Computers & Geosciences* 29 (4): 469 -485
- Noh, M., L. W. Lake, S. L. Bryant, and A. Araque-Martinez. 2007. Implications of coupling fractional flow and geochemistry for CO₂ injection in aquifers *SPE Reservoir Evaluation & Engineering* 10 (4): 406-414.
- Oldenburg, C. 2003. *Proceedings, Tough Symposium, May 12-14, 2003: Carbon Sequestration in Natural Gas Reservoirs: Enhanced Gas Recovery and Natural Gas Storage*. Berkeley, California U.S.A.: DOE Scientific and Technical Information. <http://www.osti.gov/bridge> (accessed April 14,2009).

- Oldenburg, C., and S. Benson. 2002. CO₂ Injection for Enhanced Gas Production and Carbon Sequestration. In *SPE International Petroleum Conference and Exhibition in Mexico* Villahermosa, Mexico. SPE 74367.
- Oldenburg, C., K. Pruess, and S. Benson. 2001. Process modeling of CO₂ injection into natural gas reservoirs for carbon sequestration and enhanced gas recovery. *Energy and Fuels* 15: 293-298.
- Perkins, T. K., and O. C. Johnston. 1963. A review of diffusion and dispersion in porous media. *SPE Journal* 3 (1): 70-84.
- Peters, E. J., and S. Khataniar. 1987. The effect of instability on relative permeability curves obtained by the dynamic-displacement method. *SPE Formation Evaluation* 2 (4): 469-474.
- Pojman, J., C. Whitmore, M. Turco Liveri, R. Lombardo, J. Marszalek, R. Parker, and B. Zoltowski. 2006. Evidence for the Existence of an Effective Interfacial Tension between Miscible Fluids: Isobutyric Acid–Water and 1-Butanol–Water in a Spinning-Drop Tensiometer. *Langmuir* 22 (6): 2569-2577.
- Pope, G. A., W. Wu, G. Narayanaswamy, M. Delshad, M. Sharma, and P. Wang. 1998. *SPE Annual Technical Conference and Exhibition, September, 27-30 1998: Modeling Relative Permeability Effects in Gas-Condensate Reservoirs* New Orleans, Louisiana, U.S.A.: SPE 49266. <http://www.onepetro.org/> (accessed June, 18 2009).
- Prey, L. d. 1973. Factors affecting liquid-liquid relative permeabilities of a consolidated porous medium. *SPE Journal* 13 (1): 39-47.
- Pruess, K., T. Xu, J. A. Apps, and J. Garcia. 2003. Numerical modeling of aquifer disposal of CO₂. *Society Petroleum Engineering Journal* 8 (1): 49-60.
- Richards, L. A. 1931. Capillary conduction of liquids through porous media. *Physics* 1: 318-333.
- Rossen, W. R., and Q. Lu. 1997. Effect of Capillary Crossflow on Foam Improved Oil Recovery In *SPE Western Regional Meeting* Long Beach, California, U.S.A. SPE 38319.
- Rossen, W. R., and Z. H. Zhou. 1995. Modeling foam mobility at the 'limiting capillary pressure'. *SPE Advanced Technology Series* 3 (1): 146-153.
- Schechter, D. S. 1988. Immiscible Flow Behaviour in Porous Media. PhD thesis, Petroleum Engineering, University of Bristol, Bristol, UK
- Schechter, D. S., and J. M. Haynes. 1992. Relative permeability of a near critical binary fluid. *Transport in Porous Media* 9 (3): 241-260.

- Scheidegger, A. E. 1974. *The Physics of Flow Through Porous Media*. Toronto, Ontario, Canada: University of Toronto Press.
- Sengul, M. 2006. *SPE international conference on health, safety, and environment in oil and gas exploration and production April 2-4, 2006: CO₂ Seuestration—A Safe Transition Technology*-. Abu Dhabi, U.A.E.: SPE 98617. <http://www.spe.org/elibrary/app/newSearch.do> (accessed March 10, 2008).
- Seo, G., and D. Mamora. 2003. *SPE/EPA/DOE Exploration and Production Environmental Conference, March 10-12, 2003: Experimental and Simulation Studies of Sequestration of Supercritical Carbon Dioxide in Depleted Gas Reservoirs*. San Antonio, Texas, U.S.A.: SPE 81200. <http://www.spe.org/elibrary/app/newSearch.do> (accessed March 13, 2006).
- Seo, J. 2004. Experimental and Simulation Studies of Sequestration of Supercritical Carbon Dioxide in Depleted Gas Reservoirs. PhD thesis, Petroleum Engineering, Texas A&M University, Texas.
- Seo, Y., H. Lee, and T. Uchida. 2002. Methane and carbon dioxide hydrate phase behavior in small porous silica gels: Three-phase equilibrium determination and thermodynamic modeling. *Langmuir* 18: 9164-9170. <http://pubs.acs.org> (accessed May 12, 2009).
- Shi, J. Q., and S. Durucan. 2003. A bidisperse pore diffusion model for methane displacement desorption and coal by CO₂ injection. *Fuel* 82: 1219.
- Sidiq, H., and R. Amin. 2009. Mathematical model for calculating the dispersion coefficient of super critical CO₂ from the results of laboratory experiments on enhanced gas recovery. *Journal of Natural Gas Science and Engineering* 1: 177-182.
- Sloan, E. D. 1998. *Clathrate Hydrates of Natural Gases*. 2nd Edit ed. New York Marcel Dekker Inc.
- Stegemeier, G. L. 1977. *Oil Entrapment and Mobilization in Porous Media*. Edited by D. S. a. R. Schechter, *Improved Oil Recovery by Surfactant and Polymer Flooding*. New York: Academic Press, Inc.
- Stevens, S. H., and P. Riemer. 1998. Enhanced Coalbed Methane Recovery Using CO₂ Injection: Worldwide Resource and CO₂ Sequestration Potential. In *SPE International Conference and Exhibition*. Beijing, China. SPE 48881.
- Syahrial, E. 2005. *Asia Pacific Oil and Gas Conference and Exhibition, April, 5-7 2005: Coalbed Methane Simulator Development for Improved Recovery of Coalbed Mehtane and CO₂ Sequestration*. Jakarta, Indonesia: SPE 93160. <http://www.onepetro.org/> (accessed July, 5 2009).

- Taber, J. J. 1981. Research on enhanced oil recovery: Past present and future. *Pure & Appl. Chem* 52: 1323—1347.
- Taber, J. J., F. D. Martin, and R. S. Seright. 1997. EOR screening criteria revisited—part 2: Applications and impact of oil prices. *SPE Reservoir Engineering* 12 (3): 199-205.
- Tanzil, D. 2001. Foam Generation and Propagation in Heterogeneous Porous Media. PhD Thesis, Rice University, Houston, Texas.
- Tao, T. M., and A. T. Watson. 1984a. Accuracy of JBN estimates of relative permeability: Part 1 - Error analysis. *SPE Journal* 24 (2): 209-214.
- Tao, T. M., and A. T. Watson. 1984b. Accuracy of JBN estimates of relative permeability: Part 2- Algorithms *SPE Journal* 24 (2): 215-223.
- Teletzke, G. F., L. E. Scriven, and H. T. Davis. 1981. *SPE Annual Technical Conference and Exhibition, October, 4-7 1981: Patterns of Wetting Behavior in Multicomponent Systems* San Antonio, Texas, U.S.A.: SPE 10112. <http://www.onepetro.org/> (accessed July, 4 2009).
- Thiéry, R., Van den Kerkhof AM, and J. Dubessy. 1994. vX properties of CO₂-CH₄ and CO₂-N₂ fluid inclusions: modelling for T < 31 °C and P < 400 bars. *European Journal of Mineralogy* 6: 47–55.
- Todd, M. R., and G. W. Grand. 1993. Enhanced oil recovery using carbon dioxide. *Energy Conversion and Management* 34: 1157-1164.
- Todd, M. R., and W. J. Longstaff. 1972. The development, testing and application of a numerical simulator for predicting miscible flood performance. *Jouranal of Petroleum Technology* 24 (7): 874-882.
- Van der Burgt, M. J., J. Cattle, and V. K. Boutkan. 1992. Carbene dioxide diposal from coal-based IGCC's in depleted gas fields. *Convers. Mgmt* 33 (5-8): 603.
- Van Lingen, P. P. 1998. Quantification and Reduction of Capillary Entrapment in Cross-Laminated Oil Reservoirs. PhD thesis, Dietz Laboratory, Delft University of Technology Delft
- Vizika, O., D. G. Avraam, and A. C. Payatakes. 1994. On the role of the viscosity ratio during low-capillary-number forced imbibition in porous media. *Journal of Colloid and interface Science* 165 (2): 386-401.
- Watson, A. T., P. C. Richmond, P. D. Kerig, and T. M. Tao. 1988. A Regression-Based Method for Estimating Relative Permeabilities From Displacement Experiments. *SPE reservoir Engineering* 3 (3): 953-958.
- Wei, Y. S., and R. J. Sadus. 1996. Vapour-liquid and liquid-liquid-phase equilibria of binary mixtures containing helium: comparison of experiment with

predictions using equations of state. *Fluid Phase Equilibria* 122 (Elsevier Science): 1-15.

- White, H. 1972. *Modern College Physics*. New York: Van Nostrand Reinhold Co.
- Wyckoff, R. D., and H. G. Botset. 1936. The flow of gas-liquid mixtures through unconsolidated sand. *Physics* 7: 325-345.
- Xu, T., J. A. Apps, and K. Pruess. 2000. *Analysis of mineral trapping for CO₂ disposal in deep qauifers*. California, U.S.A.: Lawrence Berkeley National Laboratory. <http://www.osti.gov/bridge/purl.cover.jsp?purl=/789133-LyYk7x/native/> (accessed July, 8 2009).
- Yasuhiko, S., O. Koji, H. Akihideo, T. Manabu, and K. Takenhiko. 2004. Effect of interfacial tension of two miscible liquid flow in micro fluidic device. *Nippon Dennetsu Shinpojiumu Koen Ronbunshu* 41 (2): 391-392.
- Young, T. 1805. An essay on the cohesion of fluids. *Philosophical Transactions of the Royal Society of London* 95: 65-87.
- Zhenhao, D., and S. Rui. 2003. An improved model calculating CO₂ solubility in pure water and aqueous NaCl solutions from 273 to 533 K and from 0 to 2000 bar. *Chemical Geology* 193: 257-271.
- Zhu, T., B.P.McGrail, A.S.Kulkarni, M.D.White, H. Phale, and D.Ogbe. 2005. Development of a Thermodynamic Model and Reservoir Simulator for the CH₄, CO₂, and CH₄-CO₂ Gas Hydrate System. In *SPE Western Regional Meeting*. Irvine, California, U.S. A. SPE 93976.
- Zoltowski, B., Y. Chekanov, J. Masere, J. A. Pojman, and V. Volpert. 2007. Evidence for the Existence of an Effective Interfacial Tension between Miscible Fluids. 2. Dodecyl Acrylate-Poly(Dodecyl Acrylate) in a Spinning Drop Tensiometer. *Langmuir* 23: 5522-5531.

Every reasonable effort has been made to acknowledge the owners of copyright material. I would be pleased to hear from any copyright owner who has been omitted or incorrectly acknowledged.

Appendix

Appendix A:

Table A-1: Equipment types and specifications.

S.N.	Instruments	Type	Model	Specification
1	Syringe pump	Shimadzu	LC-20AT	0.001 to 10.0mL/min
2	BPR	Swageloke	KHB1X0A4C2P20000	100-10000 psig
3	Flow meter 1	King	74C102G021313410	200 psi, 93 °C
4	Flow meter 2	Sierra Instrument	Smart-track 2	0-50 slpm
5	Thermometer	K, J type	Deluxe dual input	-200 to 1,370 °C
6	Pressure transducer	Gems	3100B10KPS01B0	0-10000 psia
7	CO ₂ analyzer	PemTeck	PT605	0-100%
8	Data taker	Data taker	DT50	-----
9	Air bath	Sanchez technology	PVT 70-1500	-20-300 °C
10	Tubes	Swageloke	1/16 and 1/8 inch	11000 psi@250 °C
11	Micro metering valve	Autoclave	10VRMM2812	Cv 0.004, 0-15000 psi
12	Core holder	Hassler Type	Stainless steel	0-11000 psi, 250 °C
13	Core sleeve	Ergo-Tech	ECS378/36/050V in 75 IRHD FPM 'B'	-10 to 250 °C

Appendix B:

Table B-1: Decane-Brine relative permeability for sample S_C_1A at ambient condition by centrifuge.

COMPANY : SHELL AUSTRALIA LIMITED
WELL

Decane-Brine relative permeability by centrifuge at ambient

PRELIMINARY RESULTS

Sample no	Depth (metres)
S.C.1A	4144.28

At Ambient	
Porosity (%)	K air (md)
17.9	391

Water-displacing-Decane			Oil-displacing-Decane		
Initial water sat. (%pv)	K decane at Swi (md)	K water at Swr (md)	Residual decane sat. (%pv)	K decane at Swr (md)	Final water sat. (%pv)
7.2	364	98.6	34.3	106	12.5

**Relative to the effective permeability to Oil at Swi.

E.F. = End Face

Water Increasing	
E.F. water saturation (%pv)	Relperm ** to Oil (fraction)
7.2	1.00E+00
15.1	4.32E-01
18.3	3.79E-01
25.9	2.20E-01
32.9	1.22E-01
37.2	7.92E-02
42.4	4.30E-02
45.4	2.79E-02
49.0	1.53E-02
52.6	7.20E-03
56.3	2.64E-03
58.9	9.89E-04
61.8	2.16E-04
63.1	8.42E-05
64.3	2.48E-05
64.8	1.33E-05
65.7	3.17E-06

Water decreasing	
E.F. water saturation (%pv)	Relperm ** to Water (fraction)
65.7	2.71E-01
62.6	9.22E-02
57.9	6.56E-02
51.3	3.90E-02
46.9	2.65E-02
43.8	1.95E-02
38.6	1.12E-02
35.4	7.46E-03
31.4	4.22E-03
28.9	2.82E-03
25.9	1.59E-03
21.8	6.01E-04
18.6	2.27E-04
17.2	1.28E-04
16.3	8.55E-05
14.8	3.89E-05
12.5	6.76E-06

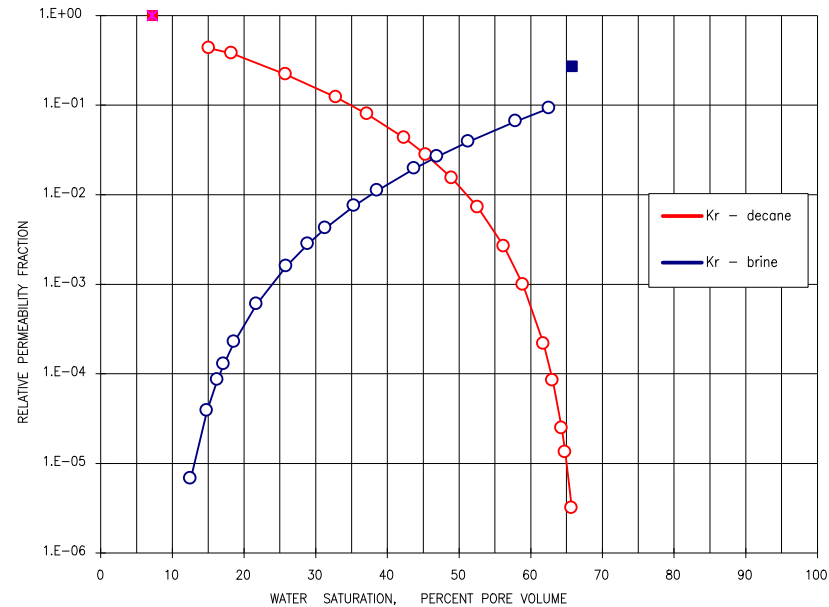


Table B-2: Decane-Brine relative permeability for sample S_C_1B at ambient condition by centrifuge.

COMPANY : SHELL AUSTRALIA LIMITED
WELL

Decane-Brine relative permeability by centrifuge at ambient

PRELIMINARY RESULTS

Sample no	Depth (metres)
S.C.1B	4144.33

At Ambient	
Porosity (%)	K air (md)
17.6	421

Water-displacing-Decane				Oil-displacing-Decane	
Initial water sat. (%pv)	K decane at Swi (md)	K water at Swr (md)	Residual decane sat. (%pv)	K decane at Swr (md)	Final water sat. (%pv)
8.3	390	98.7	36.0	170	10.4

**Relative to the effective permeability to Oil at Swi.

E.F. = End Face

Water Increasing	
E.F. water saturation (%pv)	Relperm ** to Oil (fraction)
8.3	1.00E+00
18.5	3.79E-01
27.4	2.20E-01
34.9	1.22E-01
39.2	7.92E-02
44.3	4.30E-02
47.2	2.79E-02
50.5	1.53E-02
53.8	7.20E-03
55.9	3.99E-03
57.1	2.64E-03
58.5	1.48E-03
60.0	7.23E-04
61.8	2.16E-04
62.9	8.42E-05
63.3	4.89E-05
64.0	1.95E-05

Water decreasing	
E.F. water saturation (%pv)	Relperm ** to Water (fraction)
64.0	2.53E-01
59.4	9.57E-02
54.3	5.92E-02
50.8	4.18E-02
46.3	2.54E-02
43.3	1.78E-02
41.1	1.35E-02
37.4	8.19E-03
35.0	5.75E-03
31.8	3.50E-03
29.8	2.46E-03
27.1	1.50E-03
23.1	6.52E-04
19.6	2.85E-04
16.6	1.25E-04
14.4	6.50E-05
10.4	1.55E-05

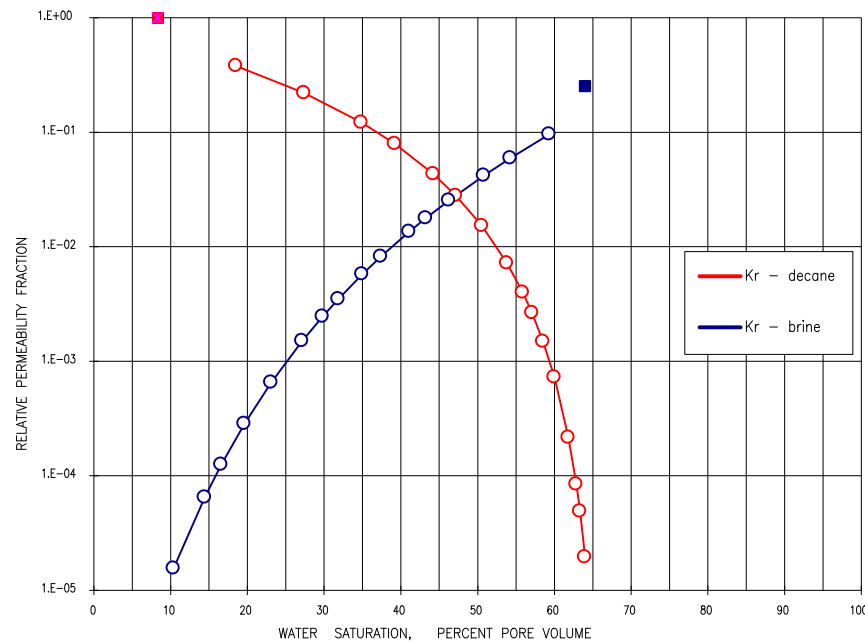


Table B-3: Decane-Brine relative permeability for sample S_C_2A at ambient condition by centrifuge.

COMPANY : SHELL AUSTRALIA LIMITED
WELL

Decane-Brine relative permeability by centrifuge at ambient

PRELIMINARY RESULTS

Sample no	Depth (metres)
S.C.2A	4160.68

At Ambient	
Porosity (%)	K air (md)
14.1	115

Water-displacing-Decane				Oil-displacing-Decane	
Initial water sat. (%pv)	K decane at Swi (md)	K water at Swr (md)	Residual decane sat. (%pv)	K decane at Swr (md)	Final water sat. (%pv)
9.6	105	47.7	27.5	42.8	8.3

** Relative to the effective permeability to Oil at Swi.

E.F. = End Face

Water Increasing	
E.F. water saturation (%pv)	Relperm ** to Oil (fraction)

9.6	1.00E+00
17.3	1.50E-01
24.0	9.92E-02
32.2	5.50E-02
37.2	3.62E-02
43.1	2.00E-02
46.7	1.32E-02
49.2	9.58E-03
53.1	5.37E-03
55.5	3.57E-03
58.4	2.02E-03
62.3	7.77E-04
65.3	3.03E-04
67.6	1.20E-04
69.4	4.79E-05
70.6	2.31E-05
72.5	4.73E-06

Water decreasing	
E.F. water saturation (%pv)	Relperm ** to Water (fraction)

72.5	4.54E-01
64.2	1.2E-01
55.6	7.1E-02
50.3	4.7E-02
43.7	2.7E-02
39.6	1.8E-02
36.8	1.3E-02
32.3	7.4E-03
29.5	5.0E-03
26.1	2.8E-03
24.0	1.9E-03
21.4	1.1E-03
17.7	4.4E-04
14.8	1.8E-04
12.5	7.3E-05
10.7	3.0E-05
8.3	7.6E-06

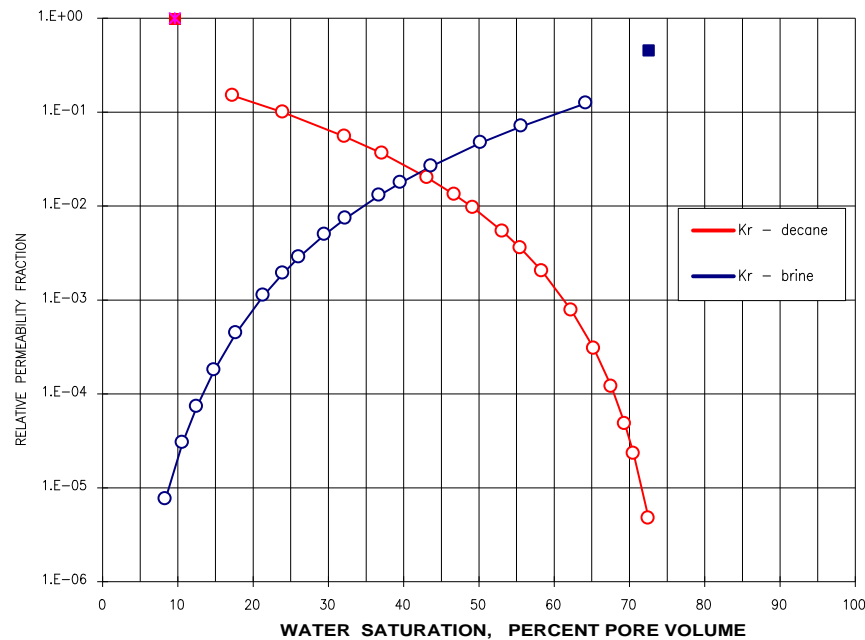


Table B-4: Decane-Brine relative permeability for sample S_C_2B at ambient condition by centrifuge.

COMPANY : SHELL AUSTRALIA LIMITED
WELL

Decane-Brine relative permeability by centrifuge at ambient

PRELIMINARY RESULTS

Sample no	Depth (metres)
S.C.2B	4160.75

At Ambient	
Porosity (%)	K air (md)
14.1	123

Water-displacing-Decane				Oil-displacing-Decane	
Initial water sat. (%pv)	K decane at Swi (md)	K water at Swr (md)	Residual decane sat. (%pv)	K decane at Swr (md)	Final water sat. (%pv)
7.1	114	57.3	23.0	59.5	12.5

**Relative to the effective permeability to Oil at Swi.

E.F. = End Face

Water Increasing	
E.F. water saturation (%pv)	Relperm ** to Oil (fraction)
7.1	1.00E+00
14.0	1.86E-01
23.4	1.21E-01
35.0	6.45E-02
41.8	4.10E-02
49.8	2.15E-02
54.4	1.36E-02
57.5	9.48E-03
62.1	4.93E-03
64.8	3.10E-03
67.9	1.60E-03
71.6	5.06E-04
74.1	1.53E-04
75.6	4.23E-05
76.5	9.21E-06
76.8	2.66E-06
77.0	4.50E-07

Water decreasing	
E.F. water saturation (%pv)	Relperm ** to Water (fraction)
77.0	5.03E-01
71.9	2.4E-01
62.6	1.3E-01
57.0	8.7E-02
50.2	4.9E-02
46.1	3.2E-02
41.1	1.8E-02
38.0	1.2E-02
35.9	9.1E-03
32.5	5.3E-03
27.7	2.1E-03
23.9	8.5E-04
20.9	3.5E-04
18.5	1.5E-04
16.4	6.2E-05
14.7	2.7E-05
12.5	7.1E-06

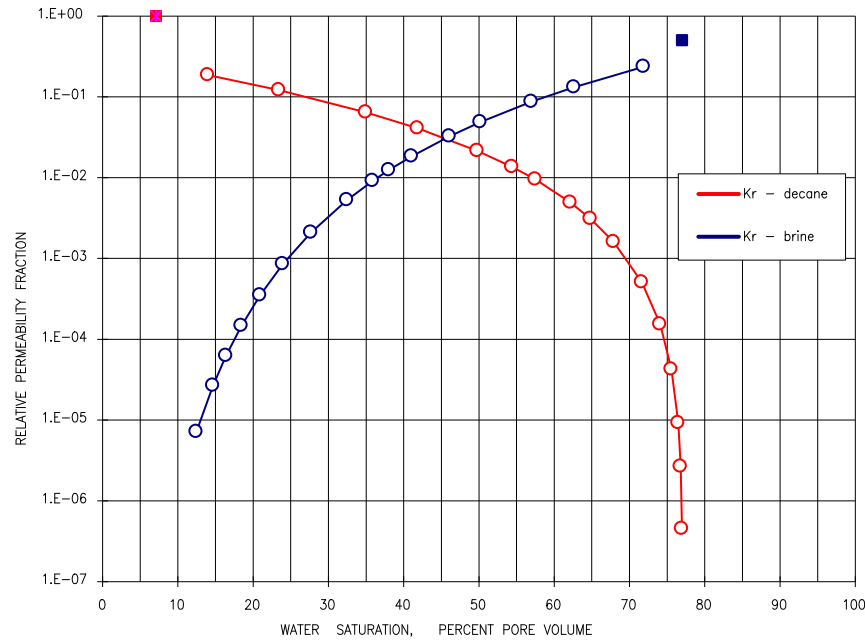


Table B- 5: Decane-Brine relative permeability for sample S_C_3A at ambient condition by centrifuge.

COMPANY : SHELL AUSTRALIA LIMITED
WELL

Decane-Brine relative permeability by centrifuge at ambient

PRELIMINARY RESULTS

Sample no	Depth (metres)
S.C.3A	4184.37

At Ambient	
Porosity (%)	K air (md)
9.9	8.37

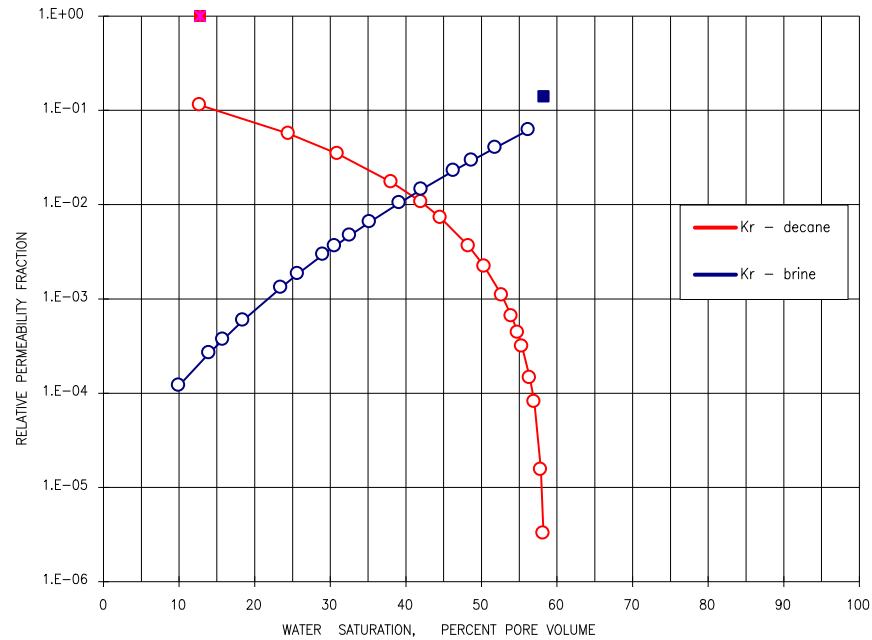
Water-displacing-Decane				Oil-displacing-Decane	
Initial water sat. (%pv)	K decane at Swi (md)	K water at Swr (md)	Residual decane sat. (%pv)	K decane at Swr (md)	Final water sat. (%pv)
12.8	6.95	0.980	41.8	7.70	10.0

**Relative to the effective permeability to Oil at Swi.

E.F. = End Face

Water Increasing	
E.F. water saturation (%pv)	Relperm ** to Oil (fraction)
12.8	1.00E+00
12.7	1.14E-01
24.5	5.67E-02
31.0	3.46E-02
38.1	1.73E-02
42.0	1.06E-02
44.6	7.25E-03
48.3	3.62E-03
50.4	2.21E-03
52.7	1.09E-03
54.0	6.55E-04
54.8	4.38E-04
55.4	3.13E-04
56.4	1.45E-04
57.0	8.10E-05
57.9	1.54E-05
58.2	3.24E-06

Water decreasing	
E.F. water saturation (%pv)	Relperm ** to Water (fraction)
58.2	1.41E-01
56.2	6.2E-02
51.9	4.0E-02
48.7	2.9E-02
46.3	2.3E-02
42.1	1.4E-02
39.2	1.0E-02
35.2	6.5E-03
32.6	4.7E-03
30.6	3.6E-03
29.0	2.9E-03
25.7	1.8E-03
23.5	1.3E-03
18.5	5.9E-04
15.8	3.7E-04
14.0	2.7E-04
10.0	1.2E-04



Appendix C:

Permeability calculation:

To calculate permeability from experimental data the modified Darcy are used as follow to obtain K in (md):

$$K = 14700 \cdot Q \cdot \mu \cdot \left(\frac{L}{A}\right) / (\Delta p \cdot 60) \quad (C1)$$

Where K is permeability to liquid, md, L sample length, cm, Q flow rate, cm^3 per min, Δp Pressure difference across the core sample, atmospheres, μ viscosity, centipoise, A cross sectional area, cm^2 .

Effective permeability for any phase is calculated when Δp across the core sample stabilized at the end of the run and the effluent composition approach influent composition.

Table C-1: Endpoint relative permeability calculated from brine displacement by $90C_1$.

Samples	L	A	Displacement	Test condition	Δp (psi)	Flow rate		Speed cm/hr	Visc (cp)	Kg (md)	Swi
						Reservoir (cc/min)	Ambient (cc/min)				
S_C_1A	5	12.25	$90C_1@Swi$	160 C and 5900 psia	3.7	0.336	89.1	9.3	0.0252	61.7	11.3
S_C_2A	5.05	11.89	$90C_1@Swi$	160 C and 5900 psia	5	0.284	75	9.7	0.0252	40.3	14.5
S_C_3A	5.1	12.01	$90C_1@Swi$	160 C and 5900 psia	8.6	0.198	50	9.2	0.0252	16.5	9.6
S_V_1	19.41	11.95	$90C_1@Swi$	160 C and 5900 psia	4.8	0.291	76	10	0.0252	156.4	14.7

Table C-2: Endpoint relative permeability calculated from $90C_1$ displacement by SCO_2 .

Samples	L	A	Displacement	Test condition	Δp (psi)	Flow rate		Speed cm/hr	Visc (cp)	Kg (md)	B.T (Pv)
						Reservoir (cc/min)	Ambient (cc/min)				
S_C_1A	5	12.25	$98SCO_2@C_1$	160 C and 5900 psia	5	0.341	98	9.6	0.0497	97.4	4.8
S_C_2A	5.05	11.89	$98SCO_2@C_1$	160 C and 5900 psia	6.6	0.272	86	9.2	0.0497	67.4	5.4
S_C_3A	5.1	12.01	$98SCO_2@C_1$	160 C and 5900 psia	9.1	0.201	58	9.4	0.0497	32.9	0.62
S_V_1	19.41	11.95	$98SCO_2@C_1$	160 C and 5900 psia	5.8	0.265	79	9.1	0.0497	270	7.2

Table C-3: Endpoint relative permeability obtained from displacement tests at different injection rates.

S_V_1	19.41	11.95	$98SCO_2@C_1$	160 C and 5900 psia	3.4	0.0297	9.1	1.03	0.0497	52.9	0.16
S_V_1	19.41	11.95	$98SCO_2@C_1$	160 C and 5900 psia	3.8	0.0656	18.2	2.27	0.0497	94.7	0.24
S_V_1	19.41	11.95	$98SCO_2@C_1$	160 C and 5900 psia	4.5	0.143	41.5	4.94	0.0497	182.4	0.35
S_V_1	19.41	11.95	$98SCO_2@C_1$	160 C and 5900 psia	4.9	0.209	60	7.3	0.0497	242.2	0.49
S_V_1	19.41	11.95	$98SCO_2@C_1$	160 C and 5900 psia	5.8	0.265	79	9.1	0.0497	270	0.72

Table C-4: Endpoint relative permeability calculated from displacement tests at different pore-pressures.

S_V_1	19.41	11.95	$98SCO_2@C_1$	160 C and 1500 psia	3.6	0.284	20	9.8	0.0241	53.3	0.43
S_V_1	19.41	11.95	$98SCO_2@C_1$	160 C and 2500 psia	4	0.294	39	10.2	0.0282	109.4	0.45
S_V_1	19.41	11.95	$98SCO_2@C_1$	160 C and 3500 psia	4.35	0.284	55	9.8	0.034	171.1	0.54
S_V_1	19.41	11.95	$98SCO_2@C_1$	160 C and 4500 psia	4.7	0.275	65	9.5	0.0404	222.3	0.6
S_V_1	19.41	11.95	$98SCO_2@C_1$	160 C and 5900 psia	5.8	0.265	79	9.1	0.0497	270	0.72

Appendix D:

Table D-1: Gas-water relative permeability by using JBN method and Darcy's law.

PV		JBN Method														Darcy's law			
Sample S_C_2A																Eq. C1			
V inj	V pro	$\frac{W_i}{V_{gas}/P_v}$	$\frac{N_p}{V_{wat}/P_v}$	Δp_{psia}	Sw_{av}	Sw_2	I_r	f_w	f_g	WiI_r	d ($1/WiI_r$)	d ($1/Wi$)	K_{rw}	k_{rgas}	K_{rw}	k_{rgas}	f_w	f_g	
	0	0	0		0.083														
2.2	2.2	0.28	0.28	5.8	0.36	0.083	1.10	1	0	0.31	3.23	3.61	1.11	0	0.04	0.001	0.26	0	
2.7	2.6	0.34	0.33	5.7	0.41	0.14	1.12	0.8	0.2	0.38	13.14	15.9	0.97	0.033	0.0054	0.089	0.18	21.7	
4.3	3.6	0.54	0.45	5.5	0.54	0.2	1.22	0.63	0.38	0.66	3.57	4.97	0.87	0.071	0.0044	0.13	0.14	30.3	
6.2	4.5	0.78	0.57	5.4	0.65	0.28	1.34	0.47	0.53	1.05	2.58	4.18	0.77	0.12	0.0056	0.094	0.18	21.7	
8.5	5.5	1.07	0.69	5.6	0.78	0.31	1.35	0.44	0.57	1.45	2.51	3.46	0.6	0.11	0.0036	0.1544	0.12	37.1	
11.5	6.3	1.45	0.79	5.7	0.88	0.5	1.36	0.27	0.73	1.98	1.88	2.65	0.38	0.141	0.0024	0.19	0.08	46.4	
18.6	6.7	2.34	0.84	5.4	0.93	0.79	1.39	0.056	0.94	3.24	0.79	1.12	0.08	0.181	0.00045	0.28	0.014	63.7	
23.3	6.8	2.93	0.86	5.1	0.94	0.88	1.53	0	1	4.48	0.81	1.69	0	1	0.001	0.31	0	67.6	

Initial $q/\Delta p = 9.4$, Absolute permeability=115 md

Table D-2: Gas-water relative permeability by using JBN method and Darcy's law.

PV		JBN Method														Darcy's law			
Sample S_C_3A																Eq. C1			
V inj	V pro	$\frac{W_i}{V_{gas}/P_v}$	$\frac{N_p}{V_{wat}/P_v}$	Δp_{psia}	Sw_{av}	Sw_2	I_r	f_w	f_g	WiI_r	d ($1/WiI_r$)	d ($1/Wi$)	K_{rw}	k_{rgas}	K_{rw}	k_{rgas}	f_w	f_g	
1.8	1.8	0.34	0.32	9.7	0.42	0.1	1.0	1	0	0.32	3.16	3.17	1.00	0	0.075	0.001	0.195	0	
2.67	2.6	0.45	0.46	9.4	0.56	0.13	0.99	0.92	0.08	0.47	6.72	6.55	0.90	0.011	0.046	0.084	0.185	2.5	
4	3.55	0.70	0.62	9.3	0.72	0.22	1.0	0.71	0.29	0.72	3.94	4.29	0.78	0.042	0.041	0.28	0.164	8.1	
5.5	4.5	0.96	0.79	9.5	0.89	0.28	1.0	0.63	0.37	1.0	3.48	3.8	0.69	0.054	0.038	0.37	0.155	11.1	
6.68	4.9	1.17	0.86	10.2	0.96	0.56	1.0	0.34	0.66	1.18	5.69	4.83	0.29	0.076	0.014	1.04	0.06	33.3	
7.22	5	1.27	0.88	9.9	0.98	0.74	1.0	0.19	0.82	1.27	11.70	10.56	0.17	0.01	0.0040	1.30	0.017	40.5	
11	5.2	1.93	0.91	9.2	1.01	0.91	0.97	0.053	0.95	1.88	1.64	1.51	0.049	0.12	0.0031	1.7	0.012	47.9	
20	5.2	3.51	0.91	8.6	1.01	1.01	1.11	0	1	3.89	0.50	0.63	0	1	0.001	1.8	0	48.8	

Initial $q/\Delta p = 5.25$, Absolute permeability=8.4 md

Table D-3: Gas-water relative permeability by using JBN method and Darcy's law.

PV		32.99		JBN Method											Darcy's law			
Sample S_V_1													Eq. C1					
V inj	V pro	$\frac{W_i}{V_{gas/P_v}}$	$\frac{N_p}{V_{wat/P_v}}$	Δp psia	S_{wav}	S_{w2}	I_r	f_w	f_g	$W_i I_r$	$\frac{d}{(1/W_i I_r)}$	$\frac{d}{(1/W_i)}$	K_{rw}	k_{rgas}	K_{rw}	k_{rgas}	f_w	f_g
	0.000	0.000	0.000		0.080													
21.20	21.2	0.64	0.64	6.00	0.723	0.080	1.499	1.000	0.000	0.963	1.038	1.556	1.499	0.001	0.0750	0.0010	0.29	0.00
23.90	23.0	0.72	0.68	5.80	0.777	0.294	1.621	0.667	0.333	1.174	4.740	12.219	1.719	0.117	0.0068	0.0820	0.19	16.32
27.15	24.4	0.82	0.74	5.50	0.820	0.465	1.658	0.431	0.569	1.364	5.257	10.151	0.832	0.149	0.0033	0.1931	0.09	36.44
30.0	25.3	0.91	0.76	5.30	0.847	0.560	1.697	0.316	0.684	1.543	5.599	11.575	0.653	0.192	0.0017	0.2723	0.04	49.52
35.40	26.2	1.07	0.79	5.50	0.874	0.695	1.669	0.167	0.833	1.791	4.029	6.109	0.253	0.172	0.0010	0.2549	0.03	48.10
41.20	26.9	1.25	0.81	5.60	0.895	0.745	1.634	0.121	0.879	2.040	4.012	5.688	0.171	0.169	0.0006	0.2307	0.02	44.32
46.0	27.2	1.39	0.82	5.30	0.904	0.817	1.703	0.063	0.938	2.374	2.997	6.873	0.143	0.292	0.0005	0.2616	0.01	47.57
53.0	27.5	1.61	0.83	5.00	0.914	0.845	1.824	0.000	1.000	2.930	1.800	4.713	0.000	1.000	0.0003	0.2875	0.00	49.31

Initial $q/\Delta p = 8$, Absolute permeability=92 md

Table D-4: CO_2 -methane relative permeability for sample S_V_1 by using JBN method and Darcy's law.

T °C		160		JBN Method											Darcy's law			
P psia		5900													Eq. C1			
98 CO_2 @ 90 C1																		
$\frac{W_i}{V_{gas/P_v}}$	Produced con. %	$\frac{N_p}{V_{wat/P_v}}$	Δp psia	q ambient cc	S_{wav}	S_{w2}	I_r	f_{C1}	f_{CO2}	$W_i I_r$	$\frac{d}{(1/W_i I_r)}$	$\frac{d}{(1/W_i)}$	K_{rC1}	k_{rCO2}	k_{rCO2}	K_{rC1}	f_{CO2}	f_{C1}
0.00	0.00	0.00			0.08						0.00	0.00	1.00	0.00				
0.686	0.90	0.62	4.90	71.00	0.70	0.08	0.93	0.90	0.10	0.64	1.56	1.46	0.84	0.18	0.11	0.89	7.10	63.90
0.735	0.84	0.66	5.00	72.50	0.74	0.12	0.94	0.84	0.16	0.69	21.60	20.41	0.79	0.26	0.15	0.83	10.15	60.90
0.784	0.79	0.70	5.10	74.00	0.78	0.16	0.94	0.79	0.21	0.73	21.58	20.41	0.75	0.34	0.22	0.78	15.54	58.46
0.833	0.55	0.72	5.50	80.00	0.80	0.35	0.94	0.55	0.45	0.78	20.93	20.41	0.54	0.49	0.48	0.54	36.00	44.00
0.882	0.18	0.73	5.70	83.00	0.81	0.65	0.94	0.18	0.82	0.83	21.33	20.41	0.17	0.84	0.87	0.18	68.06	14.94
0.980	0.05	0.74	6.10	89.50	0.82	0.77	0.95	0.05	0.95	0.93	10.09	10.20	0.05	0.98	0.99	0.05	83.24	4.48

Initial $q/\Delta p = 15.5$, CO_2 effective permeability=270 md and methane effective permeability=156

Table D-5: SCO₂-methane relative permeability for sample S_V_1 by using JBN.

T °C	160	JBN Method													Power Model		
P psia	5900	JBN Method													Power Model		
98 SCO ₂ @ 75 C1		JBN Method													Power Model		
W_i V_{CO_2}/P_V	Produced con. %	N_p V_{C1}/P_V	Δp psia	q ambient cc	S_{av}	S_2	I_r	f_{C1}	f_{CO_2}	W_{iR}	d (1/ W_{iR})	d (1/ W_i)	Kr_{C1}	kr_{CO_2}	S_{CO_2}	Kr_{CO_2}	kr_{C1}
0.00	0	0.00			0.07						0.00	0.00	1.00	0.00	0.070	0.283	0.518
0.32	0.75	0.25	6.2	76	0.32	0.07	0.72	0.77	0.23	0.23	4.29	3.09	0.55	0.28	0.100	0.353	0.465
0.42	0.73	0.31	6.3	77	0.38	0.10	0.72	0.68	0.32	0.30	14.33	10.20	0.48	0.36	0.200	0.542	0.306
0.47	0.42	0.33	6.75	82	0.40	0.21	0.71	0.42	0.58	0.34	30.14	20.41	0.28	0.51	0.260	0.638	0.221
0.52	0.14	0.34	7.05	87	0.41	0.34	0.73	0.14	0.86	0.38	24.46	20.41	0.12	0.79	0.360	0.780	0.101
0.57	0.05	0.34	7.1	89	0.41	0.39	0.74	0.05	0.95	0.42	23.76	20.41	0.04	0.83	0.390	0.820	0.069

Initial $q/\Delta p = 17$

Table D-6: SCO₂-methane relative permeability for sample S_V_1 by using JBN.

T °C	160	JBN Method													Power Model		
P psia	5900	JBN Method													Power Model		
98 SCO ₂ @ 50 C1		JBN Method													Power Model		
W_i V_{CO_2}/P_V	Produced con. %	N_p V_{C1}/P_V	Δp psia	q ambient cc	S_{av}	S_2	I_r	f_{C1}	f_{CO_2}	W_{iR}	d (1/ W_{iR})	d (1/ W_i)	Kr_{C1}	kr_{CO_2}	S_{CO_2}	Kr_{CO_2}	kr_{C1}
0.00	0	0.000			0.06						0.00	0.00	1.00	0.00	0.060	0.448	0.344
0.29	0.48	0.141	7	80	0.20	0.06	0.63	0.48	0.52	0.19	5.36	3.40	0.30	0.45	0.100	0.581	0.263
0.34	0.44	0.163	7.1	81	0.22	0.07	0.63	0.44	0.56	0.22	32.54	20.41	0.28	0.46	0.130	0.664	0.208
0.39	0.33	0.179	7.2	84	0.24	0.11	0.65	0.33	0.67	0.25	27.26	20.41	0.25	0.61	0.160	0.738	0.157
0.44	0.11	0.184	7.2	87	0.24	0.20	0.67	0.11	0.89	0.30	23.83	20.41	0.09	0.81	0.190	0.806	0.112
0.49	0.05	0.187	7.1	89	0.25	0.22	0.70	0.05	0.95	0.34	22.13	20.41	0.05	0.89	0.230	0.888	0.058

Initial $q/\Delta p = 18$

Table D-7: SCO₂-methane relative permeability for sample S_V_1 by using JBN.

T °C		JBN Method														Power Model		
P psia		JBN Method														Power Model		
98 SCO ₂ @ 25 C1		JBN Method														Power Model		
W_i V_{CO_2}/P_V	Produced con. %	N_p V_{C1}/P_V	Δp psia	q ambient cc	S_{av}	S_2	I_r	f_{C1}	f_{CO_2}	$W_{i,r}$	d (1/ $W_{i,r}$)	d (1/ W_i)	Kr_{C1}	kr_{CO_2}	S_{CO_2}	Kr_{CO_2}	kr_{C1}	
0.00	0	0.000	0		0.05						0.00	0.00	1.00	0.00				
0.16	0.25	0.039	7.2	85	0.09	0.05	0.76	0.25	0.75	0.12	8.37	6.38	0.19	0.67	0.050	0.645	0.181	
0.20	0.25	0.049	7.25	85	0.10	0.05	0.76	0.25	0.75	0.15	34.69	25.51	0.18	0.64	0.070	0.725	0.113	
0.24	0.21	0.057	7.4	86	0.11	0.06	0.75	0.21	0.79	0.18	35.59	25.51	0.15	0.64	0.100	0.822	0.046	
0.27	0.15	0.063	7.45	87	0.11	0.07	0.75	0.15	0.85	0.21	32.91	25.51	0.12	0.72	0.120	0.876	0.020	
0.31	0.05	0.065	7.5	89	0.12	0.10	0.77	0.05	0.95	0.24	29.98	25.51	0.04	0.82				

Initial $q/\Delta p = 15.5$

Table D-8: SCO₂-methane relative permeability at speed 7 cm/hr using JBN method.

T °C		JBN Method														Power Model		
P psia		JBN Method														Power Model		
98 SCO ₂ @ 90 C1		JBN Method														Power Model		
W_i V_{CO_2}/P_V	Produced con. %	N_p V_{C1}/P_V	Δp psia	q ambient cc	S_{av}	S_2	I_r	f_{C1}	f_{CO_2}	$W_{i,r}$	d (1/ $W_{i,r}$)	d (1/ W_i)	Kr_{C1}	kr_{CO_2}	S_{CO_2}	Kr_{CO_2}	kr_{C1}	
0.00	0	0.000	0		0.07						0.00	0.00	1.00	0.00	0.070	0.151	0.691	
0.44	0.9	0.397	4.4	51.5	0.47	0.07	0.78	0.90	0.10	0.34	2.91	2.27	0.70	0.15	0.100	0.204	0.623	
0.49	0.85	0.439	4.55	53	0.51	0.09	0.78	0.85	0.15	0.38	27.47	20.41	0.63	0.20	0.200	0.365	0.451	
0.54	0.69	0.472	4.65	53.6	0.54	0.17	0.77	0.69	0.31	0.41	29.69	20.41	0.47	0.33	0.300	0.513	0.302	
0.59	0.43	0.493	4.95	56.5	0.56	0.31	0.76	0.43	0.57	0.45	30.09	20.41	0.29	0.50	0.400	0.653	0.178	
0.64	0.25	0.506	5.2	59.5	0.58	0.42	0.76	0.25	0.75	0.49	25.99	20.41	0.20	0.69	0.500	0.788	0.078	
													1.00	0.00	0.540	0.840	0.052	

Initial $q/\Delta p = 15$

Table D-9: SCO₂-methane relative permeability at speed 5 cm/hr using JBN method.

T °C	160	JBN Method													Power Model		
P psia	5900	JBN Method													Power Model		
98 SCO ₂ @ 90 C1		JBN Method													Power Model		
W_i V_{CO_2}/P_v	Produced con. %	N_p V_{C1}/P_v	Δp psia	q ambient cc	S_{av}	S_2	I_r	f_{C1}	f_{CO_2}	W_{iR}	d (1/ W_{iR})	d (1/ W_i)	Kr_{C1}	kr_{CO_2}	S_{CO_2}	Kr_{CO_2}	kr_{C1}
0.00	0	0.000	0		0.060						0.00	0.00	1.00	0.00			
0.32	0.9	0.291	3.8	35	0.351	0.06	0.61	0.90	0.10	0.20	5.04	3.09	0.55	0.12	0.060	0.117	0.535
0.37	0.7	0.325	3.95	36	0.385	0.12	0.61	0.70	0.30	0.23	36.11	20.41	0.40	0.27	0.100	0.188	0.455
0.42	0.36	0.343	4.1	37	0.403	0.25	0.60	0.36	0.64	0.25	36.69	20.41	0.20	0.45	0.230	0.408	0.236
0.47	0.16	0.351	4.3	39	0.411	0.34	0.60	0.16	0.84	0.28	32.36	20.41	0.10	0.59	0.360	0.619	0.078
0.52	0.05	0.353	4.55	42	0.413	0.39	0.62	0.05	0.95	0.32	28.41	20.41	0.04	0.70	0.400	0.682	0.041

Initial $q/\Delta p = 15$

Table D-10: SCO₂-methane relative permeability at speed 2 cm/hr using JBN method.

T °C	160	JBN Method													Power Model		
P psia	5900	JBN Method													Power Model		
98 SCO ₂ @ 90 C1		JBN Method													Power Model		
W_i V_{CO_2}/P_v	Produced con. %	N_p V_{C1}/P_v	Δp psia	q ambient cc	S_{av}	S_2	I_r	f_{C1}	f_{CO_2}	W_{iR}	d (1/ W_{iR})	d (1/ W_i)	Kr_{C1}	kr_{CO_2}	S_{CO_2}	Kr_{CO_2}	kr_{C1}
0.00	0	0.000	0		0.050						0.00	0.00	1.00	0.00			
0.23	0.89	0.201	3.1	13.5	0.251	0.05	0.62	0.89	0.11	0.14	7.13	4.44	0.55	0.13	0.050	0.138	0.500
0.27	0.68	0.234	3.4	14.5	0.284	0.10	0.61	0.68	0.32	0.17	37.10	20.41	0.37	0.27	0.100	0.256	0.377
0.32	0.3	0.249	3.6	15	0.299	0.20	0.60	0.30	0.70	0.19	39.49	20.41	0.16	0.44	0.180	0.433	0.228
0.37	0.12	0.255	3.7	15.5	0.305	0.26	0.60	0.12	0.88	0.22	32.93	20.41	0.07	0.59	0.250	0.579	0.100
0.42	0.05	0.257	4	17	0.307	0.29	0.61	0.05	0.95	0.26	30.32	20.41	0.03	0.65	0.300	0.682	0.040

Initial $q/\Delta p = 7$

Table D-11: SCO₂-methane relative permeability at speed 1 cm/hr using JBN method.

T °C	160	JBN Method													Power Model		
P psia	5900	JBN Method													Power Model		
98 SCO ₂ @ 90 C1		JBN Method													Power Model		
W_i V_{CO_2}/P_v	Produced con. %	N_p V_{C1}/P_v	Δp psia	q ambient cc	S_{av}	S_2	I_r	f_{C1}	f_{CO_2}	W_{iR}	d (1/ W_{iR})	d (1/ W_i)	Kr_{C1}	kr_{CO_2}	S_{CO_2}	Kr_{CO_2}	kr_{C1}
0.00	0	0.000	0		0.030						0.00	0.00	1.00	0.00	0.030	0.124	0.524
0.15	0.9	0.132	2.9	7	0.162	0.03	0.60	0.90	0.10	0.09	11.27	6.80	0.54	0.11	0.060	0.231	0.413
0.18	0.72	0.153	3.1	7.3	0.183	0.06	0.59	0.72	0.28	0.10	66.04	34.01	0.37	0.23	0.090	0.332	0.312
0.21	0.48	0.168	3.2	7.4	0.198	0.10	0.58	0.48	0.52	0.12	66.09	34.01	0.25	0.36	0.120	0.430	0.223
0.24	0.36	0.178	3.35	7.7	0.208	0.12	0.57	0.36	0.64	0.14	61.83	34.01	0.20	0.45	0.150	0.526	0.146
0.26	0.23	0.185	3.6	8.4	0.215	0.15	0.58	0.23	0.77	0.15	52.09	34.01	0.15	0.58	0.180	0.620	0.082
0.29	0.13	0.189	3.7	8.7	0.219	0.18	0.59	0.13	0.87	0.17	54.13	34.01	0.08	0.59	0.210	0.712	0.031
0.32	0.07	0.191	3.8	9.1	0.221	0.20	0.60	0.07	0.93	0.19	48.10	34.01	0.05	0.67	0.030	0.124	0.524

Initial $q/\Delta p = 4$

Table D-12: SCO₂-methane relative permeability at speed 10 cm/hr using JBN method.

T °C	160	JBN Method													Power Model		
P psia	4500	JBN Method													Power Model		
98 SCO ₂ @ 90 C1		JBN Method													Power Model		
W_i V_{CO_2}/P_v	Produced con. %	N_p V_{C1}/P_v	Δp psia	q ambient cc	S_{av}	S_2	I_r	f_{C1}	f_{CO_2}	W_{iR}	d (1/ W_{iR})	d (1/ W_i)	Kr_{C1}	kr_{CO_2}	S_{CO_2}	Kr_{CO_2}	kr_{C1}
0.00	0	0.00			0.08						0.00	0.00	1.00	0.00	0.070	0.104	0.673
0.59	0.9	0.54	4.2	58	0.62	0.08	0.81	0.92	0.08	0.48	2.09	1.70	0.75	0.12	0.120	0.169	0.589
0.64	0.82	0.58	4.4	60	0.66	0.13	0.80	0.84	0.16	0.51	30.02	20.41	0.57	0.18	0.280	0.363	0.375
0.69	0.57	0.61	4.7	63	0.69	0.29	0.79	0.58	0.42	0.54	33.40	20.41	0.36	0.36	0.440	0.545	0.202
0.74	0.23	0.62	5	67	0.70	0.53	0.79	0.23	0.77	0.58	26.01	20.41	0.18	0.68	0.600	0.720	0.073
0.78	0.05	0.62	5.15	69	0.70	0.66	0.79	0.05	0.95	0.62	25.95	20.41	0.04	0.76	0.660	0.784	0.040

Initial $q/\Delta p = 17$

Table D-13: CO₂-methane relative permeability at speed 10 cm/hr using JBN method.

T °C	160	JBN Method													Power Model		
P psia	3500	JBN Method													Power Model		
98 SCO ₂ @ 90 C1		JBN Method													Power Model		
W_i V_{CO_2}/P_v	Produced con. %	N_p V_{C1}/P_v	Δp psia	q ambient cc	S_{av}	S_2	I_r	f_{C1}	f_{CO_2}	$W_{i,r}$	d (1/ $W_{i,r}$)	d (1/ W_i)	Kr_{C1}	kr_{CO_2}	S_{CO_2}	Kr_{CO_2}	kr_{C1}
0.00	0	0.00			0.07						0.00	0.00	1.00	0.00	0.070	0.119	0.637
0.52	0.9	0.47	4	48	0.54	0.07	0.71	0.90	0.10	0.37	2.73	1.93	0.64	0.12	0.100	0.162	0.588
0.62	0.66	0.53	4.3	51	0.60	0.19	0.70	0.66	0.34	0.43	15.60	10.20	0.43	0.31	0.260	0.372	0.355
0.72	0.33	0.56	4.6	54	0.63	0.40	0.69	0.33	0.67	0.49	15.81	10.20	0.21	0.51	0.420	0.564	0.176
0.81	0.12	0.58	4.7	56	0.65	0.55	0.70	0.12	0.88	0.57	13.14	10.20	0.09	0.72	0.580	0.747	0.051
0.91	0.05	0.58	4.8	58	0.65	0.61	0.71	0.05	0.95	0.65	12.87	10.20	0.04	0.77	0.610	0.781	0.034

Initial $q/\Delta p = 17$

Table D-14: CO₂-methane relative permeability at speed 10 cm/hr using JBN method.

T °C	160	JBN Method													Power Model		
P psia	2500	JBN Method													Power Model		
98 SCO ₂ @ 90 C1		JBN Method													Power Model		
W_i V_{CO_2}/P_v	Produced con. %	N_p V_{C1}/P_v	Δp psia	q ambient cc	S_{av}	S_2	I_r	f_{C1}	f_{CO_2}	$W_{i,r}$	d (1/ $W_{i,r}$)	d (1/ W_i)	Kr_{C1}	kr_{CO_2}	S_{CO_2}	Kr_{CO_2}	kr_{C1}
0.00	0	0.00			0.07						0.00	0.00	1.00	0.00	0.070	0.119	0.637
0.43	0.9	0.39	3.8	34	0.46	0.07	0.75	0.90	0.10	0.32	3.11	2.32	0.67	0.11	0.100	0.162	0.588
0.53	0.76	0.46	4.1	36	0.53	0.13	0.73	0.76	0.24	0.39	15.22	10.20	0.51	0.22	0.180	0.270	0.465
0.63	0.53	0.51	4.3	37	0.58	0.25	0.72	0.53	0.47	0.45	16.00	10.20	0.34	0.36	0.340	0.469	0.259
0.73	0.35	0.55	4.4	37.5	0.62	0.36	0.71	0.35	0.65	0.52	15.31	10.20	0.23	0.49	0.500	0.657	0.107
0.82	0.12	0.56	4.5	38.5	0.63	0.53	0.71	0.12	0.88	0.59	13.92	10.20	0.09	0.67	0.580	0.747	0.051
0.92	0.05	0.57	4.60	40	0.64	0.59	0.72	0.05	0.95	0.67	12.40	10.20	0.04	0.79	0.610	0.781	0.034

Initial $q/\Delta p = 12$

Table D-15: SCO₂-methane relative permeability at speed 10 cm/hr using JBN method.

T °C	160	JBN Method												Power Model			
P psia	1500	JBN Method												Power Model			
98 SCO ₂ @ 90 C1		JBN Method												Power Model			
W_i V_{CO_2}/P_v	Produced con. %	N_p V_{C1}/P_v	Δp psia	q ambient cc	S_{av}	S_2	I_r	f_{C1}	f_{CO_2}	W_{iR}	d (1/ W_{iR})	d (1/ W_i)	Kr_{C1}	kr_{CO_2}	S_{CO_2}	Kr_{CO_2}	kr_{C1}
0.00	0	0.00			0.06						0.00	0.00	1.00	0.00	0.060	0.101	0.630
0.39	0.9	0.35	3.5	19	0.41	0.06	0.72	0.90	0.10	0.28	3.52	2.55	0.65	0.10	0.120	0.192	0.533
0.49	0.79	0.43	3.7	20	0.49	0.10	0.72	0.79	0.21	0.35	14.41	10.20	0.56	0.21	0.240	0.366	0.343
0.59	0.5	0.48	4	21	0.54	0.25	0.70	0.50	0.50	0.41	17.11	10.20	0.30	0.34	0.360	0.534	0.191
0.69	0.22	0.50	4.2	22	0.56	0.41	0.70	0.22	0.78	0.48	14.81	10.20	0.15	0.57	0.480	0.697	0.076
0.78	0.05	0.51	4.3	23	0.57	0.53	0.71	0.05	0.95	0.56	12.50	10.20	0.04	0.78	0.530	0.765	0.034

Initial $q/\Delta p = 7.5$

Table D-16: SCO₂-methane relative permeability at speed 10 cm/hr for sample S_C_1A using JBN method.

T °C	160	JBN Method												Power Model			
P psia	5900	JBN Method												Power Model			
98 SCO ₂ @ 90 C1		JBN Method												Power Model			
W_i V_{CO_2}/P_v	Produced con. %	N_p V_{C1}/P_v	Δp psia	q ambient cc	S_{av}	S_2	I_r	f_{C1}	f_{CO_2}	W_{iR}	d (1/ W_{iR})	d (1/ W_i)	Kr_{C1}	kr_{CO_2}	S_{CO_2}	Kr_{CO_2}	kr_{C1}
0.00	0	0.000	0		0.07						0.00	0.00	1.000	0.000	0.070	0.184	0.700
0.48	0.89	0.427	4.35	93	0.50	0.07	0.86	0.89	0.11	0.41	2.44	2.08	0.761	0.176	0.100	0.240	0.640
0.53	0.75	0.464	4.45	95	0.53	0.14	0.85	0.75	0.25	0.45	24.24	20.41	0.631	0.344	0.200	0.401	0.482
0.58	0.47	0.487	4.7	99	0.56	0.29	0.84	0.47	0.53	0.49	28.36	20.41	0.338	0.511	0.300	0.542	0.341
0.63	0.28	0.501	4.9	103	0.57	0.40	0.84	0.28	0.72	0.53	24.88	20.41	0.230	0.707	0.400	0.670	0.217
0.68	0.1	0.506	5.1	107	0.58	0.51	0.84	0.10	0.90	0.57	24.93	20.41	0.082	0.779	0.500	0.790	0.108
0.73	0.05	0.508	5.2	109	0.58	0.54	0.84	0.05	0.95	0.61	24.65	20.41	0.041	0.803	0.540	0.837	0.076

Initial $q/\Delta p = 25$

Table D-17: SCO₂-methane relative permeability at speed 10 cm/hr for sample S_C_2A using JBN method.

T °C	160	JBN Method													Power Model		
P psia	5900	JBN Method													Power Model		
98 SCO ₂ @ 90 C1		JBN Method													Power Model		
W_i V_{CO_2}/P_v	Produced con. %	N_p V_{C1}/P_v	Δp psia	q ambient cc	S_{av}	S_2	I_r	f_{C1}	f_{CO_2}	W_{iR}	d (1/ W_{iR})	d (1/ W_i)	Kr_{C1}	kr_{CO_2}	S_{CO_2}	Kr_{CO_2}	kr_{C1}
0.000	0.000	0.000	0		0.075						0.000	0.000	1.000	0.000	0.070	0.131	0.624
0.519	0.900	0.467	5.1	75	0.542	0.075	0.735	0.900	0.100	0.382	2.618	1.925	0.662	0.139	0.100	0.174	0.536
0.568	0.830	0.508	5.3	77	0.583	0.111	0.726	0.830	0.170	0.413	32.276	20.408	0.525	0.185	0.200	0.304	0.406
0.617	0.620	0.539	5.6	80	0.614	0.231	0.714	0.620	0.380	0.441	35.580	20.408	0.356	0.328	0.300	0.420	0.288
0.666	0.280	0.552	6	85	0.627	0.441	0.708	0.280	0.720	0.472	32.223	20.408	0.177	0.546	0.400	0.528	0.185
0.715	0.120	0.558	6.2	88	0.633	0.547	0.710	0.120	0.880	0.508	28.035	20.408	0.087	0.685	0.500	0.632	0.093
0.764	0.050	0.561	6.3	90	0.636	0.597	0.714	0.050	0.950	0.546	26.112	20.408	0.039	0.758	0.590	0.721	0.059

Initial $q/\Delta p = 20$

Table D-18: SCO₂-methane relative permeability at speed 10 cm/hr for sample S_C_3A using JBN method sample.

T °C	160	JBN Method													Power Model		
P psia	5900	JBN Method													Power Model		
98 SCO ₂ @ 90 C1		JBN Method													Power Model		
W_i V_{CO_2}/P_v	Produced con. %	N_p V_{C1}/P_v	Δp psia	q ambient cc	S_{av}	S_2	I_r	f_{C1}	f_{CO_2}	W_{iR}	d (1/ W_{iR})	d (1/ W_i)	Kr_{C1}	kr_{CO_2}	S_{CO_2}	Kr_{CO_2}	kr_{C1}
0.00	0	0.000	0		0.07						0.00	0.00	1.00	0.00	0.060	0.094	0.521
0.62	0.9	0.556	7.7	54	0.63	0.07	0.58	0.90	0.10	0.36	2.77	1.62	0.53	0.11	0.120	0.160	0.457
0.67	0.79	0.594	7.9	55	0.66	0.14	0.58	0.79	0.21	0.39	38.75	20.41	0.42	0.19	0.240	0.270	0.339
0.72	0.54	0.621	8.3	57	0.69	0.30	0.57	0.54	0.46	0.41	43.88	20.41	0.25	0.30	0.360	0.368	0.234
0.76	0.33	0.637	8.8	60	0.71	0.45	0.57	0.33	0.67	0.43	40.16	20.41	0.17	0.42	0.480	0.458	0.144
0.81	0.15	0.644	8.9	61	0.71	0.59	0.57	0.15	0.85	0.46	33.04	20.41	0.09	0.57	0.600	0.543	0.069
0.86	0.05	0.647	9	62	0.72	0.67	0.57	0.05	0.95	0.50	32.79	20.41	0.03	0.60	0.660	0.583	0.037

Initial $q/\Delta p = 12$

Table D-19: SCO₂-methane relative permeability at speed 10 cm/hr using JBN method sample S_C_1A.

T °C	95	JBN Method													Power Model		
P psia	5900	JBN Method													Power Model		
98 SCO ₂ @ 90 C1		JBN Method													Power Model		
W_i V_{CO_2}/P_v	Produced con. %	N_p V_{C1}/P_v	Δp psia	q ambient cc	S_{av}	S_2	I_r	f_{C1}	f_{CO_2}	W_{iR}	d (1/ W_{iR})	d (1/ W_i)	Kr_{C1}	kr_{CO_2}	S_{CO_2}	Kr_{CO_2}	kr_{C1}
0.00	0	0.00			0.07						0.00	0.00	1.00	0.00	0.070	0.194	0.755
0.470	0.89	0.42	4.5	106	0.49	0.07	0.89	0.89	0.11	0.42	2.39	2.13	0.79	0.22	0.100	0.251	0.686
0.568	0.6	0.48	4.7	107	0.55	0.18	0.86	0.65	0.35	0.49	14.25	10.20	0.46	0.43	0.220	0.447	0.446
0.666	0.46	0.53	5.1	112	0.60	0.29	0.83	0.46	0.54	0.55	15.64	10.20	0.30	0.53	0.340	0.614	0.259
0.764	0.32	0.56	5.3	115	0.63	0.38	0.82	0.32	0.68	0.63	13.58	10.20	0.24	0.69	0.460	0.766	0.124
0.862	0.16	0.57	5.5	119	0.64	0.51	0.82	0.16	0.84	0.70	12.78	10.20	0.13	0.78	0.580	0.907	0.036
0.960	0.05	0.58	5.5	121	0.65	0.60	0.83	0.05	0.95	0.80	10.73	10.20	0.05	0.93	0.610	0.941	0.022

Initial $q/\Delta p = 26.5$

Table D-20: SCO₂-methane relative permeability at speed 10 cm/hr using JBN method sample S_C_2A.

T °C	95	JBN Method													Power Model		
P psia	5900	JBN Method													Power Model		
98 SCO ₂ @ 90 C1		JBN Method													Power Model		
W_i V_{CO_2}/P_v	Produced con. %	N_p V_{C1}/P_v	Δp psia	q ambient cc	S_{av}	S_2	I_r	f_{C1}	f_{CO_2}	W_{iR}	d (1/ W_{iR})	d (1/ W_i)	Kr_{C1}	kr_{CO_2}	S_{CO_2}	Kr_{CO_2}	kr_{C1}
0.00	0	0.00			0.07						0.00	0.00	1.00	0.00	0.070	0.202	0.727
0.519	0.9	0.47	4.4	75	0.54	0.07	0.85	0.90	0.10	0.44	2.26	1.93	0.77	0.19	0.100	0.256	0.670
0.617	0.7	0.54	4.6	77	0.61	0.17	0.84	0.70	0.30	0.52	13.50	10.20	0.53	0.42	0.230	0.444	0.476
0.715	0.5	0.59	4.9	80	0.66	0.30	0.82	0.50	0.50	0.58	14.87	10.20	0.34	0.54	0.360	0.596	0.310
0.813	0.33	0.62	5.3	85	0.69	0.42	0.80	0.33	0.67	0.65	14.65	10.20	0.23	0.62	0.490	0.731	0.173
0.911	0.18	0.64	5.5	88	0.71	0.54	0.80	0.18	0.82	0.73	13.01	10.20	0.14	0.76	0.620	0.853	0.067
1.009	0.05	0.64	5.6	91	0.71	0.66	0.81	0.05	0.95	0.82	10.99	10.20	0.05	0.91	0.660	0.889	0.045

Initial $q/\Delta p = 20$

Table D-21: SCO₂-methane relative permeability at speed 10 cm/hr using JBN method sample S_C_3A.

T °C	95	JBN Method													Power Model		
P psia	5900																
98 SCO ₂ @ 90 C1																	
W_i V_{CO_2}/P_V	Produced con. %	N_p V_{C1}/P_V	Δp psia	q ambient cc	S_{av}	S_2	I_r	f_{C1}	f_{CO_2}	W_{ir}	d (1/ W_{ir})	d (1/ W_i)	Kr_{C1}	kr_{CO_2}	S_{CO_2}	Kr_{CO_2}	kr_{C1}
0.00	0	0.00			0.06						0.00	0.00	1.00	0.00	0.060	0.157	0.546
0.608	0.89	0.54	7.4	53	0.60	0.06	0.65	0.89	0.11	0.40	2.53	1.65	0.58	0.16	0.100	0.210	0.510
0.706	0.76	0.62	7.75	55	0.68	0.10	0.65	0.82	0.18	0.46	16.77	10.20	0.50	0.21	0.260	0.362	0.360
0.804	0.59	0.68	8.2	57	0.74	0.27	0.63	0.59	0.41	0.51	19.01	10.20	0.32	0.38	0.420	0.476	0.231
0.902	0.42	0.72	8.6	59	0.78	0.40	0.62	0.42	0.58	0.56	18.35	10.20	0.23	0.47	0.580	0.572	0.124
1.000	0.26	0.75	8.7	59.5	0.81	0.55	0.62	0.26	0.74	0.62	16.90	10.20	0.16	0.57	0.740	0.657	0.042
1.098	0.16	0.76	8.9	61	0.82	0.65	0.62	0.16	0.84	0.68	16.02	10.20	0.10	0.62	0.770	0.672	0.027

Initial $q/\Delta p = 11$

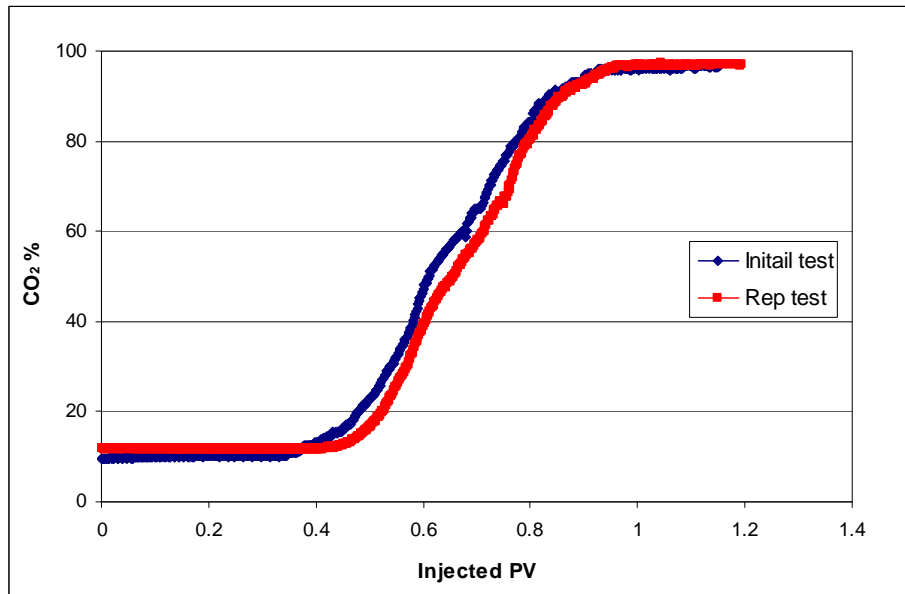


Figure D-1: Initial and repeatability tests at 2500 psia of sample S_V_1.

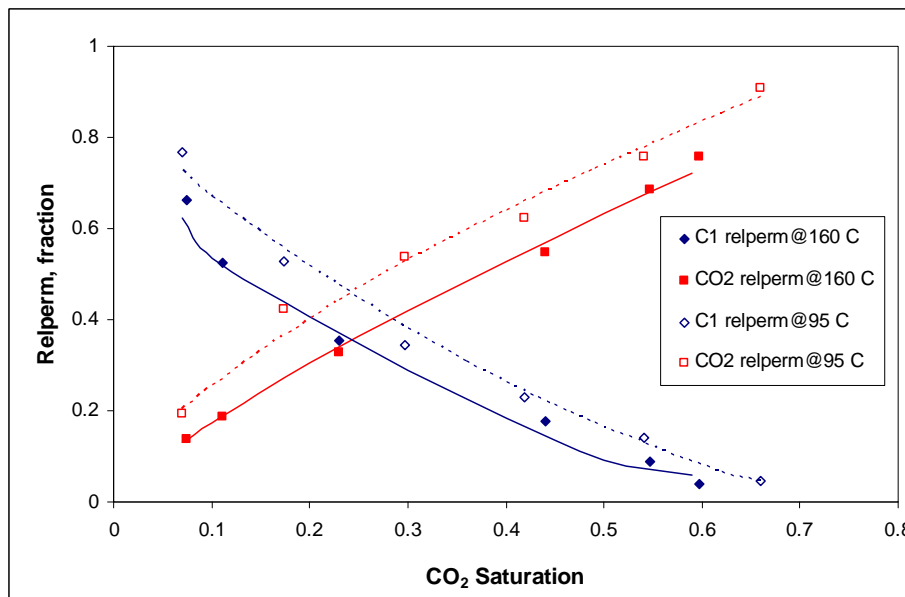


Figure D-2: SCO₂-methane relative permeability curves versus SCO₂ saturation for sample S_C_2A. Test condition; pore pressure 5900 psia, temperature 95 °C and 160 °C and displacement rate 10 cm/hr.

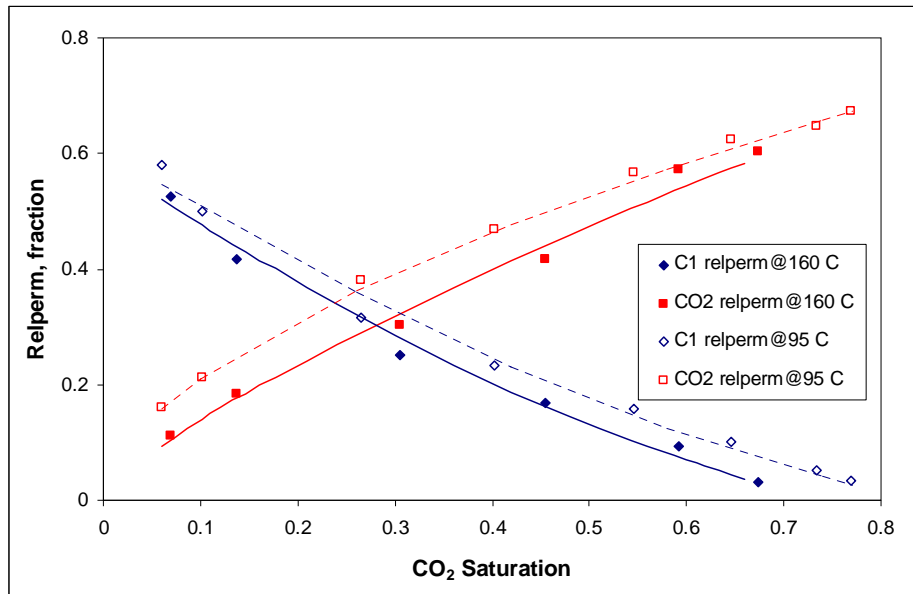


Figure D-3: SCO₂-methane relative permeability curves versus SCO₂ saturation for sample S_C_3A. Test condition; pore pressure 5900 psia, temperature 95 °C and 160 °C and displacement rate 10 cm/hr.

Appendix E:

Steady state test Relperm calculation:

Relative permeability is calculated for any phase by dividing their permeability during steady state test to their effective permeability. For example, relative permeability of a CO₂ phase from a steady state test is calculated by dividing CO₂ phase relative permeability at each subsequent percentage to its effective permeability when it comprised 98% of the effluent. In the same way for the methane phase, steady state relative permeability is obtained by dividing steady state methane permeability for each percentage to its effective permeability through (that) the sample when it comprised 90%.

The following Tables contain values which were used in calculating relative permeability of sample S_V_1 at 160 °C and 5900 psia. The effective permeability of CO₂ is used for calculating CO₂ phase relative permeability and it is acquired from CO₂ flooding to core sample S_V_1. While for methane its effective permeability obtained from the SCO₂ displacement by methane tests. Refer to Tables C-6 to C-8 for other sample relative permeability calculation.

Table E-1: Steady state Relperm calculation for sample S_V_1.

CO ₂ (%)	Δp (psi)	Visc (cp)	Flow rate (cc/min)	CO ₂ Relperm		
				Kg (md)	K _{CO2} 98%	Rel perm fraction
0.1	6.4	0.0252	8	12.22	270.00	0.05
0.2	5.5	0.029	20	40.92	270.00	0.15
0.5	5.9	0.0363	45	107.43	270.00	0.40
0.75	6.5	0.0426	69	175.48	270.00	0.65
CO ₂ (%)	Δp (psi)	Visc (cp)	Flow rate (cc/min)	C ₁ Relperm		
				Kg (md)	K _{CO2} 98%	Rel perm fraction
0.1	4.7	0.0252	68	141.48	156.00	0.91
0.2	5	0.029	58	130.54	156.00	0.84
0.5	6.2	0.0363	36	81.79	156.00	0.52
0.75	8.1	0.0426	16	32.65	156.00	0.21

Table E-2: Steady state relperm calculation for sample S_C_1A.

CO ₂ (%)	$\Delta\rho$ (psi)	Visc (cp)	Flow rate (cc/min)	CO ₂ Relperm		
				Kge (md)	K _{CO2} 98%	Rel perm fraction
0.1	5.8	0.0252	10	4.43	97.00	0.05
0.2	3.2	0.029	21	19.40	97.00	0.20
0.5	3.5	0.0363	55	58.16	97.00	0.60
0.75	4.6	0.0426	81	76.48	97.00	0.79
CO ₂ (%)	$\Delta\rho$ (psi)	Visc (cp)	Flow rate (cc/min)	C ₁ Relperm		
				Kge (md)	K _{CO2} 98%	Rel perm fraction
0.1	3.6	0.0252	83	59.24	61.00	0.97
0.2	3.9	0.029	74	56.10	61.00	0.92
0.5	4.1	0.0363	44	39.72	61.00	0.65
0.75	7.6	0.0426	26	14.86	61.00	0.24

Table E- 3: Steady state relperm calculation for sample S_C_2A.

CO ₂ (%)	$\Delta\rho$ (psi)	Visc (cp)	Flow rate (cc/min)	CO ₂ Relperm		
				Kge (md)	K _{CO2} 98%	Rel perm fraction
0.1	5.3	0.0252	7	3.39	67.00	0.05
0.2	5.5	0.029	18	9.68	67.00	0.14
0.5	5.7	0.0363	46	29.87	67.00	0.45
0.75	6.2	0.0426	70	49.04	67.00	0.73
CO ₂ (%)	$\Delta\rho$ (psi)	Visc (cp)	Flow rate (cc/min)	C ₁ Relperm		
				Kge (md)	K _{CO2} 98 %	Rel perm fraction
0.1	4.8	0.0252	68	36.40	40.00	0.91
0.2	5.2	0.029	59	33.55	40.00	0.84
0.5	6.5	0.0363	36	20.50	40.00	0.51
0.75	7.5	0.0426	16	9.27	40.00	0.23

Table E-4: Steady state relperm calculation for sample S_C_3A.

CO ₂ (%)	$\Delta\rho$ (psi)	Visc (cp)	Flow rate (cc/min)	CO ₂ Relperm		
				Kge (md)	K _{CO2} 98%	Rel perm fraction
0.1	12	0.0252	5.5	1.18	32.90	0.04
0.2	11.5	0.029	14	3.60	32.90	0.11
0.5	13	0.0363	36	10.25	32.90	0.31
0.75	13.5	0.0426	50	16.09	32.90	0.49
CO ₂ (%)	$\Delta\rho$ (psi)	Visc (cp)	Flow rate (cc/min)	C ₁ Relperm		
				Kge (md)	K _{CO2} 98%	Rel perm fraction
0.1	10.5	0.0252	49.5	12.11	16.50	0.73
0.2	11	0.029	42	11.29	16.50	0.68
0.5	12.5	0.0363	24	7.11	16.50	0.43
0.75	13.5	0.0426	10	3.22	16.50	0.19

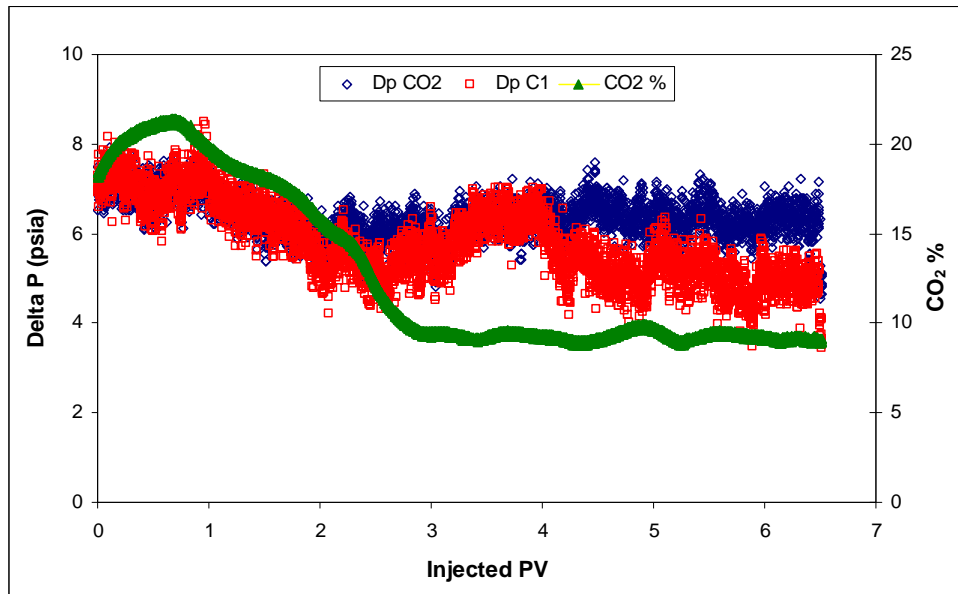


Figure E-1: Pressure drop versus injected pore volume from the simultaneous injection of SCO₂-methane through S_V_1 at 160 °C, 5900 psia and 10 cm/hr. SCO₂ concentration 10%.

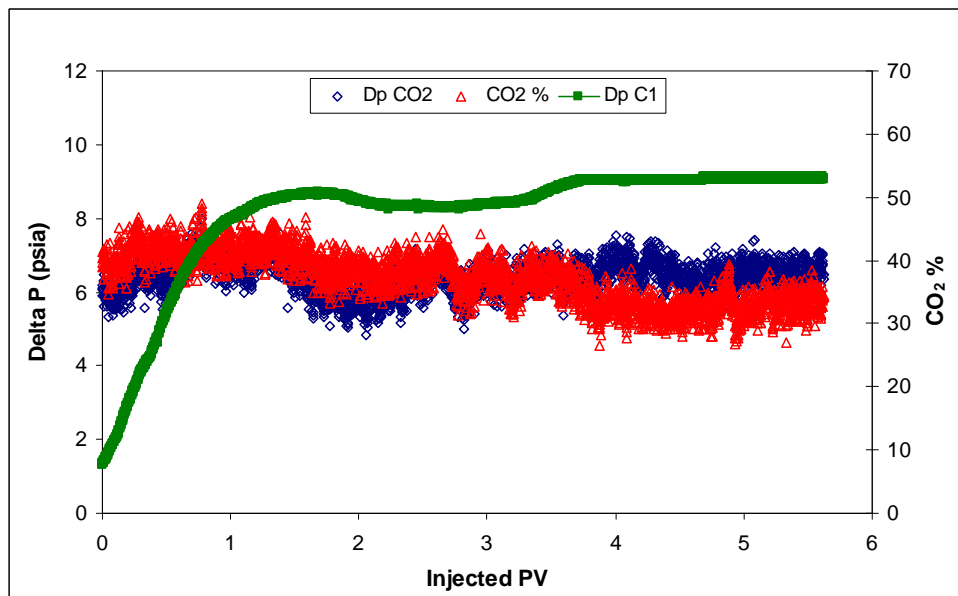


Figure E-2: Pressure drop versus injected pore volume from the simultaneous injection of SCO₂-methane through S_V_1 at 160 °C, 5900 psia and 10 cm/hr. SCO₂ concentration 50%.

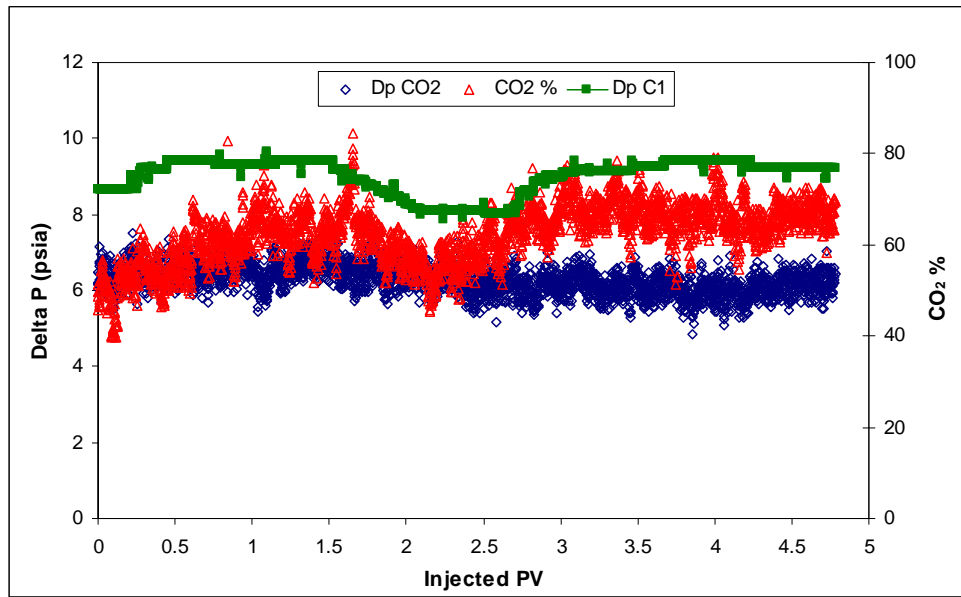


Figure E-3: Pressure drop versus injected pore volume from the simultaneous injection of SCO₂-methane through S_V_1 at 160 °C, 5900 psia and 10 cm/hr. SCO₂ concentration 20%.